A new air quality modelling approach at the regional scale using lidar data assimilation

Yiguo Y. Wang

Thèse de doctorat de l'École Polytechnique

Présentée et soutenue publiquement le 20 décembre 2013 par

Yiguo WANG

pour l'obtention du diplôme de docteur
de l'École Polytechnique

Spécialité: Physique

Une nouvelle approche de modélisation de la qualité de l'air à l'échelle régionale par assimilation de mesures lidar

---

Jury composé de

Pr Hervé Le Treut	IPSL, LMD	Président
Dr Matthias Beekmann	CNRS, LISA	Rapporteur
Dr Pierre Tulet	CNRS, LACy	Rapporteur
Pr Bertrand Calpini	MeteoSwiss	Examinateur
Dr Alain Dabas	Météo-France, CNRM	Examinateur
Dr Patrick Chazette	CEA, LSCE	Directreur de thèse
Dr Marc Bocquet	ENPC, CEREA	Co-directreur de thèse
Dr Karine Sartelet	ENPC, CEREA	Co-directrice de thèse

Acknowledgements

This thesis was supported by CEA (Commissariat à l'Énergie Atomique) and CEREA, joint laboratory École des Ponts ParisTech EDF R&D. Many thanks to all these institutions for financing this thesis.

I would like to express my sincere gratitude to my supervisors Karine Sartelet, Marc Bocquet and Patrick Chazette for their patience, motivation, and enthusiasm. I think they are the best mentors, who greatly enlarge my knowledge about air quality modelling, data assimilation and lidar observations. Also, it was them who sincerely helped me to polish papers and this manuscript. I will not forget these enjoyably three years studying with them.

I am also deeply grateful to my thesis committee, Dr Matthias Beekmann, Dr Pierre Tulet, Prof Bertrand Calpini, Dr Alain Dabas and Prof Hervé Le Treut for their attendance and encouragement. In particular, I sincerely thank my thesis referees, Dr Matthias Beekmann and Dr Pierre Tulet, for their helpful comments. Additionally, I thank Dr Pierre Tulet for coming to Paris from La Réunion.

I thank my former colleague in CEREA, Youngseob Kim, for his help to use the air quality platform POLYPHEMUS in my first year and for sharing his knowledge. I thank my former colleague in CEREA, Lin Wu, for his geostatistical algorithms in Chapter 2 and for his help in data assimilation. Also I thank my colleague in CEREA, Vivien Mallet, for his help to use the data in format HDF and to update the algorithm for the ECMWF data. I thank research engineers Pierre Tran and Sylvain Doré for their help on computer techniques.

My stay in CEREA was unforgettable. I enjoyed the cakes and chocolates shared by my colleagues: Christian Seigneur, Véronique Dehlinger, Yelva Roustan, Jérôme Drevet, Laëtitia Girault, Yongfeng Qu, Nicolas Yan, Giuliana Becerra, Mohammad Reza Koohkan, Stéphanie Deschamps, Masoud Fallah Shorshani, Nicolas Chérin (in the same room during three years), Eve Lecoeur, Victor Winiarek, Florian Couvidat, Shupeng Zhu and Régis Briant, Elsa Real, Nora Duhanyan and Antoine Waked, etc. Also, it was unforgettable to have lunch with my colleagues Philippe Royer and Xiaoxia Shang in CEA.

Finally, I would like to sincerely thank my family for their support and encouragement. In particular, I am grateful to my wife, Shuo Wang, for accompanying me in France.

Abstract

Assimilation of lidar observations for air quality modelling is investigated via the development of a new model, which assimilates ground-based lidar network measurements using optimal interpolation (OI) in a chemistry transport model. First, a tool for assimilating PM_{10} (particulate matter with a diameter lower than 10 μm) concentration measurements on the vertical is developed in the air quality modelling platform POLYPHEMUS. It is applied to western Europe for one month from 15 July to 15 August 2001 to investigate the potential impact of future ground-based lidar networks on analysis and short-term forecasts (the description of the future) of PM_{10}. The efficiency of assimilating lidar network measurements is compared to the efficiency of assimilating concentration measurements from the AirBase ground network, which includes about 500 stations in western Europe. A sensitivity study on the number and location of required lidars is also performed to help define an optimal lidar network for PM_{10} forecasts.

Secondly, a new model for simulating normalised lidar signals (PR_2) is developed and integrated in POLYPHEMUS. Simulated lidar signals are compared to hourly ground-based mobile and *in-situ* lidar observations performed during the MEGAPOLI (Megacities : Emissions, urban, regional and Global Atmospheric POLlution and climate effects, and Integrated tools for assessment and mitigation) summer experiment in July 2009. It is found that the model correctly reproduces the vertical distribution of aerosol optical properties and their temporal variability. Additionally, two new algorithms for assimilating lidar signals are presented and evaluated during MEGAPOLI. The aerosol simulations without and with lidar data assimilation are evaluated using the AIRPARIF (a regional operational network in charge of air quality survey around the Paris area) database to demonstrate the feasibility and the usefulness of assimilating lidar profiles for aerosol forecasts.

Finally, POLYPHEMUS with the model for assimilating lidar signals is applied to the Mediterranean basin, where 9 ground-based lidar stations from the ACTRIS/EARLINET network and 1 lidar station in Corsica performed a 72-hour period of intensive and continuous measurements in July 2012. Several parameters of the assimilation system are also studied to better estimate the spatial and temporal influence of the assimilation of lidar signals on aerosol forecasts.

Résumé

L'assimilation de données lidar pour la modélisation de la qualité de l'air est étudiée via le développement d'un modèle d'assimilation des observations d'un réseau lidar au sol par la méthode d'interpolation optimale (IO) dans un modèle de chimie-transport. Dans un premier temps, un outil d'assimilation des concentrations de PM_{10} (particules en suspension dans l'air dont le diamètre est inférieur à 10 μm) sur la verticale est développé dans la plateforme de modélisation de la qualité de l'air POLYPHEMUS. Cet outil est appliqué sur l'Europe de l'Ouest, du 15 juillet au 15 août 2001, afin d'étudier l'impact potentiel d'un futur réseau lidar au sol sur la modélisation et les prévisions (la description de l'avenir) des PM_{10}. En utilisant un réseau lidar fictif, l'efficacité de l'assimilation des mesures d'un réseau lidar est comparée à celle d'assimiler des mesures de concentrations du réseau au sol AirBase, qui comprend environ 500 stations sol en Europe de l'Ouest. Des études de sensibilité sur le nombre et la position géographique des lidars sont également menées afin d'aider à définir un réseau lidar optimal pour les prévisions des PM_{10}.

Ensuite, un modèle de simulation de signal lidar normalisé (PR_2) est construit et intégré dans POLYPHEMUS. Il est évalué par comparaison aux mesures d'un lidar mobile et d'un lidar fixe en Île-de-France durant la campagne d'été du programme de recherche européen MEGAPOLI (Megacities : Emissions, urban, regional and Global Atmospheric POLlution and climate effects, and Integrated tools for assessment and mitigation, juillet 2009). Les résultats montrent que ce modèle reproduit correctement la distribution verticale des propriétés optiques des aérosols et leur variabilité temporelle. Deux nouveaux algorithmes d'assimilation de signaux lidar sont également introduits et évalués durant la campagne MEGAPOLI. Les simulations des concentrations en masse d'aérosol avec et sans assimilation de données lidar sont évaluées en utilisant les données d'AIRPARIF (un réseau opérationnel régional pour la qualité de l'air en Île-de-France) pour démontrer la faisabilité et l'utilité de l'assimilation des signaux lidar pour les prévisions d'aérosols.

Enfin, POLYPHEMUS, avec le modèle d'assimilation des signaux lidar, est appliqué dans le bassin Méditerranéen, où 9 lidar du réseau ACTRIS/EARLINET et 1 lidar à Corse ont effectué une période de 72 heures de mesures intensives et continues en juillet 2012 (Pre-CHArMEx). Les paramètres dans le modèle d'assimilation des signaux lidar sont aussi étudiés pour mieux caractériser son impact spatial et temporel sur les prévisions d'aérosols.

List of Figures

List of Tables

Contents

Chapter 1

Introduction

Sommaire

1.1 Atmospheric particulate matter

Atmospheric particulate matter, also known as particles or particulate matter (PM), consists of tiny pieces of solid or liquid matter in suspension in the atmosphere. They are suspended in the Earth's atmosphere as atmospheric aerosols, which refer to the particulate-air mixture as opposed to the particulate matter alone. However, we commonly use the term "aerosol" to refer to the particle component alone. Aerosols can be emitted as particles (primary sources), for example soil dust and sea-salt particles. They can also be formed in the atmosphere from precursor gases (secondary sources) via dynamic processes. Some aerosol sources are natural, e.g., volcanic emissions and sea spray from oceans. Other sources, such as sulfate and nitrate particles resulting from fossil-fuel burning, are anthropogenic. Sometimes, particles are formed from the interaction of chemical components from natural and anthropogenic origins, e.g. organic compounds formed from the interaction of biogenic precursors with anthropogenic oxidants. Aerosol sources are shown in Figure 1.1. Aerosols can be removed from the atmosphere by

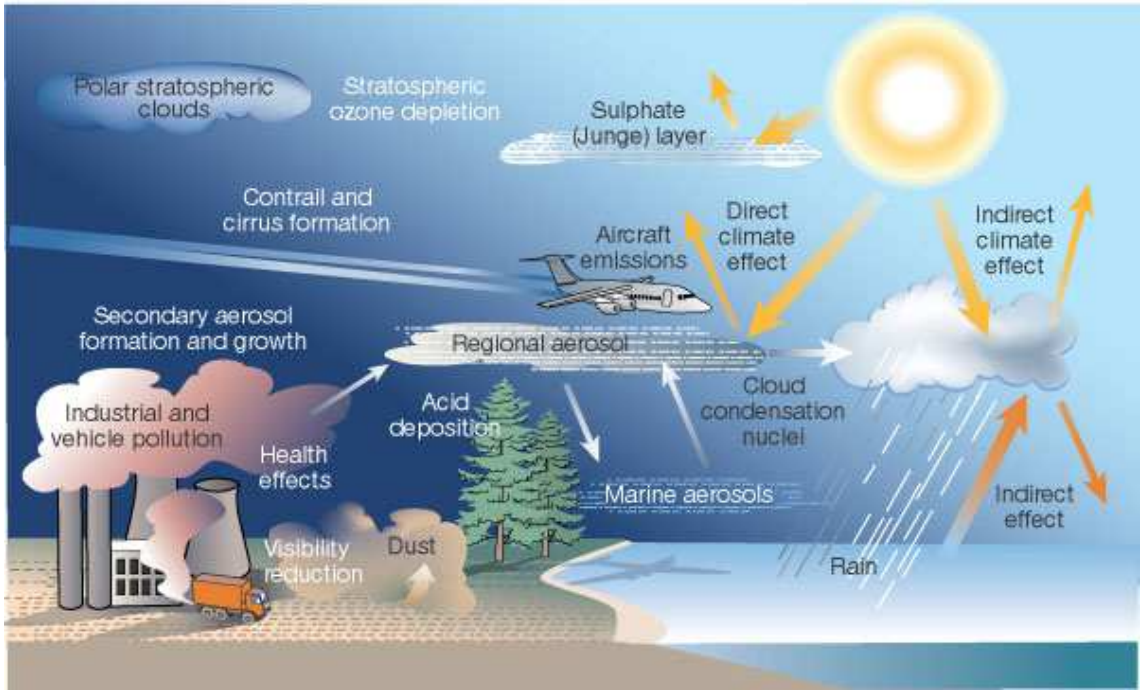

Figure 1.1: Scheme representing aerosol sources (anthropogenic and natural sources) and their effects (from Kolb [2002]).

sedimentation due to gravity or by impaction onto obstacles on the Earth's surface, i.e. "dry deposition" or "dry scavenging". Aerosols are also removed by collision with rain drops and snow flakes and by uptake into cloud droplets or ice crystals. The removal of aerosols in-cloud and below-cloud by precipitation is called "wet deposition" or "wet scavenging". In an annual global mean, wet deposition is the main removal process of atmospheric aerosols, which removes 80%-90% of the aerosol mass. The remaining 10%-20% are removed by dry deposition [Anthony and Mary-Scott, 1990].

The diameters of aerosols span over four orders of magnitude, from a few nanometres to

several tens of micrometres. The size of particles affects both their lifetime in the atmosphere and their chemical and physical properties. An example of the aerosol mass concentration (μg m^{-3}), aerosol number concentration (cm^{-3}) and aerosol lifetime in hours as function of particle size in Beijing is given in Figure 1.2. The high number of particles of diameter lower than 0.1 μm are believed to originate from vehicle emissions or secondary particle formation (such as nucleation). However, they have short lifetimes, since they diffuse very quickly toward other particles and coagulate. In addition, the total mass of these particles (of diameter lower than 0.1 μm, ultrafine particles) represents a very small fraction of the aerosol mass concentration in the atmosphere. Particles of diameter between 0.1 and 2 μm suspend at a longer time in the atmosphere, up to 1 or 2 weeks. They represent a larger fraction of the aerosol mass concentration in the atmosphere, whereas their number concentration is much lower than that of ultrafine particles. Particles of this size range can act as nuclei for the formation of cloud droplets and this process is their main removal path way [Twomey, 1977] (see section 1.1.3). Coarse particles are characterised by low number, relatively large mass per particle, and short lifetimes (see Figure 1.2). Particles of diameter larger than 10 μm are quickly deposited by gravitational settling.

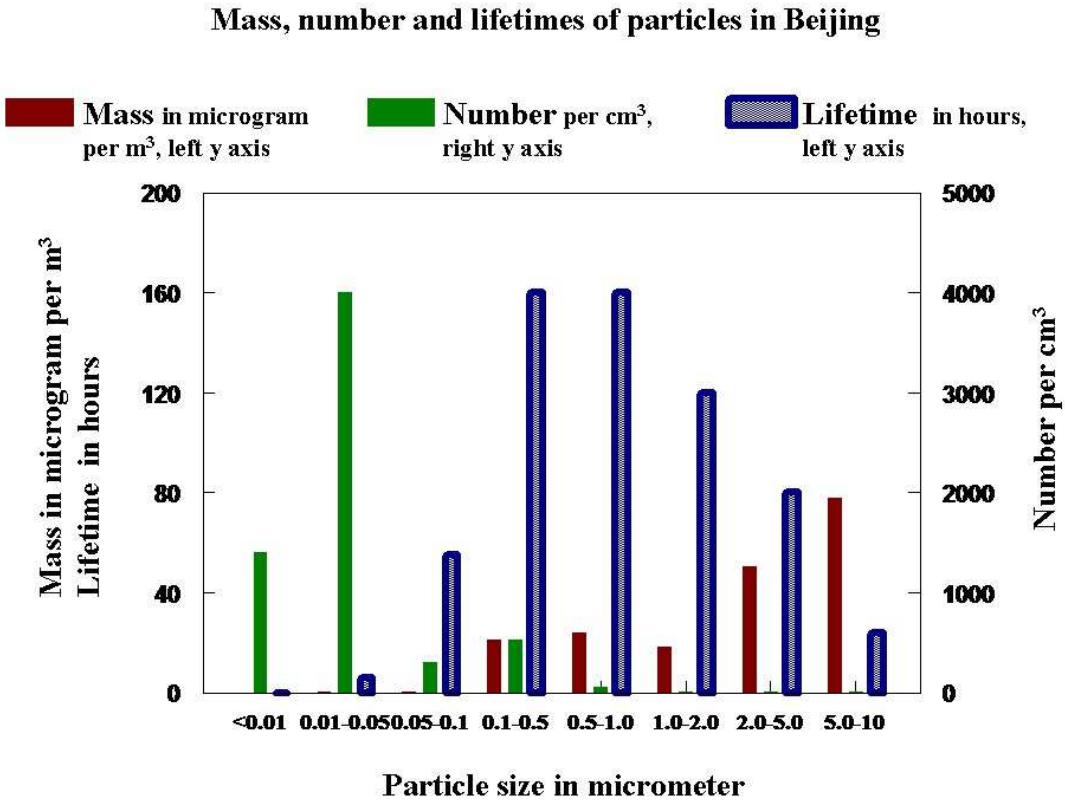

Figure 1.2: Mass, number and lifetimes of particles in Beijing in summer 2004 (from `http://www.eoearth.org/`).

1.1.1 Health effects

Epidemiological studies established that particles have a large impact on human health. Aerosol pollution associated to deaths and health problems were first demonstrated in the early 1970s. It has been confirmed in many studies since then. For example, Mokdad et al. [2004] reported that aerosol pollution causes 22,000-52,000 deaths per year in the United States (from 2000) and [European Environment Agency (EEA), 2009] reported that about 370,000 premature deaths in Europe in 2005 were caused by aerosol pollution.

The health effects of inhaling particles have been widely studied in humans and animals. They include asthma, lung cancer, cardiovascular issues, respiratory diseases, birth defects, and premature death. The size of the particle determines where in the respiratory tract the particle will rest after being inhaled. Larger particles, such as particles of diameter higher than 10 μm, are usually filtered by the nose and the throat via cilia and mucus. However, particles of diameter lower than 10 μm, referred to as PM_{10}, can reach the bronchi or lungs and cause health problems. The 10 μm cut-off size has been used for monitoring of atmospheric particles by most regulatory agencies in the U.S and in Europe.

Particles of diameter lower than 2.5 μm, referred to as $PM_{2.5}$, may be inhaled in the gas exchange regions of the lung. Ultra-fine particles (of diameter lower than 0.1 μm or $PM_{0.1}$) may pass through lungs to affect other organs and may damage the cardiovascular system [Satariano, 2008]. Recently, overviews have been compiled to analyse the impact of $PM_{2.5}$ on human health, in terms of decreased lifespan in months, in Europe (Clean Air for Europe Report [Amann et al., 2005]). For example, Figure 1.3 shows the large impact of $PM_{2.5}$ on diminished life expectancy (dark areas). Presently, the European legislation on emission controls is being fully implemented. It is estimated that in 2020 the forthcoming reductions in European emissions will extend life expectancy in Europe by about 2.5 months. Moreover, a study performed in the U.S for the period between 1970 and 2000 showed that a decrease of 10 $\mu\mathrm{g\ m^{-3}}$on $PM_{2.5}$ led to an augmentation of life expectancy between of 5 and 9 months [Pop et al., 2009].

Considering the health effects of particles, WHO (the World Health Organization) set guideline values for aerosol concentrations in 2005. They recommend that the annual mean concentrations should be less than 20 μg m^{-3} for PM_{10} and 10 μg m^{-3} for $PM_{2.5}$, and that the 24-hour mean concentrations should be less than 50 μg m^{-3} for PM_{10} and 25 μg m^{-3} for $PM_{2.5}$. However, governments set their own air quality standards, which may differ from the recommendations of WHO. Europe has set limits for PM_{10} since 2005: the annual mean concentrations should be less than 40 μg m^{-3} and the 24-hour mean concentrations should be less than 50 μg m^{-3}. The European regulation for $PM_{2.5}$ will enter into force in 2015: the annual mean concentrations should be less than 25 μg m^{-3}; in 2020, it will be lowered to 20 μg m^{-3}.

1.1.2 Visibility effects

Visibility affects all traffic types, e.g. roads, sailing and aviation. Low visibility may lead to traffic accidents. The visibility degradation is also one of the most obvious manifestations of air pollution and can bring prejudices to potential tourists. Poor visibility in natural areas (e.g. parks, forests, seashores) affects negatively the perception of the natural environment and, consistently, leads to economic disbenefits. Aerosols have a large impact on visibility, as they scatter light. Depending on their chemical composition, particles can also absorb visible light (such as black carbon). An example of the visibility degradation due to particles in Beijing is

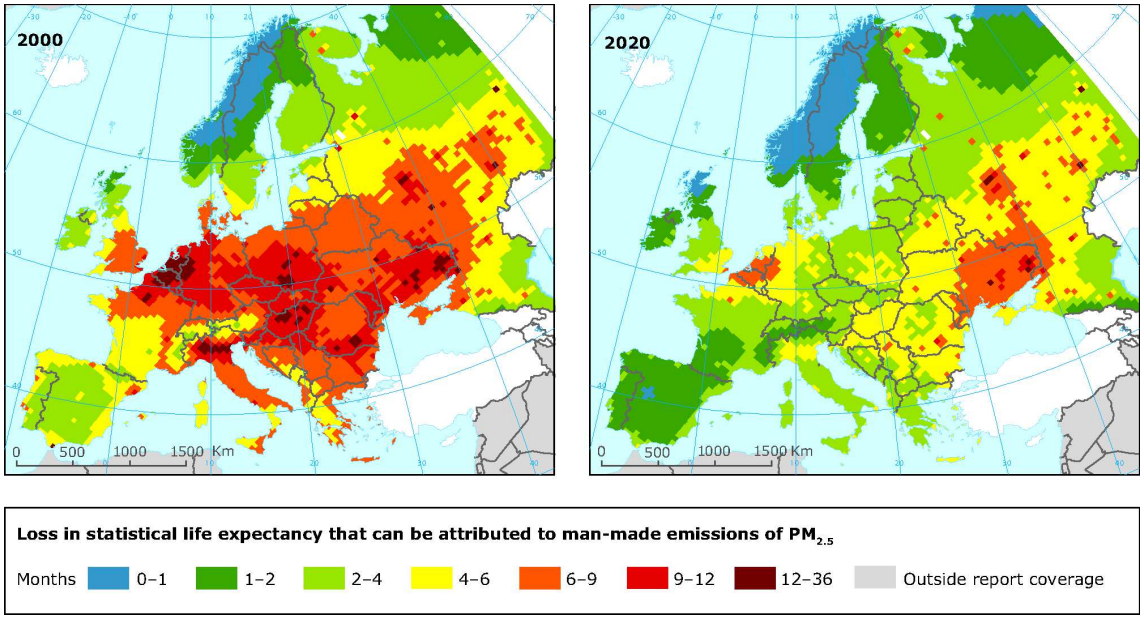

Figure 1.3: Loss of statistical life expectancy attributed to anthropogenic contributions to $PM_{2.5}$, in 2000 and 2020 (from Amann et al. [2005]).

shown in Figure 1.4.

1.1.3 Climate effects

Aerosols can affect the Earth's climate [Intergovernment Panel on Climate Control (IPCC), 2007]. This is because of their effects on the incoming solar radiation and outgoing terrestrial long-wave radiation. Aerosol effects can be split into direct, semi-direct and indirect effects.

Direct aerosol radiative effects

Direct aerosol effects consist of direct radiation interactions with aerosols, such as absorption or scattering (see section 1.1.2). Aerosols impact both short-wave and long-wave radiations. Thus, they can alter the radiative balance of the Earth-atmosphere system. The direct radiative forcing is determined by aerosol optical properties, such as the single scattering albedo, specific extinction coefficient and the scattering phase function, etc. These aerosol optical properties depend on the wavelength, aerosol chemical compositions, relative humidity, and aerosol size distribution of the aerosols. As deduced from models [Intergovernment Panel on Climate Control (IPCC), 2007], anthropogenic aerosols (sulphate, organic carbon, black carbon, nitrate and dust) tend to produce a cooling effect, with a total direct radiative forcing of -0.5 [-0.9 to -0.1] W/m^2 (see Figure 1.5).

Semi-direct aerosol radiative effects

Semi-direct effects are associated with radiative effects caused by absorbing particles such as soot (see section 1.1.2), except for direct effects (absorption or scattering). For example, the

Figure 1.4: A composite photograph shows Beijing's skyline during the sandstorm on Feb. 28 2013 and during good air quality condition on Feb. 19 2013 (taken by Feng Li).

surrounding air heated by absorbing aerosols inhibits the condensation of water vapour. That leads to less cloud formation in the atmosphere [Hansen et al., 1997; Ackerman et al., 2000]. Additionally, the heated air inhibits atmospheric convection, and inhibits the convective uplift of water vapour, which also reduces cloud formations. Moreover, the heating of the atmosphere leads to a cooling of the surface, and leads to less evaporation of surface water. These effects increase the Earth's albedo due to the reduction of cloud cover. Semi-direct effects due to particles have a negative radiative forcing [Intergovernment Panel on Climate Control (IPCC), 2007].

Indirect aerosol radiative effects

Indirect aerosol effects consist of several different effects. Aerosols can serve as condensation nuclei for water vapour (cloud condensation nuclei, CCN). For a given meteorological condition, increasing CCN due to aerosols leads to an increase in the number of cloud droplets. That leads to an increase in the albedo of the cloud [Twomey, 1977]. An increase in the number of cloud droplets due to aerosols reduces the cloud droplet size, because the same amount of water vapour is divided into more cloud droplets. This reduces precipitation and increases the cloud droplet lifetime. Aerosols tend to produce an indirect cooling effect, with a total radiative forcing on the order of -0.7 [-1.8 to -0.3] W/m^2 [Intergovernment Panel on Climate Control (IPCC), 2007] (see Figure 1.5).

1.2 Aerosol monitoring

In order to better understand atmospheric aerosols, measurements of aerosol spatial distributions and properties have been performed over the years. Measurements of aerosol properties consist of the number concentration, mass concentration, size distribution, chemical composition and optical properties either routinely sites or during intensive field campaigns.

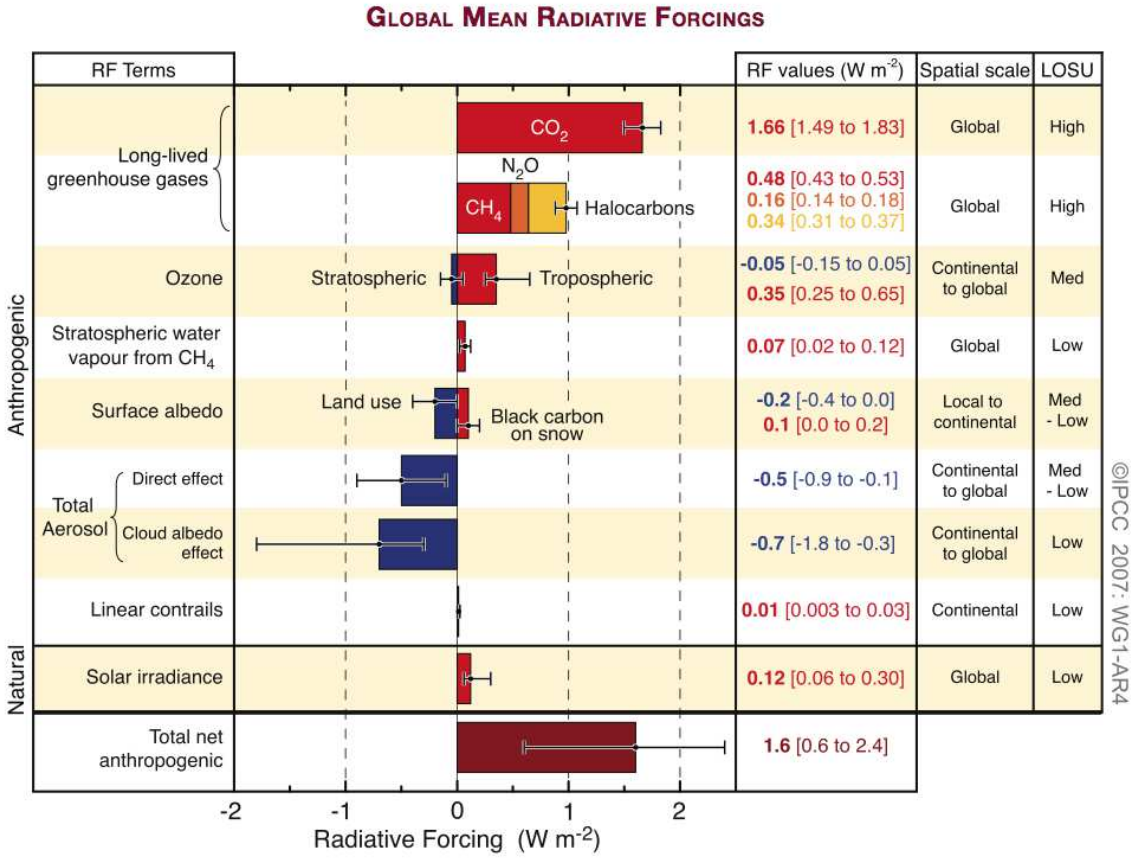

Figure 1.5: Global average radiative forcing (RF) in 2005 with respect to 1750 for CO_2, CH_4, N_2O, aerosols and other important agents and mechanisms. LOSU stands for the level of scientific understanding. Blue bars indicate a negative or cooling effect on the climate. Red bars indicate a positive or heating effect. From Intergovernment Panel on Climate Control (IPCC) [2007].

1.2.1 Surface measurements

Most of the national ambient air quality standards are based on the mass concentrations of PM_{10} and $PM_{2.5}$ (see section 1.1.1). Therefore, aerosol mass concentrations are routinely measured by monitoring stations at various locations around the world. Measurements of the aerosol mass were first presented in 1885. They were implemented by drawing the atmospheric air through filter paper, which collected particulate matters. With the development of science and technology in the 20th century, the PM measurement technology has improved. The PM mass concentration can now be measured by both manual methods and automated methods.

Manual methods are commonly used techniques for measuring PM mass concentrations, since they are easily performed. They employ a filter. The filter is weighed before and after sampling under the same temperature and relative humidity conditions. These conditions are typically different from the atmospheric sampling conditions. There may be sampling artifacts associated with semi-volatile components of PM including positive artifacts (gases absorbing

to the filter) and negative artifacts (volatilization from the filter). These artifacts may be minimised by using denuder tubes (to minimise positive artifacts), back-up filters (to minimise negative artifacts). Thus, PM mass concentrations are determined from the mass increase in filter and the volume of air sampled. A filter sampler includes common inlets. Most common, inlets are designed to deliver all particles of diameter lower than a specified size, e.g. 10 or 2.5 μm. There are, however, sampling artifacts as some particles of diameter larger than that of the inlet cutoff can be sampled and some particles of diameter smaller than that of the inlet cutoff may not. Automated methods for PM mass concentration measurements have been discussed in Williams et al. [1993]. The advantages of automated methods are that they may improve precision compared to manual methods and can provide real-time data with short time resolution. However, there are artifacts associated with semi-volatile components.

In situ PM mass concentration measurements may provide high-quality information, and the most frequently used data are retrieved from in situ surface networks, e.g. AirBase (`http://www.eea.europa.eu/`) and EMEP (European Monitoring and Evaluation Programme) over Europe, BDQA (Base de Données de la Qualité de l'Air) in France [Sartelet et al., 2007; Konovalov et al., 2009]. However, they do not provide direct information on vertical profiles, and their spatial and temporal representativeness is limited.

1.2.2 Satellite remote sensing

The satellite is an advanced tool to monitor aerosols and to improve our understanding of aerosol properties. An advantage of the use of satellites is that they can provide routine measurements on a global scale.

Presently, the "A-train" constellation of satellites has been established, which includes GCOM-W1 (SHIZUKU), Aqua, CloudSat, CALIPSO and Aura satellites, and travels across the equator at around 1:30 p.m. local time each afternoon. The "A" stands for "afternoon" (see Figure 1.6). These five satellites contain more than 15 separate scientific instruments to observe atmospheric components. For example, the Cloud-Aerosol Lidar and Infrared Pathfinder Satellite Observations (CALIPSO) spaceborne lidar provides backscattering coefficient profiles of aerosols and clouds at 532 and 1064 nm from 2 to 40 km above ground level. The radar onboard CloudSat, the polarisation sensitive radiometer POLDER onboard Parasol and MODIS spectra onboard Aqua satellite provide data, which produce the most complete description of clouds and aerosols on a global scale.

In terms of information content, satellite data can be classified into three categories. The first is devoted to scanning the spatial and temporal distributions of aerosols. The second aims at columnar aerosol properties retrievals, through the use of spectral, polarisation, and angular characteristics of backscattered solar light. The third aims at providing information on the vertical profile of aerosols from the surface into the stratosphere. In certain satellites, a combination of sensors may be used.

In terms of the observation geometry, there are two basic types of satellite instruments: vertical (nadir) and horizontal (limb) measurements. In vertical observations, the instrument looks straight down to sense the radiation coming from the Earth, and measures columnar observation. Most instruments employ this concept to provide column integrated products (see Figure 1.6). Horizontal observations can probe the Earth's atmosphere at various altitudes. They provide a longer path through the atmosphere than vertical observations (see Figure 1.6).

Aerosol properties retrievals from satellites depend on the interaction of the radiation scat-

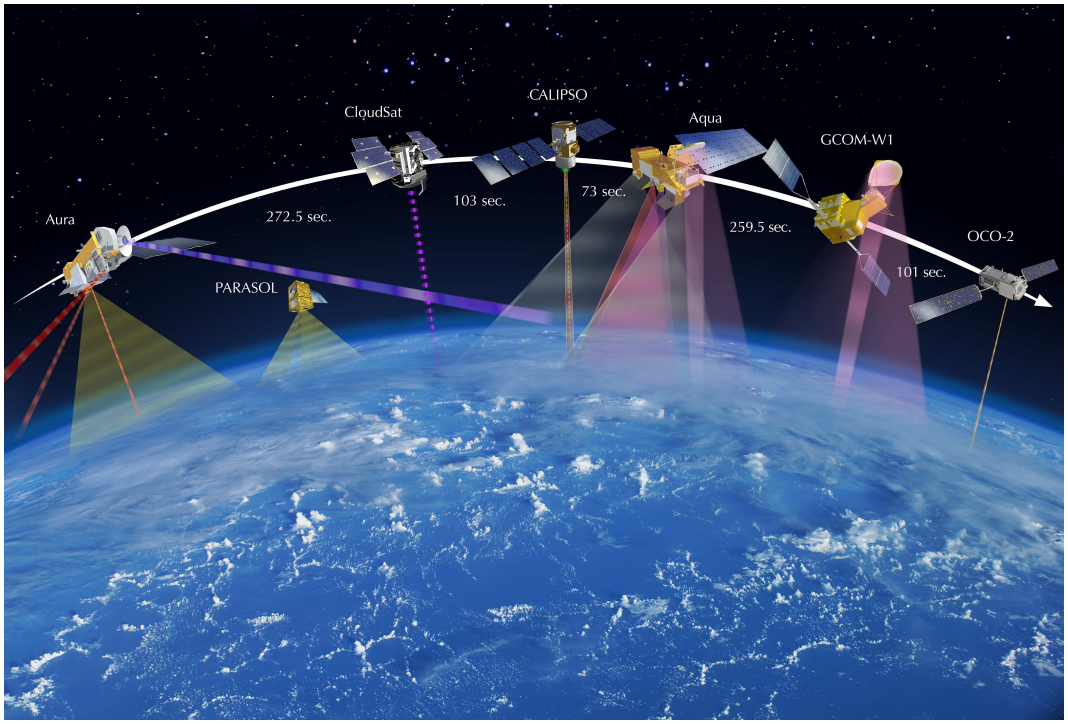

Figure 1.6: Concept of the "A-Train" constellation of satellites. From NASA.

tered and/or absorbed by the atmospheric components and the Earth's surface. There are two basic types of sensors, passive and active, to receive the radiation. Passive sensors receive the radiation emitted by the Sun and reflected by the atmosphere and the Earth's surface. Active sensors receive the energy emitted by the sensor itself, such as CALIPSO. Usually, the observations of satellite remote sensing mix all information of atmospheric gases, aerosols, the surface, and clouds [Lee et al., 2009].

Although satellite remote sensing can provide vertical observations, it is very expensive and data are often limited to low horizontal and temporal resolutions. Passive instruments can only retrieve column-integrated aerosol concentrations [Kaufman et al., 2002]. Spaceborne lidars (such as CALIPSO) improve the vertical resolution of aerosol measurements at the global scale [Winker et al., 2003; Berthier et al., 2006; Chazette et al., 2010]. However, spaceborne lidar measurements are only performed along the satellite ground track.

1.2.3 Ground-based lidar networks

1.2.3.1 Lidar technique

The light detection and ranging (lidar) is, along with radiowave detection and ranging (radar) or sound detection and ranging (sodar), a widely used tool for atmospheric remote sensing. It can provide vertical information on molecules and aerosols, as well as the altitude of clouds.

The lidar system consists of a laser transmitter and an optical receiver in parallel, an analog-to-digital converter and data processing by a computer (see Figure 1.7). The intensity of the backscattered light is measured versus time by the optical receiver. The signal profile will be

stored by a fast analog-to-digital converter or by a photon counting device. Since the laser is normally vertically directed, it is possible to obtain information on vertical profiles.

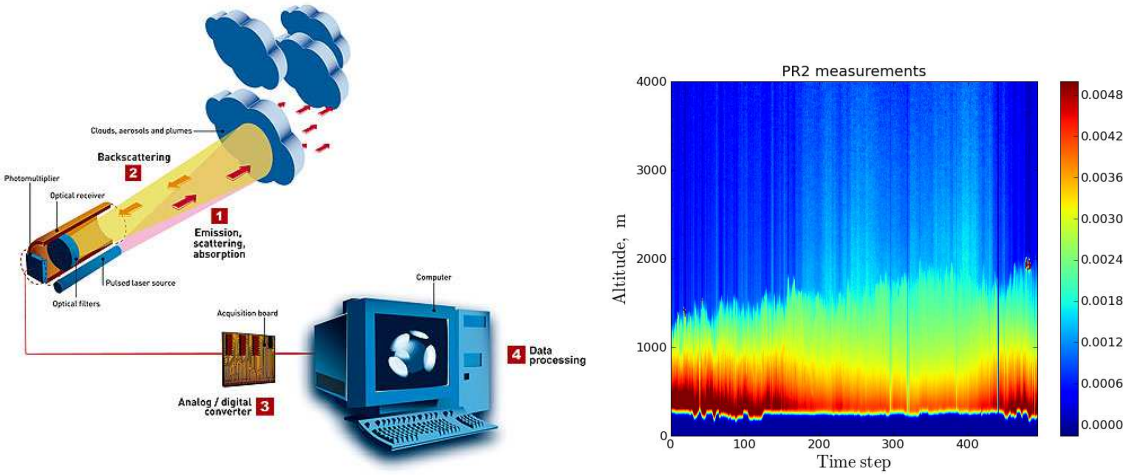

Figure 1.7: Schematic representation of a lidar system showing the laser transmitter, the optical receiver, the analog-to-digital converter and data processing by a computer on the left (from `http://www.leosphere.com`). On the right, range-corrected signal (PR_2) for EZ lidar on 01 July 2009 from 10:48 to 13:58 UTC.

The basic lidar measures aerosol backscatter signals at only one wavelength. For obtaining aerosol optical properties from these lidar signals, critical assumptions have to be make in the inversion of the lidar signal. Many techniques have been used in the inversion of the lidar signal in the past years, such as column closure by the use of ancillary optical depth information [Chazette, 2003]. However, basic lidar measurements only estimate either the backscatter or the extinction if only basic lidar data are available. It is because the backscatter to extinction ratio (BER) or the lidar ratio (LR, inverse of BER) that actually depends on the microphysical, chemical, and morphological properties of aerosols, must be assumed constant. On the other hand, measurements of two independent signals can provide accurate retrieval of extinction and backscatter coefficients without assuming that BER or LR is a constant. For example, the Raman-N_2 lidar and the High Spectral Resolution Lidar (HSRL) allow the independent determination of aerosol backscattering and extinction coefficients. In the near-range, lidar data are not available due to the receiver field of view and incomplete overlap of the laser beam [Royer, 2011]. A good knowledge of this overlap helps for an estimation of the backscatter or the extinction coefficient in the usually most polluted part of the atmosphere.

Lidar measurements were used in several campaigns to study the impact of anthropogenic and/or natural particles, such as the TARFOX (Tropospheric Aerosol Radiative Forcing Observational Experiment) [Hobbs, 1999; Ferrare et al., 2000], ACE-2 (the Aerosol Characterisation Experiment 2) [Raes et al., 2000], the Indian Ocean Experiment [Ramanathan et al., 2001; Hudson and Yum, 2002], ESQUIF (Étude et Simulation de la Qualité de l'air en Île-de-France) [Chazette et al., 2005], MEGAPOLI (Megacities: Emissions, urban, regional and Global Atmospheric POLlution and climate effects, and Integrated tools for assessment and mitigation) summer experiment in July 2009 [Royer et al., 2011] and during the eruption of the Icelandic volcano Eyjafjallajökull on 14 April 2010 [Chazette et al., 2012].

1.2.3.2 Lidar networks

Following the example of the AERONET (AErosol RObotic NETwork) program, a global network of systematic column-integrated aerosol optical depth observations, the Global Atmosphere Watch (GAW) aerosol program attempts to coordinate and homogenise different existing networks, and to provide the spatio-temporal distribution of aerosol properties on a global scale [Bosenberg and Hoff, 2007]. This global lidar network is referred to as the GAW Aerosol Lidar Observation Network (GALION). Presently, several lidar networks have been established to perform lidar measurements on continental scales. Those lidar networks include MPLNet (the Micro-pulse lidar network), EARLINET (the European Aerosol research lidar network), AD-Net (the Asian Dust Network), CISLiNet (the Commonwealth of independent states lidar network), REALM (Regional East Aerosol Lidar Mesonet) and ALINE (the American LIdar Network) (see Figure 1.8).

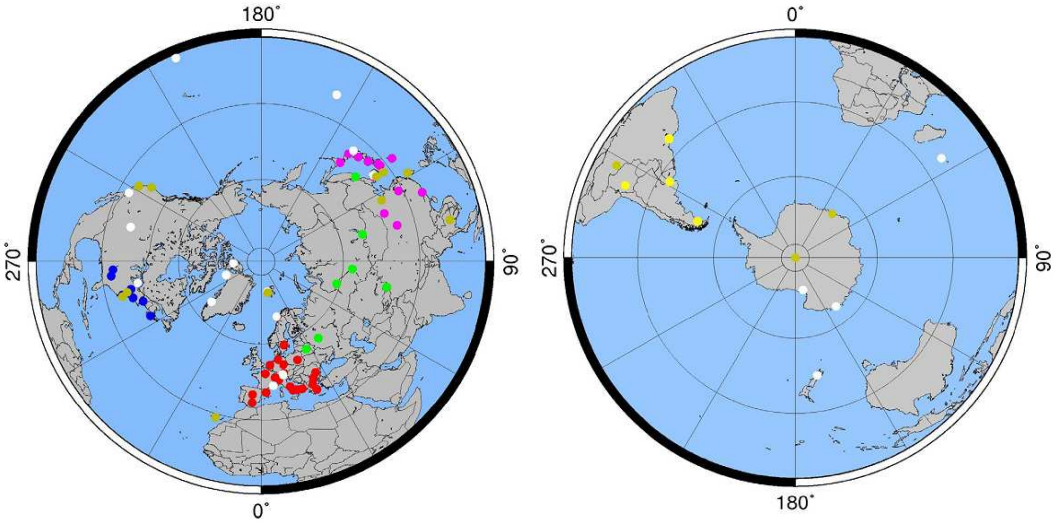

Figure 1.8: Distribution of the GALION sites, in 2010. The different networks are indicated by the coloured dots: AD-NET violet, ALINE yellow, CIS-LiNet green, EARLINET red, MPLNET brown, NDACC white, CLN blue. From GAW Report No. 178.

The NASA MPLNET (`http://mplnet.gsfc.nasa.gov/`) is the only tropospheric profiling network that claims global coverage. It was designed to continuously (day and night) measure aerosol and cloud vertical distributions and to provide satellite validations. Nowadays, Micro-Pulse Lidars (MPL) are operated at 22 stations around the world. Most MPLNET stations are co-located with AERONET sites for producing aerosol and cloud vertical distributions by synergy with sunphotometer measurements. The combination of MPLNET with AERONET is also a successful example of the application of the lidar-photometer technique.

The European Aerosol Research Lidar Network, referred to as EARLINET (`http://www.earlinet.org`) is a voluntary association of scientists concerned with studies of aerosol remote sensing by lidars. At present, EARLINET comprises 28 stations distributed over Europe. Since most EARLINET lidars existed before the network was established in 2000, its station sites are rather inhomogeneous.

The Asian Dust Network, referred as AD-Net (`http://www-lidar.nies.go.jp/AD-Net/`)

is an international virtual community designed to continuously observe vertical distributions of Asian dust and other aerosols (including industrial, forest fire, volcanic), and to study aerosol effects on the environment in East Asia. Presently, AD-Net provides continuous observations with automatic lidars. Most AD-Net stations are co-located with skyradiometer from SKYNET (http://skyrad.sci.u-toyama.ac.jp/). Measured data are transferred to the National Institute for Environmental Studies, Japan (NIES) in realtime and processed automatically. Since December 2012, measured data are updated at 00:00 local time on the site of AD-Net, such as attenuated backscattering coefficients at 1064 nm and 532 nm, volume depolarisation ratios, aerosol extinction coefficients, dust extinction coefficients, spherical particle extinction coefficients, aerosol depolarisation ratios at 532 nm and mixing layer height.

The Commonwealth of Independent States lidar network (CIS-LiNet, http://www.cis-linet.basnet.by) was established by lidar teams from Belarus, Russia and Kyrgyz Republic. The goal of this lidar network is to carry out lidar measurements from Minsk to Vladivostok in cooperation with EARLINET and AD-Net. All CIS-LiNet lidar stations are equipped with a three-wavelength lidar (355, 532 and 1064 nm) with Raman channel (387 or 607 nm) and can perform aerosol measurements in the troposphere and stratosphere. Certain lidars can also provide depolarisation measurements.

The Regional East Aerosol Lidar Mesonet (REALM), is operative since 2002. The NOAA Cooperative Remote Sensing Science and Technology (CREST) Lidar Network (CLN, http://crest.ccny.cuny.edu/) is based on the REALM Lidar Network. However, there are only two groups and three lidars voluntarily contributing lidar data to the network. Campaign style activities are contributed by two other groups.

Finally, the American LIdar Network (ALINE, http://lalinet.no-ip.org/) consists of the existing lidar groups in Latin America for measuring aerosol backscatter and extinction coefficient profiles over Latin America.

There are also other lidar networks, such as Network for the Detection of Atmospheric Composition Change (NDACC, previously NDSC), but with a different research aim. NDACC monitors the upper troposphere and the stratosphere for more than 20 years. NDACC consists of more than 70 high-quality remote-sensing research sites. But only a subset of the stations are equipped with lidars. In this subset, lidars are designed mainly for stratospheric O_3 and aerosols.

1.3 Air quality modelling of aerosols

As described in previous sections, modellers have developed various chemical transport models (CTM) in the past several years, in order to simulate the formation and evolution of aerosols, and predict levels of air pollution. However, a model can only represent a limited number of species, whereas several millions of organic reactants and products are involved in aerosol and ozone formation. Condensed chemical mechanisms were therefore developed. For example, the chemical mechanism CB05 (Carbon Bond version 5) [Yarwood et al., 2005] can simulate more than fifty gaseous species, such as O_3, NO_2, NH_3 and SO_2. The module Super-SORGAM (Secondary ORGanic Aerosol Model) [Schell et al., 2001; Kim et al., 2011a] of the air-quality platform POLYPHEMUS [Mallet et al., 2007] includes 20 aerosol species: 3 primary species (mineral dust, black carbon and primary organic species), 5 inorganic species (ammonium, sulphate, nitrate, chloride and sodium) and 12 organic species. In this section, the development,

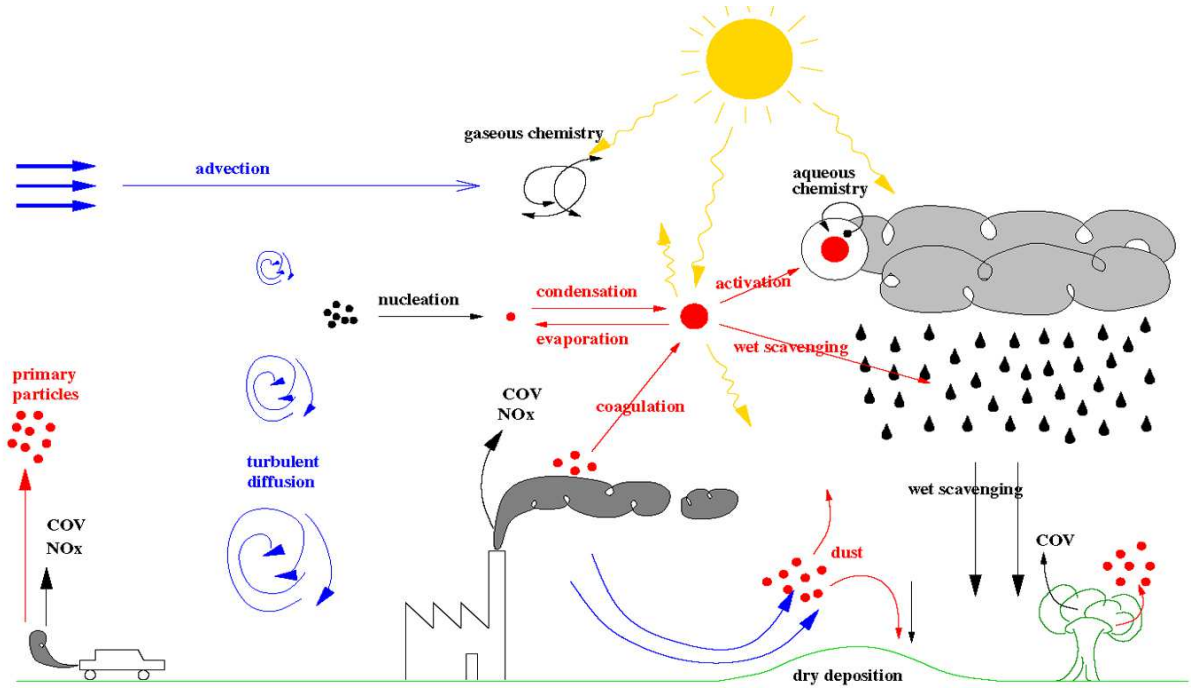

Figure 1.9: Processes described in a CTM [Sportisse, 2008].

important processes, numerical approach and performance evaluation of CTM are introduced.

1.3.1 Historical model development

Air quality models have first been developed in the 1970s for air quality impact and scenario studies [Seinfeld, 2004; Seigneur, 2005; Vautard et al., 2012]. In the first-generation models, only a few chemical species and reactions were considered. In the second-generation models, the number of chemical species, reactions and physical processes such as deposition and scavenging was expanded. In the third-generation models, chemistry, meteorology, and other physical processes are now coupled. Current air quality models can simulate both gaseous species and particles, e.g. POLYPHEMUS [Mallet et al., 2007].

Nowadays, in air quality modelling, the evolution equations of chemical species used in CTMs can describe atmospheric transport and chemistry (see Seinfeld and Pandis [1998]) as well as dry and wet deposition. Figure 1.9 describes the main processes that drive the evolution of species. The essence of a CTM is the simulation of the time evolution of chemical concentrations over a given domain. It takes into account transport, chemical reactions and additional processes such as emissions and deposition. For "off-line" CTMs, the forcing conditions (meteorological conditions, emissions) are obtained from meteorological and emission models.

Let c_i stand for the concentration of a chemical species i. The evolution of species concentrations is governed by a reaction-diffusion-advection equation (equation of reactive disper-

sion):

$$\frac{\partial c_i}{\partial t} + \underbrace{\mathrm{div}\,(V c_i)}_{\text{advection}} = \underbrace{\mathrm{div}\left(\rho K \nabla \frac{c_i}{\rho}\right)}_{\text{turbulent diffusion}} + \underbrace{\chi_i(c)}_{\text{chemistry}} + \underbrace{D_i}_{\text{deposition}} + \underbrace{S_i(x,t)}_{\text{emission}}, \tag{1.1}$$

where

- $\overrightarrow{V}$ is the wind velocity;
- ρ is the air density;
- K is the eddy diffusion coefficient;
- χ stands for the production and loss due to chemical reactions;
- $\mathbf{D}$ is the vector of deposition fluxes;
- $\mathbf{S}$ is the vector of the elevated sources treated as volume emissions.

Boundary conditions are specified, e.g. at the ground level we have

$$-K_z \frac{\partial c_i}{\partial z} = E_i - v_i^{dep} c_i, \tag{1.2}$$

where K_z is the vertical eddy coefficient, E_i is the flux of surface emission and v_i^{dep} is the dry deposition velocity.

1.3.2 Important processes

In this section, the important processes in aerosol modelling, including emissions, transport, diffusion, chemistry as well as dry and wet deposition, are described. Discussions are based on those processes simulated in the air-quality platform POLYPHEMUS.

1.3.2.1 Emissions

The most significant limiting factor on the quality of regional models is emissions [Russell and Dennis, 2000]. The accuracy of emissions have a significant impact on the quality of the model output. The large emission uncertainties are unavoidable, since it is difficult to measure the emissions with high accuracy. Emission uncertainties are also partly due to the high temporal variations of emissions. Over Europe, a commonly used anthropogenic emission inventory is provided by EMEP (European Monitoring and Evaluation Program) [Simpson et al., 2003] with a horizontal resolution of about 50 km $\times$ 50 km. However, over smaller-scale air quality domains, higher-resolution emission data are needed, for instance, national level emissions. For example, over Île-de-France, Airparif (Association agréée de surveillance de la qualité de l'air en Île-de-France) provides emission data with a spatial resolution as high as 1 km. Biogenic emissions come from natural sources. They are typically computed using a model, such as MEGAN (Model of Emissions of Gases and Aerosols from Nature) [Guenther et al., 2006].

1.3.2.2 Meteorology

Air quality models rely strongly on the accuracy of the outputs from meteorological models, e.g. the accuracy of the boundary layer height, wind direction and wind speed. The boundary layer height determines the volume in which pollutants are mixed. Errors in either wind direction or wind speed can lead to errors in the dispersion of pollutants. Pielke and Uliasz [1998] showed that limits on the accuracy of meteorological models led to an upper limit to the ability of air quality models. Over Europe, in the current air quality platform POLYPHEMUS, meteorological inputs for regional modelling are usually obtained from reanalysis provided by the European Centre for Medium-Range Weather Forecasts (ECMWF). When working on smaller scales, e.g. Île-de-France, the meteorological model WRF (Weather Research and Forecasting) [Skamarock et al., 2008] can be used to provide high spatial resolution meteorological data. However, WRF needs global model outputs, like data provided by the National Centers for Environmental Prediction (NCEP), as input data.

1.3.2.3 Deposition

Deposition is a sink for atmospheric chemical species. Its intensity depends on the type of pollutants, weather, location (type and density of vegetation), season (state of the vegetation), etc. Deposition is stronger during the daytime due to the radiation which increases the turbulent vertical transport. Above water, deposition increases with the solubility of species. Deposition is split into two types namely dry deposition and wet deposition (see section 1.1).

Dry deposition

Dry deposition describes how particles and gases are removed from the atmosphere close to the ground. The dry deposition flux is directly proportional to the concentration above the ground:

$$F = -v_d c, \tag{1.3}$$

where F is the flux, e.g. the quantity of the chemical species which is deposited per unit area per unit time. v_d is the deposition velocity and c is the mass concentration.

The deposition process is usually interpreted in analogy to electrical resistances. For gases, the deposition to the surface is supposed to be controlled by three resistances: the aerodynamic resistance (R_a), the quasi-laminar layer resistance (R_b) and the surface resistance (R_s). The dry deposition velocity is defined as the inverse of the sum of these three resistances [Wesely, 1989; Sportisse, 2007a]:

$$v_d = \frac{1}{R_a + R_b + R_s}. \tag{1.4}$$

For particles, settling by gravitational sedimentation is supposed to operate in parallel with the previous processes. Moreover, the surface resistance is neglected because the particles adhere to the surface. The dry deposition velocity is defined [Venkatram and Pleim, 1999] as follows:

$$v_d = \frac{u_{grav}}{1 - \exp\left(-(R_a + R_b)u_{grav}\right)}, \tag{1.5}$$

where u_{grav} is the gravitational settling velocity.

Wet deposition

Wet deposition can occur in three ways. First, for gases by uptake, e.g. cloud droplets in a cloud or fog. Second, for particles acting as cloud condensation nuclei. Third, when particles or gas molecule collide with a cloud droplet or a rain drop. Wet deposition can occur both inside and outside a cloud. Scavenging coefficients are used to describe wet deposition in air quality models. Wet deposition is the most important removal process for fine particles in the atmosphere [Anthony and Mary-Scott, 1990] (see section 1.1).

Wet deposition does not only affect the lowest layer of the PBL, the precipitation scavenging affects all volume elements aloft inside the precipitation layer. The wet flux of the chemical species to surface [Seinfeld and Pandis, 1998] is

$$W_g = \int_0^{z_{\mathrm{TOA}}} \Lambda(z,t)c(x,y,z,t)dz \tag{1.6}$$

for gases and

$$W_p = \int_0^{z_{\mathrm{TOA}}} \Lambda(d_p,z,t)c(d_p,x,y,z,t)dz \tag{1.7}$$

for particles, where Λ is the washout coefficient, c the concentration and d_p the diameter of the particles and z_{TOA} the altitude at the top of atmosphere. Techniques are available for estimating Λ as a function of storm type and precipitation amounts [Scott, 1982].

1.3.2.4 Aerosol dynamics

CTMs model the evolution of gaseous species and particles. This includes the description of the chemical composition and size distribution of aerosols. Both have an influence on the radiative behaviour of aerosols, on microphysical processes (see section 1.1.3) and on the assessment of health impacts (see section 1.1.1). The evolution of the size distribution and chemical composition of aerosols is governed by the General Dynamic Equation (GDE). It describes the impact of processes such as nucleation, coagulation, and condensation/evaporation (see Figure 1.10).

Nucleation

The smallest aerosols are formed by the aggregation of gaseous molecules through thermodynamically stable clusters. Since the mechanism and corresponding species are not yet well understood, binary nucleation (H_2O-H_2SO_4) or ternary nucleation (H_2O-H_2SO_4-NH_3) [Zhang et al., 2010a, b] are usually parametrised.

Coagulation

In practice, the Brownian coagulation due to thermal agitation is often the only one modelled. Other effects due to gradients in fields (such as temperature, electric fields, van der Waals forces, etc) are often neglected. Coagulation may be neglected for the evolution of particles above a few μm. However, coagulation significantly affects the number concentration of urtrafine particles while retaining their total mass [Seinfeld and Pandis, 1998].

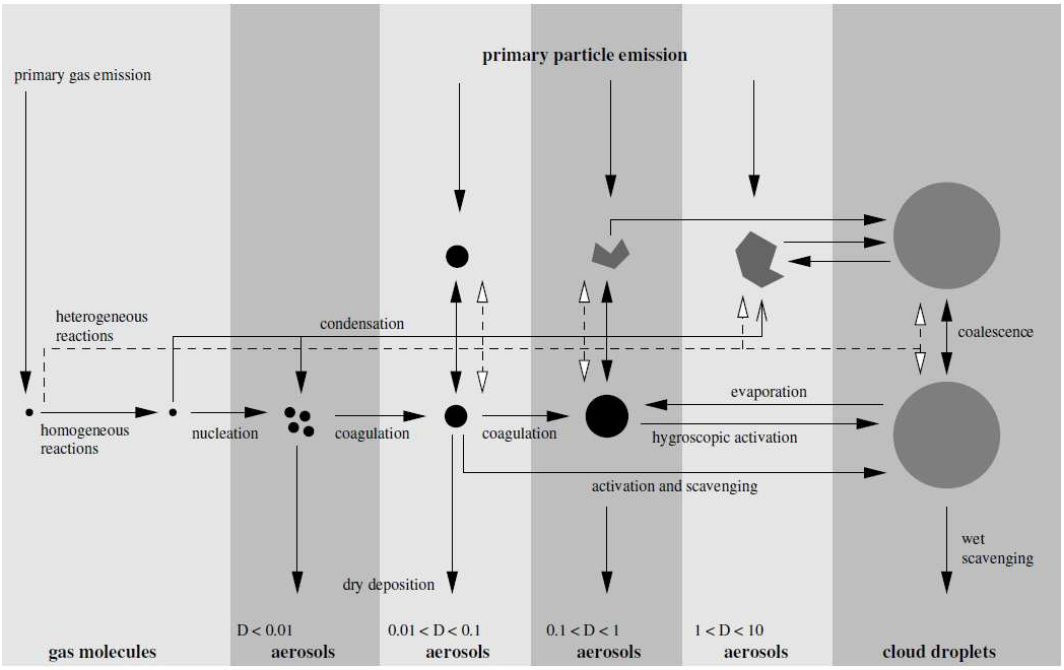

Figure 1.10: Aerosol dynamics (the particle diameter D is in micrometers) [Sportisse, 2007b].

Condensation/evaporation

Many gaseous species with a low saturation vapour pressure may condense onto or evaporate from existing particles. This mass transfer is governed by the gradient between the concentration at the aerosol surface and the concentration far from the aerosol [Pilinis et al., 2000]. Condensation increases the particle mass; conversely, evaporation decreases the particle mass. Because modelling condensation/evaporation dynamically is very CPU consuming, an assumption of thermodynamic equilibrium between the gas and the particulate phases is often made. The state of the hydrophilic aerosol, liquid or solid, is determined by the relative humidity (RH). When the humidity increases, the solid aerosol may become liquid (deliquescence) and grow by absorbing water (hygroscopicity). For example, ammonium nitrate is typically formed in areas where concentrations of ammonia and nitric acid are high and concentrations of sulfate are low. Depending on RH, ammonium nitrate can exist in the solid phase (NH_4NO_3) or aqueous phase (NH_4^+ and NO_3^- ions). The equilibrium gas-phase concentrations of NH_3 and HNO_3, and the concentration of solid or aqueous ammonium nitrate can be calculated from thermodynamic fundamentals [Seinfeld and Pandis, 1998]. The mineral composition of aerosols is strongly driven by the interactions between sulfate, nitrate, ammonium, chloride and sodium. Thermodynamic models, such as ISORROPIA [Nenes et al., 1998a], are used to compute gas/-particle partitioning. The module Super-SORGAM [Schell et al., 2001; Kim et al., 2011a] is used for aerosol organic species in this thesis.

General Dynamic Equation

For simulating the number/mass distribution of aerosols, let $n(m,t)$ be the number distribution (for instance with respect to aerosol mass) and $q_i(m,t)$ the mass distribution for species i. m_0

is the smallest aerosol dry mass (in practice given by the nucleation threshold). An aerosol of mass m is composed by n_c components of mass $m_i(m)$, such that $\sum_{i=1}^{n_c} m_i(m) = m$. An aerosol with a given mass is assumed to have a unique composition (internal mixing). The General Dynamic Equation (GDE) is composed of the following equations [Sportisse, 2007b]:

- For the number distribution:

$$\frac{\partial n}{\partial t}(m,t) = \underbrace{\frac{1}{2}\int_{m_0}^{m-m_0} K(u, m-u)n(u,t)n(m-u,t)du}_{\text{coagulation}} - \underbrace{n(m,t)\int_{m_0}^{\infty} K(m,u)n(u,t)du}_{\text{coagulation}} - \underbrace{\frac{\partial I_0 n}{\partial m}}_{\text{mass transfer}} + \underbrace{\delta(m_0,m)J_0(t)}_{\text{nucleation}} \tag{1.8}$$

- For the mass distribution:

$$\begin{aligned}\frac{\partial q_i}{\partial t} = &\int_{m_0}^{m-m_0} K(u, m-u)n(u,t)n(m-u,t)du \\ &- q_i(m,t)\int_{m_0}^{\infty} K(m,u)n(u,t)du - \frac{\partial I_0 q_i}{\partial m} \\ &+ I_i(m_1,...,m_{n_c},t)n(m,t) + \underbrace{\chi_i(m_1,...,m_{n_c})n(m,t)}_{\text{internal chemistry}}\end{aligned} \tag{1.9}$$

K is the coagulation kernel due to Brownian motion. I_i is the condensation/evaporation rate for volatile species i. Notice that $I_0 = \sum_i I_i$. J_0 is the nucleation rate, given by parameterisations as a function of thermodynamic conditions, such as temperature and relative humidity, and of some gaseous concentrations, such as water, ammonium, and sulfate.

For details, we refer to Sportisse et al. [2006a, b] for a description of the parameterisations used in the aerosol models that have been developed in POLYPHEMUS: the Model Aerosol Model (MAM) [Sartelet et al., 2006] and the SIze REsolved Aerosol Model (SIREAM) [Debry et al., 2007]. In our study, SIREAM is used.

1.3.3 Numerical approach

In practice, splitting methods are used to solve Equation 1.1 in the CTM POLAIR3D. The processes are solved in a sequential way. Let Δt be the splitting time step, L_{adv} be the advection operator in three dimensions, L_{diff} be the diffusion operator, L_{chem} be the operator chemistry and sources, and L_{aero} be the aerosol operator. The splitting can be defined in the following way:

- Integrate L_{adv} on $[t, t+\Delta t]$;
- Integrate L_{diff} on $[t, t+\Delta t]$;
- Integrate L_{chem} on $[t, t+\Delta t]$;
- Integrate L_{aero} on $[t, t+\Delta t]$;

After each sequence, initial conditions are changed. In these sequences, the integration of chemistry has prominent computational cost, because chemical reactions have strongly different reaction rates, also due to the number of modelled chemical species. At present, several chemical mechanisms may be used for photochemistry in POLAIR3D: RACM [Stockwell et al., 1997], RACM2 [Goliff and Stockwell, 2008] and CB05 [Yarwood et al., 2005]. Aerosols can be solved by MAM and SIREAM. The Super-SORGAM module can be used to model organic aerosol species. In this thesis, the chemical mechanism CB05 is used to solve the gas chemistry and the aerosol model SIREAM-SuperSORGAM is used to model aerosols.

1.3.4 Model performance evaluation

The model algorithms, chemistry/physics, assumptions, and codes should be examined for their accuracy, efficiency, and sensitivity in a scientific evaluation [Seigneur et al., 2000]. For instance, Mallet and Sportisse [2006] have estimated the uncertainty due to physical parameterisations and numerical approximations though an ensemble approach of a reference simulation in the CTM POLAIR3D. They showed that a CTM is sensitive to its physical and chemical parameterisations (e.g deposition, biogenic emissions and the turbulent closure scheme), to the associated input data (e.g. emissions, meteorology) and to the numerical approximations (e.g. the timestep and the spatial resolution). They also showed that the choice of the turbulent closure scheme (vertical turbulent diffusion) and the chemical mechanism introduce the highest uncertainty for ozone modelling.

Model outputs, such as one-hour averaged concentration, 24-hour averaged concentration, and Aerosol Optical Thickness (AOT), should be examined in statistical evaluations, to see how well they match observations. For example, Sartelet et al. [2007] presented a validation of multi-pollutants over Europe with a focus on aerosols. In Sartelet et al. [2007], a comprehensive set of model-to-data statistics was computed with observational data extracted from three European databases (the EMEP, AirBase and BDQA databases). Comparisons of correlations and root mean square errors (RMSE) with those generated by other models run over Europe and North America for July and August 2006 indicate a good performance of POLYPHEMUS [Sartelet et al., 2012]. Furthermore, a model-to-data comparison of AOT and of a few sparse data for Single Scattering Albedo (SSA) over Europe for 2001 was presented by Tombette et al. [2008]. Statistics and monthly time series for the simulation and AERONET data were used to evaluate the ability of the model to reproduce AOT and vertically averaged SSA fields and their variability. Of course, it is possible for a model to simulate concentrations which compare well to measurements, but there are often compensating errors [Seigneur et al., 2000; Chang and Hanna, 2004]. The focus of this section will be mainly on statistical model evaluation.

1.3.4.1 Model evaluation methods

Model evaluation methods depend on the pollutant to be evaluated. The US EPA [EPA, 1991; Russell and Dennis, 2000] recommends using the mean normalised bias error (MNBE) and the mean normalised gross error (MNGE) with an observation-based minimum threshold of 40-60 ppb (about 80-120 $\mu\mathrm{g\ m^{-3}}$) to evaluate hourly ozone. The suggested performance criteria is MNBE $\leq \pm 15\%$ and MNGE $\leq 30\%$. Let $\{o_i\}_{i=1,n}$ and $\{s_i\}_{i=1,n}$ be the observed and the modelled concentrations, respectively. Let n be the number of available observations. The

MNBE and MNGE are defined as follow:

$$\text{MNBE} = \frac{1}{n}\sum_{i=1}^{n}\frac{s_i - o_i}{o_i}, \tag{1.10}$$

$$\text{MNGE} = \frac{1}{n}\sum_{i=1}^{n}\frac{|s_i - o_i|}{o_i}. \tag{1.11}$$

However, the US EPA provided minimal guidance on PM model performance evaluation metrics, goals, and criteria. Boylan and Russell [2006] defined PM model performance goal and criterion that are based upon an analysis of numerous PM modelling studies. The PM model performance goal corresponds to the level of accuracy that is considered to be close to the best a model can be expected to achieve. The PM model performance criterion corresponds to the level of accuracy that is considered to be acceptable for modelling applications, e.g. predictions of pollutants and regulatory applications. In opposition to the ozone evaluation, according to Boylan and Russell [2006], the MNBE and MNGE may not be appropriate to evaluate PM. They suggested using instead the mean fractional bias MFB (%) and the mean fractional error MFE (%), because they bound the maximum bias and error. The MFB and MFE are defined as follow:

$$\text{MFE} = \frac{1}{n}\sum_{i=1}^{n}\frac{|s_i - o_i|}{(s_i + o_i)/2}, \tag{1.12}$$

$$\text{MFB} = \frac{1}{n}\sum_{i=1}^{n}\frac{s_i - o_i}{(s_i + o_i)/2}, \tag{1.13}$$

If both MFB and MFE are in the range $[-30\,\%,\, 30\,\%]$ and $[0\,\%,\, 50\,\%]$ respectively, then the model performance goal is met; if both the MFB and MFE are in the range $[-60\,\%,\, 60\,\%]$ and $[0\,\%,\, 75\,\%]$ respectively, the model performance criterion is met.

In addition, the root mean square error (RMSE) and the (Pearson) correlation can be used as statistical measures. The RMSE is a measure of the extent that the model deviates from the observations. The correlation is a measure of statistical relationships involving dependence between the observed and modelled concentrations. The statistical indicators are defined as follow:

$$\text{RMSE} = \sqrt{\frac{1}{n}\sum_{i=1}^{n}(o_i - s_i)^2}, \tag{1.14}$$

$$\text{correlation} = \frac{\sum_{i=1}^{n}(o_i - \bar{o})(s_i - \bar{s})}{\sqrt{\sum_{i=1}^{n}(o_i - \bar{o})^2 \sum_{i=1}^{n}(s_i - \bar{s})^2}}, \tag{1.15}$$

where $\bar{o} = \frac{1}{n}\sum_{i=1}^{n} o_i$ and $\bar{s} = \frac{1}{n}\sum_{i=1}^{n} s_i$. Those performance measures (RMSE, correlation, MNBE/MNGE for ozone, MFB/MFE for PM) widely used in many studies, such as in Sartelet et al. [2007], Tombette et al. [2009], Roustan et al. [2010], Couvidat et al. [2012] and Sartelet et al. [2012].

1.3.4.2 Model uncertainty

Uncertainties in air quality modelling are due to variability because of random turbulence, input data errors, model temporal and spatial resolutions, and errors/uncertainties in model

physics. These uncertainties can be assessed by sensitivity studies of uncertain parameters, multi-forecasts, or ensemble forecasts [Mallet and Sportisse, 2006]. Uncertainties can be reduced by a better understanding of model description and by the improvement of the meteorological models and of the emission inventory. Sportisse [2007b] suggested to increase the resolution of CTMs and to have a better representation of modelled species especially aerosols. Furthermore, another field of growing interest is the use of *data assimilation* techniques, which couple model outputs and observational data provided by monitoring networks (see section 1.2) to improve the forecasts and/or to reduce the uncertainties of some input data [Bouttier and Courtier, 2002; Kalnay, 2003; Lahoz et al., 2010]. Therefore, some *data assimilation* techniques are introduced in the next section.

1.4 Data assimilation for aerosol forecasting

1.4.1 Background

A CTM can be used to simulate the chemical composition of the atmosphere (forward mode). However, it is always a simplification of the real atmosphere (see section 1.3). It is limited in terms of spatial and temporal resolution and it is also limited to a restrictive selection of physical and chemical processes. Initial and boundary conditions are two crucial factors for forecasting. Since these conditions themselves are often outputs from other simulations, or from a fixed set of climatological average values based on long term observations or investigation of relevant data sets, they are usually far from accurate.

Measurements are an important source of information on the state of the atmosphere (see section 1.2). Unfortunately, observations do not directly provide the necessary initial and boundary conditions to the model. For example, their spatial distribution tends to be rather inhomogeneous and most measurement sites are not representative of an area of the size of a model grid cell. Sometimes, the desired species are not measured directly, e.g. satellite retrievals of AOT instead of aerosol concentrations.

Altogether, although the observations of the atmospheric state and composition can be very precise, they are limited in time and space. CTMs can deliver a continuous and smooth image of the atmosphere, but are restricted to discretization and a limited set of equations describing the major processes, e.g. physical and chemical processes. The technique known as *data assimilation* has emerged from the desire of "using all available information, to determine as accurately as possible the atmospheric or oceanic flow" as stated by Talagrand [1997]. *data assimilation* (DA hereafter) can couple the numerical model and observations of the atmosphere state to yield more exact initial conditions with a view to forecasting.

In meteorology, DA has been traditionally applied to improve forecasts [Bouttier and Courtier, 2002; Kalnay, 2003; Lahoz et al., 2010]. DA methods were used for the first time in the 1960s [Park and Xu, 2009]. The 3-dimensional variational (3D-Var) or optimal interpolation (OI) method was put into practical use in many NWP centres due to its relatively cheap computation and programming burden. For example, the Japan Meteorological Agency (JMA) have used OI for their operational numerical weather prediction (NWP) from the 1980s until 2002. Several NWP centres have adopted the 4-dimensional variational method (4D-Var) system since the early 2000s [Rabier et al., 2000]. However, the computational cost of a 4D-Var system is high, since the 4D-Var calculation requires a tangent linear model and an adjoint model of the forecast model. Another DA method, the Kalman filter (KF), has been well known since the 1960s

[Kalman, 1960]. The disadvantage of KF is that it requires the update of the background error covariance matrix with the dimensions of the model state space, which is crucial but difficult. A new method based on KF, the ensemble Kalman filter (EnKF), was developed to reduce the computational cost [Evensen, 1994, 2009]. The basic concept of EnKF is that the ensemble of the forward model forecasts is able to approximate the error covariance distribution.

In this section, we will outline the theory of data assimilation. Furthermore, the main DA methods will be described, e.g. OI/3D-Var, 4D-Var and EnKF.

We rewrite the CTM dynamical differential equation in discrete form from time t_{k-1} to t_k,

$$\mathbf{x}_k = M_k(\mathbf{x}_{k-1}) + \mathbf{w}_k, \tag{1.16}$$

where $\mathbf{x}_k$ denotes the true state vector at time t_k, M_k corresponds to the model operator from time t_{k-1} to t_k, and $\mathbf{w}_k$ is the model error assumed to have a normal distribution with zero mean and covariance matrix $\mathbf{Q}_k$. All available data at time t_k are gathered into an observation vector $\mathbf{y}_k$. An observation operator from model states to the observation space at time t_k noted by H_k:

$$\mathbf{y}_k = H_k(\mathbf{x}_k) + \epsilon_k, \tag{1.17}$$

ϵ_k is the observation error vector assumed to have a normal distribution with zero mean and covariance matrix $\mathbf{R}_k$. Usually, the number of observations is much less than that of variables in the model.

We ignore the index k to simplify the mathematical notations in the following. But notice that we do assimilation at time t_k. Let $\mathbf{x}_b$ be the background state just before performing an analysis, the background error $\epsilon_b = \mathbf{x}_b - \mathbf{x}_t$ of zero mean and covariance matrix $\mathbf{B}$, and $\mathbf{x}_a$ the analysis state with error $\epsilon_a = \mathbf{x}_a - \mathbf{x}_t$ of covariance matrix $\mathbf{A}$. The DA problem is to determine the optimal analysis state $\mathbf{x}_a$ by minimising the trace of the analysis error covariance matrix $\mathbf{A}$ given the background $\mathbf{x}_b$, the observation $\mathbf{y}$, and the error covariance matrices $\mathbf{B}$ and $\mathbf{R}$.

1.4.2 OI/3D-Var

OI searches for an optimal linear combination between the background state and observations [Daley, 1991]. It means that we look for an analysis defined to correct the background state $\mathbf{x}_b$, which depends linearly on the observations $\mathbf{y}$:

$$\mathbf{x}_a = \mathbf{L}\mathbf{x}_b + \mathbf{K}\mathbf{y}, \tag{1.18}$$

where $\mathbf{L}$ and $\mathbf{K}$ are two matrices. Considering Equation 1.17, we have

$$\epsilon_a = \mathbf{L}\epsilon_b + \mathbf{K}\epsilon + (\mathbf{L} + \mathbf{K}\mathbf{H} - \mathbf{I})\mathbf{x}_t, \tag{1.19}$$

$\mathbf{H}$ is the tangent linear operator of H (in the following, the observation operator is linear). Here, we look for an analysis state whose mean $\mathbf{E}(\epsilon^a) = 0$. Since the expectation of the background and observation errors is zero, we have that $(\mathbf{L} + \mathbf{K}\mathbf{H} - \mathbf{I})\mathbf{E}(\mathbf{x}_t) = 0$ and we can set $\mathbf{L}$ such that $\mathbf{L} = \mathbf{I} - \mathbf{K}\mathbf{H}$ to satisfy this condition. Then we rewrite equation 1.18 as follows:

$$\mathbf{x}_a = (\mathbf{I} - \mathbf{K}\mathbf{H})\mathbf{x}_b + \mathbf{K}\mathbf{y} = \mathbf{x}_b + \mathbf{K}\left(\mathbf{y} - \mathbf{H}\mathbf{x}_b\right). \tag{1.20}$$

Expressions for the analysis error covariance matrix $\mathbf{A} = \mathbf{E}\left(\epsilon_a \epsilon_a^{\mathrm{T}}\right)$ are obtained by rewriting the analysis equation 1.20 in terms of the background, analysis and observation errors:

$$\epsilon_a = (\mathbf{I} - \mathbf{K}\mathbf{H})\epsilon_b + \mathbf{K}\epsilon. \tag{1.21}$$

Under the hypotheses that observation and background errors are independent, we find the expression of $\mathbf{A}$

$$\mathbf{A} = (\mathbf{I} - \mathbf{KH})\,\mathbf{B}\,(\mathbf{I} - \mathbf{KH})^{\mathrm{T}} + \mathbf{KRK}^{\mathrm{T}}. \tag{1.22}$$

Finally, in order to find the expression of the matrix $\mathbf{K}$, we minimise the trace of the analysis error covariance matrix, i.e. the total error variance:

$$\mathbf{Tr}(\mathbf{A}) = \mathrm{Tr}(\mathbf{B}) + \mathrm{Tr}\left(\mathbf{KHBH}^{\mathrm{T}}\mathbf{K}^{\mathrm{T}}\right) - 2\mathrm{Tr}\left(\mathbf{BH}^{\mathrm{T}}\mathbf{K}^{\mathrm{T}}\right) + \mathrm{Tr}\left(\mathbf{KRK}^{\mathrm{T}}\right), \tag{1.23}$$

which is a continuous differentiable scalar function of the matrix $\mathbf{K}$. We can express its derivative $d_{\mathbf{K}}$ as the first order term in $\mathbf{K}$. Let $\mathbf{D}$ be an arbitrary test matrix. We have

$$\begin{aligned} d_{\mathbf{K}}[\mathbf{Tr}\,(\mathbf{A})]\mathbf{D} &= 2\mathrm{Tr}\left(\mathbf{KHBH}^{\mathrm{T}}\mathbf{D}^{\mathrm{T}}\right) - 2\mathrm{Tr}\left(\mathbf{BH}^{\mathrm{T}}\mathbf{D}^{\mathrm{T}}\right) + 2\mathrm{Tr}\left(\mathbf{KRD}^{\mathrm{T}}\right) \\ &= 2\mathrm{Tr}\left([\mathbf{K}(\mathbf{HBH}^{\mathrm{T}} + \mathbf{R}) - \mathbf{BH}^{\mathrm{T}}]\mathbf{D}^{\mathrm{T}}\right). \end{aligned} \tag{1.24}$$

The last line shows that the derivative is zero for any choice of $\mathbf{D}$ if and only if

$$\mathbf{K}(\mathbf{HBH}^{\mathrm{T}} + \mathbf{R}) - \mathbf{BH}^{\mathrm{T}} = 0,$$

which is equivalent to

$$\mathbf{K} = \mathbf{BH}^{\mathrm{T}}\left(\mathbf{HBH}^{\mathrm{T}} + \mathbf{R}\right)^{-1}, \tag{1.25}$$

where the matrix $\mathbf{HBH}^{\mathrm{T}} + \mathbf{R}$ is assumed to be invertible.

Finally, by the optimal least-squares estimator or Best Linear Unbiased Estimator (BLUE) analysis, we obtain the following interpolation equations:

$$\mathbf{x}_a = \mathbf{x}_b + \mathbf{K}\left(\mathbf{y} - \mathbf{Hx}_b\right), \tag{1.26}$$

$$\mathbf{K} = \mathbf{BH}^{\mathrm{T}}\left(\mathbf{HBH}^{\mathrm{T}} + \mathbf{R}\right)^{-1}. \tag{1.27}$$

The OI can algebraically simplify the computation of the weight $\mathbf{K}$ in equations 1.26 and 1.27. For the computation of the matrix $\mathbf{K}$, it can be implemented as follows:

- Define the matrix $\mathbf{B}$, e.g. by the Balgovind approach [Balgovind et al., 1983];
- Compute the matrices $\mathbf{BH}^{\mathrm{T}}$ and $\mathbf{HBH}^{\mathrm{T}}$;
- Form the matrix $\mathbf{HBH}^{\mathrm{T}} + \mathbf{R}$;
- Compute the inverse of the matrix formed in the previous step;
- Multiply it by the $\mathbf{BH}^{\mathrm{T}}$ to get $\mathbf{K}$.

An advantage of OI is that its cost is relatively low. In this thesis, we use all available observations for each model variable x_i [Wu et al., 2008; Tombette et al., 2009]. In addition, the same matrix inverse, i.e. $(\mathbf{HBH}^{\mathrm{T}} + \mathbf{R})^{-1}$, can be reused for the analysis increment of each x_i. Bouttier and Courtier [2002] proposed the observation selection for x_i in order to keep the matrix inversions at low computational cost. However, it leads to different sets of observations being used on different parts of the model state.

In order to pose a variational optimisation problem (3D-Var), we assume that there is a probability density function (PDF) $p(\mathbf{x})$ for the state of the atmosphere. The PDF $p(\mathbf{y}|\mathbf{x})$

describes the probability of observing $\mathbf{y}$ when $\mathbf{x}$ is known. Following the Bayes' theorem, the posterior PDF $p(\mathbf{x}|\mathbf{y})$ can be derived by

$$p(\mathbf{x}|\mathbf{y}) = \frac{p(\mathbf{y}|\mathbf{x})p(\mathbf{x})}{p(\mathbf{y})} \tag{1.28}$$

With the further assumption that these PDFs are Gaussian, the background, observation and analysis PDFs can be expressed as follows:

$$\begin{aligned}
p(\mathbf{x}) &\propto \exp\left(-\frac{1}{2}\left(\mathbf{x}-\mathbf{x}_b\right)^{\mathrm{T}}\mathbf{B}^{-1}\left(\mathbf{x}-\mathbf{x}_b\right)\right), \\
p(\mathbf{y}|\mathbf{x}) &\propto \exp\left(-\frac{1}{2}\left(\mathbf{y}-\mathbf{H}\mathbf{x}\right)^{\mathrm{T}}\mathbf{R}^{-1}\left(\mathbf{y}-\mathbf{H}\mathbf{x}\right)\right), \\
p(\mathbf{x}|\mathbf{y}) &\propto \exp\left(-\frac{1}{2}\left(\mathbf{x}-\mathbf{x}_b\right)^{\mathrm{T}}\mathbf{B}^{-1}\left(\mathbf{x}-\mathbf{x}_b\right)\right)\exp\left(-\frac{1}{2}\left(\mathbf{y}-\mathbf{H}\mathbf{x}\right)^{\mathrm{T}}\mathbf{R}^{-1}\left(\mathbf{y}-\mathbf{H}\mathbf{x}\right)\right) \\
&\propto \exp\left(-\frac{1}{2}\left(\mathbf{x}-\mathbf{x}_b\right)^{\mathrm{T}}\mathbf{B}^{-1}\left(\mathbf{x}-\mathbf{x}_b\right)-\frac{1}{2}\left(\mathbf{y}-\mathbf{H}\mathbf{x}\right)^{\mathrm{T}}\mathbf{R}^{-1}\left(\mathbf{y}-\mathbf{H}\mathbf{x}\right)\right), \qquad (1.29)
\end{aligned}$$

where the analysis state PDF is obtained from the equation 1.28. Thus, the model state with the maximum likelihood is the one that minimises the cost function $J(\mathbf{x})$ defined by

$$\begin{aligned}
J(\mathbf{x}) &= \frac{1}{2}\left(\mathbf{x}-\mathbf{x}_b\right)^{\mathrm{T}}\mathbf{B}^{-1}\left(\mathbf{x}-\mathbf{x}_b\right)+\frac{1}{2}\left(\mathbf{y}-\mathbf{H}\mathbf{x}\right)^{\mathrm{T}}\mathbf{R}^{-1}\left(\mathbf{y}-\mathbf{H}\mathbf{x}\right) \qquad (1.30)\\
&= J_b(\mathbf{x})+J_o(\mathbf{x}),
\end{aligned}$$

where J_b is the background term and J_o is the observation term. The cost function terms J_b and J_o are both convex and continuous (see Figure 1.11). Thus the minimum of their sum always exists. An advantage of using the Bayesian approach is that it can be extended to non-Gaussian distributions.

The minimisation of $J(\mathbf{x})$ requires that the gradient of J is zero at the optimum $\mathbf{x}_a$ (see Figure 1.11):

$$\begin{aligned}
\nabla J(\mathbf{x}_a) &= \mathbf{B}^{-1}\left(\mathbf{x}_a-\mathbf{x}_b\right)-\mathbf{H}^{\mathrm{T}}\mathbf{R}^{-1}\left(\mathbf{y}-\mathbf{H}\mathbf{x}_a\right)=0 \\
0 &= \mathbf{B}^{-1}\left(\mathbf{x}_a-\mathbf{x}_b\right)-\mathbf{H}^{\mathrm{T}}\mathbf{R}^{-1}\left(\mathbf{y}-\mathbf{H}\mathbf{x}_b\right)-\mathbf{H}^{\mathrm{T}}\mathbf{R}^{-1}\mathbf{H}\left(\mathbf{x}_a-\mathbf{x}_\mathbf{b}\right) \\
\mathbf{x}_a &= \mathbf{x}_b+\left(\mathbf{B}^{-1}+\mathbf{H}^{\mathrm{T}}\mathbf{R}^{-1}\mathbf{H}\right)^{-1}\mathbf{H}^{\mathrm{T}}\mathbf{R}^{-1}\left(\mathbf{y}-\mathbf{H}\mathbf{x}_b\right). \qquad (1.31)
\end{aligned}$$

On the other hand, we have

$$\begin{aligned}
\mathbf{H}^{\mathrm{T}}\mathbf{R}^{-1}\left(\mathbf{H}\mathbf{B}\mathbf{H}^{\mathrm{T}}+\mathbf{R}\right) &= \left(\mathbf{B}^{-1}+\mathbf{H}^{\mathrm{T}}\mathbf{R}^{-1}\mathbf{H}\right)\mathbf{B}\mathbf{H}^{\mathrm{T}}, \\
\left(\mathbf{B}^{-1}+\mathbf{H}^{\mathrm{T}}\mathbf{R}^{-1}\mathbf{H}\right)^{-1}\mathbf{H}^{\mathrm{T}}\mathbf{R}^{-1} &= \mathbf{B}\mathbf{H}^{\mathrm{T}}\left(\mathbf{H}\mathbf{B}\mathbf{H}^{\mathrm{T}}+\mathbf{R}\right)^{-1}. \qquad (1.32)
\end{aligned}$$

Finally, we find that the BLUE analysis defined by equation 1.26 is equivalent to the solution obtained by the variational optimisation problem:

$$\mathbf{x}_a = \underset{\mathbf{x}}{\operatorname{argmin}}\, J(\mathbf{x}), \tag{1.33}$$

where the cost function is defined by 1.30.

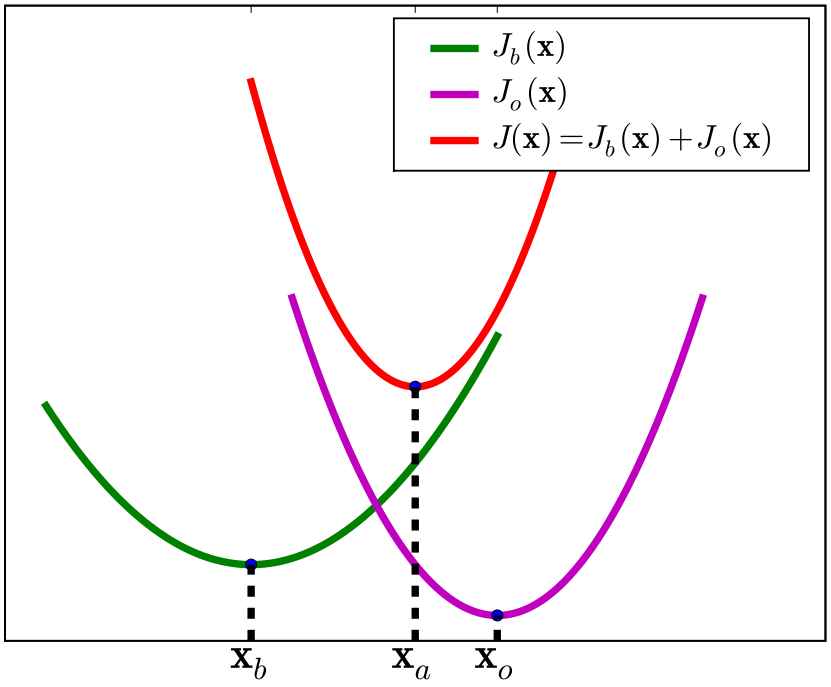

Figure 1.11: Schematic representation of the variational form of the analysis $\mathbf{x}_a$

3D-Var avoids the computation of matrix $\mathbf{K}$ defined in 1.27 and looks for $\mathbf{x}_a$ as an approximate solution to the cost function 1.30. The minimisation is done by numerical methods, like a Conjugate Gradient or a quasi-Newton algorithm [Nocedal and Wright, 2006]. It is accomplished by computing the gradient of J. The geometry of the minimisation is explained in Figure 1.12, where the quadratic cost function has the shape of a paraboloid in a two variables model space.

If the minimisation is satisfactory, the analysis $\mathbf{x}_a$ will not depend on the choice of the initial point. In practice, the initial point of the minimisation, is taken at the background state $\mathbf{x}_b$. As long as it is strictly convex, there is one and only one analysis $\mathbf{x}_a$. A significant difficulty with 3D-Var is the need to design and to invert the matrix $\mathbf{B}$. In particular, when the dimension of $\mathbf{x}$ or $\mathbf{B}$ is very large, the computation of the inverse matrix $\mathbf{B}^{-1}$ or of the preconditioner $\mathbf{B}^{-1/2}$ is expensive.

In practice, H may not be linear. H usually needs to be linearised in the vicinity of the background state (i.e. we assume that $\mathbf{x_a}$ is close to $\mathbf{x}_b$). In this case, we have

$$H(\mathbf{x}) - H(\mathbf{x}_b) \approx \mathbf{H}\,(\mathbf{x} - \mathbf{x}_b)\,. \tag{1.34}$$

Then $\mathbf{K}$ is a continuous function of $\mathbf{H}$, and the least-squares equations for the analysis yield a nearly optimal $\mathbf{x}_a$.

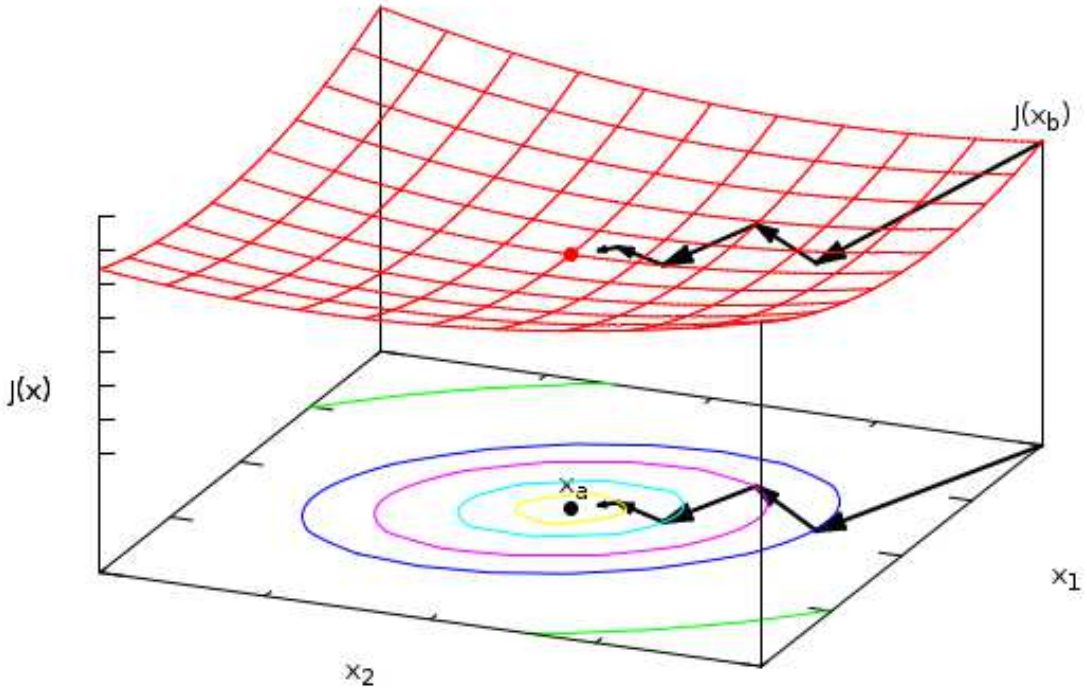

Figure 1.12: Schematic representation of the variational cost function minimisation in a two variables space.

1.4.3 4D-Var

With 3D-Var/OI, we gather a background state $\mathbf{x}_b$ with available observations at some time k. The minimisation of the cost function $J(\mathbf{x})$ will produce an estimate of the state at time k (see section 1.4.2). It is always desirable to use as many measurements as possible. However, these measurements are generally distributed not only in space but also in time. A more complex situation consists in assimilating observations distributed over a time period. *4D-Var* is an assimilation method minimising the misfit between a temporal sequence of model states and the available observations over a given assimilation window. Contrary to 3D-Var/OI, it propagates the information contained in observations both forward and backward in time (see Figure 1.13).

If model error is ignored, the cost function is defined as follows:

$$\begin{aligned} J(\mathbf{x}) &= J_b(\mathbf{x}) + J_o(\mathbf{x}) \\ &= \frac{1}{2}\left(\mathbf{x}-\mathbf{x}_b\right)^{\mathrm{T}} \mathbf{B}\left(\mathbf{x}-\mathbf{x}_b\right) \\ &\quad + \frac{1}{2}\sum_{k=0}^{N}\left(\mathbf{y}_k - \mathbf{H}_k\mathbf{x}_k\right)^{\mathrm{T}} \mathbf{R}_k^{-1}\left(\mathbf{y}_k - \mathbf{H}_k\mathbf{x}_k\right), \end{aligned} \tag{1.35}$$

under the constraint $\mathbf{x}_k = M_{1\rightarrow k}(\mathbf{x}) = M_k M_{k-1} \ldots M_2 M_1(\mathbf{x})$. The minimisation of $J(\mathbf{x})$ will define the initial condition of the model solution $\mathbf{x}_a$ that leads to the best fit to observations.

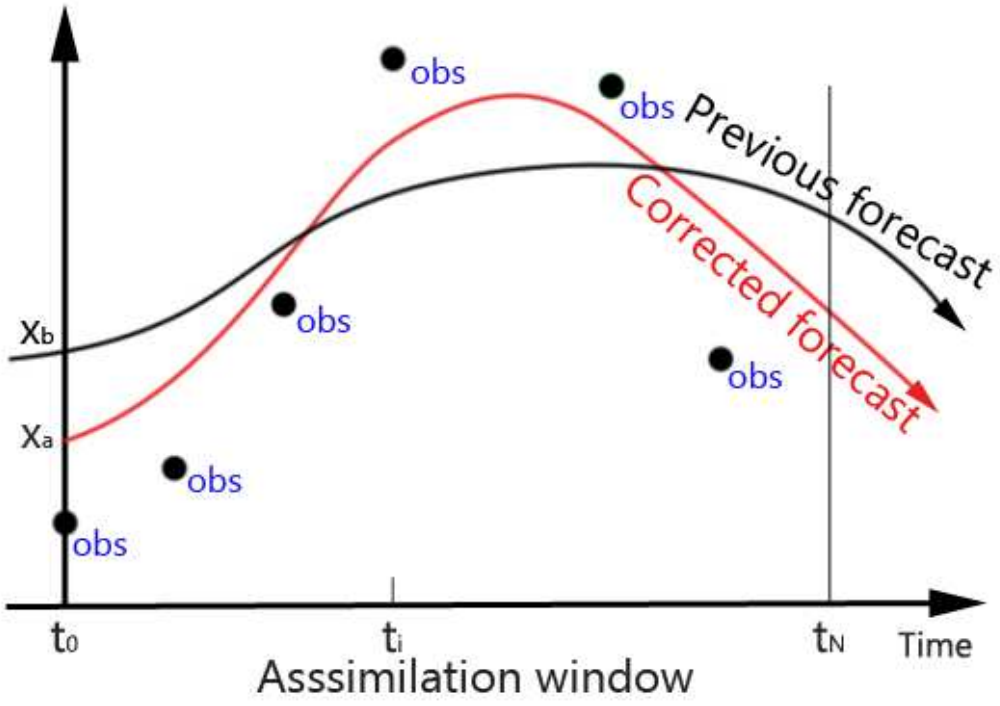

Figure 1.13: Schematic representation of 4D-Var intermittent assimilation in a numerical forecasting system.

The theory of the BLUE requires the operators (e.g. H_k and M_k) to be linear. In practice, this condition is rarely verified. The variational assimilation form given by 1.35 is almost always implemented with a non-linear model.

We denote by $\partial J/\partial \mathbf{x}$ the gradient of J with respect to $\mathbf{x}$ and have

$$\frac{\partial J}{\partial \mathbf{x}} = \left(\frac{\partial J}{\partial x_i}\right)_{i=1,\ldots,n}. \tag{1.36}$$

The gradient is equal to zero at the minimum of the cost function. In simple and small dimensional problems, determining the argument of the minimum of the cost function is to determine analytical expressions for $\partial J/\partial x_i$ and to solve a system of scalar equations. In meteorological and oceanographic applications, it is inconceivable to obtain analytical expressions for the gradient $\partial J/\partial \mathbf{x}$ due to the complexity of the computations of the cost function and the temporal integration of a numerical dynamical model. In this case, we employ an iterative minimisation algorithm, such as a Conjugate Gradient or a quasi-Newton algorithm. It determines the minimising value of the cost function at $\mathbf{x}_a$ though a sequence of successive approximations $\mathbf{x}^{(l)}$:

$$\mathbf{x}^{(l+1)} = \mathbf{x}^{(l)} + \mathbf{d}^{(l)}, \tag{1.37}$$

where $\mathbf{d}^{(l)}$ is the direction of the local gradient $\partial J/\partial \mathbf{x}$ or a combination of the local gradient and of a number of gradients computed at previous iteration steps. In practice, an analytical expression for the gradient is determined numerically by finite differences. Let Δx_i be a perturbation on component x_i of the vector $\mathbf{x}$. The approximation of the partial derivative $\partial J/\partial \mathbf{x}$

is given by the difference quotient

$$\frac{\partial J}{\partial \mathbf{x}} \approx \frac{J(\mathbf{x} + \Delta x_i) - J(\mathbf{x})}{\Delta x_i}. \tag{1.38}$$

However, it is numerically too imprecise for high-dimensional models.

The adjoint method allows the numerical computation of the gradient of the cost function. In order to stress the possible non-linearity of the model, we introduce the notations $\mathbf{M}_k$ which is hereafter the tangent linear operator of M_k. For any perturbation $\delta\mathbf{x}$ of the vector $\mathbf{x}$, the corresponding variation of J, δJ, is expressed as follows,

$$\delta J = \left(\frac{\partial J}{\partial \mathbf{x}}\right)^{\mathrm{T}} \delta\mathbf{x}. \tag{1.39}$$

On the other hand, the first order variation of the cost function J is given by the differentiation of 1.35

$$\delta J = (\mathbf{x} - \mathbf{x}_b)^{\mathrm{T}} \mathbf{B}^{-1}\delta\mathbf{x} + \sum_{k=0}^{N} (\mathbf{H}_k\mathbf{x}_k - \mathbf{y}_k)^{\mathrm{T}} \mathbf{R}_k^{-1}\mathbf{H}_k\delta\mathbf{x}_k, \tag{1.40}$$

where

$$\delta\mathbf{x}_{k+1} = \mathbf{M}_k\delta\mathbf{x}_k. \tag{1.41}$$

The goal is to obtain a direct dependence of δJ with respect to $\delta\mathbf{x}$ of form given by 1.39. We introduce N Lagrange vectors λ_k, $k = 1, \ldots, N$, to enforce the dynamical constraints

$$\begin{aligned} \delta J &= (\mathbf{x} - \mathbf{x}_b)^{\mathrm{T}} \mathbf{B}^{-1}\delta\mathbf{x} + \sum_{k=0}^{N} (\mathbf{H}_k\mathbf{x}_k - \mathbf{y}_k)^{\mathrm{T}} \mathbf{R}_k^{-1}\mathbf{H}_k\delta\mathbf{x}_k \\ &\quad + \sum_{k=1}^{N} \lambda_k^{\mathrm{T}} \left(\delta\mathbf{x}_k - \mathbf{M}_{k-1}\delta\mathbf{x}_{k-1}\right). \end{aligned} \tag{1.42}$$

We rewrite 1.42 on terms of $\delta\mathbf{x}_k$ as follows

$$\begin{aligned} \delta J &= \left[\mathbf{B}^{-1}(\mathbf{x} - \mathbf{x}_b) + \mathbf{H}_0^{\mathrm{T}}\mathbf{R}_0^{-1}(\mathbf{H}_0\mathbf{x}_0 - \mathbf{y}_0) + \mathbf{M}_0^{\mathrm{T}}\lambda_1\right]^{\mathrm{T}} \delta\mathbf{x}_0 \\ &\quad + \sum_{k=1}^{N-1} \left[\mathbf{H}_k^{\mathrm{T}}\mathbf{R}_k^{-1}(\mathbf{H}_k\mathbf{x}_k - \mathbf{y}_k) - \lambda_k + \mathbf{M}_k^{\mathrm{T}}\lambda_{k+1}\right]^{\mathrm{T}} \delta\mathbf{x}_k \\ &\quad + \left[\mathbf{H}_N^{\mathrm{T}}\mathbf{R}_N^{-1}(\mathbf{H}_N\mathbf{x}_N - \mathbf{y}_N) - \lambda_N\right]^{\mathrm{T}} \delta\mathbf{x}_N. \end{aligned} \tag{1.43}$$

This expression is valid for any choice of the λ_k. Thus we recursively choose λ_k as follows

$$\lambda_N = \mathbf{H}_N^{\mathrm{T}}\mathbf{R}_N^{-1}(\mathbf{H}_N\mathbf{x}_N - \mathbf{y}_N) \tag{1.44}$$

$$\lambda_k = \mathbf{H}_k^{\mathrm{T}}\mathbf{R}_k^{-1}(\mathbf{H}_k\mathbf{x}_k - \mathbf{y}_k) + \mathbf{M}_k^{\mathrm{T}}\lambda_{k+1} \text{ for } k = N-1, \ldots, 1 \tag{1.45}$$

$$\lambda_0 = \mathbf{M}_0^{\mathrm{T}}\lambda_1 + \mathbf{B}^{-1}(\mathbf{x} - \mathbf{x}_b) + \mathbf{H}_0^{\mathrm{T}}\mathbf{R}_0^{-1}(\mathbf{H}_0\mathbf{x}_0 - \mathbf{y}_0), \tag{1.46}$$

to eliminates all $\delta\mathbf{x}_k$ terms, except the $\delta\mathbf{x}_0$ term. There remains

$$\delta J = \lambda_0^{\mathrm{T}}\delta\mathbf{x}_0, \tag{1.47}$$

where λ_0 is the required gradient of the cost function with respect to the initial condition $\mathbf{x}_0$.

The computations performed for determining the gradient $\partial J/\partial\mathbf{x}$ for a given initial condition $\mathbf{x_0}$ are now clearly defined:

- Starting from $\mathbf{x}_0$, integrate equation 1.16 for $k = 1, \ldots, N$. Store the corresponding solution $\mathbf{x}_k$ in memory.

- Starting from time N, recursively integrate the adjoint equations 1.44, 1.45 and 1.46 backward in time. The required gradient is λ_0.

Notice that $\mathbf{x}_k$ is necessary for computing the term $\mathbf{H}_k^{\mathrm{T}}\mathbf{R}_k^{-1}\left(\mathbf{H}_k\mathbf{x}_k - \mathbf{y}_k\right)$. When the equation 1.16 is non-linear, it is also necessary to determine the tangent linear operator $\mathbf{M}_k$.

4D-Var does not take into account model errors. If model errors are large, problems can be expected. To taken into account model errors in DA, we use a weak-constraint variational assimilation method, i.e. weak-constraint 4D-Var [Trémolet, 2006]. However, it is more complex than 4D-Var. In addition, 4D-Var requires the implementation of the adjoint model $\mathbf{M}_k^{\mathrm{T}}$. This can be expensive when the forecast model is complex.

1.4.4 Ensemble Kalman filter

The Kalman filter (KF) [Kalman, 1960] is similar to OI with the major difference that the error covariances are propagated by the model. OI calculates a constant estimate whereas KF uses the model to propagate the error covariance matrix. The ensemble Kalman filter (EnKF) [Evensen, 2009] provides an approximation to KF when the ensemble size increases. The update step of (stochastic) EnKF provides an ensemble of analyses, while the forecast step consists of an ensemble forecast using the analysis ensemble as initial conditions (see Figure 1.14).

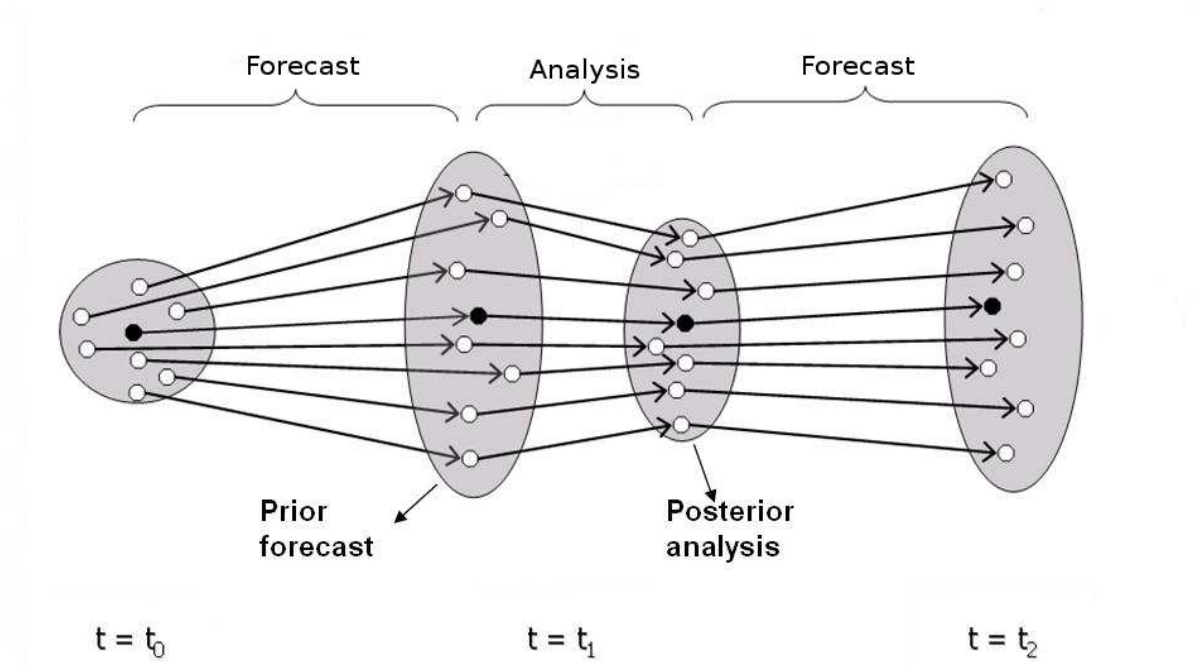

Figure 1.14: Schematic representation of the EnKF method in a numerical forecasting system.

Let $\mathbf{x}$ be a random variable with density $p(\mathbf{x})$ and $\{\mathbf{x}^i, i = 1, \ldots, N_e\}$ is a random sample of $\mathbf{x}$. We consider this random sample as an ensemble. Two important quantities derived from this random sample are the sample mean

$$\hat{\mathbf{x}} = \frac{1}{N_e} \sum_{i=1}^{N_e} \mathbf{x}^i, \tag{1.48}$$

and the sample covariance

$$\hat{\mathbf{P}} = \frac{1}{N_e - 1} \sum_{i=1}^{N_e} \left(\mathbf{x}^i - \hat{\mathbf{x}}\right) \left(\mathbf{x}^i - \hat{\mathbf{x}}\right)^{\mathrm{T}} = \mathbf{X}\mathbf{X}^{\mathrm{T}}, \tag{1.49}$$

where $\mathbf{X}$ is a matrix whose columns are the ensemble perturbations scaled $(N_e - 1)^{-1/2}$, i.e. $(N_e - 1)^{-1/2} \left(\mathbf{x}^i - \hat{\mathbf{x}}\right)$.

The idea in the ensemble data assimilation is to avoid directly using the full covariance matrices, and to work instead with a random sample. We derive the "stochastic" form of the EnKF. In the linear, Gaussian case, the EnKF approaches the KF method as the ensemble size grows.

Let $\mathbf{x} \sim \mathcal{N}(\mathbf{x}_f, \mathbf{P}_f)$, a Gaussian distribution with mean $\mathbf{x}_f$ and covariance matrix $\mathbf{P}_f$, where $\mathbf{x}_f = \hat{\mathbf{x}}$ and $\mathbf{P}_f = \hat{\mathbf{P}}$. We consider the random variable

$$\xi = \mathbf{x} + \mathbf{K} \left(\mathbf{y} - (\mathbf{H}\mathbf{x} + \epsilon)\right), \tag{1.50}$$

with the gain $\mathbf{K} = \mathbf{P}_f \mathbf{H}^{\mathrm{T}} \left(\mathbf{H}\mathbf{P}_f\mathbf{H}^{\mathrm{T}} + \mathbf{R}\right)^{-1}$ and the observation error $\epsilon \sim \mathcal{N}(\mathbf{0}, \mathbf{R})$. Since ξ is a linear function of the Gaussian random variables $\mathbf{x}$ and ϵ, it is also Gaussian. Its mean is

$$\mathbf{E}(\xi) = \mathbf{x}_f + \mathbf{K} \left(\mathbf{y} - \mathbf{H}\mathbf{x}\right) = \mathbf{x}_a. \tag{1.51}$$

The covariance of ξ is calculated in a way similar to the error covariance of the BLUE. Since ϵ and $\mathbf{x}$ are independent, we have

$$\begin{aligned} \mathrm{cov}(\xi) &= \mathbf{P}_f - \mathbf{P}_f \mathbf{H}^{\mathrm{T}} \left(\mathbf{H}\mathbf{P}_f\mathbf{H}^{\mathrm{T}} + \mathbf{R}\right)^{-1} \mathbf{H}\mathbf{P}_f \\ &= \mathbf{P}_a. \end{aligned} \tag{1.52}$$

Finally, we have $\xi \sim \mathcal{N}(\mathbf{x}_a, \mathbf{P}_a)$, with $\mathbf{x}_a$ and $\mathbf{P}_a$ given by 1.51 and 1.52. Therefore, a random draw of ξ is draw from the desired conditional distribution.

Starting from $\mathbf{x}^i$ drawn from the forecast distribution $N(\mathbf{x}_f, \mathbf{P}_f)$ and ϵ^i from $N(0, \mathbf{R})$, we update each $\mathbf{x}^i$ by

$$\xi^i = \mathbf{x}^i + \mathbf{K} \left(\mathbf{y} - \left(\mathbf{H}\mathbf{x}^i + \epsilon^i\right)\right). \tag{1.53}$$

Here, we replace the covariances $\mathbf{K}$ by sample estimates based on the forecast ensemble $\{\mathbf{x}^i, i = 1, \ldots, N_e\}$. Let the sample mean $\hat{\mathbf{x}}_f = N_e^{-1} \sum \mathbf{x}^i$. We define the matrix $\mathbf{X}$ as a matrix with columns $(N_e - 1)^{-1/2} \left(\mathbf{x}^i - \hat{\mathbf{x}}_f\right)$ and the matrix $\mathbf{Y}$ as a matrix with columns $(N_e - 1)^{-1/2} \left(\mathbf{H}\left(\mathbf{x}^i - \hat{\mathbf{x}}_f\right) + \epsilon^i - \hat{\epsilon}\right)$. Thus according to 1.49, we have $\mathbf{P}_f\mathbf{H}^{\mathrm{T}} = \mathbf{X}\mathbf{Y}^{\mathrm{T}}$ and $\mathbf{H}\mathbf{P}_f\mathbf{H}^{\mathrm{T}} = \mathbf{Y}\mathbf{Y}^{\mathrm{T}}$. The approximate gain matrix becomes

$$\hat{\mathbf{K}} = \mathbf{X}\mathbf{Y}^{\mathrm{T}} \left(\mathbf{Y}\mathbf{Y}^{\mathrm{T}}\right)^{-1}. \tag{1.54}$$

Then the basic stochastic form of EnKF is

$$\xi^i = \mathbf{x}^i + \hat{\mathbf{K}}\left(\mathbf{y} - \left(\mathbf{H}\mathbf{x}^i + \epsilon^i\right)\right). \tag{1.55}$$

This update step involves performing a separate analysis for each member ξ^i, using the approximate gain $\hat{\mathbf{K}}$ and the observation error ϵ.

The result of the update step is an ensemble of analyses $\{\xi_i,\ i = 1, \ldots, N_e\}$.The sample mean is

$$\hat{\mathbf{x}}_a = \hat{\xi} = \hat{\mathbf{x}}_f + \hat{\mathbf{K}}\left(\mathbf{y} - \left(\mathbf{H}\hat{\mathbf{x}} + \hat{\epsilon}\right)\right), \tag{1.56}$$

which agrees with the KF update of the mean. If we define $\mathbf{X}_a$ as the matrix with columns $(N_e - 1)^{-1/2}\left(\xi^i - \hat{\mathbf{x}}_a\right)$, $i = 1, \ldots, N_e$, we have

$$\begin{aligned} \mathbf{X}_a &= \mathbf{X} - \hat{\mathbf{K}}\mathbf{Y}, \\ \hat{\mathbf{P}}_a &= \mathbf{X}\mathbf{X}^{\mathrm{T}} - \mathbf{X}\mathbf{Y}^{\mathrm{T}}\left(\mathbf{Y}\mathbf{Y}^{\mathrm{T}}\right)^{-1}\mathbf{Y}\mathbf{X}^{\mathrm{T}}, \end{aligned}$$

where $\hat{\mathbf{P}}_a$ agrees with the KF result. Covariance matrices are replaced with sample estimates from the ensemble.

When $N_e \to \infty$, the sample estimates converge to their correct values and the mean and covariance of the ensemble of EnKF converge to those given by KF. As shown in this section, the fundamental approximation in EnKF is to replace the mean and covariance appearing in KF by sample estimates. Because N_e is finite, the sample estimates used in EnKF contain sampling errors, which will affect the results of the algorithm. In addition, other properties of the sample covariance suffer larger errors. The rank of $\mathbf{X}\mathbf{X}^{\mathrm{T}}$ is at most $N_e - 1$. Thus in a high-dimensional system with moderate N_e, almost all the eigenvalues of $\mathbf{P}_f$ are zero. There were also little theory to quantify how sampling error affects the EnKF. Therefore, the "localisation" of sample covariances is crucial to effective and high-dimensional EnKF. In principle, this technique sets the sample covariance to be zero for sufficiently large separation distances. It directly removes many small and potentially noisy entries from the sample covariance matrix and also greatly increases the rank of the covariance matrix.

1.4.5 Choice of DA method

In air quality, Zhang et al. [2012] review chemical DA techniques developed to improve regional real-time air quality forecasting model performance for ozone, PM_{10}, and dust. Among the widely used DA algorithms, the optimal interpolation (OI) is used in our work, as it is the most computationally efficient [Denby et al., 2008; Tombette et al., 2008; Wu et al., 2008; Li et al., 2013]. In applications of DA to aerosol forecast, Tombette et al. [2009] have used the OI over western Europe for assimilating observations from the BDQA network, which covers France. Denby et al. [2008] have used two different DA techniques, the OI and EnKF, to assimilate PM_{10} concentrations over Europe. They showed OI can be more effective than the EnKF. Pagowski et al. [2010] have used the OI over the United States of America for data assimilation of $PM_{2.5}$ observations. Li et al. [2013] have used the OI for multiple aerosol species and for prediction of $PM_{2.5}$ in the Los Angeles basin. Although aerosol assimilation could be performed with 4D-Var [Benedetti and Fisher, 2007], it may be limited to the use of a simplified aerosol model, as it is numerically very costly.

1.5 Objectives and plan of thesis

Aerosols have an impact on human health, visibility and climate of the Earth (see section 1.1). Thus aerosol measurements have been performed for years to monitor aerosol spatial distributions and properties for better comprehension of atmospheric aerosols (see section 1.2). However, aerosol measurements cannot directly be used to map and forecast levels of pollution. In order to understand aerosol processes and forecast levels of pollution, modellers have developed various chemistry transport models (CTM) in the past several years (see section 1.3). Uncertainties in aerosol modelling are high. Data assimilation (DA) is a technique which can reduce the uncertainties in input data such as the initial conditions or the boundary conditions by coupling models to observations (see section 1.4). Aerosols data from in situ surface measurements and satellite passive remote sensing are often assimilated. However, they either do not provide information on vertical profiles or provide vertical observations limited to low horizontal and temporal resolutions. Accurate vertical profiles of aerosols can now be measured due to a new generation of portable lidar systems. Although the spaceborne lidar CALIPSO promises to improve the vertical resolution of aerosol measurements at the global scale, observations are only performed along the satellite track. At present, several lidar networks could perform regular measurements at continental scales (see section 1.2).

The objective of this work is to assimilate ground-base lidar network measurements so as to reduce the uncertainties in aerosol modelling and improve the forecast capacity of air quality models. We expect this work to prove the usefulness and the feasibility of assimilating ground-based lidar network observations for aerosol forecasts. Also, we expect it will help future lidar network projects to design lidar networks, e.g. number and locations of lidar stations. The outline of this thesis follows.

In Chapter 2, since a lidar network with continuous measurements did not exist over Europe before 2012, an Observing System Simulation Experiment (OSSE) is built over Europe to investigate the potential impact of future ground-based lidar networks on analysis and short-term forecasts of PM_{10} over one month. Moreover, a sensitivity study on the number and location of required lidars is performed to help define an optimal lidar network in western Europe for PM_{10} forecasts.

In Chapter 3, the ability of the air quality modelling platform POLYPHEMUS to simulate lidar backscattered profiles from model aerosol concentration outputs is studied. Simulated lidar signals are compared to hourly lidar observations performed during the MEGAPOLI (Megacities: Emissions, urban, regional and Global Atmospheric POLlution and climate effects, and Integrated tools for assessment and mitigation) summer experiment in July 2009. This evaluation can also be regarded as a validation of the lidar observation operator (i.e. the operator H in section 1.4). Moreover, two new algorithms for assimilating lidar observations are presented.

In Chapter 4, we present the application of assimilating lidar signals over the Mediterranean basin, where a network performed a 72-hour period of intensive and continuous measurements in July 2012. Meanwhile, we study how several parameters of the assimilation system modify the horizontal and temporal impacts.

Finally, in Chapter 5, we summarise the results found in the previous chapters and give conclusions of this work. This chapter also describes possible future directions and new perspectives on the basis of the present data assimilation results.

Chapter 2

Assimilation of ground versus lidar observations for PM_{10} forecasting

Preamble

In this chapter, a tool for assimilating PM_{10} concentration measurements on the vertical profile is developed using the optimal interpolation (OI) method. This tool is meant to investigate the potential impact of future ground-based lidar networks on analysis and short-term forecasts of PM_{10}. We make the hypothesis that there exists a relation between PM_{10} mass concentration and optical properties of aerosols. Such relation was determined for aerosol pollution over Greater Paris by Raut and Chazette [2009].

Raut and Chazette [2009] reported two methods, a theoretical method and an empirical method, to estimate PM_{10} from extinction coefficients.

The theoretical relationship between PM_{10} and aerosol extinction coefficients at 355 nm is given as a function of the density of particle ρ, the mean cubic radius $\overline{r^3}$ and the mean extinction cross-section $\overline{\sigma_{\mathrm{ext},355}}$:

$$\mathrm{PM}_{10} = \rho \, \frac{4}{3} \, \pi \, \frac{\overline{\mathrm{r}^3}}{\overline{\sigma_{\mathrm{ext},355}}} \, \alpha_{\mathrm{ext},355,\mathrm{dry}}, \tag{2.1}$$

where the extinction coefficient $\alpha_{\mathrm{ext},355,\mathrm{dry}}$ can be determined by coupling lidar measurements retrieved from a Rayleigh-Mie lidar and photometer measurements, or by measurements retrieved from a Raman-N_2 lidar. The density of particle ρ is estimated as a constant which depends on the aerosol type. The mean cubic radius $\overline{r^3}$ can be estimated by the size distribution [Raut et al., 2009a]. The mean extinction cross-section $\overline{\sigma_{\mathrm{ext},355}}$ can be estimated from the model. This method was applied to assess the pollution level of PM_{10} from mobile lidar observations over Greater Paris by Raut and Chazette [2009] and Royer et al. [2011]. As detailed in Raut and Chazette [2009], Figure 2.1 shows the route followed by a mobile lidar on 25 May 2005 and the lidar-derived PM_{10} concentrations. Also, this method was used to determine ash concentrations in Paris, following the eruption of the Icelandic volcano Eyjafjallajökull on 14 April 2010 [Chazette et al., 2012]. Figure 2.2 shows the temporal evolutions of AOT and aerosol mass concentrations derived from a ground-based lidar at 355 nm.

The empirical relationship between dry PM_{10} and aerosol extinction coefficients at 355 nm is given as follows:

$$\mathrm{PM}_{10} = C_0 \, \omega_{0,355} \left(\frac{700}{355} \right)^{-a} \alpha_{\mathrm{ext},355,\mathrm{dry}}, \tag{2.2}$$

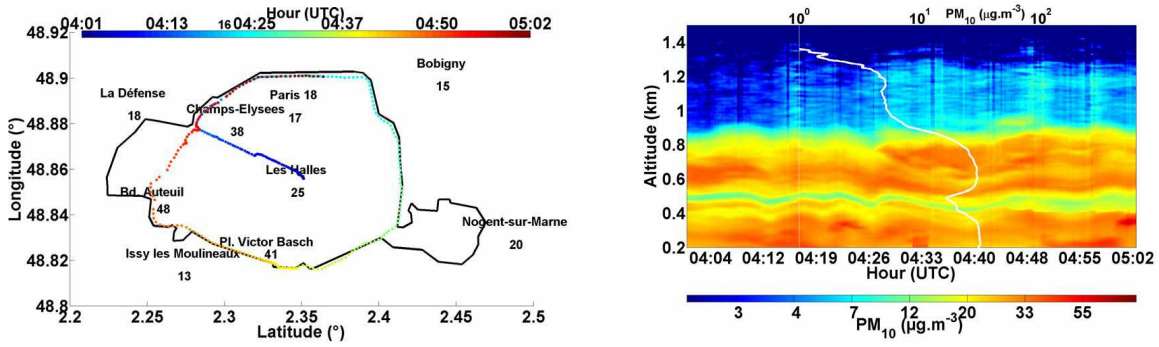

Figure 2.1: Left panel shows the route followed by a small vehicle embarking a lidar on 25 May 2005 on the Paris Peripherique before rush-hour traffic and the hourly averaged PM_{10} values measured at AIRPARIF network stations. The black line circling Paris is the geographic of Paris city. Right panel corresponds to the temporal evolution of lidar-derived PM_{10} concentrations along the vehicle route. The mean PM_{10} profile retrieved from lidar signals is shown in white. From Raut and Chazette [2009].

where C_0 is the slope of regression analysis between the nephelometer scattering coefficients at 700 nm and the TEOM PM_{10} measurements, $\omega_{0,355}$ is the albedo at 355 nm, a is the Angström exponent between 355 and 700 nm. Royer et al. [2011] generalised those relationships to wet PM_{10} concentrations by take into account the effect of humidity.

Presently, several lidar networks could perform regular measurements at continental scales to establish a comprehensive dataset of the aerosol vertical distribution and also to assess volcanic, dust, fires or pollution events (see Chapter 1). However, no lidar network performed operational measurements before December 2012. Thus, an Observing System Simulation Experiment (OSSE) is built over western Europe for one month from 15 July to 15 August 2001 in this chapter (see section 2.4). Although there exists the European Aerosol Research Lidar Network (EARLINET) comprising 28 lidar stations over Europe (see Figure 2.3), their instrumentation is rather inhomogeneous. Therefore, in OSSE, we defined a network of 12 fictitious ground-based lidar stations covering western Europe, which is based on the lidar sites of existing observation stations, i.e. a subset of EARLINET stations.

Representing the "true" atmosphere by a simulation called "nature run" in OSSE, the efficiency of assimilating the lidar network (with 12 stations) measurements is compared to the efficiency of assimilating surface concentration measurements from the AirBase ground network, which includes about 500 stations in western Europe in 2001. It is found that assimilating the lidar observations decreases by about 54 % the root mean square error (RMSE) of PM_{10} concentrations after 12 h of assimilation and during the first forecast day, against 59 % for the assimilation of AirBase measurements. However, the assimilation of lidar observations leads to similar scores as AirBase's during the second forecast day. The RMSE of the second forecast day is improved on average over the summer month by 57 % by the lidar DA, against 56 % by the AirBase DA. Moreover, the spatial and temporal influence of the assimilation of lidar observations is larger and longer.

A sensitivity study on the number and location of required lidars is also performed to help define an optimal lidar network for PM_{10} forecasts (section 2.7). Two lidar networks of 12 lidar stations, whose locations are very different, were compared. It is found that spreading out

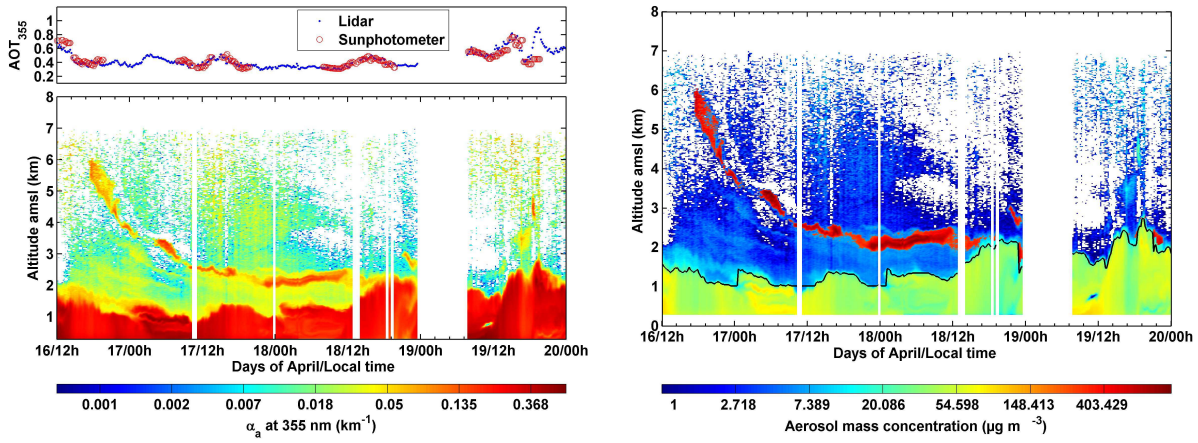

Figure 2.2: Left column: AOT at 355 nm derived from sunphotometer (red circles) and lidar measurements (blue points), and temporal evolution of the vertical profile of the aerosol extinction coefficient (α_{ext}) derived from a ground-base lidar at 355 nm. Right column: temporal evolution of the aerosol mass concentration (PM) derived from a ground-based lidar at 355 nm. The PBL top height is indicated by the black line. From Chazette et al. [2012].

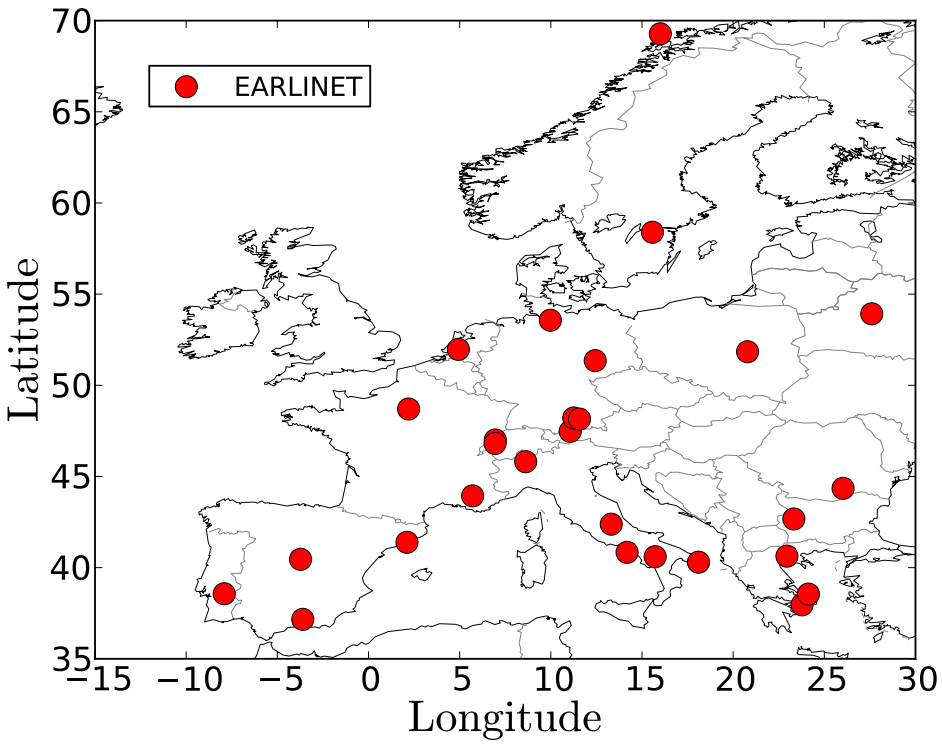

Figure 2.3: Distribution of the EARLINET sites. The red discs show the locations of EARLINET stations.

the lidars regularly over Europe can improve the PM_{10} forecast. Moreover, the efficiencies of assimilating measurements from the lidar network of 26, 76 and 488 (the same as the number of AirBase stations) lidar stations are presented. We find that increasing the number of lidar improves the forecast scores. For example, during the first forecast day, the assimilation of 76 lidar stations measurements leads to a better score (the RMSE decreased by about $65\,\%$) than AirBase's (the RMSE decreased by about $59\,\%$).

This chapter consists of
Wang, Y., Sartelet, K. N., Bocquet, M. and Chazette, P. : **Assimilation of ground versus lidar observations for PM_{10} forecasting**, Atmos. Chem. Phys., 13, 269-283, doi:10.5194/acp-13-269-2013, 2013.

Sommaire

2.1 Introduction

Aerosols have an impact on regional and global climates [Ramanathan et al., 2001; Léon et al., 2002; Sheridan et al., 2002; Intergovernment Panel on Climate Control (IPCC), 2007] as well as on ecological equilibrium [Barker and Tingey, 1992] and human health by penetrating the respiratory system and leading to respiratory and cardiovascular diseases [Lauwerys et al., 2007; Dockery and Pope, 1996]. Aerosols influence the photo-dissociation of gaseous molecules [Randriamiarisoa et al., 2004] and can thus have a significant impact on photochemical smog [Dickerson et al., 1997]. Thus the accurate prediction of aerosol concentration levels has signification human and economic cost implications.

Various chemistry transport models are used to simulate or predict aerosol concentrations over Europe, e.g. EMEP (European Monitoring and Evaluation Programme) [Simpson et al., 2003], LOTOS (Long Term Ozone Simulation) – EUROS (European Operational Smog) [Schaap et al., 2004], CHIMERE [Hodzic et al., 2006], DEHM (Danish Eulerean Hemispheric Model) [Brandt et al., 2007] and POLYPHEMUS [Sartelet et al., 2007]. However, uncertainties in modelling atmospheric components, in particular aerosols are high [Roustan et al., 2010], which leads to significant differences between model simulations and observations [Sartelet et al., 2007]. Data assimilation (DA hereafter) can reduce the uncertainties in input data such as the initial conditions or the boundary conditions by coupling models to observations [Bouttier and Courtier, 2002]. In meteorology, DA has been traditionally applied to improve forecasts [Kalnay, 2003; Lahoz et al., 2010]. In air quality, Zhang et al. [2012] review chemical DA techniques developed to improve regional real-time air quality forecasting model performance for ozone, PM_{10}, and dust. However, applications of DA to PM_{10} forecasts are still sparse. They include Tombette et al. [2009] and Denby et al. [2008] over Europe and Pagowski et al. [2010] over the United States of America. They demonstrated the feasibility and the usefulness of DA for aerosol forecasts.

As in Tombette et al. [2009], in situ surface measurements are often assimilated, e.g. AirBase, BDQA (Base de Données de la Qualité de l'Air) or EMEP. However, they do not provide information on vertical profiles. Niu et al. [2008] used both satellite retrieval data and surface observations to assimilate dust for sand and dust storm (SDS) forecasts. They found that information on the vertical profiles of the SDS was needed for the SDS forecasts. Although satellite passive remote sensing can provide vertical observations, it is very expensive and data are often limited to low horizontal (e.g. $10 \times 10\,\mathrm{km}^2$ for the Moderate Resolution Imaging Spectroradiometers (MODIS) [Kaufman et al., 2002]) and temporal resolutions (e.g., approximately twice a day for polar orbiting satellites). Passive instruments can only retrieve column-integrated aerosol concentration [Kaufman et al., 2002]. Spaceborne lidar promises to improve the vertical resolution of aerosol measurements at the global scale [Winker et al., 2003; Berthier et al., 2006; Chazette et al., 2010]. Nevertheless, the spaceborne lidar measurements are only performed along the satellite ground track.

Thanks to the new generation of portable lidar systems developed in the past five years, accurate vertical profiles of aerosols can now be measured [Raut and Chazette, 2007; Chazette et al., 2007]. Such instruments document the mid and lower troposphere by means of aerosol optical properties. Lidar measurements were used in several campaigns, such as ESQUIF (Étude et Simulation de la Qualité de l'air en Île-de-France) [Chazette et al., 2005], MEGAPOLI (Megacities: Emissions, urban, regional and Global Atmospheric POLlution and climate effects, and Integrated tools for assessment and mitigation) summer experiment in July 2009

[Royer et al., 2011] and during the eruption of the Icelandic volcano Eyjafjallajökull on 14 April 2010 [Chazette et al., 2012]. Raut and Chazette [2009] established a reliable relation between the mass concentration and the optical properties of PM_{10}. Because the surface-to-mass ratio for fine particles ($PM_{2.5}$, particulate matter with a diameter smaller than $2.5\,\mu$m) is high, they largely contribute to the measured lidar signal. However, the contribution of coarse particles may not be negligible as shown by Randriamiarisoa et al. [2006] who estimated it to be about $19\,\%$. The relative contribution of $PM_{2.5}$ may increase with altitude [Chazette et al., 2005], but it is difficult to quantify. Thereby, the PM_{10} concentrations above urban areas can be retrieved from a ground-based lidar system with an uncertainty of about $25\,\%$.

Because a lidar network with continuous measurements does not yet exist, lidar observations have not yet been used for DA. This work aims to investigate the usefulness of future ground-based lidar network on analyses and short-term forecasts of PM_{10} and to help future lidar network projects to design lidar networks, e.g. number and locations of lidar stations. Building and maintaining observing systems with new instruments is very costly, especially for ground-based lidars. Therefore, an Observing System Simulation Experiment (OSSE) can be used to effectively test proposed observing strategies before a field experiment takes place, and it can provide valuable information for the design of field experiments [Masutani et al., 2010].

An OSSE is constituted by a nature run, simulated observations, and DA experiments. The nature run is usually a simulation from a high-resolution state-of-the-art model forecast, and is used to create observations and validate DA experiments [Chen et al., 2011]. Many applications use OSSEs, such as for investigating the accuracy of diagnostic heat and moisture budgets [Kuo and Anthes, 1984], studying carbon dioxide measurements from the Orbiting Carbon Observatory using a four-dimensional variational assimilation [Chevallier et al., 2007; Baker et al., 2010], demonstrating the data impact of Doppler wind lidar [Masutani et al., 2010; Tan et al., 2007], defining quantitative trace carbon monoxide measurement requirements for satellite missions [Edwards et al., 2009], comparing the relative capabilities of two geostationary thermal infrared instruments to measure ozone and carbon monoxide [Claeyman et al., 2011], evaluating the contribution of column aerosol optical depth observations from a future imager on a geostationary satellite [Timmermans et al., 2009], and studying the impact of observational strategies in field experiments on weather analysis and short-term forecasts [Chen et al., 2011].

This paper is organised as follows. Section 2.2 provides a description of the DA methodology used in this study. Section 2.3 describes the experiment setup, i.e. the chemistry transport model used and real observations. An OSSE is built in Sect. 2.4. Results of the OSSE are shown in Sects. 2.5 and 2.6. Sensitivity studies with respect to the number and locations of lidar stations are conducted in Sect. 2.7. The findings are summarised and discussed in Sect. 2.8.

2.2 Choice of DA method

Data assimilation couples model with simulated observations in an OSSE. Different DA algorithms may be used, e.g. OI, reduced-rank square root Kalman filter, ensemble Kalman filter (EnKF) and four-dimensional variational assimilation (4D-Var). Wu et al. [2008] have illustrated their limitations and potentials. They found that in the air quality context the OI provides overall strong performances and it is easy to implement. In terms of performance, the reduced-rank square root Kalman filter is quite similar to the EnKF. Denby et al. [2008]

compared two different DA techniques, the OI and EnKF, for assimilating PM_{10} concentration at the European scale. They showed OI can be more effective than the EnKF. Although aerosol assimilation could be performed with 4D-Var [Benedetti and Fisher, 2007], it may be limited to the use of a simplified aerosol model, as it is quite expensive for computation.

In this paper, we use the OI as it is the simpler method for PM_{10} DA and it performs well [Denby et al., 2008; Wu et al., 2008]. Furthermore, the OI method can be used in operational mode for real-time forecasts, as the computational cost of OI is low. It was used by Tombette et al. [2009] and Pagowski et al. [2010] for DA of conventional aerosol ground observations. In the OI method, DA is performed at the frequency of measurements to produce analysed concentrations, which are closer to reality (measurements) than forecasts and which are used as initial conditions for the next model iteration. The equation to compute the analysed concentrations from the model concentrations is given by:

$$\mathbf{x}_\mathrm{a} = \mathbf{x}_\mathrm{b} + \mathbf{B}\mathbf{H}^\mathrm{T}\left(\mathbf{H}\mathbf{B}\mathbf{H}^\mathrm{T} + \mathbf{R}\right)^{-1}\left(\mathbf{y} - H[\mathbf{x}_\mathrm{b}]\right), \tag{2.3}$$

where $\mathbf{x}_\mathrm{a}$ is the analysed concentrations, $\mathbf{x}_\mathrm{b}$ is the model concentrations, $\mathbf{y}$ is the observation vector, H is an operator that maps $\mathbf{x}_\mathrm{b}$ to the observational data, $\mathbf{H}$ is the tangent linear operator of H (in the following, the observation operator is linear), $\mathbf{B}$ and $\mathbf{R}$ are respectively the background and observation error covariance matrices. They require the specification of the background and observation error covariance matrices (see Sects. 2.4.2, 2.4.4 and 2.5). The background error covariance matrix determines how the corrections of the concentrations should be distributed over the domain during DA. The observation error covariance matrix specifies instrumental and representativeness errors. As in Tombette et al. [2009], after DA of PM_{10} concentrations, the analysed PM_{10} concentrations are redistributed over the model variables following the initial chemical and size distributions.

2.3 Experimental setup

2.3.1 Model

For our study, the chemistry transport model POLAIR3D [Sartelet et al., 2007] of the air-quality platform POLYPHEMUS, available at `http://cerea.enpc.fr/polyphemus/` and described in Mallet et al. [2007] is used. Aerosols are modelled using the SIze-REsolved Aerosol Model (SIREAM-SuperSorgam), which is described in Debry et al. [2007] and Kim et al. [2011a]. SIREAM-SuperSorgam includes 20 aerosol species: 3 primary species (mineral dust, black carbon and primary organic species), 5 inorganic species (ammonium, sulphate, nitrate, chloride and sodium) and 12 organic species. It models coagulation and condensation. Five bins logarithmically distributed over the size range $0.01\,\mu$m–$10\,\mu$m are used. The gas chemistry is solved with the chemical mechanism CB05 (Carbon Bond version 5) [Yarwood et al., 2005]. POLAIR3D/SIREAM has been used for several applications. For example, it was compared to measurements for gas and aerosols over Europe by Sartelet et al. [2007] and Kim et al. [2010], and it was compared to lidar measurements over Greater Paris by Royer et al. [2011].

2.3.2 Input data

The modelling domain covers western and part of eastern Europe ([10.5° W, 23° E] × [35° N, 58° N]) with a horizontal resolution of 0.5° × 0.5°. Nine vertical levels are considered from the ground to 12 000 m. The heights of the cell interfaces are 0, 40, 120, 300, 800, 1500, 2400, 3500, 6000 and 12 000 m. The simulations are carried out for one month from 15 July to 15 August 2001, with a time step of 600 s. Meteorological inputs are obtained from reanalysis provided by the European Centre for Medium-Range Weather Forecasts (ECMWF). Anthropogenic emissions of gases and aerosols are generated with the EMEP inventory for 2001. For gaseous boundary conditions, daily means are extracted from outputs of the global chemistry-transport model MOZART2 (Model for OZone And Related chemical Tracers version 2) [Horowitz et al., 2003]. For aerosol boundary conditions, daily means are based on outputs of the Goddard Chemistry Aerosol Radiation and Transport model (GOCART) for the year 2001 for sulphate, dust, black carbon and organic carbon [Chin et al., 2000; Sartelet et al., 2007].

2.3.3 Observational data

In this paper, as in Sartelet et al. [2007] and Tombette et al. [2009], we use the locations of stations of two ground databases for the comparisons to ground data measurements:

- the EMEP database, available on the EMEP Chemical Co-ordinating Centre (EMEP/CCC) web site at `http://www.emep.int/`;

- the AirBase database, available on the European Environment Agency (EEA) web site at `http://air-climate.eionet.europa.eu/databases/airbase/`. Note that the traffic and industrial stations are not used, because the simulation horizontal scale (0.5° × 0.5°) can not be representative of these station types.

In 2001, PM_{10} concentrations are provided on a daily basis at EMEP stations, against an hourly basis at most AirBase stations. Moreover, data are provided at only 27 EMEP stations, against 509 AirBase stations. Therefore, the EMEP network is only used for the performance assessment of the nature run, whereas the AirBase network is used for both the performance assessment of the nature run and assimilations in the OSSE. Figure 2.4 shows the location of the EMEP and AirBase stations used in this study.

In this work, a network of 12 fictitious ground-based lidar stations covering western Europe is defined, as shown in Fig. 2.4, based on the lidar locations of existing observation stations, e.g. a subset of stations from the European Aerosol Research Lidar Network (`http://www.earlinet.org/`). A relation between PM_{10} mass concentration and optical properties of aerosols is assumed to exist, although it has so far only been determined for pollution aerosols over Greater Paris [Raut and Chazette, 2009] and it needs to be generalised to other measurement sites.

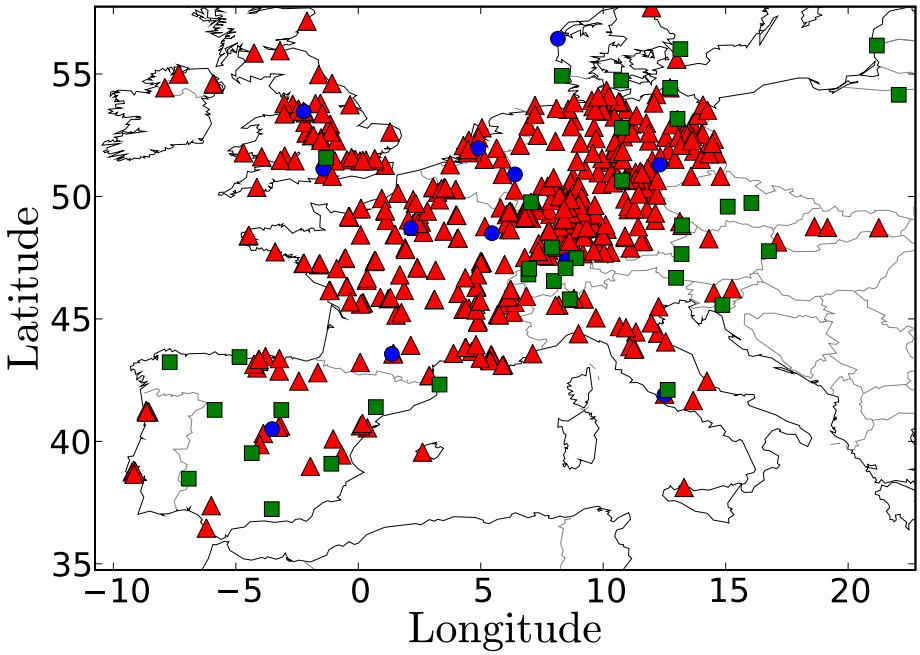

Figure 2.4: The green squares show the locations of EMEP stations, the red triangles show the locations of AirBase stations, and the blue discs show the locations of the lidar network.

2.4 Observing system simulation experiment

2.4.1 Nature run

Observation impact experiments for not-yet-existing observing systems require an atmospheric state, from which the hypothetical observations can be generated. Since the true atmosphere is inherently unknown, a synthetic atmosphere state, in the remainder denoted "truth", needs to be defined. In an OSSE, the "true" state is used to create the observational data from existing and future instruments. In this paper, the "truth" is obtained from a simulation, called nature run, performed between 00:00 UTC 15 July to 00:00 UTC 15 August 2001 using the model [Kim et al., 2010, 2011b] and the input data described in the previous section. Here, we first evaluate the results of this simulation with the AirBase and EMEP networks.

For an OSSE study, the accuracy of the nature run compared with real observations is important, and the nature run should produce typical features of the phenomena of interest. According to Boylan and Russell [2006], if both the Mean Fractional Bias (MFB) and the Mean Fractional Error (MFE) are in the range $[-30\,\%,\ 30\,\%]$ and $[0,\ 50\,\%]$ respectively, then the model performance goal is met; if both the MFB and MFE are in the range $[-60\,\%,\ 60\,\%]$ and $[0,\ 75\,\%]$ respectively, the model performance criterion is met. As shown in Table 2.1, for PM_{10}, the model performance criterion is met for the two networks, whereas for $PM_{2.5}$ the model performance goal is met for both networks, suggesting that this simulation compares well to observations. Furthermore, as shown in Fig. 2.5, the spatial distribution of PM_{10} concentration corresponds to previously published results [Sartelet et al., 2007]. This "true" simulation is subsequently used for the creation of observations from the observing system un-

Table 2.1: Statistics (see Appendix A) of the simulation results for the AirBase and EMEP networks from 15 July to 14 August. Ammon. stands for ammonium. Obs. stands for observation. Sim. stands for simulation. Corr. stands for correlation.

Species	Database	Stations	Obs. mean	Sim. mean	RMSE	Corr.	MFB	MFE
			$\mu g\,m^{-3}$	$\mu g\,m^{-3}$	$\mu g\,m^{-3}$	%	%	%
PM_{10}	AirBase	419	22.5	12.7	17.3	35	−47	69
	EMEP	27	18.8	12.3	9.6	67	−39	48
$PM_{2.5}$	AirBase	3	11.2	13.1	8.7	45	7	44
	EMEP	18	13.2	11.5	7.2	64	−16	45
Sulphate	AirBase	11	2.2	3.0	1.7	59	41	60
	EMEP	51	2.9	2.6	1.7	61	−3	45
Nitrate	AirBase	8	2.8	5.1	4.0	51	23	72
	EMEP	13	1.7	2.2	1.9	20	−16	78
Ammon.	AirBase	8	1.7	2.5	1.3	62	28	43
	EMEP	8	1.6	1.8	1.1	39	6	47
Sodium	EMEP	1	1.4	2.4	1.6	82	44	52
Chloride	AirBase	7	0.6	2.2	1.9	70	1	1

der investigation and will also be used to evaluate the results of DA experiments, for example the calculation of the Root Mean Square Error (RMSE) and correlation over land grid points from the ground level to the sixth level (1950 m above the ground) against the nature run.

2.4.2 Simulated observations and error modelling

The "true" state of the atmosphere (the nature run) is used to calculate the concentrations at both stations of the AirBase network and of the future ground-based lidar network. For example for the lidar network, Fig. 2.6 shows the "true" state of PM_{10} at two arbitrary chosen lidar stations: Madrid [Perez et al., 2004] and Saclay [Raut and Chazette, 2009]. We find that the high PM_{10} concentrations in Madrid are mostly made of Sahara dust. Because the AirBase network covers well western Europe and provides in situ surface measurements (which have been used for the performance assessment of the nature run in section 2.4.1) and because AirBase measurements have been used for DA of PM_{10} [Denby et al., 2008; Tombette et al., 2009], we took AirBase as an assimilation reference network in order to quantitatively show the potential impact of future ground-based lidar networks on analysis and short-term forecasts of PM_{10}. However, real observations at AirBase stations are not used for the assimilation, but the "truth" is used to calculate the "true" states (e.g., concentrations), in order to be consistent with the lidar data.

The "true" state at each station is perturbed depending on estimated observation errors. For the network AirBase, the observation errors mainly correspond to the representativeness errors, and they are estimated to be about 35%. For the ground-based lidar network, the observation errors include the representativeness errors (about 35%) and the instrumental errors, which are estimated to be about 25% for PM_{10} concentrations obtained from lidar observations [Raut and

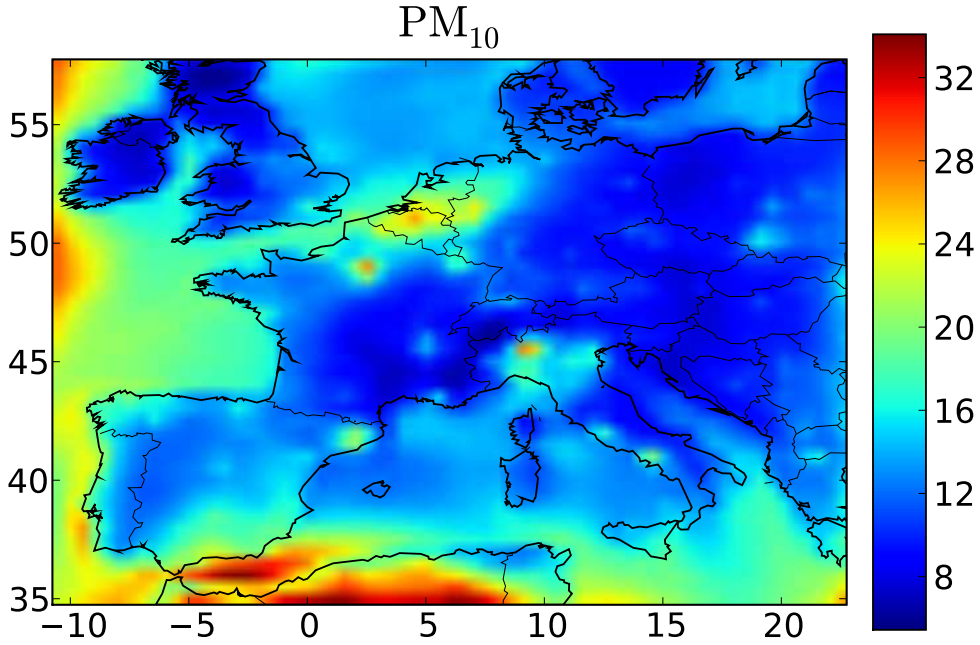

Figure 2.5: Mean concentrations of PM_{10} over Europe (in $\mu g\,m^{-3}$). It ranges from $6\,\mu g\,m^{-3}$ (dark blue) to $34\,\mu g\,m^{-3}$ (dark red).

Chazette, 2009]. These instrumental errors are linked to errors in estimating the extinction coefficients using the inversion of the lidar signal [Klett, 1981] and extinction coefficient cross sections. The covariance between the representativeness and instrumental errors is set to zero since they are independent. Finally, the observation errors of the concentrations obtained from the lidar network are estimated to be about 43 % (the square root of the sum of the representativeness error variance and the instrumental error variance, $\sqrt{35\%^2 + 25\%^2}$). Note that when comparing the nature run to the real data, the errors include both the representativeness errors and the model errors. They are therefore different from the observation errors used to perturb the simulated observations.

After defining the observation errors, the observations obtained from the “true" state are perturbed. For each station, let $\mathbf{x}$ be a vector, whose component x_i is a hourly mean concentration and i depends on vertical level and time. The perturbation is implemented as follows:

- Define the observational error covariance matrix $\mathbf{\Sigma}$ by the Balgovind approach [Balgovind et al., 1983]. The error covariance between two points is

$$f(d_v, d_t) = e\left(1 + \frac{d_v}{L_v}\right)\exp\left(-\frac{d_v}{L_v}\right) \times \left(1 + \frac{d_t}{L_t}\right)\exp\left(-\frac{d_t}{L_t}\right), \qquad (2.4)$$

  where e is the observational error variance, d_v is the vertical distance between the 2 points, d_t is the temporal difference between the 2 points, $L_\mathrm{v} = 200\,\mathrm{m}$ and $L_\mathrm{t} = 2\,\mathrm{h}$ are the vertical and temporal correlation lengths. Each component of the covariance matrix

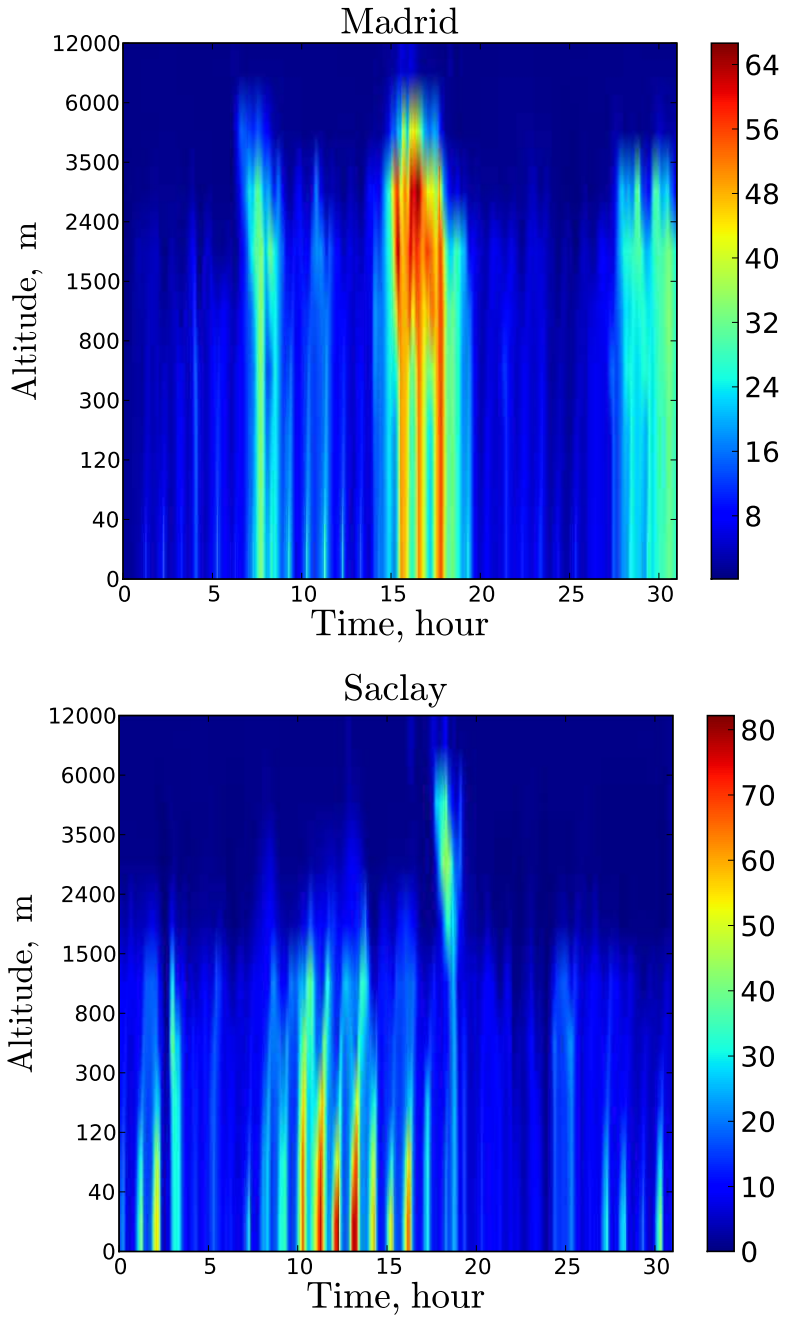

Figure 2.6: The "true" state of PM_{10} from 01:00 UTC 15 July to 00:00 UTC 15 August 2001 at the lidar stations Madrid (left panel) and Saclay (right panel). Dark and red colours correspond to high and low PM_{10} concentrations (μg m^{-3}), respectively.

$\mathbf{\Sigma}$ may be written as $\Sigma_{ij} = f\left(d_{\mathrm{v}}(x_i, x_j), d_{\mathrm{t}}(x_i, x_j)\right)$. Each component of the covariance matrix depends smoothly on the altitude of the points and time.

- Use the Cholesky decomposition:

$$\mathbf{\Sigma} = \mathbf{C}\mathbf{C}^{\mathrm{T}}, \tag{2.5}$$

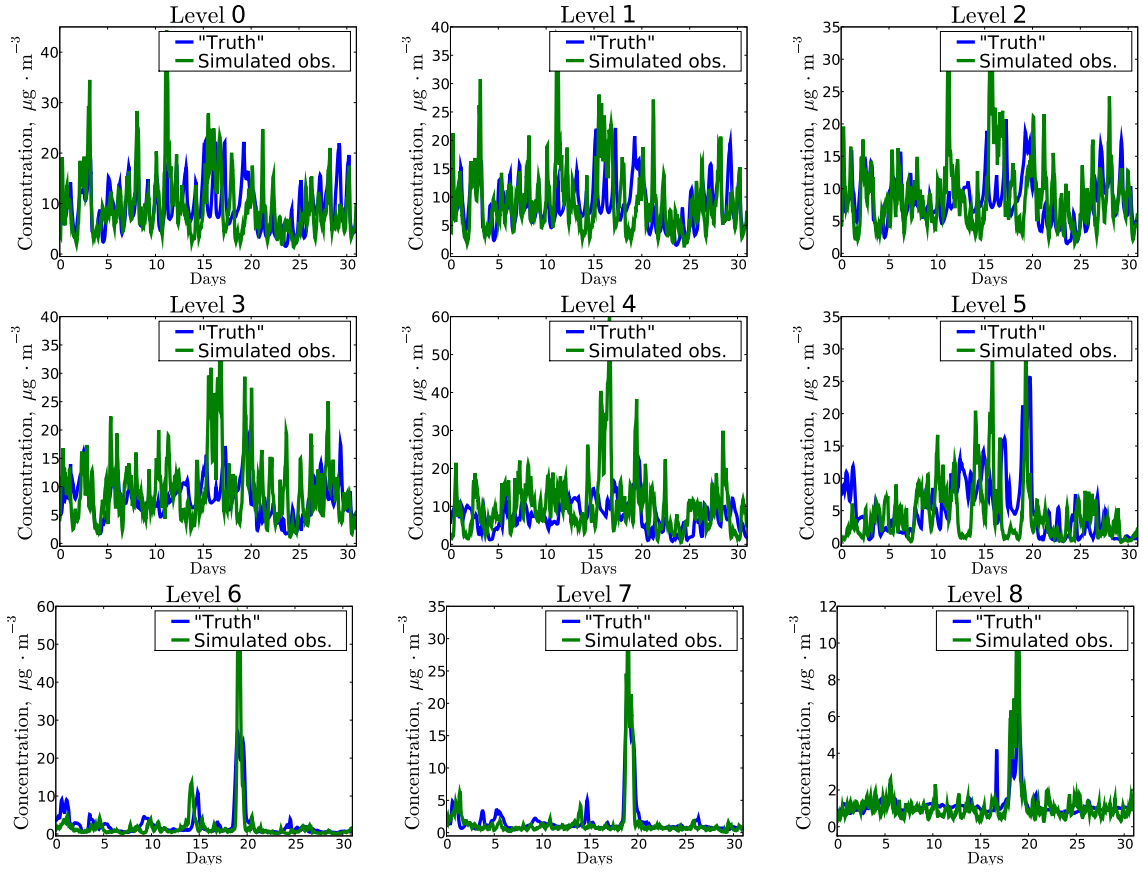

Figure 2.7: Perturbation at a random AirBase station from 15 July to 15 August 2001 at from the first vertical level in the model (top left) to the last vertical level in the model (bottom right). The blue lines show the "true" PM_{10} concentrations ($\mu g\ m^{-3}$). The green lines show the simulated PM_{10} concentrations ($\mu g\ m^{-3}$).

where $\mathbf{C}$ is a lower triangular matrix with strictly positive diagonal entries.

The perturbation of $\mathbf{x}$ is then

$$\mathbf{x}' = \mathbf{x} + \mathbf{C}\gamma, \tag{2.6}$$

where γ is a random vector whose components are a standard normal distribution (of mean 0 and variance 1). Figure 2.7 shows an example of perturbations at an arbitrarily chosen station. We can see that the perturbations depend continuously on the vertical level and the time thanks to matrix $\mathbf{C}$. The perturbed observations are subsequently used for the assimilation of the ground-based lidar network and AirBase data.

2.4.3 Control run

The control run is a simulation that is meant to represent the best modellers' simulation of the atmosphere. If the same model is used for both the nature run and the control run, this is called an identical twin OSSE; if the nature run model is a different version of the control run model, the OSSEs are called fraternal twin OSSEs [Liu and Kalnay, 2007; Masutani et al., 2010]. We follow a "perfect model" OSSE setup, in which the model used to generate the "true"

observations is the same as the one used in the control run and DA. The identical twin OSSEs are easy to set up. However, input data, such as meteorological fields, emissions [Edwards et al., 2009] or initial conditions [Liu and Kalnay, 2007] have to be perturbed. In order to be able to interpret more easily the results, we choose to perturb only initial conditions. This allows us to avoid the complications of defining model errors, and the only source of forecast errors comes from the initial conditions. With the identical twin scenario, the numerical model becomes perfect (i.e., no model error); this is counter to what happens in reality (i.e., models are never perfect) and the identical twin OSSEs usually overestimate the impact of observations on model forecasts [Chen et al., 2011].

Although the impact of PM_{10} DA may be over-optimistic, it will be so for both ground observations and lidar observations (the assimilation of both ground and lidar observations lead to corrections at high vertical levels, as discussed in Sect. 2.5). As in Sect. 2.4.2, we use the Balvogind approach [Balgovind et al., 1983], the Cholesky decomposition and the normal distribution to perturb all model concentrations (gaseous and aerosols). In air quality models, the impact of initial conditions on PM_{10} concentrations lasts for a few hours to a few days at most. For this impact to last as long as possible, both gaseous and aerosol concentrations are perturbed. As shown in Fig. 2.8, the differences between "true" and perturbed PM_{10} concentrations in certain parts of Europe are higher than in other parts of Europe. This is due to the normal distribution, which can produce very high or low concentrations in one grid cell. Although the perturbed initial conditions are not necessarily consistent with the true state of atmosphere, they are suitable for our experiments with DA.

2.4.4 Parameters of the DA runs

The experiments consist of two steps: the DA analysis part and the forecast. During the assimilation period, say between $[t_0, t_N]$, at each time step, the observations are assimilated. During the subsequent forecast period, say between $[t_{N+1}, t_T]$, the aerosol concentrations are obtained from the model simulations initialised from the analysed model state at t_N.

Since only the initial conditions are perturbed in our experiments (see Sect. 2.4.3), the difference between two forecasts initialised with different initial conditions only lasts for a few days. For the choice of t_N, Fig. 2.9 compares the RMSE between the true observations and the forecast concentrations from 18 July at 01:00 UTC to 20 July at 00:00 UTC, obtained for different assimilation periods varying from 6 h to 3 days and always ending at 00:00 UTC 18 July. The longer the assimilation period is, the lower the RMSE is. An assimilation period of 12 h seems a good compromise between a low RMSE and a short assimilation time.

Two different types of DA runs are performed in our OSSE, depending on whether ground or vertical observations are assimilated. The simulations use the same setup as the one of the control run. We use the perturbed PM_{10} observations that are produced by the nature run (see Sect. 2.4.2). The first DA run uses only simulated data at AirBase stations. It is performed from the first level (20 m above the ground) to the sixth level (1950 m above the ground) of the model. The second DA run uses only the ground-based lidar network simulated data. It is performed from the third level (210 m above the ground) to the sixth level (1950 m above the ground), because the lidar measurements are not available from the ground to about 200 m above the ground [Raut and Chazette, 2009; Royer et al., 2011].

In this paper, DA experiments are carried out for 27 five-day experiments between 15 July 2001 and 15 August 2001. The first experiment is from 15 to 19 July 2001, the second one is

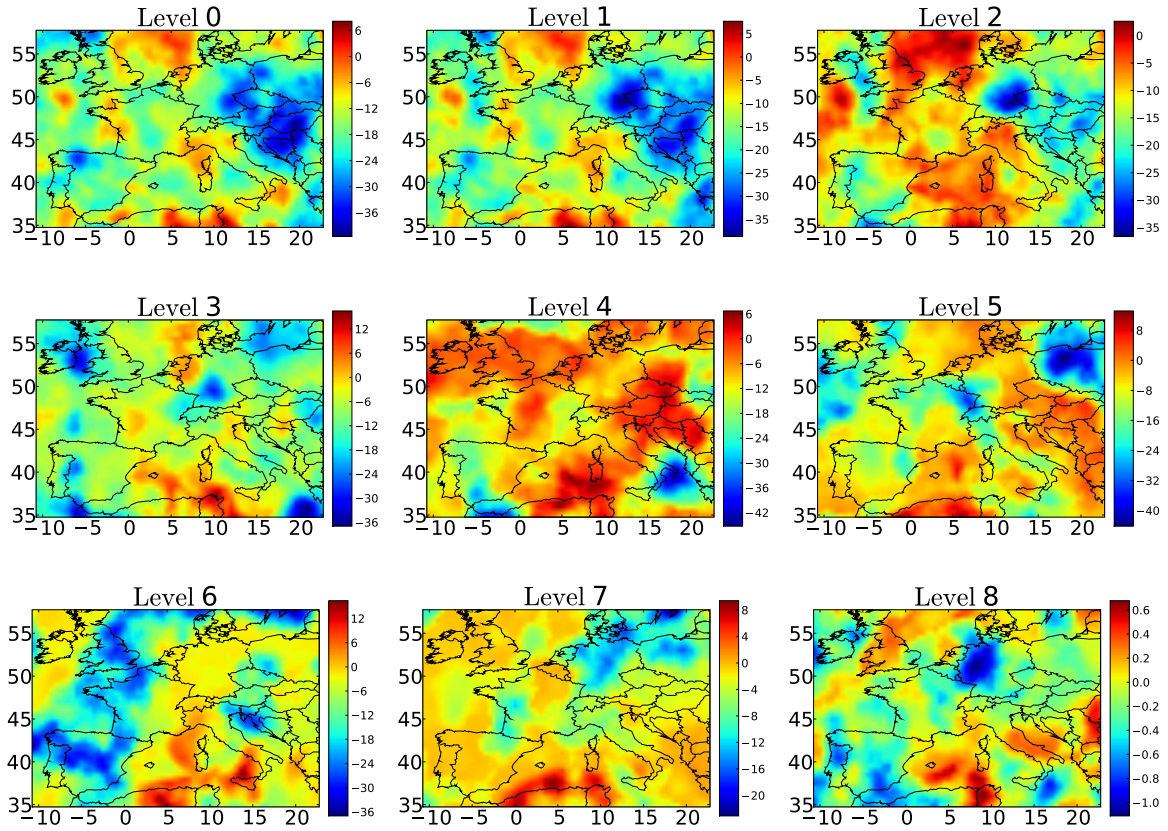

Figure 2.8: Differences between "true" and perturbed PM_{10} concentration at 0000 UTC 15 July 2001, which is the initial time of the first five-day experiment, from the first vertical level in the model (top left) to the last vertical level in the model (bottom right). Differences ($\mu g\ m^{-3}$) vary from negative values in dark blue colour to positive values in dark red colour.

from 16 to 20 July 2001, and so on until 15 August 2001. For each experiment, the observation data are assimilated from 01:00 UTC to 12:00 UTC every hour, thereafter the model runs and produces a forecast for the next four and half days.

In the OI method, the background and observation error covariance matrices need to be set. The observation error covariance matrix depends on the observational error variance, which varies with vertical levels. For ground measurements, we set the error variance to be $20\,\mu g^2\,m^{-6}$, the square of 35 % (see section 2.4.2) of PM_{10} concentration averaged over AirBase stations. For lidar measurement, we set the error variance to be the square of 43 % ($\sqrt{35\%^2 + 25\%^2}$, see section 2.4.2) of PM_{10} concentration averaged over lidar stations for each level from the third level to the sixth level, which is respectively 28, 24, 16 and $5\,\mu g^2\,m^{-6}$.

In the Balgovind parametrisation of the background error covariance matrix [Wu et al., 2008; Tombette et al., 2009], the variance v is set to $60\,\mu g^2\,m^{-6}$, which is obtained from the difference between the nature run and the control run. The correct specification of the background error correlations is crucial to the quality of the analysis, because they determine to what extent the fields will be corrected to match the observations. The horizontal correlation length and the vertical correlation length are two parameters of the Balgovind approach. While the definition of background error correlations is straightforward, since they correspond to the

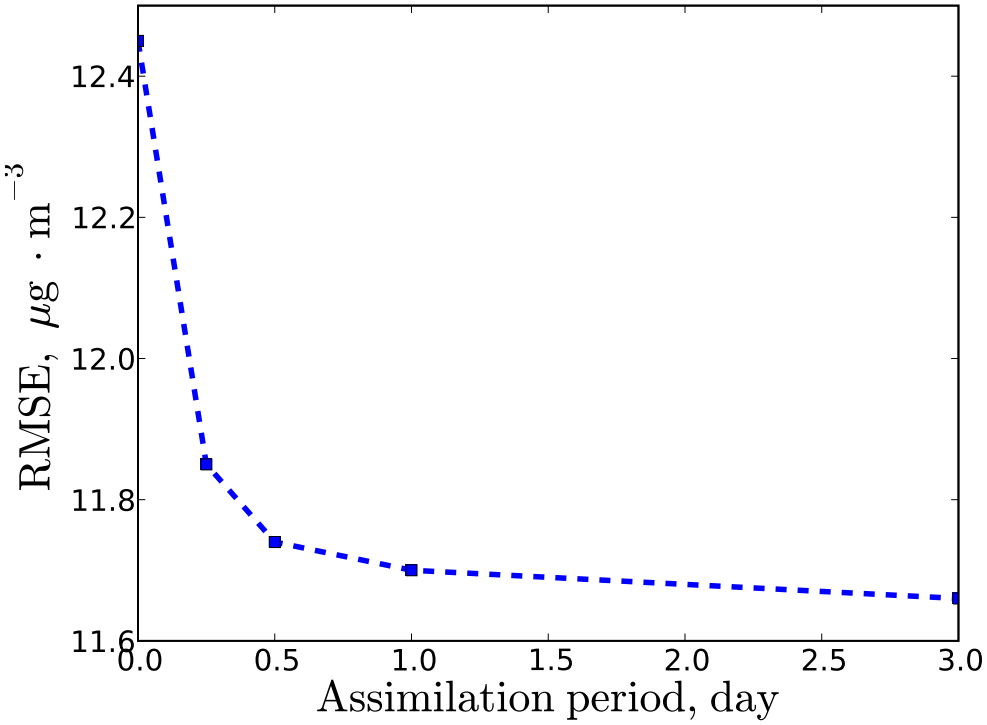

Figure 2.9: RMSE (in $\mu g\, m^{-3}$) between the real AirBase observations and forecast concentrations from 18 July to 20 July against assimilation period (in days).

difference between the background state and the true state, the true atmospheric state is never exactly known. The next section details the choice of the horizontal and vertical correlation length.

2.5 Choice of the horizontal and vertical correlation lengths

The National Meteorological Center (NMC) method [Parrish and Derber, 1992] is used for the choice of the horizontal correlation length L_h and the vertical correlation length L_v. The background error is estimated by the differences of PM_{10} concentrations between two simulations. The two simulations start with the same initial conditions and last 24 hours. A 24 hours forecast is performed in the first simulation, while AirBase data of PM_{10} concentrations are assimilated hourly in the second simulation. In the analysis, the background error covariance matrix is assumed to be a diagonal matrix to avoid adding special error correlations (e.g. the Balgovind approach with a given horizontal and vertical correlation length) in the NMC method. In order to eliminate potential bias due to the diurnal cycle, 24 h forecasts are issued at 00:00 UTC and 12:00 UTC. This estimation of the background error is performed for 27 consecutive days from 15 July 2001 at 00:00 UTC and 12:00 UTC.

To estimate the horizontal correlation length, at each model level, we calculate the covariance value for each site pair. We then obtain a cloud of covariance values. The covariance clouds are averaged within continuous tolerance regions. The length of the tolerance region is

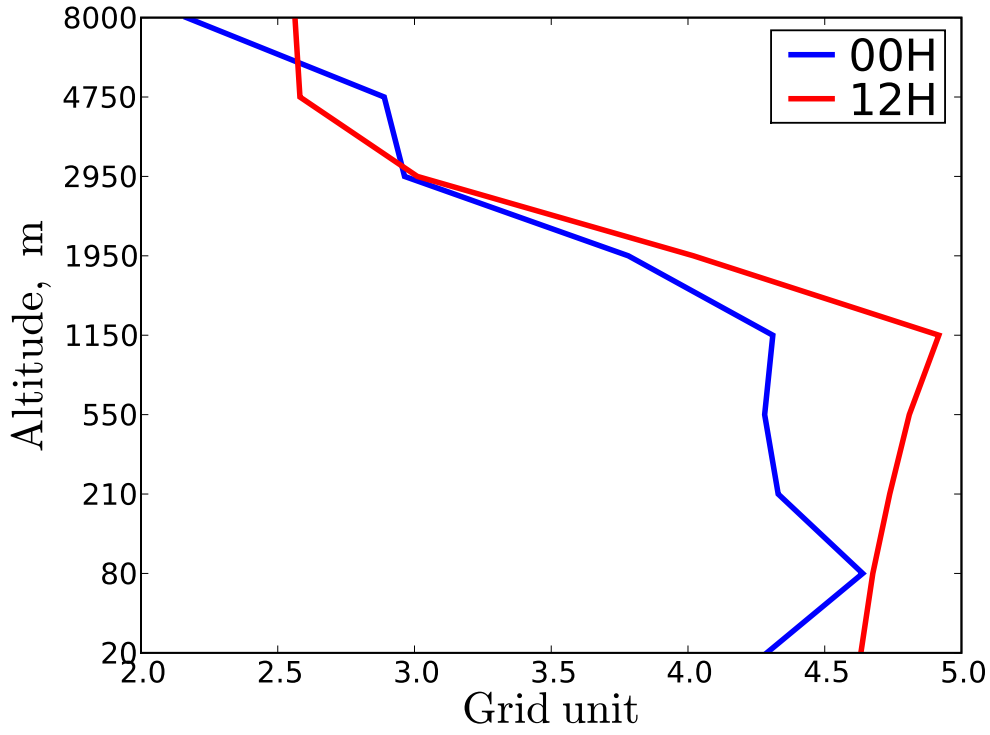

Figure 2.10: The blue (resp. red) line shows the horizontal correlation length L_{h} (grid unit) at 00:00 UTC (resp. 12:00 UTC) versus altitude. Note that a grid unit is about 50 km.

set to 4 grid units, so that there are enough site pairs for each tolerance region. Thus, L_{h} is estimated at all model levels by a least-square fitting of Balgovind functions to the curves of the regionalized covariances (the covariance clouds averaged within tolerance regions). Figure 2.10 shows the horizontal correlation length L_{h} of the background error covariance matrix at 00:00 UTC and 12:00 UTC. The variation of the horizontal correlation length is comparable to that of meteorology [Daley, 1991]. The horizontal correlation length is relatively constant in the boundary layer, and it is about 4 grid units (200 km). Above the boundary layer, the horizontal correlation length decreases. This is a consequence of the prescribed aerosol boundary conditions and the numerical algorithm. Because the background error is estimated by the differences between a simulation with 24 h forecast and a simulation with assimilating ground measurements in the NMC method (the error sources are the ground measurements) and the same boundary conditions are used for both simulations, the background errors at the upper levels are very small. By contrast, the numerical noise can become significant and leads to short length correlations at high levels. A similar behaviour is shown in Benedetti and Fisher [2007]; Pagowski et al. [2010]. In the DA experiments, we should therefore use a horizontal correlation length scale of 200 km. The Lidar In-Space Technology Experiment (LITE) [Winker et al., 1996] data suggest that aerosol fields have a horizontal correlation length scale of 200 km. Similarly to the horizontal correlation length, we find that the vertical correlation length L_{v} is about 250 m at the ground level.

Although the NMC method gives us estimates of the horizontal and vertical correlation lengths, DA tests with different correlation lengths are performed to assess the optimum lengths,

Table 2.2: DA tests with different configurations for Balgovind Scale Parameters. AB stands for AirBase. Col. stands for column. × indicates the type of DA runs used (AirBase DA or Column DA).

Simulation name	AirBase DA	Column DA	L_h (km)	L_v (m)
AB 50 km 1500 m	×		50	1500
AB 200 km 250 m	×		200	250
AB 200 km 1500 m	×		200	1500
AB 200 km 50/1500 m	×		200	50 (nighttime)
				1500 (daytime)
AB 400km 1500 m	×		400	1500
Col. 50 km 0 m		×	50	0
Col. 200 km 0 m		×	200	0
Col. 400 km 0 m		×	400	0

i.e., the lengths which lead to the best forecast. The different tests performed are summarised in Table 2.2. Assimilation is performed with three different horizontal lengths: $L_h = 50$ km, $L_h = 200$ km and $L_h = 400$ km. For AirBase DA, assimilation is also performed with three different vertical correlation lengths: $L_v = 250$ m, $L_v = 1500$ m and L_v varying between nighttime and daytime. Because lidar provides us vertical profiles, the lidar DA can directly correct PM_{10} concentrations at each model level (higher than 200 m above the ground). Therefore, we do not consider L_v in the background error covariance matrix (we assume $L_v = 0$). Moreover, column DA tests with different L_v show that $L_v \neq 0$ does not lead to a better forecast for the column DA run. The scores (RMSE and correlation) calculated over land grid points from the ground level to the sixth level (1950 m above the ground) are shown in Fig. 2.11. Because only the initial conditions (pollutant concentrations) are different between the nature run and the control runs (see Sect. 2.4.3), and because the influence of initial conditions fades out with the forecast time, all control runs converge (RMSEs decrease to 0 and correlations increase to 1 in Fig. 2.11). The role of DA is to accelerate this convergence, to make RMSEs decrease and correlations increase faster. For AirBase DA, choosing $L_v = 1500$ m (DA test "AB 200km 1500m") leads to better scores (lower RMSE and lower correlation) than choosing $L_v = 250$ m (DA test "AB 200km 250m"), as estimated from the NMC method. Choosing $L_v = 50$ m in the nighttime and $L_v = 1500$ m in the daytime (DA test "AB 200km 50/1500m") does not lead to better scores than $L_v = 1500$ m (DA test "AB 200km 1500m"). A possible explanation is that the particles are mixed by turbulence more effectively in the model than in the true state of the atmosphere. The comparison of DA tests "AB 50km 1500m", "AB 200km 1500m" and "AB 400km 1500m" for AirBase and DA tests "Col. 50km 0m", "Col. 200km 0m" and "Col. 400km 0m" for the lidar network shows that $L_h = 200$ km, as estimated from the NMC method, leads to good scores. The scores are better than with $L_h = 50$ km, and similar to those obtained with $L_h = 400$ km.

We also studied the sensitivity of the results to the maximum altitude at which PM_{10} DA is performed during the column DA. We tested the column DA until the eighth level (4750 m above the ground) instead of the sixth level (1950 m above the ground). We found small dif-

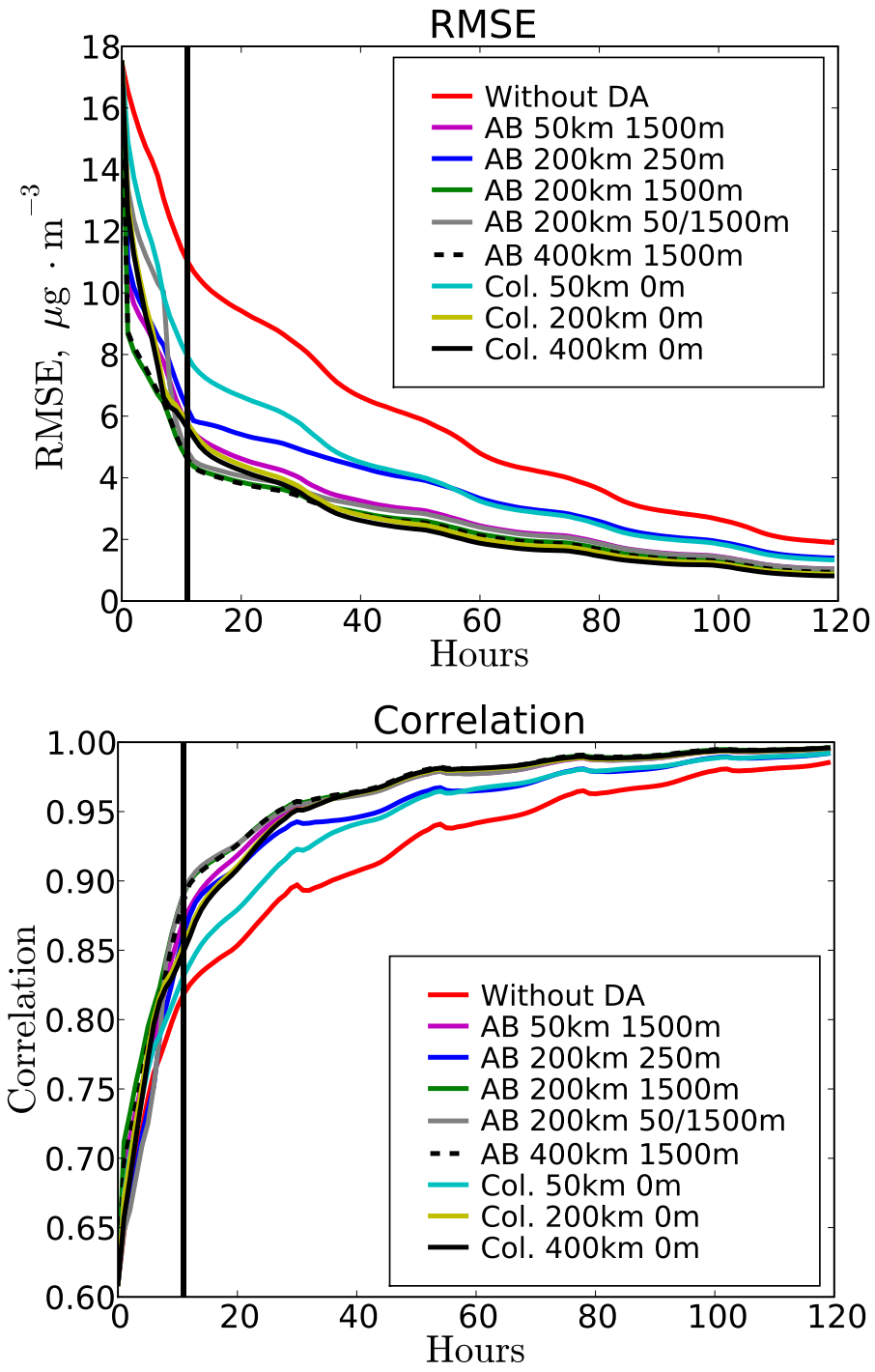

Figure 2.11: Top (resp. bottom) figure shows the time evolution of the RMSE in $\mu g\ m^{-3}$ (resp. correlation) of PM_{10} averaged over the different DA tests from 15 July to 10 August 2001. The scores are computed over land grid points from the ground to the sixth level (1950 m above the ground). The forecast is performed either without DA (red lines), or after AirBase DA or after column DA. The vertical black lines denote the separation between the assimilation period (to the left of the black lines) and the forecast (to the right of the black lines).

ferences between the PM_{10} forecasts at the ground level. It is mostly because the planetary boundary layer (PBL) is usually lower than 2000 m, and PM_{10} concentrations above the PBL have limited impact on surface PM_{10}.

2.6 Comparison between AirBase and 12 lidars network DA

In the following, we compare the DA test "AB 200km 1500m" of Fig. 2.11 for AirBase ($L_{\mathrm{h}} = 200\,\mathrm{km}$ and $L_{\mathrm{v}} = 1500\,\mathrm{m}$) and the DA test "Col. 200km 0m" of Fig. 2.11 for the lidar network ($L_{\mathrm{h}} = 200\,\mathrm{km}$ and $L_{\mathrm{v}} = 0$).

Overall, the simulations with DA lead to better scores (lower RMSE and higher correlations) than the simulation without DA. But as shown in Tombette et al. [2009], the assimilation procedure has almost no impact on PM_{10} concentrations after several days of forecast, because assimilation influences only initial conditions of the forecast period and the influence of initial conditions on PM_{10} concentrations does not last for more than a few days. The AirBase DA forecast has always better scores than the column DA forecast in the first several hours of assimilation (to the left of the black line). This may be explained by the fact that the AirBase DA run assimilates from the first level of the model ($20\,\mathrm{m}$ above the ground) to the sixth level ($1950\,\mathrm{m}$ above the ground) and the column DA run assimilates from the third level ($210\,\mathrm{m}$ above the ground) to the sixth level ($1950\,\mathrm{m}$ above the ground). It takes several hours for the column DA to influence ground concentrations.

However, during the forecast period, the RMSE of the column DA run decreases faster than the AirBase DA run (to the right of the black line). After 24 hours forecast, the column DA has better scores than the AirBase DA run. It is mostly because the impact of the column DA run is higher than the AirBase DA run at high levels.

Figure 2.12 shows the RMSE for the PM_{10} forecast without DA, with the AirBase DA and with the column DA for each one-day forecast period between 15 July and 10 August. Assimilation improves the forecast RMSE for each forecast. The averaged RMSE over all forecasts is $9.1\,\mu\mathrm{g\,m^{-3}}$ without DA, $3.7\,\mu\mathrm{g\,m^{-3}}$ ($59\,\%$ less) with the AirBase DA and $4.2\,\mu\mathrm{g\,m^{-3}}$ ($54\,\%$ less) with the column DA. Although the AirBase DA leads to lower RMSE than the column DA for most forecasts in Fig. 2.12, the column DA can also lead to lower or similar RMSE as the AirBase DA for some forecasts, e.g. the forecasts starting 19, 20, 21, 23, 26 July and 3, 5, 8 August. It is mostly because the lidar network provides more accurate information than AirBase on those days at high altitude, e.g. Sahara dust in Madrid as shown in Fig. 2.6 (upper panel).

Figure 2.13 shows the RMSE for the PM_{10} forecast without DA, with the AirBase DA and with the column DA during the second forecast day for each experiment between 15 July and 10 August. The averaged RMSE over all forecasts is $6.1\,\mu\mathrm{g\,m^{-3}}$ without DA, $2.7\,\mu\mathrm{g\,m^{-3}}$ ($56\,\%$ less) with the AirBase DA and $2.6\,\mu\mathrm{g\,m^{-3}}$ ($57\,\%$ less) with the column DA. For the second forecast day (Fig. 2.13), the relative impact of column DA and AirBase DA is different from the first forecast day (Fig. 2.13) : the column DA leads to lower or similar RMSE as the AirBase DA for most forecasts.

The results show that the impact on PM_{10} forecast of assimilating data from a lidar network with 12 stations and data from a ground network AirBase with 488 stations are similar in terms of scores, although AirBase (resp. lidar) DA leads to slightly better scores for the first (resp. second) forecast day. We will study the sensitivity to the number and to the lidar locations in

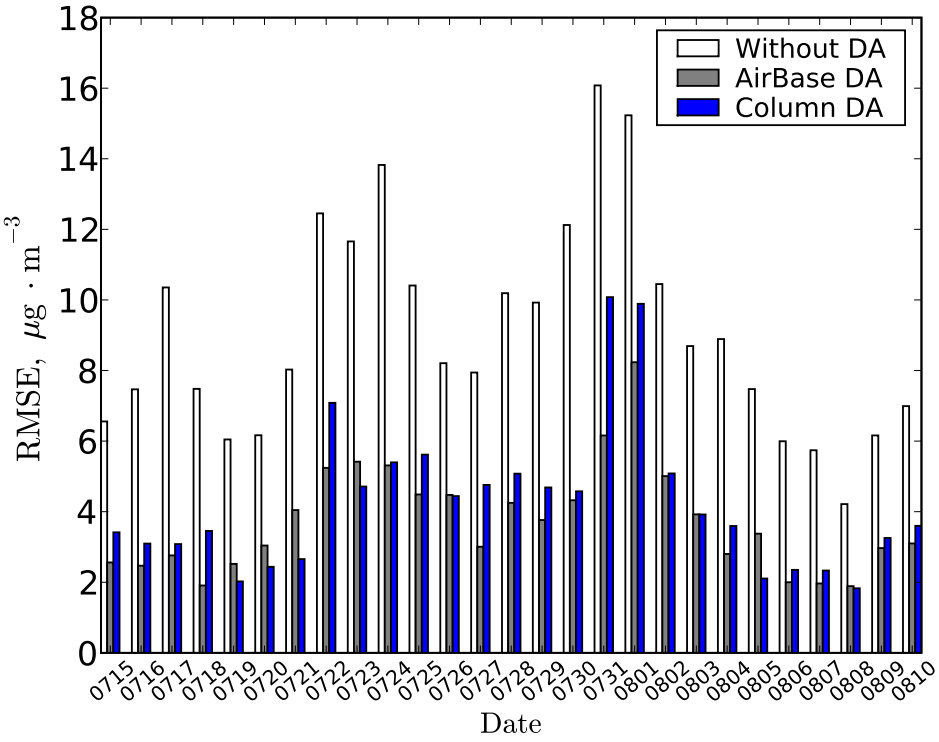

Figure 2.12: RMSE (in $\mu g\,m^{-3}$) computed over land grid points from the ground to the sixth level (1950 m above the ground) for PM_{10} one-day forecast without DA (white columns), with the AirBase DA (grey columns) and with the column DA (blue columns).

the next section.

2.7 Sensitivity to the number and position of lidars

In this section, we study the sensitivity of the results to the number and to the locations of lidars. Forecasts after DA with four different lidar networks are compared to DA with the previously-used lidar network (blue discs in Fig. 2.14). Data assimilation is performed with another lidar network of 12 lidar stations (denoted Network 12, yellow discs in Fig. 2.14), with a lidar network of 26 stations (denoted Network 26, magenta diamonds in Fig. 2.14), with a lidar network of 76 stations (denoted Network 76, cyan thin diamonds in Fig. 2.14) and DA with a lidar network made of all AirBase stations over western Europe (denoted Network 488, the red triangles in Fig. 2.4).

Figures 2.15 and 2.16 show the time evolution of the RMSE and the correlation respectively, averaged over all land grids and the vertical for the different tests. Comparing the previously-used lidar network with Network 12 in Fig. 2.14, we can see that although they have the same number of stations, the locations are very different. Because the stations of Network 12 are more regularly spaced than the stations of the previously-used lidar network, Network 12 stations are better spread out over Europe than the previously-used lidar network. Network 12 leads to better scores in the first forecast day than the reference network. This shows that the

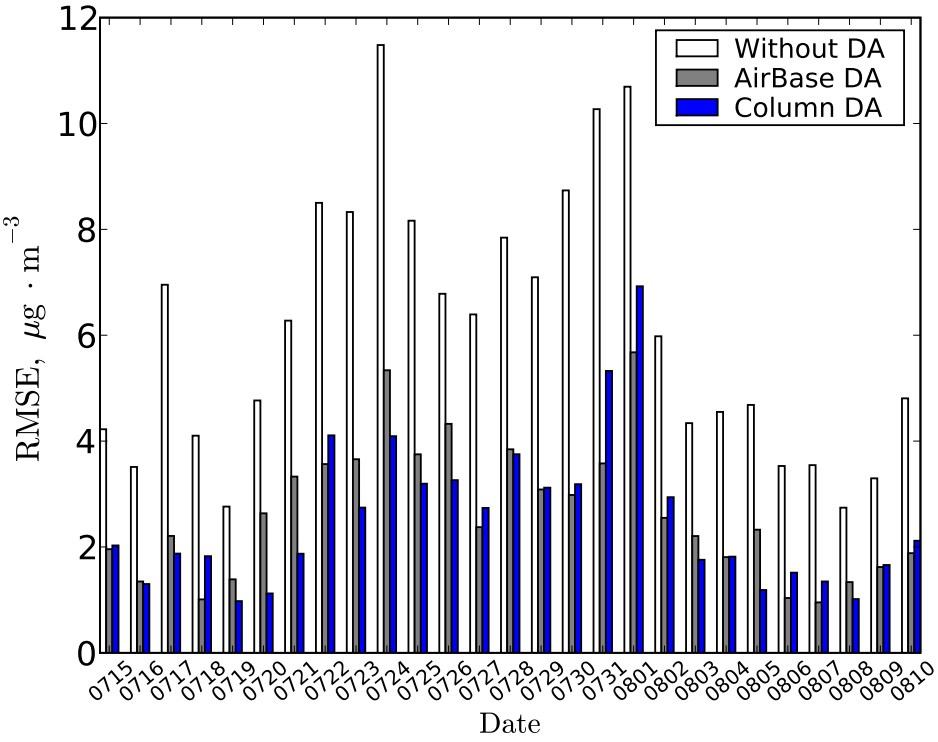

Figure 2.13: RMSE (in $\mu g\,m^{-3}$) computed over land grid points from the ground to the sixth level (1950 m above the ground) for PM_{10} second forecast day without DA (white columns), with the AirBase DA (grey columns) and with the column DA (blue columns).

lidar stations need to be regularly distributed over Europe for an overall improvement of the PM_{10} forecast. The lidar networks 26, 76 and 488 which have more lidar stations perform better (lower RMSE, higher correlation) than the two others. The lidar network 26 DA run has less than $0.15\,\mu g\,m^{-3}$ of RMSE higher than AirBase DA at the beginning of forecast window and has a better score than AirBase DA run after several hours forecast. If one increases the number of lidar stations from 26 to 76, the lidar network 76 DA run has better scores than the AirBase DA run at the beginning of the forecast window and has better scores than the AirBase DA during the forecast days. If one increases the number of lidar stations to 488 (the same as the number of AirBase stations), the lidar network 488 DA run has much better scores than the AirBase DA run during the forecast days. Although increasing the number of lidar gives better forecast scores, such lidar networks may be too expensive.

2.8 Conclusions

In order to investigate the potential impact of a ground-based lidar network on short-term forecasts of PM_{10}, an OSSE has been implemented. Because the AirBase network covers well western Europe and provides in situ surface measurements and because AirBase measurements have been used for DA of PM_{10}, we took AirBase as an assimilation reference network. We have compared the impacts of assimilating ground-based lidar network data to assimilating the

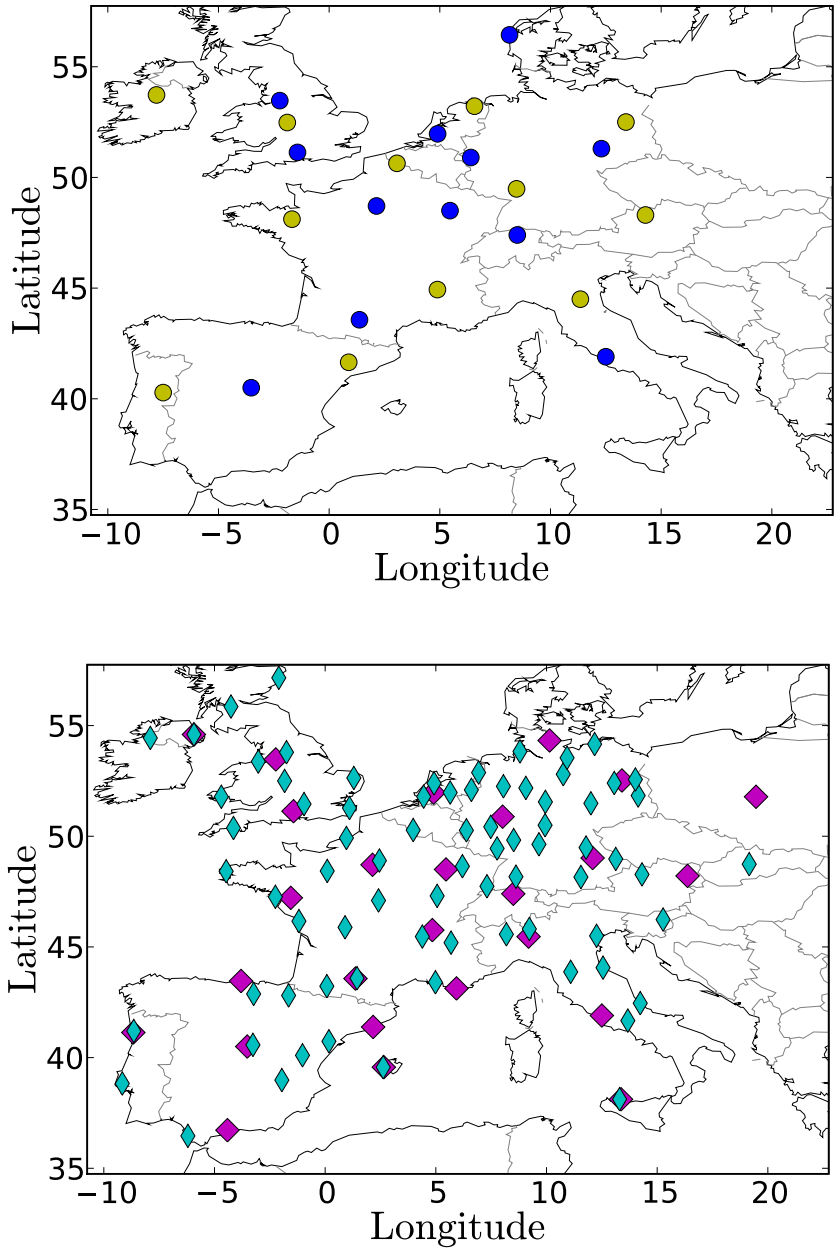

Figure 2.14: Four potential lidar networks in Europe. The blue discs in the top figure show the locations of the reference lidar network. The yellow discs in the top figure show the locations of the lidar Network 12. The magenta diamonds in the bottom figure show the locations of the lidar Network 26. The cyan thin diamonds in the bottom figure show the locations of the lidar Network 76.

AirBase surface network data.

Because we made several simplifying assumptions: we used an identical twin scenario (perfect model) and assumed uncorrelated observational errors, the PM_{10} improvements from assimilating lidar and ground observations may be over optimistic. Compared to the RMSE

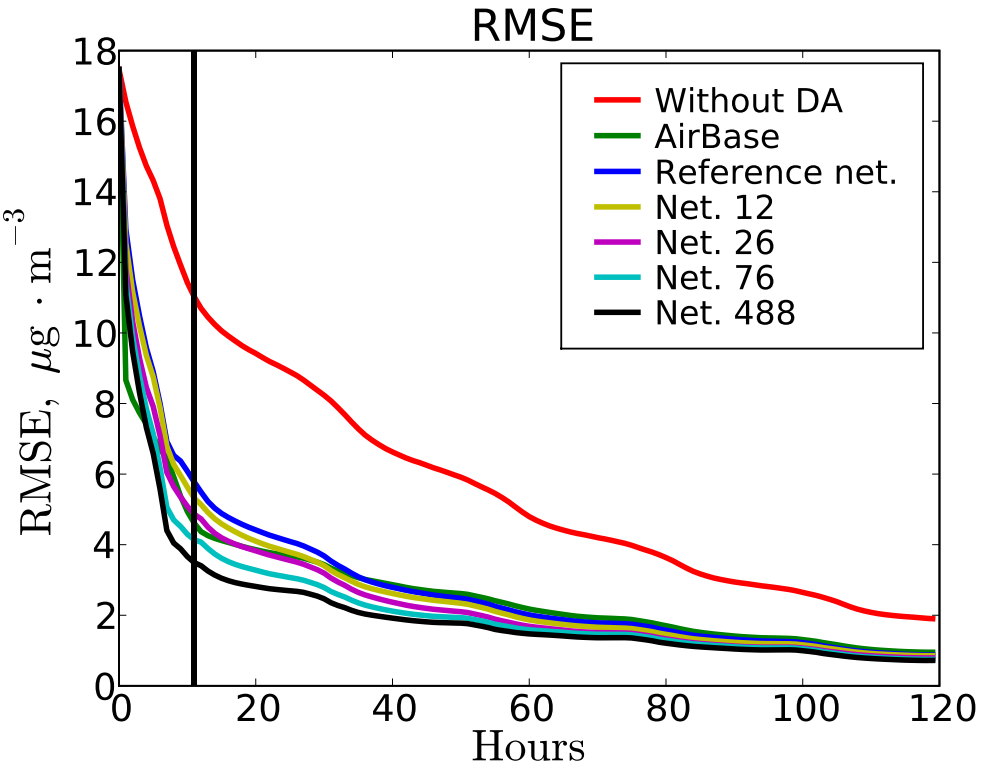

Figure 2.15: Hourly evolution of the RMSE (in $\mu g\,m^{-3}$) of PM_{10} averaged over the different experiments from 15 July to 10 August 2001. The RMSE is computed over land grid points from the ground to the sixth level (1950 m above the ground). The runs are performed without DA (red line), with AirBase DA (green line), with the reference lidar network DA (12 stations, blue line), with Network 12 DA (12 stations, yellow line), with Network 26 DA (26 stations, magenta line), with Network 76 DA (76 stations, cyan line) and with Network 488 DA (488 stations, black line). Net. stands for network.

for one-day forecasts without DA, the RMSE between one-day forecasts and the truth states is improved on average over the summer month from 15 July to 15 August 2001 by 54 % by the lidar DA with 12 lidars, and by 59 % by the AirBase DA. For the second forecast days, compared to the RMSE for second forecast days without DA, the RMSE is improved on average over the summer month from 15 July to 15 August 2001 by 57 % by the lidar DA, and by 56 % by the AirBase DA. Although AirBase DA can correct PM_{10} concentrations at high levels because of the long vertical correlation length of the background errors, the lidar DA corrects PM_{10} concentrations more accurately than the AirBase DA at high levels. The spatial and temporal influence of the assimilation of lidar observations is larger and longer. The results shown in this paper suggest that the assimilation of lidar observations would improve PM_{10} forecast over Europe.

As lidar stations are developing over Europe following volcanic eruptions in Iceland [Chazette et al., 2012; Pappalardo et al., 2010], a sensitivity analysis has also been conducted on the number and locations of lidars. We found that spreading out the lidars regularly over Europe can improve the PM_{10} forecast. Compared to the RMSE for one-day forecasts without DA, the RMSE between one-day forecast and the truth states is improved on average over the summer

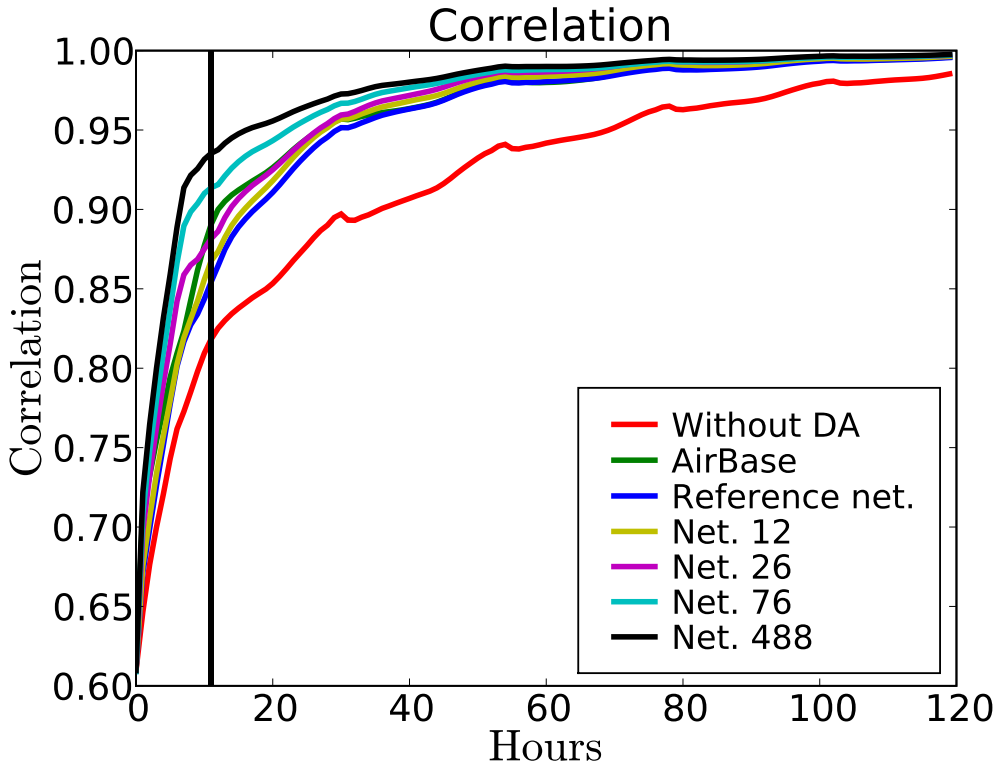

Figure 2.16: Hourly evolution of the PM_{10} correlation averaged over the different experiments from 15 July to 10 August 2001. The correlation is computed over land grid points from the ground to the sixth level (1950 m above the ground). The runs are performed without DA (red line), with AirBase DA (green line), with the reference lidar network DA (12 stations, blue line), with Network 12 DA (12 stations, yellow line), with Network 26 DA (26 stations, magenta line), with Network 76 DA (76 stations, cyan line) and with Network 488 DA (488 stations, black line).

month from 15 July to 15 August 2001 by 57 % by the lidar DA with 12 optimised lidars, and by 59 % by the AirBase DA. Increasing the number of lidar improves the forecast scores. For example, the improvement of the RMSE becomes as high as 65 % (compared to the RMSE for one-day forecasts without DA) if 76 lidars are used, but a lidar network with many stations may be too expensive.

For future works, we will use real measurements from lidar stations, directly assimilating the lidar signals in the chemistry transport model and performing DA with a combination of lidar and AirBase observations.

Chapter 3

Modelling and assimilation of lidar signals over Greater Paris

Preamble

Vertical profiles of PM_{10} mass concentrations were assimilated in Chapter 2, under the hypothesis that we can derive PM_{10} mass concentrations from optical properties of aerosols for all lidar measurement sites. However, it is very tedious to generalise the relation between PM_{10} mass concentration and optical properties of aerosols determined by Raut and Chazette [2009] for aerosol pollution over Greater Paris to all other lidar sites. Therefore, we thought that it would be more accurate to either assimilate lidar signals or lidar backscatter/extinction coefficients [Huneeus and Boucher, 2007; Sekiyama et al., 2010]. The lidar signal allows the retrieval of the aerosol backscatter/extinction coefficients. However, critical assumptions have to be made in the inversion of the lidar signal in order to obtain aerosol optical properties [Chazette, 2003]. Because estimating the backscatter/extinction coefficients from lidar signals using a lidar depolarization ratio brings in errors, we decided to assimilate directly the lidar signal (PR_2) in CTMs for aerosol forecasting.

In this chapter, an important preprocessing stage of data assimilation (DA), a validation of the lidar observation operator, is first performed. A model of the lidar signal (PR_2) is developed by simulating the aerosol complex refractive index (ACRI) and the wet particle diameter. It is based on the model developed by Tombette et al. [2008] within POLYPHEMUS. Tombette et al. [2008] computed AOT (aerosol optical thickness) and SSA (Single Scattering Albedo) using the extinction coefficient b_{ext}, as follows:

$$\mathrm{AOT} = \int_0^{z_{\mathrm{top}}} b_{\mathrm{ext}}(z)dz, \tag{3.1}$$

where z_{top} is the altitude at the top of the atmosphere. SSA was computed as the ratio between the aerosol optical thickness due to scattering ($\mathrm{AOT}_{\mathrm{sca}}$) and AOT. $\mathrm{AOT}_{\mathrm{sca}}$ was computed in the same way as AOT, from the scattering coefficient. Also, they used statistics and monthly time series for the AOT/SSA simulation and AERONET (AErosol RObotic NETwork) data to evaluate the ability of the model to reproduce AOT and vertically averaged SSA fields and their variability. Comparisons between simulated AOT and AERONET data showed good agreements.

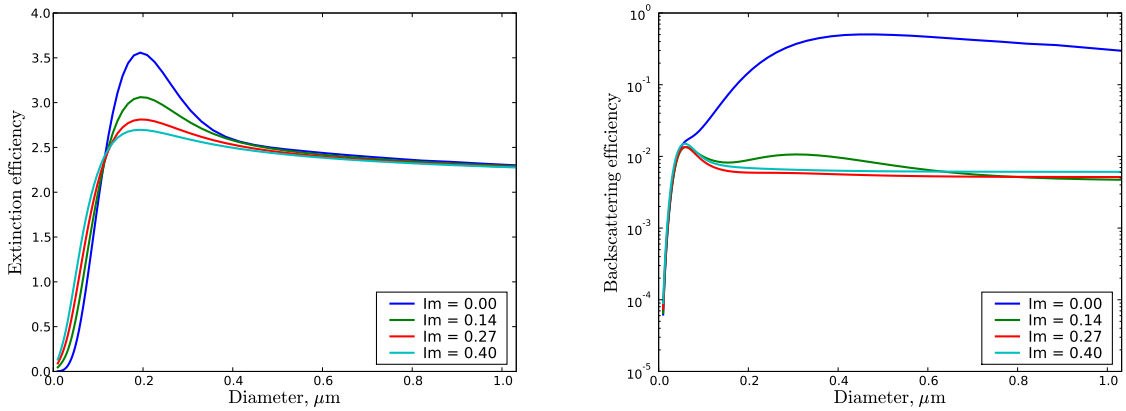

Figure 3.1: Extinction and backscatter efficiencies versus the aerosol size at 355 nm with the real part of CRI Re = 1.5 and the imaginary part of CRI Im = 0.0, 0.14, 0.27 and 0.40.

The lidar signal depends on the aerosol and molecular extinction coefficients, but also on the aerosol and molecular backscatter coefficients (section 3.3). The molecular extinction and backscatter coefficients can be well simulated from the pressure, the temperature and the Boltzmann constant [Nicolet, 1984]. However, Tombette et al. [2008] did not compute aerosol backscatter coefficients. Because the Mie code of Wiscombe [1980] used by Tombette et al. [2008] cannot compute the phase function and backscatter efficiency, we employ the Mie code of Mishchenko et al. [2002] to compute the aerosol extinction and backscatter efficiencies. Mishchenko et al. [2002] defined the backscatter efficiency Q_{bsca} as follows:

$$Q_{\mathrm{bsca}} = Q_{\mathrm{sca}} \frac{a_1(180^\circ)}{4\pi}, \tag{3.2}$$

where Q_{sca} is the scattering efficiency and the a_1 is the phase function. Aerosol extinction and backscatter efficiencies depend on the wet particle size, ACRI (i.e. the real and imaginary parts of ACRI) and the wavelength (fixed at 355 nm in our study). They are tabulated due to high computational costs. Figure 3.1 shows an example of aerosol extinction and backscatter efficiencies computed by the Mie code of Mishchenko et al. [2002] as a function of size at 355 nm. In this thesis, aerosol extinction and scattering coefficients are simulated through the tabulations of extinction and scattering efficiencies.

In this chapter, simulation are performed over the Greater Paris area for the summer month July 2009. The goal is to investigate the ability of the chemistry transport model POLAIR3D of the air quality modelling platform POLYPHEMUS for simulating lidar backscattered profiles from model aerosol concentration outputs. Simulated lidar signals are compared to hourly ground-based mobile and *in situ* lidar observations performed during the MEGAPOLI (Megacities: Emissions, urban, regional and Global Atmospheric POLlution and climate effects, and Integrated tools for assessment and mitigation) summer experiment on July 2009. In the frame of the MEGAPOLI, an intensive campaign was organized over Greater Paris on July 2009. Figure 3.2 shows the spatio-temporal variability of the aerosol backscattered signals measured from the mobile lidar on 04, 16 and 21 July.

The results show that if the aerosol layer is well simulated, the optical property module of

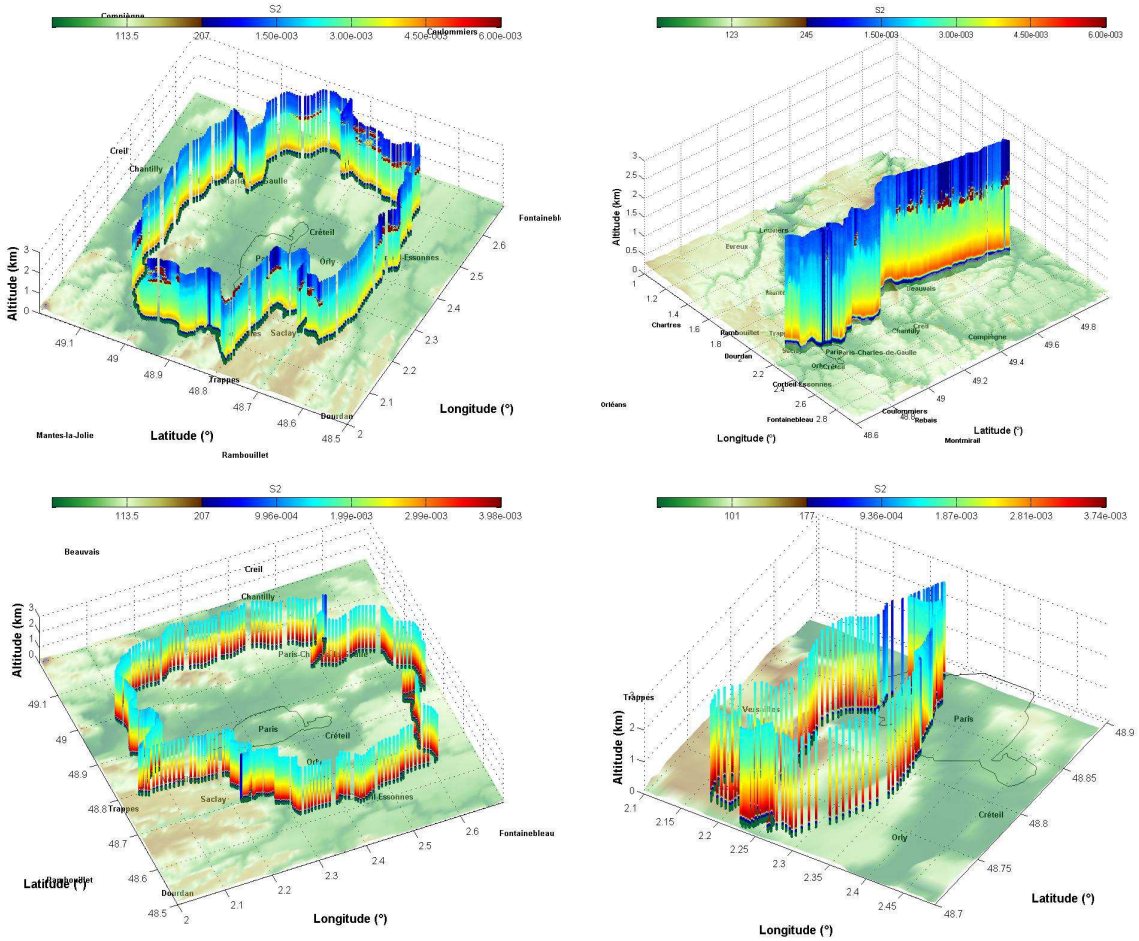

Figure 3.2: Three-dimensional view on the spatio-temporal variability of the aerosol backscattered signal intensity measured from the mobile lidar on 04 (upper left), 16 (upper right) and 26 (lower left and right) July 2009 during MEGAPOLI.

POLYPHEMUS would correctly reproduce lidar signals in the model. That evaluation can be regarded as a validation of the lidar observation operator (i.e. the operator H) in DA. In addition, two new algorithms for assimilating lidar signals are presented and tested. That depends on whether PM_{10} is analysed or $PM_{2.5}$ and $PM_{2.5-10}$ are separately but simultaneously analysed. DA tests are performed for 01 and 26 July 2009. The aerosol simulations without and with lidar DA are evaluated using the AIRPARIF (a regional operational network in charge of air quality survey around the Paris area) database. The results of DA demonstrate the feasibility and the usefulness of assimilating lidar profiles for aerosol forecasts.

This chapter consists of
Wang, Y., Sartelet, K. N., Bocquet, M. and Chazette, P. : **Modelling and assimilation of lidar signals over Greater Paris during the MEGAPOLI summer campaign**, Atmos. Chem. Phys., in press, 2014.

Sommaire

3.1 Introduction

Aerosols are key air quality species to monitor and model as they impact vegetation and as they impact human health by penetrating the respiratory system and leading to respiratory and cardiovascular diseases [Kelly et al., 2011; Lauwerys et al., 2007; Dockery and Pope, 1996]. They also impact visibility [Wang et al., 2009], and they represent an uncertain component of climate changes due to their effects on the Earth's radiative budget [Intergovernment Panel on Climate Control (IPCC), 2007]. For air quality, in order to simulate and predict particle concentrations, modellers have developed various chemistry transport models (CTM), e.g. EMEP (European Monitoring and Evaluation Programme) [Simpson et al., 2003], LOTOS (Long Term Ozone Simulation) - EUROS (European Operational Smog) [Schaap et al., 2004], CHIMERE [Hodzic et al., 2006], DEHM (Danish Eulerean Hemispheric Model) [Brandt et al., 2012] and POLYPHEMUS [Sartelet et al., 2007]. However, the aerosol vertical distribution is poorly quantified, because of numerous uncertainties on their sources (direct emissions) and on processes affecting their formation, e.g. nucleation, condensation, evaporation, and coagulation, as well as on meteorological conditions. Since aerosol lifetime ranges from 1 to 10 days [Seinfeld and Pandis, 1998], improvements in the representation of their vertical distribution may lead to improved surface concentrations (lower error and higher correlation against observations) [Wang et al., 2013a].

Various measurement types have been used to evaluate these models. The most frequently used data are *in situ* surface measurements, e.g. AirBase (`http://www.eea.europa.eu/`) and EMEP over Europe, BDQA (Base de Données de la Qualité de l'Air) [Sartelet et al., 2007; Konovalov et al., 2009]. However, they do not provide direct information on vertical profiles.

Satellite passive remote sensors (e.g. the Moderate Resolution Imaging Spectroradiometers (MODIS)) and sun-photometer surface stations (e.g. the AErosol RObotic NETwork (AERONET)) have greatly enhanced our ability to evaluate such models. Comparisons between observed and simulated Aerosol Optical Depth (AOD) have been performed for global models and regional models [Kinne et al., 2006; Tombette et al., 2008; Péré et al., 2010]. However, instruments, such as sun photometers can only retrieve column-integrated aerosol properties and can only work during daytime.

Since accurate vertical profiles of aerosols can be measured by aerosol lidars, lidar measurements were used in several campaigns, for example to evaluate the transport of particles [Chazette et al., 2012]. Moreover, aerosol lidar networks, such as the European Aerosol Research Lidar Network (EARLINET), are being developed at *in situ* sites. In space, measurements are performed with the Cloud-Aerosol Lidar with Orthogonal Polarisation (CALIOP) lidar [Winker et al., 2007]. Lidar measurements have been used for the validation of aerosol models. For example, Hodzic et al. [2004] compared vertical profiles simulated by CHIMERE with those observed by lidars, from EARLINET, and Stromatas et al. [2012] used observations from the CALIOP space-based lidar. Royer et al. [2011] used an optical-to-mass relationships (urban, pre-urban and rural) to retrieve the PM_{10} (particulate matter with diameter less than 10 μm) concentrations from lidar signals [Raut et al., 2009a, b]. In Royer et al. [2011], lidar-derived PM_{10} concentrations were compared with simulations from POLYPHEMUS and CHIMERE during the MEGAPOLI (Megacities: Emissions, urban, regional and Global Atmospheric POLlution and climate effects, and Integrated tools for assessment and mitigation) summer experiment in July 2009.

Data assimilation (DA hereafter) can reduce the uncertainties in input data such as initial

or boundary conditions by coupling models to observations [Bouttier and Courtier, 2002]. In air quality, applications of DA to PM_{10} forecast using *in situ* surface measurements have been performed by Denby et al. [2008] and Tombette et al. [2009] over Europe, and Pagowski et al. [2010]; Pagowski and Grell [2012]; Li et al. [2013] over the United States of America. Over Europe, the efficiency of assimilating lidar measurements to improve PM_{10} forecast has been compared to the efficiency of assimilating *in situ* surface measurements by Wang et al. [2013a]. Using an Observing System Simulation Experiment (OSSE), they suggested that the assimilation of lidar observations may be more efficient to improve PM_{10} forecast, although it depends on the number of lidar stations used. However, Wang et al. [2013a] did not directly assimilate the lidar signal, but they used a relation between mass concentration and optical properties of pollution aerosol. Although this kind of relation has been determined for pollution aerosols over Greater Paris [Raut et al., 2009a], it needs to be generalised to other measurement sites before operationally assimilating the mass concentration converted from the lidar signal. Moreover, the uncertainly linked to the estimation of mass concentrations may be about 25% [Raut et al., 2009a] which is mostly due to uncertainties in estimating the specific cross sections. Because uncertainties in the lidar signal may be less than 5%, it is more accurate to directly assimilate lidar signals.

This paper aims at evaluating the lidar signals simulated by POLYPHEMUS and at testing new DA algorithms for assimilating lidar signals. We used measurements performed during the MEGAPOLI summer experiment, when a ground-based mobile lidar (GBLM) was deployed around Paris on-board a van. Measurements from a ground-based *in situ* lidar at Saclay were also performed on 01 July 2009. The evaluation of lidar signals can also be regarded as a preprocessing stage of DA (validation of the observation operator).

This paper is organised as follows. Section 3.2 describes the experiment setup, i.e. the chemistry transport model used (POLYPHEMUS) and the observations. In section 3.3, the lidar observation operator is presented. Section 3.4 describes the evaluation of the simulation with *in situ* surface measurements and AERONET data. Results of the comparisons between observed and simulated lidar signals are shown in section 3.5. A new algorithm for the assimilation of lidar observations and results are shown in section 3.6. The findings are summarised and discussed in section 3.7.

3.2 Experiment setup

3.2.1 POLAIR3D model

In this study, the POLAIR3D air quality model [Sartelet et al., 2007] of the air quality platform POLYPHEMUS, available at `http://cerea.enpc.fr/polyphemus/` and described in Mallet et al. [2007], is used to simulate air quality over the Greater Paris area. Aerosols are modelled using the SIze-REsolved Aerosol Model (SIREAM-SuperSorgam), which is described in Debry et al. [2007] and Kim et al. [2011a]. SIREAM-SuperSorgam includes 20 aerosol species: 3 primary species (mineral dust, black carbon and primary organic species), 5 inorganic species (ammonium, sulfate, nitrate, chloride and sodium) and 12 organic species. Five bins logarithmically distributed over the size range 0.01 μm - 10 μm are used. The chemical mechanism CB05 (Carbon Bond version 5) is used for the gas chemistry [Yarwood et al., 2005]. POLAIR3D/SIREAM has been used for several applications. For example, it was compared to *in situ* surface measurements for gas and aerosols over Europe by Sartelet et al. [2007,

2012]; Couvidat et al. [2012], over Greater Paris by Couvidat et al. [2013], it was compared to AERONET data over Europe by Tombette et al. [2008] and to satellite data by Zhang et al. [2013], and it was compared to lidar-derived PM_{10} over Greater Paris during MEGAPOLI by Royer et al. [2011].

3.2.2 Modelling setup and observational data

The modelling domain is the same as the one used in Royer et al. [2011] and Couvidat et al. [2013]. It covers the Greater Paris area ([$1.2°$ E, $3.5°$ E] $\times$ [$47.9°$ N, $50.1°$ N]) with a horizontal resolution of $0.02° \times 0.02°$. Because Royer et al. [2011] show that limited vertical model resolution leads to much smoother vertical profiles than those deduced from lidar signals, a finer vertical resolution is used with 23 vertical levels from the ground to 12000 m, instead of nine vertical levels in Royer et al. [2011]. The simulations are carried out for one month from 28 June to 30 July 2009. Meteorological inputs are the same as in Couvidat et al. [2013]. They are simulated with the Weather Research & Forecasting (WRF) model [Skamarock et al., 2008] using an urban canopy model and an undated Corine land-use data base [Kim et al., 2013] with the YSU parameterisation [Hong et al., 2006] for the Planetary Boundary Layer (PBL) dynamics [Kim et al., 2013]. Anthropogenic emissions of gases and aerosols are generated with the Airparif (the Paris air quality agency) inventory for the year 2005. Boundary conditions for gaseous and particulate species were obtained from nested simulations over Europe and France, presented by Couvidat et al. [2013].

The ground based mobile lidar (GBML) used during the MEGAPOLI campaign is based on an ALS450 lidar commercialised by the LEOSPHERE company and initially developed by the Commissariat à l'Energie Atomique (CEA) and the Centre National de la Recherche Scientifique (CNRS) [Chazette et al., 2007]. It provides lidar measurements at 355 nm. The main characteristics of this lidar are detailed in Royer et al. [2011]. This system is particularly well-adapted to air pollution and tropospheric aerosol studies thanks to its full overlap reached at about 150-200 m height and its increased vertical resolution of 1.5 m. Measurement days of 01, 04, 16, 21, 26 and 29 July 2009, which correspond to different levels of pollution from Airparif (low, moderate or high), are used for comparisons to the lidar signal. Moreover, ground-based *in situ* lidar measurements were performed at Saclay ($48.7°$ N, $2.14°$ E, 30 m a.s.l.) on 01 July 2009 from 06:49 to 16:44 UTC (the blue square in Fig. 3.3). These measurements are used for both the comparison and the assimilation of lidar observations.

Airparif is the regional operational network in charge of air quality survey around the Paris area (`http://www.airparif.asso.fr/`). It provides hourly gases and/or aerosol concentrations (PM_{10} and $PM_{2.5}$) measurements. Figure 3.3 shows the location of the Airparif stations with red squares and/or the black triangles. There are 17 stations at which PM_{10} and/or $PM_{2.5}$ concentration measurements are performed.

The AERONET (AErosol RObotic NETwork) program is a federation of ground-based remote sensing aerosol networks established by NASA and PHOTONS (Univ. of Lille 1, CNES, and CNRS-INSU), which provides a long-term, continuous and readily accessible public domain database of aerosol optical measurements performed by sun-photometers [Holben et al., 1998]. Sun-photometers measure AOD at different wavelengths ranging from 340 to 1024 nm. AOD data are computed for three data quality levels: Level 1.0 (unscreened), Level 1.5 (cloud-screened), and Level 2.0 (cloud-screened and quality-assured). The uncertainty of AOD measurements is less than 0.02 [Holben et al., 2001]. For this study, there are 2 available sta-

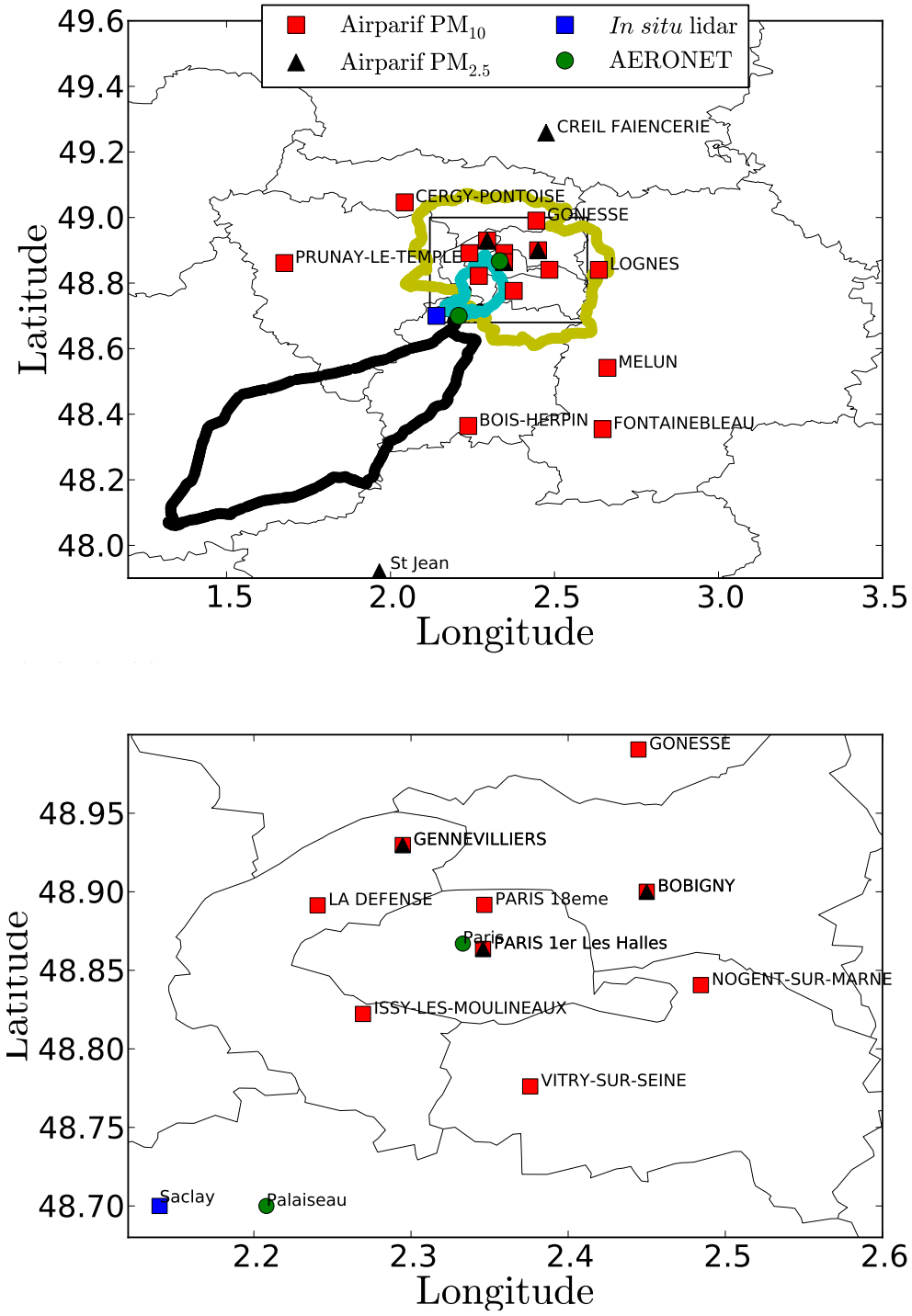

Figure 3.3: The blue square shows the location of the ground-based *in situ* lidar station, the red squares (resp. the black triangles) show the locations of Airparif stations for PM_{10} (resp. $PM_{2.5}$) measurements and the green discs show the locations of AERONET stations. The black pattern shows the GBML track on 01 July 2009. The yellow and cyan patterns show two GBML tracks on 26 July 2009. The rectangle area is detailed in the bottom figure.

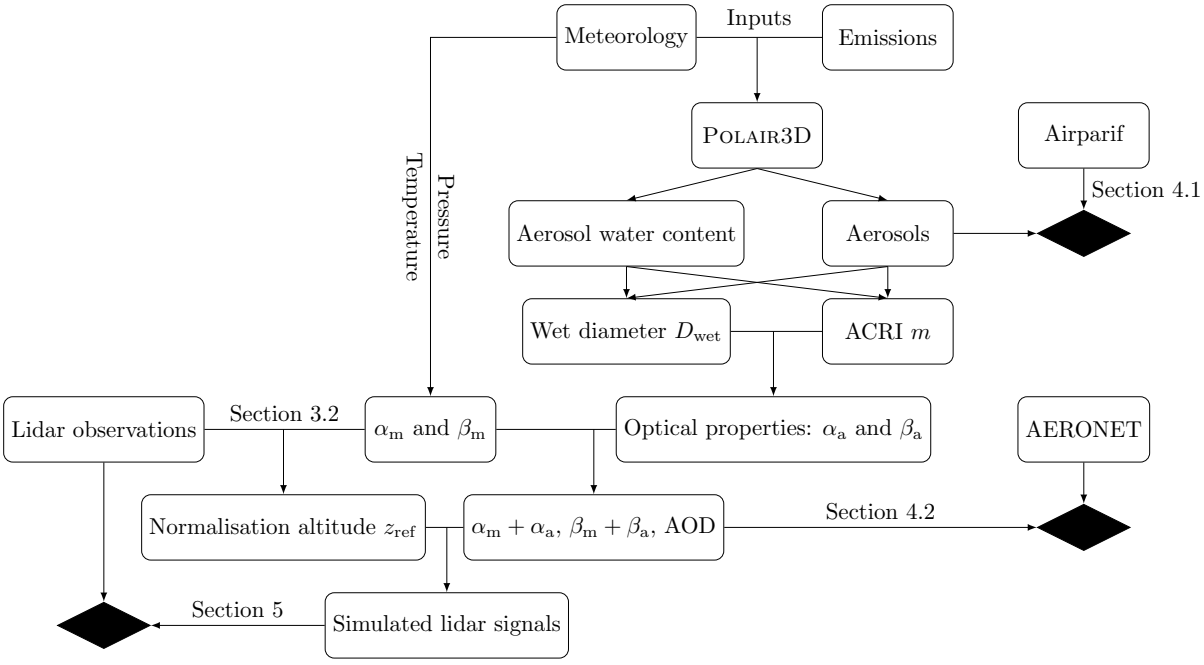

Figure 3.4: Diagram describing the methodology for lidar signals modelling from outputs of the air-quality model POLAIR3D. Comparisons to measurements are performed at black nodes. ACRI stands for aerosol complex refractive index. β_{m} (resp. β_{a}) is the molecular (resp. aerosol) backscatter coefficient. α_{m} (resp. α_{a}) is the molecular (resp. aerosol) extinction coefficient.

tions over Greater Paris: Paris (urban station, $48.87°$ N, $2.33°$ E, 50 m a.s.l.) and Palaiseau (suburban station, $48.70°$ N, $2.21°$ E, 156 m a.s.l.) (the green discs in Fig. 3.3). In this paper, Level 2.0 AOD data at 340 and 380 nm are used to derive AOD data at 355 nm following the Angström law:

$$\text{AOD}(355) = \text{AOD}(340) \left(\frac{355}{340}\right)^{-\alpha}, \tag{3.3}$$

where α is the Angström exponent defined by

$$\alpha = \ln\left(\frac{\text{AOD}(340)}{\text{AOD}(380)}\right) / \ln\left(\frac{380}{340}\right). \tag{3.4}$$

3.3 Methodology

Figure 3.4 describes the methodology used for lidar signal modelling from the outputs of the air-quality model and for comparisons to measurements (aerosol concentration measurements, AOD data and lidar vertical profiles). This section presents the methodology used in POLYPHEMUS to derive the lidar observation operator.

3.3.1 Modelling of lidar signals

The range-corrected lidar signal PR_2 measured at an altitude z is defined by Collis and Russell [1976]

$$\mathrm{PR}_2(z) = C(\beta_m(z) + \beta_a(z)) \exp\left(-2\int_0^z (\alpha_m(z') + \alpha_a(z'))dz'\right), \tag{3.5}$$

where β_m (resp. β_a) is the molecular (resp. aerosol) backscatter coefficient, α_m (resp. α_a) is the molecular (resp. aerosol) extinction coefficient, and C is the instrumental constant for each channel depending on the technical characteristics of the emitting and receiving optics. In order to eliminate the instrumental constant C (because it is unknown), PR_2 is normalised as follows

$$H(z) = \frac{\mathrm{PR}_2(z)}{\mathrm{PR}_2(z_{\mathrm{ref}})} = \frac{\beta_m(z) + \beta_a(z)}{\beta_m(z_{\mathrm{ref}}) + \beta_a(z_{\mathrm{ref}})} \exp\left(2\int_z^{z_{\mathrm{ref}}} (\alpha_m(z') + \alpha_a(z'))dz'\right), \tag{3.6}$$

where z_{ref} is taken at an altitude in the molecular zone. In equation (3.6), to estimate the normalised lidar signal H, four optical parameters β_m, β_a, α_m and α_a are needed.

The molecular backscatter coefficient (β_m) at the wavelength λ of the incident light is calculated by Nicolet [1984]

$$\beta_m = \frac{P}{k_{\mathrm{B}}T} \cdot s_{\mathrm{Ray}}, \tag{3.7}$$

where P is the pressure, T is the temperature, k_{B} is the Boltzmann constant, and the Rayleigh scattering cross section s_{Ray} is given by

$$s_{\mathrm{Ray}} = 4.678 \cdot 10^{-29} \cdot \lambda^{-(3.916+0.074\cdot\lambda+0.05/\lambda)}. \tag{3.8}$$

The molecular extinction coefficient (α_m) is given by Nicolet [1984]

$$\alpha_m = \frac{8\pi}{3}\beta_m. \tag{3.9}$$

Aerosol extinction and backscatter coefficients (β_a and α_a) are functions of the particle sizes, of the aerosol complex refractive index (ACRI) of particles m, and of the wavelength λ of the incident light. With a population of different-sized particles of identical refractive index m and with a number size distribution function $n(D_{\mathrm{wet}})$ with D_{wet} the particle wet diameter, the aerosol extinction and backscatter coefficients are given by the following formulas:

$$\alpha_a = \int_0^{D_{\mathrm{wet}}^{\max}} \frac{\pi D_{\mathrm{wet}}^2}{4} Q_{\mathrm{ext}}(m, a_{\mathrm{wet}}) n(D_{\mathrm{wet}}) dD_{\mathrm{wet}}, \tag{3.10}$$

and

$$\beta_a = \int_0^{D_{\mathrm{wet}}^{\max}} \frac{\pi D_{\mathrm{wet}}^2}{4} Q_{\mathrm{bsca}}(m, a_{\mathrm{wet}}) n(D_{\mathrm{wet}}) dD_{\mathrm{wet}}, \tag{3.11}$$

where $D_{\mathrm{wet}}^{\max}$ is a wet diameter upper limit for the particle population, $a_{\mathrm{wet}} = \frac{\pi D_{\mathrm{wet}}}{\lambda}$ a dimensionless size parameter, $Q_{\mathrm{ext}}(m, a_{\mathrm{wet}})$ and $Q_{\mathrm{bsca}}(m, a_{\mathrm{wet}})$ are extinction and backscatter efficiencies. These efficiencies are computed through the Mie code from `ftp://ftp.giss.nasa.gov/pub/crmim/spher.f` [de Rooij and van der Stap, 1984; Mishchenko et al., 2002]. The dry complex refractive index (CRI) is interpolated from the OPAC package [Hess et al., 1998] for each species at the desired wavelength λ (355 nm). The CRI and densities used for calculation of optical properties are shown in Table 3.1. The wet diameter D_{wet} is computed from

Table 3.1: Dry CRI and density for different aerosol species at $\lambda = 355$ nm. Re (resp. Im) stands for the real (resp. imaginary) part of CRI.

Species	Re	Im	density (g cm^{-3})
Nitrate	1.53	-0.005	1.5
Ammonium	1.53	-0.005	0.91
Black carbon	1.75	-0.4645	2.25
Mineral dust	1.53	-0.0166	2.33
Organics	1.53	-0.008	1.3
Sulfate	1.45	-1e-08	1.84
Sodium	1.509	-2.946e-07	0.97
Chlorate	1.509	-2.946e-07	1.15
Water	1.35738	2.72875e-08	1.0

the mean dry diameter of each section of the aerosol sectional model SIREAM and from the aerosol water content. The aerosol water content is calculated from the thermodynamic model ISORROPIA [Nenes et al., 1998a, b] which models the phase state (i.e. gas, liquid, solid) of inorganic aerosol species (i.e. ammonium, sodium, chloride, nitrate, sulfate) in equilibrium with gaseous precursors. The inputs of ISORROPIA are temperature, relative humidity (RH), gaseous precursor concentrations and inorganic aerosol concentrations. Because of the large amount of water vapour in the atmosphere, the ambient RH is assumed to be unaffected by the deliquescence of aerosol particles in ISORROPIA [Nenes et al., 1998a] and equals the water activity (referred to as a_w). The aerosol water content is estimated by the ZSR relationship [Robinson and Stokes, 2002],

$$W = \sum_i \frac{M_i}{m_{oi}(a_w)}, \tag{3.12}$$

where a_w =RH, W is the aerosol water content concentration, M_i is the molar concentration of species i (mol m^{-3}), $m_{oi}(a_w)$ is the molality of an aqueous solution of species i (mol kg^{-1}).

Computing the ACRI requires to make an assumption on the mixing state of the aerosol chemical species. The current version of POLYPHEMUS is based on an assumption of aerosol internal mixing: all the particles of a given size section at a given grid point of the domain are supposed to have the same chemical composition. Within this framework, Tombette et al. [2008] compared aerosol optical properties using 2 different assumptions for the Black Carbon (BC) mixing state: internally homogeneous mixing and core-shell mixing. In the internally homogeneous mixing case, BC is treated as the other components and a volume-weighted ACRI is calculated from the CRI of pure species. In the core-shell mixing case, each particle is assumed to have a structure : the core (BC) and the shell (all the other components). The hypothesis of an internally homogeneous mixing state seems to be unphysical as BC can not be well-mixed in the particle because of its complex geometry and solid state [Katrinak et al., 1993; Sachdeva and Attri, 2007]. Tombette et al. [2008] have shown that the use of these two mixing states leads to negligible differences on AOD, but non-negligible differences on single scattering albedo and absorption process. According to illustrations of Jacobson [2000], the BC

mixing state influences the absorption cross section at small wavelengths (lower than 1 μm) for aerosols with diameter higher than 1 μm. Thus, a core-shell mixing hypothesis is used in this study. The Maxwell-Garnett approximation is used to calculate ACRI from the core CRI (i.e., BC in this study) and the shell CRI (where all the other components are well mixed) [Tombette et al., 2008].

3.3.2 Estimation of z_{ref}

The altitude used to normalise the lidar signal does not need to correspond exactly to the beginning altitude of the molecular zone, but it could be any arbitrary chosen altitude in the molecular zone, where there is almost no aerosol. However, it is better to use an estimation of the normalisation altitude as close as possible to the beginning of the molecular zone, because lidar signals are attached to higher uncertainties at high altitudes because of a higher signal-to-noise ratio. Although the molecular zone is often determined visually from lidar vertical profiles, this method is not efficient to treat large amounts of lidar profiles. We therefore created a new algorithm which can automatically estimate the normalisation altitude z_{ref} from the lidar vertical profile.

The normalisation altitude z_{ref} is estimated from the lidar signal and the simulated molecular signal $\mathrm{PR}_{2,\mathrm{Ray}}$

$$\mathrm{PR}_{2,\mathrm{Ray}}(z) = \beta_m(z) \exp\left(-2\int_0^z \alpha_m(z')dz'\right), \tag{3.13}$$

as follows :

- Define a weight for each vertical point of the lidar signal (the vertical resolution is 1.5 m). The weights should be larger for the points that are more likely to be in the molecular zone, i.e. at high altitudes. We used $w(h) = \exp((h-h_{\max})/L)/L$, where h is the altitude of the points, $h_{\max}$ is the maximal altitude considered (e.g. 4 km) and the parameter L is taken equal to 200 m.

- Fit all lidar signal vertical points (noted as a vector $\mathbf{y}$) with a weighted least absolute deviations (LAD) regression [DasGupta and Mishra, 2007]. It is because we are here interested in the linear regression of lidar signal points at higher altitudes, e.g. the points between 2 and 3 km above the ground. However, it is difficult to know the altitude below which lidar signal points could be cut off for the estimation of z_{ref}. When considering all available lidar signal points, the disturbances are prominently non-normally distributed and contain sizeable outliers (i.e. points at lower altitudes). In such cases, the Least Squares method fails and the LAD method performs well [DasGupta and Mishra, 2007]. In detail, we minimise

  $$\| (\mathbf{y} - (a\mathbf{h} + b))^{\mathrm{T}} \mathbf{w} \|_{\mathrm{l1}} = \sum_i |w_i(y_i - ah_i - b)| \tag{3.14}$$

  to find a and b (cyan lines in Fig. 3.5).

- Calibrate the simulated molecular signal $\mathrm{PR}_{2,\mathrm{Ray}}$ with the LAD regression line at altitude $h_{\max}$, and calculate the difference between the calibrated $\mathrm{PR}_{2,\mathrm{Ray}}$ and the LAD regression line at each vertical point of the lidar signal in a loop starting from high altitudes to low altitudes. The altitude at which the difference becomes larger than a pre-assigned value (1% of the value corresponding to the LAD regression line) corresponds to z_{ref}.

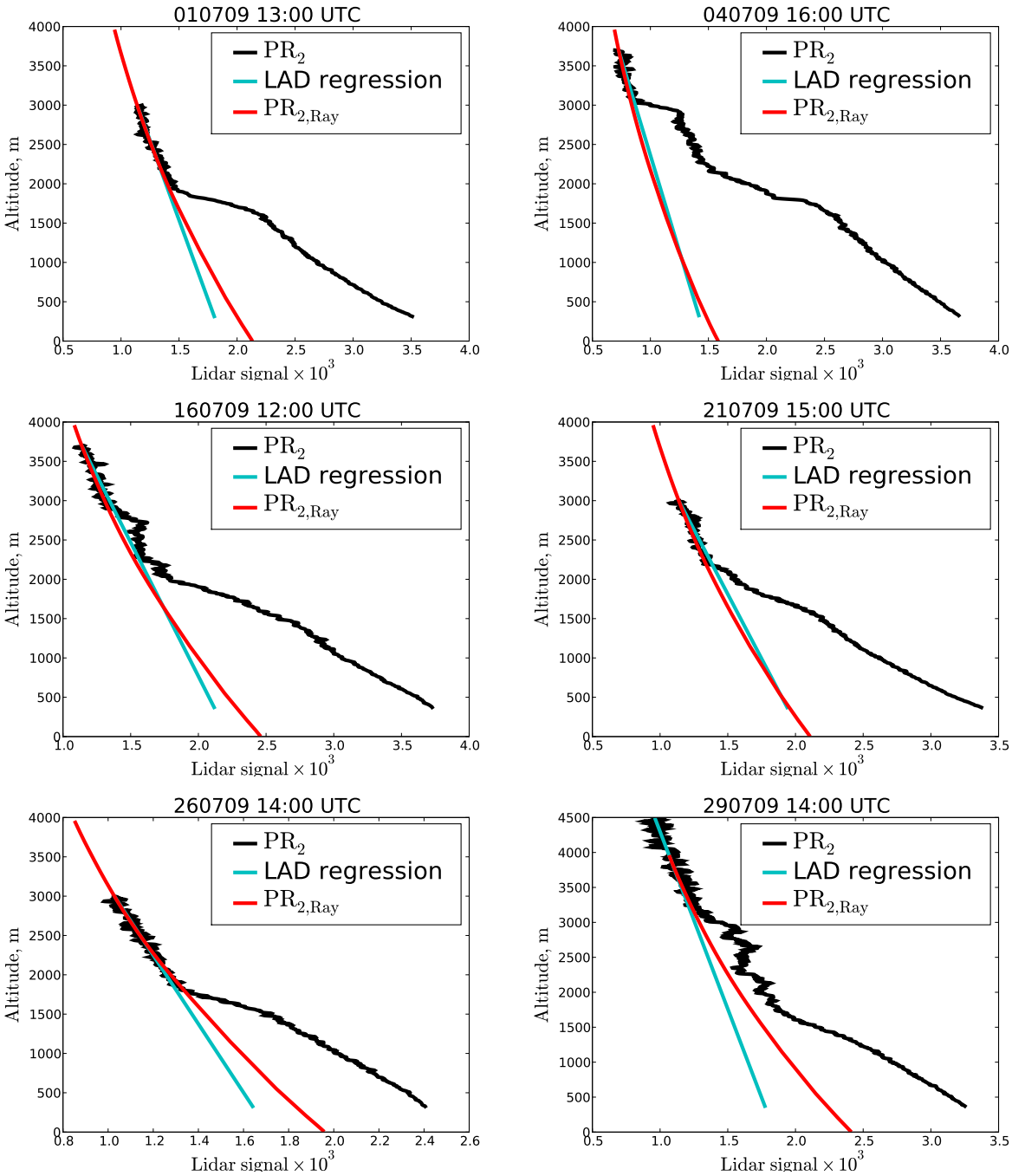

Figure 3.5: Black lines (resp. red lines) indicate lidar signals PR_2 (resp. simulated molecular signals $\mathrm{PR}_{2,\mathrm{Ray}}$) at 13:00 UTC 01, 16:00 UTC 04, 12:00 UTC 16, 15:00 UTC 21, 14:00 UTC 26 and 14:00 UTC 29 July 2009 (blue points). LAD regressions of weighted lidar measurement points are indicated by cyan lines.

Figure 3.5 shows comparisons between the lidar signal and the simulated molecular signal $\mathrm{PR}_{2,\mathrm{Ray}}$ for different lidar measurement days during MEGAPOLI. The simulated molecular signal (red lines in Fig. 3.5) agrees well with the lidar observations (black lines in Fig. 3.5) at

Table 3.2: Statistics (see Appendix A) of the simulation results for the Airparif network during the MEGAPOLI summer experiment. Obs. stands for observation. Sim. stands for simulation. Corr. stands for correlation.

Day	PM_{10}						$PM_{2.5}$					
	Obs. mean	Sim. mean	RMSE	Corr.	MFB	MFE	Obs. mean	Sim. mean	RMSE	Corr.	MFB	MFE
	$\mu g\,m^{-3}$	$\mu g\,m^{-3}$	$\mu g\,m^{-3}$	%	%	%	$\mu g\,m^{-3}$	$\mu g\,m^{-3}$	$\mu g\,m^{-3}$	%	%	%
All	21.53	14.14	10.79	64	-42	49	12.59	12.78	6.02	68	4	39
01/07	44.99	29.39	18.08	78	-45	47	28.82	27.14	7.94	74	-10	23
04/07	18.37	11.11	8.34	8	-48	48	10.80	9.99	3.90	-25	-4	31
16/07	26.25	16.47	12.28	16	-41	46	12.60	15.76	5.41	31	25	34
21/07	27.84	16.84	13.13	28	-46	50	15.46	16.19	5.84	14	6	31
26/07	18.04	10.12	9.52	-4.6	-52	53	12.32	10.27	5.05	7.1	-16	34
29/07	29.25	12.33	18.49	28	-76	78	14.82	11.78	7.32	38	-20	37

high altitudes in the molecular zone, leading to the determination of the molecular zone and z_{ref}.

3.4 Model evaluation

To evaluate air quality models, Boylan and Russell [2006] recommended PM model performance goal and criterion that are based upon an analysis of numerous PM and visibility modelling studies. The PM model performance goal corresponds to the level of accuracy that is considered to be close to the best a model can be expected to achieve. The PM model performance criterion corresponds to the level of accuracy that is considered to be acceptable for modelling applications. The Mean Fractional Bias (MFB) and the Mean Fractional Error (MFE) are proposed by Boylan and Russell [2006] to evaluate model performances against observations: if both the MFB is in the range [-30%, 30%] and the MFE is in the range [0, 50%], the PM model performance goal is met; if both the MFB is in the range [-60%, 60%] and the MFE is in the range [0, 75%], the PM model performance criterion is met. RMSE and correlation are also often used in the aerosol modelling community. The statistical indicators are defined in appendix A.

3.4.1 Model evaluation with Airparif data

Table 3.2 shows statistics for the month of simulation and for the 6 lidar measurement days. For the month of simulation, for $PM_{2.5}$, the MFB and MFE are respectively in the range [-30%, 30%] and [0, 50%], i.e. the PM model performance goal is met. For PM_{10}, the MFB and MFE are respectively in the range [-60%, 60%] and [0, 75%], i.e. the PM model performance criterion is met. For each lidar measurement day, the PM model performance goal is always met for $PM_{2.5}$, and the PM model performance criterion is met for PM_{10} except for 29 July.

Table 3.3: Statistics (see Appendix A) of the simulation results for the AERONET network for different lidar measurement days.

Day	Obs. mean	Sim. mean	RMSE	MFB	MFE
				%	%
01 July	0.59	0.47	0.20	-21	29
04 July	0.25	0.14	0.12	-58	58
16 July	0.26	0.18	0.08	-33	33
26 July	0.15	0.08	0.07	-53	53

As shown in Table 3.2, the model simulates well $PM_{2.5}$ concentrations, but PM_{10} concentrations are underestimated. In other words, coarse particles (particulate matter with a diameter higher than 2.5 μm and lower than 10 μm) are underestimated. This may be because emissions and boundary conditions of coarse particles are underestimated, e.g. road resuspensions of PM is not considered in the model and boundary conditions are obtained from nested simulations over Europe and France where coarse particles were underestimated.

3.4.2 Model evaluation with AERONET data

Table 3.3 presents statistics for hourly data. As the MFB and MFE on 01, 04, 16 and 26 July 2009 are respectively in the range [-60%, 60%] and [0, 75%], the model performance criterion of Boylan and Russell [2006] is met, despite a slight underestimation of AOD in agreement with the underestimation of PM_{10} in comparison to Airparif observations (see section 3.4.1).

3.5 Comparisons with lidar vertical profiles

The simulated lidar signal is compared with GBML observations performed during the MEGAPOLI summer experiment on the different measurement days (01, 04, 16, 21, 26 and 29 July 2009). The purpose of this section is to validate the ability of POLYPHEMUS to simulate lidar backscattered profiles and then choose suitable measurement days to do assimilation tests.

On 01 July 2009, GBML measurements are performed leeward inside the pollution plume in the Southwest of Paris between Saclay and Chateaudun during 3 hours (black track in Fig. 3.3). It is the most polluted day of the MEGAPOLI experiment. High levels of PM_{10}, on average about 45 $\mu g\, m^{-3}$ (see Tab. 3.2), are measured by the Airparif network. Figure 3.6 presents the comparison between lidar observations and the simulation at 11:00 , 12:00 and 13:00 UTC. It shows that POLYPHEMUS underestimates the lidar signal at 13:00 UTC, but it overestimates it at 14:00 UTC and it agrees well with observations at 15:00 UTC. While the PBL height increases from about 1.2 to 1.8 km from 11:00 to 13:00 UTC and the GBML runs out of the pollution plume [Royer et al., 2011], both the observed and simulated lidar signals decrease. Figures of the comparison between the simulation and observations from a ground-based *in situ* lidar at Saclay are shown later in this paper. The pollution plume covers Saclay because of the Northeast wind. Thus high lidar signal values in both the simulation and observations are seen after 10:00 UTC, although the simulated lidar signals are underestimated. Data assimilation

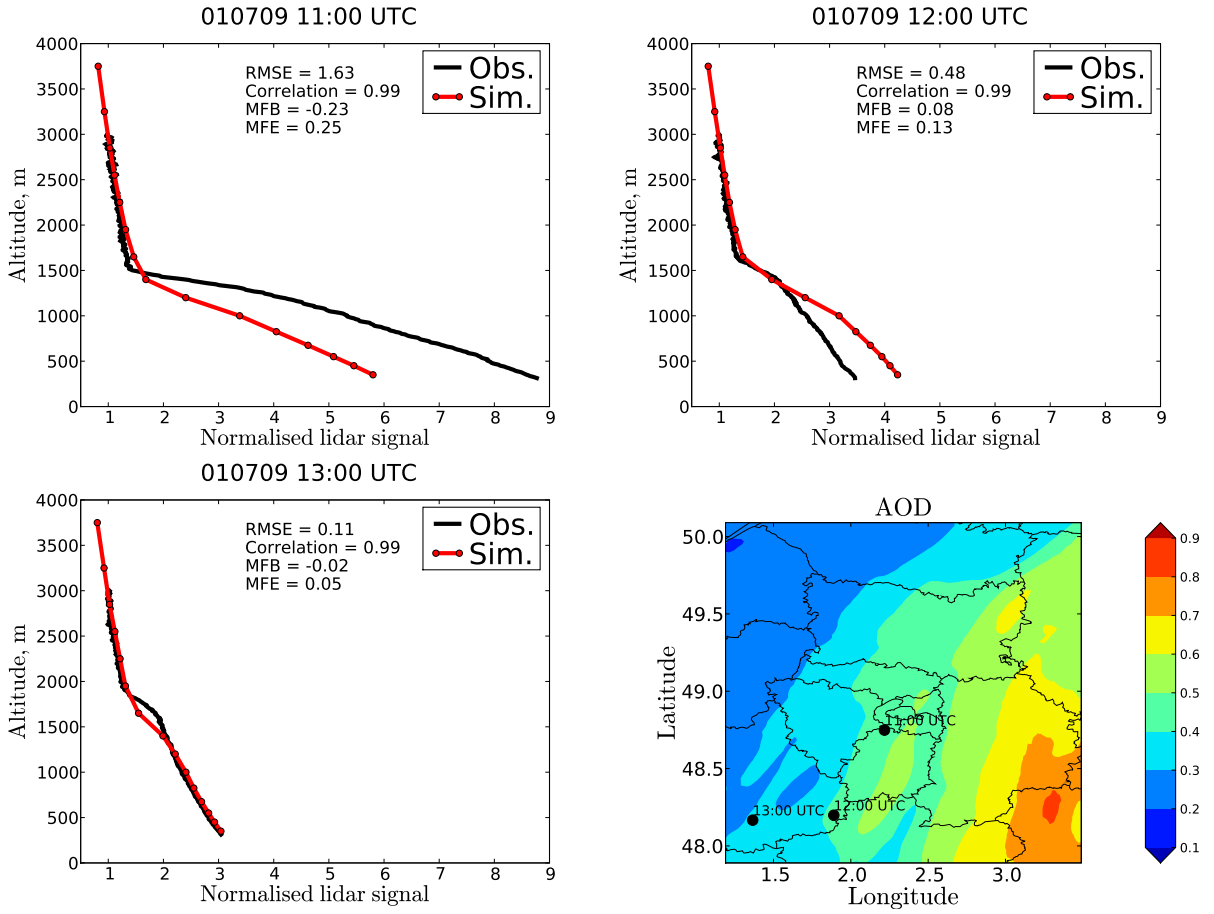

Figure 3.6: Comparisons between the vertical profiles observed by GBML (black lines) and simulated by POLYPHEMUS (red lines) on 01 July 2009 at 11:00, 12:00 and 13:00 UTC. Lidar observations below the altitude of full overlap are not represented. The lower right panel shows the positions of the different lidar profiles and the horizontal distribution of the mean of the AODs at 11:00, 12:00 and 13:00 UTC.

will be performed for this day, as it is the most polluted day with observations from both the GMBL and a ground-based in situ lidar.

On 04 July 2009, GBML measurements are performed around Paris with a circular pattern from 14:49 to 17:24 UTC. Particle AOD and concentrations are underestimated in the simulation. The daily averaged AOD from the AERONET network is about 0.25, respectively 0.14 in the simulation (see Tab. 3.3). The daily averaged PM_{10} concentration from the Airparif network is about 18.37 $\mu g\,m^{-3}$, respectively 11.11 $\mu g\,m^{-3}$ in the simulation (see Tab. 3.2). Figure 3.7 shows the comparison between the GBML measurements and the simulation at 15:03 UTC and 16:00 UTC. The simulated lidar signals are underestimated. Moreover, lidar measurements show an aerosol layer between 2.0 km and 3.0 km (probably from long-range transport), which is not present in the simulation, but impacts the lidar signal until low altitudes. It is mostly because boundary conditions do not provide information about this aerosol layer due to the large-scale model uncertainties.

On 16 July 2009, GBML measurements are performed in the North of Paris from Saclay

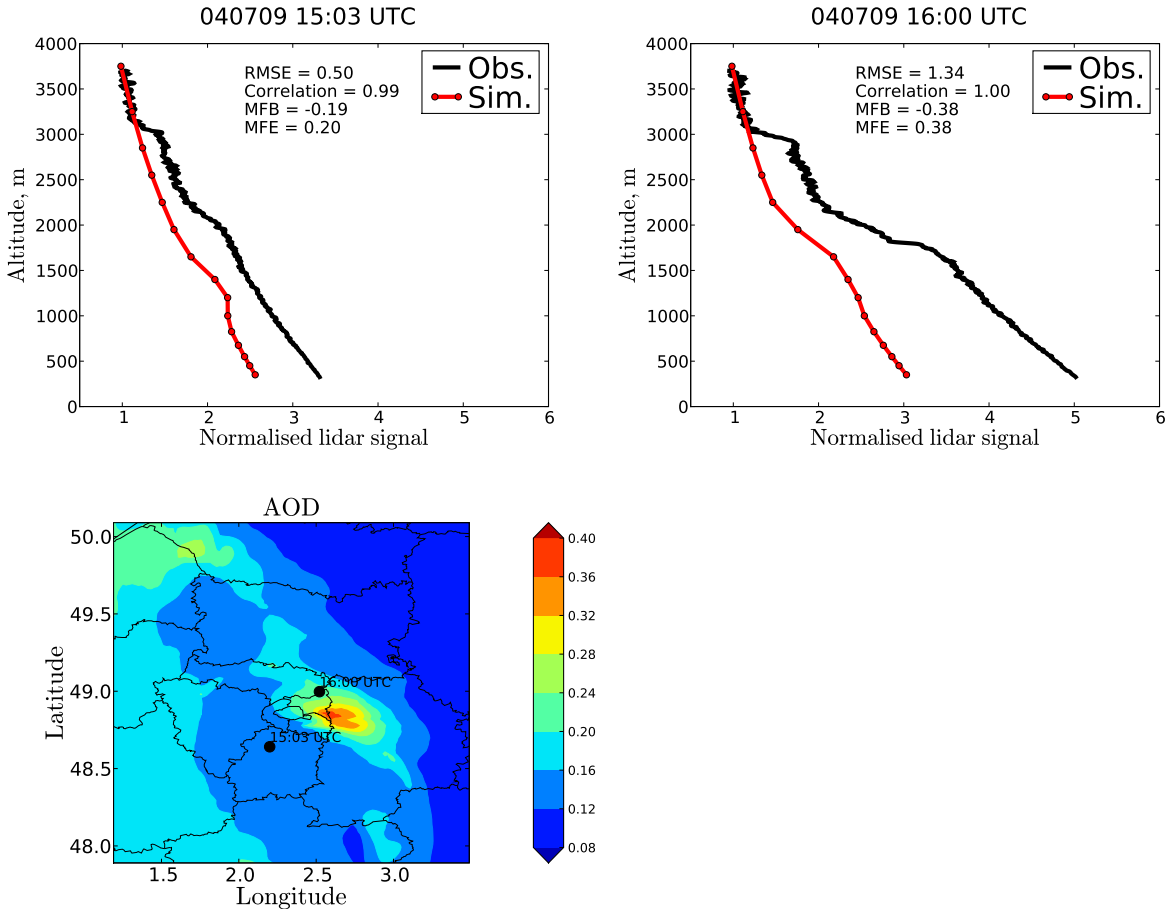

Figure 3.7: Comparisons between the vertical profiles observed by GBML (black lines) and simulated by POLYPHEMUS (red lines) on 04 July 2009 at 15:03 and 16:00 UTC. Lidar observations below the altitude of full overlap are not represented. The lower left panel shows the positions of the different lidar profiles and the horizontal distribution of the mean of the AODs at 15:00 and 16:00 UTC.

to Amiens between 11:00 UTC and 14:30 UTC. The lidar signal is overall underestimated, as shown in Fig. 3.8, in agreement with the underestimation of PM_{10} shown by the statistics in Tables 3.2 and 3.3. Surface PM_{10} concentration from the Airparif network and from the simulation are respectively 26.25 and 16.47 $\mu g\,m^{-3}$ (low-moderate level of pollution, see Tab. 3.2). The observed and simulated AOD are respectively 0.26 and 0.18 (see Tab. 3.3). The simulated AOD has a good correlation with AERONET data (up to 80 %). As deduced from the comparisons of the modelled and observed lidar signals in Fig. 3.8, the PBL height is well modelled until 12:00 UTC, but it is underestimated afterwards, e.g. the PBL height is about 2.1 km from the observed lidar signal but it is about 1.6 km in the simulation. These differences in PBL height explain that the simulated lidar signal agrees better with the observation until 12:00 UTC.

On 21 July 2009, the GBML travels from Saclay to the North of Paris across the city centre of Paris. As shown in Fig. 3.9, the lidar signal is overestimated for this measurement day. However, the surface PM_{10} concentration is underestimated. It is 27.84 and 16.84 $\mu g\,m^{-3}$ (low-

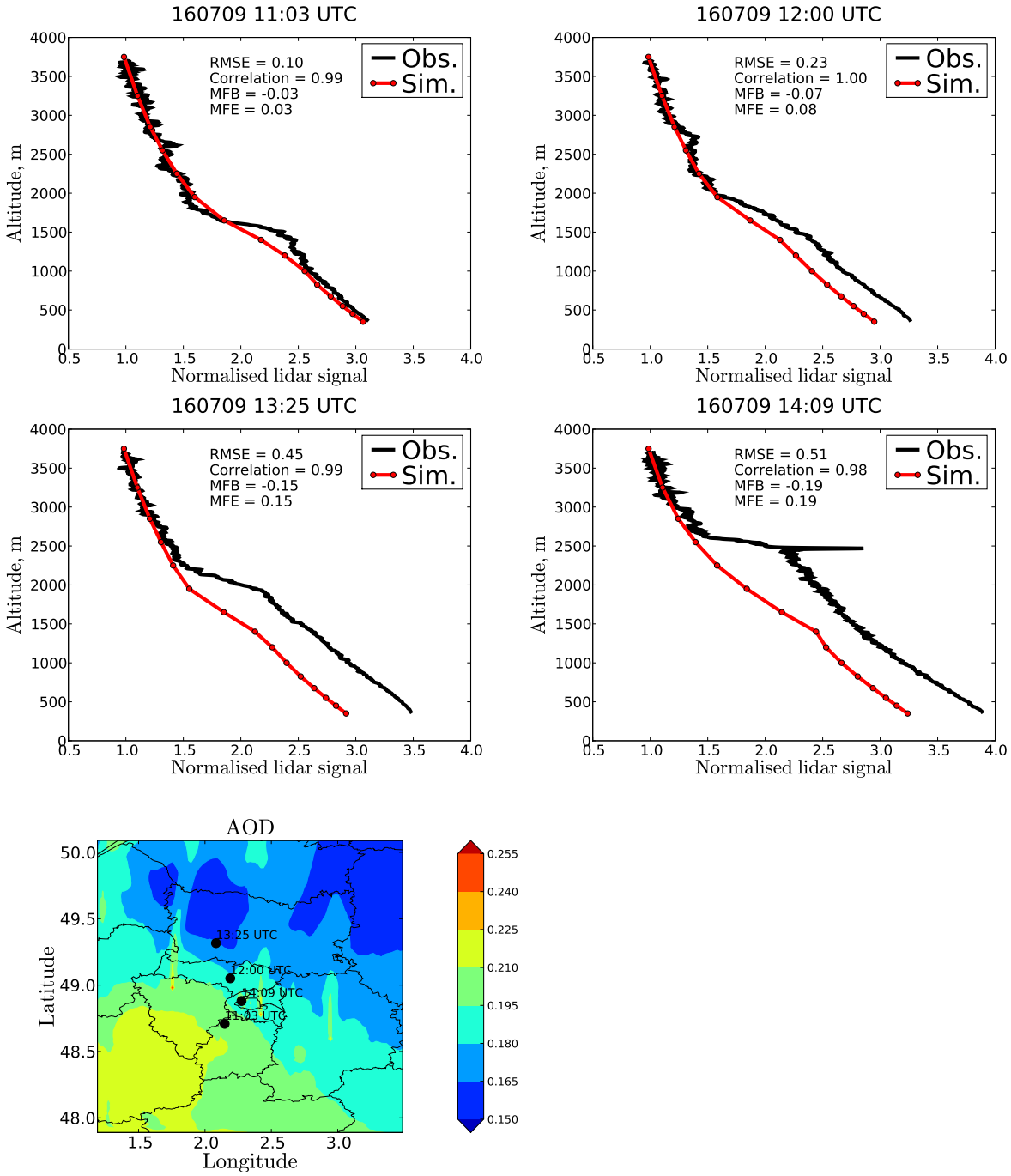

Figure 3.8: Comparisons between the vertical profiles observed by GBML (black lines) and simulated by POLYPHEMUS (red lines) on 16 July 2009 at 11:03, 12:00, 13:25 and 14:09 UTC. Lidar observations below the altitude of full overlap are not represented. The lower left panel shows the positions of the different lidar profiles and the horizontal distribution of the mean of the AODs at 11:00, 12:00, 13:00 and 14:00 UTC.

moderate level of pollution, see Tab. 3.2) from the Airparif network and from the simulation respectively. The large simulated lidar signals originate in high aerosol concentration at high altitudes, i.e. between 2.0 km and 2.5 km, which leads to higher backscattering and extinction

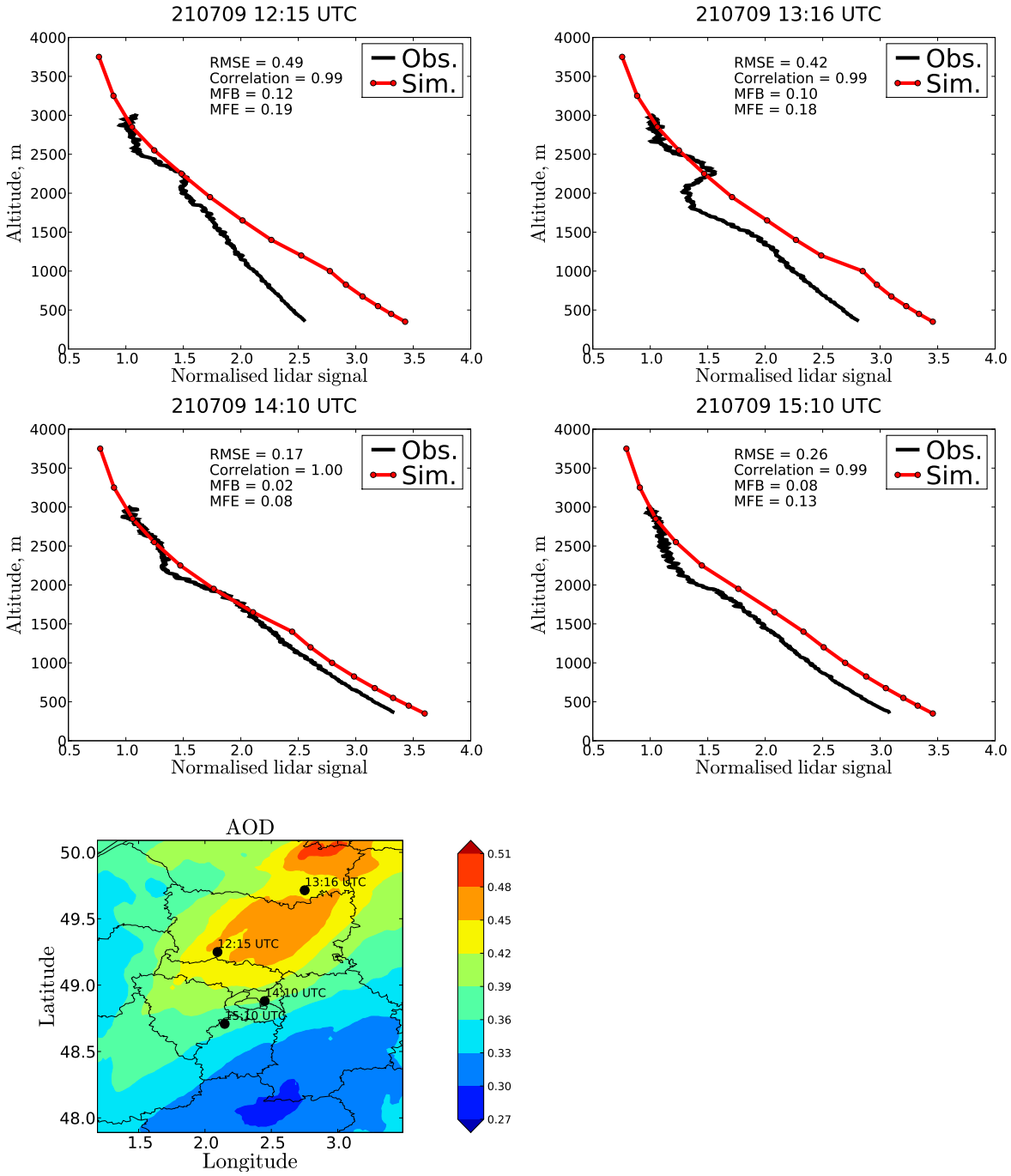

Figure 3.9: Comparisons between the vertical profiles observed by GBML (black lines) and simulated by POLYPHEMUS (red lines) on 21 July 2009 at 12:15, 13:16, 14:10 and 15:10 UTC. Lidar observations below the altitude of full overlap are not represented. The lower left panel shows the positions of the different lidar profiles and the horizontal distribution of the mean of the AODs at 12:00, 13:00, 14:00 and 15:00 UTC.

coefficients. This high-altitude aerosol layer originates in boundary conditions (large-scale model uncertainties), but it is not present in the observations. It impacts the lidar signal until low altitudes. This is why surface PM_{10} is underestimated while lidar signal is overestimated.

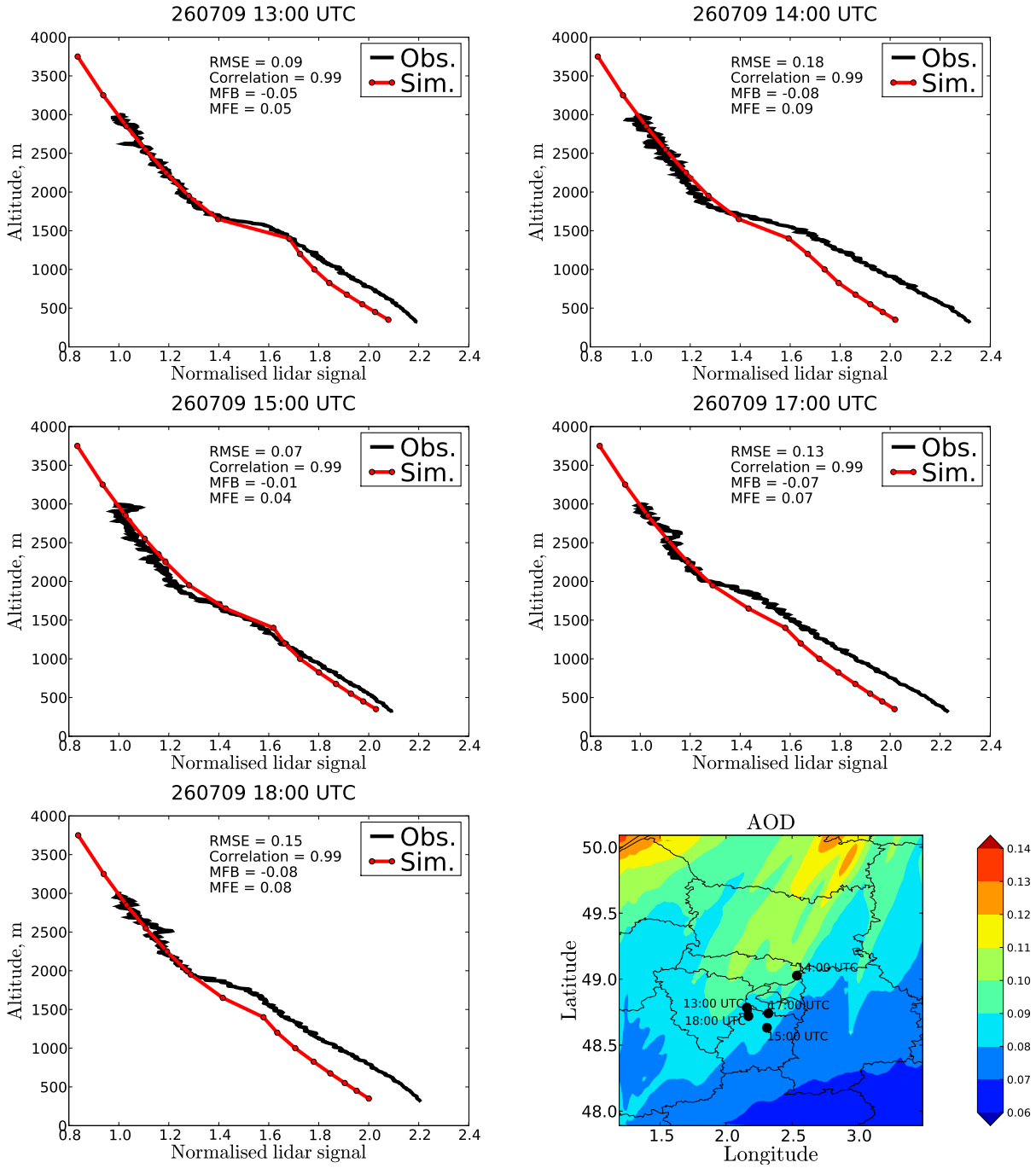

Figure 3.10: Comparisons between the vertical profiles observed by GBML (black lines) and simulated by POLYPHEMUS (red lines) on 26 July 2009 at 13:00, 14:00, 15:00, 17:00 and 18:00 UTC. Lidar observations below the altitude of full overlap are not represented. The lower right panel shows the positions of the different lidar profiles and the horizontal distribution of the mean of the AODs at 13:00, 14:00, 15:00, 17:00 and 18:00 UTC.

On 26 July 2009, the GBML followed two circular patterns (the yellow and cyan tracks in Fig. 3.3). One is performed from 12:40 to 15:30 UTC at a distance between 15 and 30 km from

the city centre. Another one is performed from 16:44 to 18:18 UTC in the South-Southwest of Paris. Low levels of pollution are observed and simulated. Surface PM_{10} concentration and AOD are underestimated. The daily averaged PM_{10} concentration from Airparif is 18.04 $\mu g\,m^{-3}$, against 10.12 $\mu g\,m^{-3}$ in the simulation. The mean observed AOD value is 0.15, against 0.08 in the simulation. Although the lidar signal is slightly underestimated in the simulation, simulated and observed lidar signals agree fairly well, as shown in Fig. 3.10. The pollution from Paris is transported by the South wind to the North. This is why the lidar signal is higher at 14:00 UTC in Fig. 3.10. Because as much as 5 hours of lidar measurements are performed, which is longer than on 04, 16, 21 and 29 July 2009, we will perform data assimilation for this day.

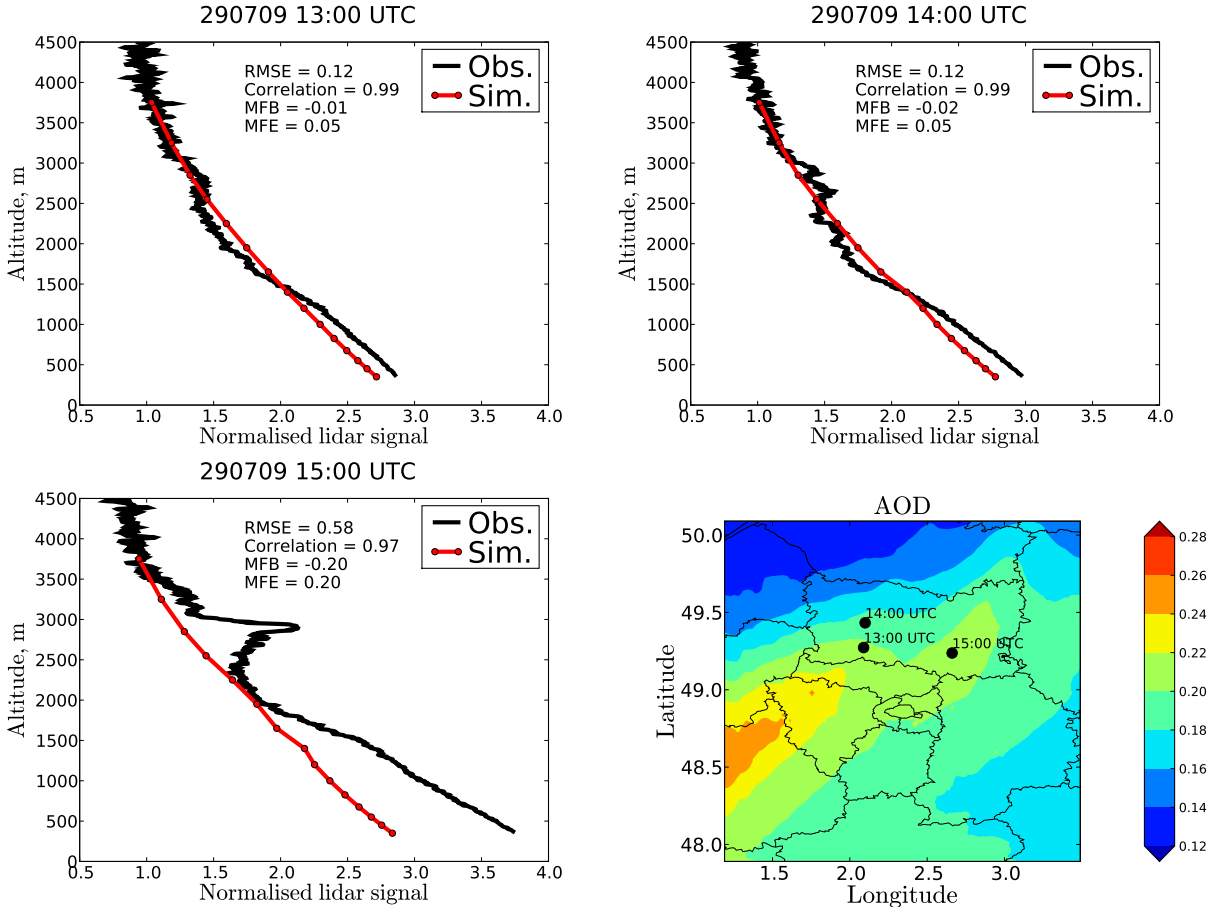

Figure 3.11: Comparisons between the vertical profiles observed by GBML (black lines) and simulated by POLYPHEMUS (red lines) on 29 July 2009 at 13:00, 14:00 and 15:00 UTC. Lidar observations below the altitude of full overlap are not represented. The lower right panel shows the positions of the different lidar profiles and the horizontal distribution of the mean of the AODs at 13:00, 14:00 and 15:00 UTC.

On 29 July 2009, GBML measurements are performed from 12:22 to 15:10 UTC in the North of Paris and in peri-urban and rural areas. While low levels of pollution (12.33 $\mu g\,m^{-3}$ of the mean PM_{10} concentration in Tab. 3.2) are simulated, moderate levels of pollution (29.25 $\mu g\,m^{-3}$ of the mean PM_{10} concentration in Tab. 3.2) is observed by the Airparif network. As

deduced from Fig. 3.11, at the beginning of measurement period, the PBL height is about 1.5 km and the simulated lidar signal agrees well with the lidar observations. At 15:00 UTC, the observed lidar signal has increased, because of an aerosol layer between 2.0 and 3.5 km. This layer is not simulated and the simulated lidar signal is underestimated.

For all measurement days, we also computed the statistics (i.e. RMSE, correlation, MFB and MFE) between observed and simulated lidar vertical profiles. The scores are shown respectively in Figures 3.6, 3.7, 3.8, 3.9, 3.10 and 3.11. Overall, RMSEs are below 1.63, the MFB ranges from -38% to 8% and the MFE ranges from 3% to 38%. Currently, there is no criterion to evaluate the comparisons for lidar signals. The criterion of Boylan and Russell [2006] was designed for PM concentration and light extinction. Because the scores of the lidar signal comparisons are extremely good compared to the criterion of Boylan and Russell [2006] with low errors and bias, the criterion of Boylan and Russell [2006] may not be restrictive enough for lidar signals.

3.6 Assimilation test of lidar observations

DA of lidar observations is performed for two out of the six different measurement days. Only two days are retained because the other days were cloudy and our algorithms do not allow us to assimilate lidar data when there are clouds. There are 13 h of cloud-cleaned measurements on 01 July, 5 h of cloud-cleaned measurements on 26 July and less than 3 h of cloud-cleaned measurements on the other measurement days. Therefore, DA run is performed on 01 and 26 July 2009 because too few data are available during the other measurement days.

In air quality, the large number of state variables leads to high computational costs when implementing DA algorithms. Among the widely used DA algorithms, the optimal interpolation (OI) is used here, as it is the most computationally efficient [Denby et al., 2008; Tombette et al., 2008; Wu et al., 2008; Li et al., 2013]. In applications of DA to aerosol forecast, Tombette et al. [2009] have used the OI over western Europe for assimilating observations from the BDQA network, which covers France. Denby et al. [2008] have used two different DA techniques, the OI and EnKF, to assimilate PM_{10} concentrations over Europe. Pagowski et al. [2010] have used the OI over the United States of America for data assimilation of $PM_{2.5}$ observations. Li et al. [2013] have used the OI for multiple aerosol species and for prediction of $PM_{2.5}$ in the Los Angeles basin. And Wang et al. [2013a] have used the OI over Europe to investigate the potential impact of future ground-based lidar networks on analysis and short-term forecasts of PM_{10}.

3.6.1 Basic formulation

A simple formulation for DA of lidar signals with OI is now described. Particles are represented in the model by mass concentrations of different chemical species for the different particle size sections.

The state vector $\mathbf{x}$ is defined by

$$\mathbf{x} = \{x^h_{i,j,k}\}_{1\leq i\leq N_b, 1\leq j\leq N_s, 1\leq k\leq n, 1\leq h\leq l}, \tag{3.15}$$

where $x^h_{i,j,k}$ is the mass concentration of the aerosol species j in section i for the horizontal spatial grid k at the model vertical level h, N_b is the number of size sections, N_s is the number

of chemical species, n is the number of horizontal grid points at each vertical level h and l is the total number of vertical levels.

The analysed state vector is a solution to the variational optimisation problem:

$$\mathbf{x}^a = \text{Argmin } J(x), \tag{3.16}$$

where J is the cost function defined by

$$\begin{aligned} J(\mathbf{x}) &= \frac{1}{2}\left(H(\mathbf{x})-\mathbf{y}\right)^{\mathrm{T}}\mathbf{R}^{-1}\left(H(\mathbf{x})-\mathbf{y}\right)+\frac{1}{2}\left(\mathbf{x}-\mathbf{x}^b\right)^{\mathrm{T}}\mathbf{B}^{-1}\left(\mathbf{x}-\mathbf{x}^b\right) \\ &\simeq \frac{1}{2}\left(H(\mathbf{x}^b)+\mathbf{LS}(\mathbf{x}-\mathbf{x}^b)-\mathbf{y}\right)^{\mathrm{T}}\mathbf{R}^{-1}\left(H(\mathbf{x}^b)+\mathbf{LS}(\mathbf{x}-\mathbf{x}^b)-\mathbf{y}\right) \\ &\quad +\frac{1}{2}\left(\mathbf{x}-\mathbf{x}^b\right)^{\mathrm{T}}\mathbf{B}^{-1}\left(\mathbf{x}-\mathbf{x}^b\right), \end{aligned} \tag{3.17}$$

where $\mathbf{x}^b$ is the model concentrations, $\mathbf{y}$ is the vector of observations, $H(\mathbf{x}) = \mathbf{L}\cdot S(\mathbf{x})$ is the lidar observation operator, S is a nonlinear operator from the model state $\mathbf{x}$ to the lidar signal state, $\mathbf{L}$ is a linear spatial interpolation operator, $\mathbf{S}$ is the tangent linear of operator S, $\mathbf{B}$ and $\mathbf{R}$ are the matrices of error covariances for backgrounds and observations respectively. In this way, we have

$$\nabla J(\mathbf{x}^a) = (\mathbf{LS})^{\mathrm{T}}\mathbf{R}^{-1}\left(H(\mathbf{x}^b)-\mathbf{y}\right)+\left(\mathbf{B}^{-1}+(\mathbf{LS})^{\mathrm{T}}\mathbf{R}^{-1}(\mathbf{LS})\right)(\mathbf{x}^a-\mathbf{x}^b)=0, \tag{3.18}$$

which leads to

$$\mathbf{x}^a-\mathbf{x}^b = \left(\mathbf{B}^{-1}+(\mathbf{LS})^{\mathrm{T}}\mathbf{R}^{-1}(\mathbf{LS})\right)^{-1}\left(\mathbf{y}-H(\mathbf{x}^b)\right) \tag{3.19}$$

$$= \mathbf{B}(\mathbf{LS})^{\mathrm{T}}\left((\mathbf{LS})\mathbf{B}(\mathbf{LS})^{\mathrm{T}}+\mathbf{R}\right)^{-1}\left(\mathbf{y}-H(\mathbf{x}^b)\right). \tag{3.20}$$

3.6.2 Construction of error covariances

Since the measurements at different levels originate from the same lidar, the matrix $\mathbf{R}$ should not be diagonal because of measurement error correlations. However, in order to simplify $\mathbf{R}$ in the first tests of DA of lidar observations, one takes $\mathbf{R} = r\mathbf{I}$ as a diagonal matrix where $\mathbf{I}$ is the identity matrix and r is an error variance. The value of the observation error variance r is determined by a χ^2 diagnosis [Ménard et al., 1999], in which the scalar

$$\chi^2 = \left(\mathbf{y}-H(\mathbf{x}^b)\right)^{\mathrm{T}}\left((\mathbf{LS})\mathbf{B}(\mathbf{LS})^{\mathrm{T}}+\mathbf{R}\right)^{-1}\left(\mathbf{y}-H(\mathbf{x}^b)\right) \tag{3.21}$$

should be equal, on average, to the number of observations (N) at each DA step.

Specifically, $\mathbf{B}$ plays a role in determining how the corrections of the concentrations should be distributed over the domain during DA. In practice, however, it is impossible to accurately know all coefficients of $\mathbf{B}$. In our simulation, the number of model grid points is of the order of 10^5. Thus the number of coefficients in the matrix $\mathbf{B}$ is about 10^{10} multiplied by the square of the number of analysis variables (about 100 variables for particles are used here). Therefore, $\mathbf{B}$ is too large to be handled numerically.

In order to reduce the size of the error covariance matrices for background, we model the matrix $\mathbf{B}$ as follows

$$\mathbf{B} = \mathbf{PDP}^{\mathrm{T}}, \tag{3.22}$$

where $\mathbf{D}$ is the error covariance matrix for PM_{10}, defined by the Balgovind approach [Balgovind et al., 1983] obtained by considering the RMSE and correlation of simulated PM_{10} concentrations. Thus, the size of $\mathbf{D}$ is much less than the one of $\mathbf{B}$. The matrix $\mathbf{P}$ is defined by

$$\mathbf{P} = \begin{bmatrix} \mathbf{v}_1 & \mathbf{0} & \dots & \mathbf{0} \\ \mathbf{0} & \mathbf{v}_2 & \dots & \mathbf{0} \\ \vdots & \vdots & \ddots & \vdots \\ \mathbf{0} & \mathbf{0} & \dots & \mathbf{v}_M \end{bmatrix}_{(M \cdot N_b \cdot N_s) \times M},$$

where M is equal to the dimension of the domain ($l \cdot n$), $\mathbf{v}_k$ is a vector of size $N_b \cdot N_s$ (the number of state variables). Each component of $\mathbf{v}_k$ corresponds to the proportion of the mass of particles for a given species in a given size section in PM_{10} mass concentrations at grid point k.

Let $\mathbf{S}' = \mathbf{SP}$ be the directional derivative of S along a given direction, and let $\mathbf{c}^b$ and $\mathbf{c}^a$ be PM_{10} concentration states before and after analysis respectively. In order to convert $\mathbf{x}$ into the PM_{10} state $\mathbf{c}$, we multiply each side of equation (3.20) by the matrix $\mathbf{Z}$:

$$\mathbf{Z} = \begin{bmatrix} 1 & \dots & 1 & 0 & \dots & 0 & 0 & \dots & 0 & 0 & \dots & 0 \\ 0 & \dots & 0 & 1 & \dots & 1 & 0 & \dots & 0 & 0 & \dots & 0 \\ \vdots & \ddots & \vdots & \vdots & \ddots & \vdots & \vdots & \ddots & \vdots & \vdots & \ddots & \vdots \\ 0 & \dots & 0 & 0 & \dots & 0 & 0 & \dots & 0 & 1 & \dots & 1 \end{bmatrix}_{M \times (M \cdot N_b \cdot N_s)}.$$

We obtain

$$\mathbf{c}^a - \mathbf{c}^b = \mathbf{D}(\mathbf{LS}')^{\mathrm{T}} \left((\mathbf{LS}')\mathbf{D}(\mathbf{LS}')^t + \mathbf{R} \right)^{-1} \left(\mathbf{y} - H(\mathbf{x}^b) \right). \tag{3.23}$$

After the analysis, the concentrations $\mathbf{c}^a$ are redistributed over particle species and size sections following the initial chemical and size distributions.

3.6.3 DA setup

DA experiments are carried out for 01 and 26 July 2009. All DA experiments are performed with a time step of 600 s and from 200 to 1800 m above the ground (10 model levels), since the lidar measurements are not available below the altitude of full overlap (200 m above the ground) and since aerosol concentrations above the PBL have limited impact on surface PM_{10} in the short term [Wang et al., 2013a]. In the Balgovind approach [Balgovind et al., 1983], the horizontal correlation length is set to $0.2°$, which is estimated from numerical DA tests. The error variances are separately set for each DA level, depending on the RMSE of PM concentrations and the variability of PM concentrations at each model level.

Two new algorithms are tested for the assimilation of lidar observations. In the first algorithm, we use the assimilation of lidar observations to analyse PM_{10} concentrations and the analysed PM_{10} concentrations are redistributed over particle species and size sections following the initial chemical and size distributions (see section 3.6.2). The background error variances of PM_{10} concentrations are estimated by the simulation without DA and Airparif observations. The value of the observation error variance r is determined by a χ^2 diagnosis, which yields $r = 1\ \mu g^2\,m^{-6}$ and $r = 0.006\ \mu g^2\,m^{-6}$ respectively for 01 and 26 July, depending on the level of uncertainties (see section 3.5). Let N be the number of lidar observations at one DA step.

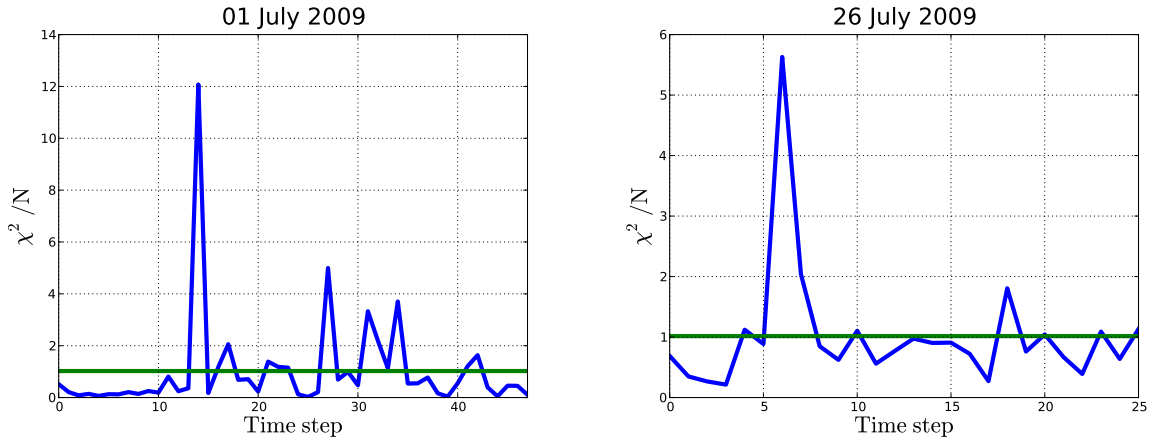

Figure 3.12: Time evolution of χ^2/N (blue lines) for DA runs on 01 and 26 July 2009. The mean over DA window of χ^2/N is 1.02 (resp. 1.02) for 01 (resp. 26) July 2009.

Figure 3.12 shows the time evolution of χ^2/N (blue lines) for DA runs on 01 and 26 July. The mean over DA window of χ^2/N is 1.02 (resp. 1.02) for 01 (resp. 26) July.

In the second algorithm, we separately analyse $PM_{2.5}$ and $PM_{2.5-10}$ (particulate matter with a diameter higher than 2.5 μm and lower than 10 μm) in the assimilation of lidar observations. We modify the matrices used in section 3.6.2 to obtain $\mathbf{c_{2.5}}$ and $\mathbf{c_{2.5-10}}$, the mass concentrations of $PM_{2.5}$ and $PM_{2.5-10}$ respectively (see Appendix B for details). We separately set the error variances for $PM_{2.5}$ and $PM_{2.5-10}$ in matrix $\mathbf{D}$. Because of the lack of $PM_{2.5-10}$ observations, we can not directly estimate the background error variances. They are determined by the χ^2 diagnosis using the observation error variance r found in the first algorithm.

In the following, we note the assimilation with the first (resp. second) DA algorithm as "DA (PM_{10})" (resp. "DA ($PM_{2.5}$ and $PM_{2.5-10}$)").

3.6.4 Results and discussions

In these DA tests, the purpose is to verify if these new algorithms are functional. Because we work at small scale, the corrections of DA are transported out of the simulation domain very quickly. Thus we only compute the statistics for the DA window to validate the DA tests.

Table 3.4 presents statistics of the simulation results without DA and with DA. Statistics are computed for both PM_{10} and $PM_{2.5}$ concentrations. Overall, both DA algorithms lead to better scores (lower RMSE, MFB and MFE, and higher correlation) than the simulation without DA for PM_{10} concentrations. Comparing the two DA algorithms, the simulation with DA ($PM_{2.5}$ and $PM_{2.5-10}$) leads to better scores than the simulation with DA (PM_{10}) for PM_{10} concentrations (see Tab. 3.4). The RMSE of PM_{10} is 11.63 $\mu g\,m^{-3}$ in the simulation with DA ($PM_{2.5}$ and $PM_{2.5-10}$), against 13.69 $\mu g\,m^{-3}$ in the simulation with DA (PM_{10}) on 01 July. The RMSE of PM_{10} is 4.73 $\mu g\,m^{-3}$ in the simulation with DA ($PM_{2.5}$ and $PM_{2.5-10}$), against 6.08 $\mu g\,m^{-3}$ in the simulation with DA (PM_{10}) on 26 July. It is because higher background error variances are set for the coarse sections in the simulation with DA ($PM_{2.5}$ and $PM_{2.5-10}$). However, the simulation with DA ($PM_{2.5}$ and $PM_{2.5-10}$) leads to similar scores to the simulation with DA (PM_{10}) for $PM_{2.5}$ concentrations (see Tab. 3.4). It is because similar background error

Table 3.4: Statistics (see Appendix A) of the simulation results (PM_{10} and $PM_{2.5}$) without DA and with DA for the Airparif network for 01 and 26 July 2009. "With DA (PM_{10})" stands for the assimilation of lidar observations correcting directly PM_{10}. "With DA ($PM_{2.5}$ and $PM_{2.5-10}$)" stands for the assimilation of lidar observations correcting separately $PM_{2.5}$ and $PM_{2.5-10}$.

Day	Species	Simulation	Stations	Obs. mean	Sim. mean	RMSE	Corr.	MFB	MFE
				$\mu g\,m^{-3}$	$\mu g\,m^{-3}$	$\mu g\,m^{-3}$	%	%	%
01/07	PM_{10}	Without DA	15	47.26	32.35	17.74	84	-41	43
		DA (PM_{10})			36.20	13.69	90	-29	32
		DA ($PM_{2.5}$ and $PM_{2.5-10}$)			39.85	11.63	84	-19	25
	$PM_{2.5}$	Without DA	5	30.52	30.21	8.54	69	-5	23
		DA (PM_{10})			33.04	10.44	59	5	27
		DA ($PM_{2.5}$ and $PM_{2.5-10}$)			33.08	10.45	58	5	27
26/07	PM_{10}	Without DA	15	16.25	9.96	6.67	-20	-47	47
		DA (PM_{10})			10.55	6.08	15	-42	42
		DA ($PM_{2.5}$ and $PM_{2.5-10}$)			12.80	4.73	26	-25	30
	$PM_{2.5}$	Without DA	5	10.25	8.99	2.80	7	-9	25
		DA (PM_{10})			9.64	2.51	22	-2	22
		DA ($PM_{2.5}$ and $PM_{2.5-10}$)			9.49	2.54	21	-4	22

variances for $PM_{2.5}$ in the simulation with DA ($PM_{2.5}$ and $PM_{2.5-10}$) to the simulation with DA ($PM_{2.5}$) are used in the χ^2 diagnosis, since fine particles contribute to more than 80% of the lidar signal [Randriamiarisoa et al., 2006]. In the following, we compare the simulation without DA and the simulation with DA ($PM_{2.5}$ and $PM_{2.5-10}$).

On 01 July, the averaged RMSE of PM_{10} is 11.63 $\mu g\,m^{-3}$ with DA ($PM_{2.5}$ and $PM_{2.5-10}$), against 17.74 $\mu g\,m^{-3}$ without DA. The decrease of the RMSE are explained by the correlation length in the matrix $\mathbf{D}$, since no Airparif station performs measurements in the Southwest of Paris (the Northeast wind). At station *Issy-Les-Moulineaux* (48.82° N, 2.27° E, 36 m a.s.l.), the closest station to Saclay, the RMSE of PM_{10} is 14.72 $\mu g\,m^{-3}$ with DA ($PM_{2.5}$ and $PM_{2.5-10}$), against 22.81 $\mu g\,m^{-3}$ without DA. However, the averaged RMSE of $PM_{2.5}$ is about 10.4 $\mu g\,m^{-3}$ with DA ($PM_{2.5}$ and $PM_{2.5-10}$), against 8.54 $\mu g\,m^{-3}$ without DA. This is due to the larger horizontal correlation length (see section 3.6.3). While DA runs increase PM concentrations in the lidar measurement grids, PM concentrations are increased at Airparif stations, where $PM_{2.5}$ concentrations is well simulated and coarse particles are underestimated. This problem can be solved by decreasing the horizontal correlation length. Figure 3.13 shows that the model underestimates the lidar signal at Saclay. The simulation with DA simulates better the lidar signal than the one without DA. It means that DA corrects well the model aerosol concentrations (the closer to the truth the model aerosol concentrations are, the better the lidar signals are simulated).

On 26 July, the averaged RMSE of PM_{10} is 4.73 $\mu g\,m^{-3}$ with DA ($PM_{2.5}$ and $PM_{2.5-10}$),

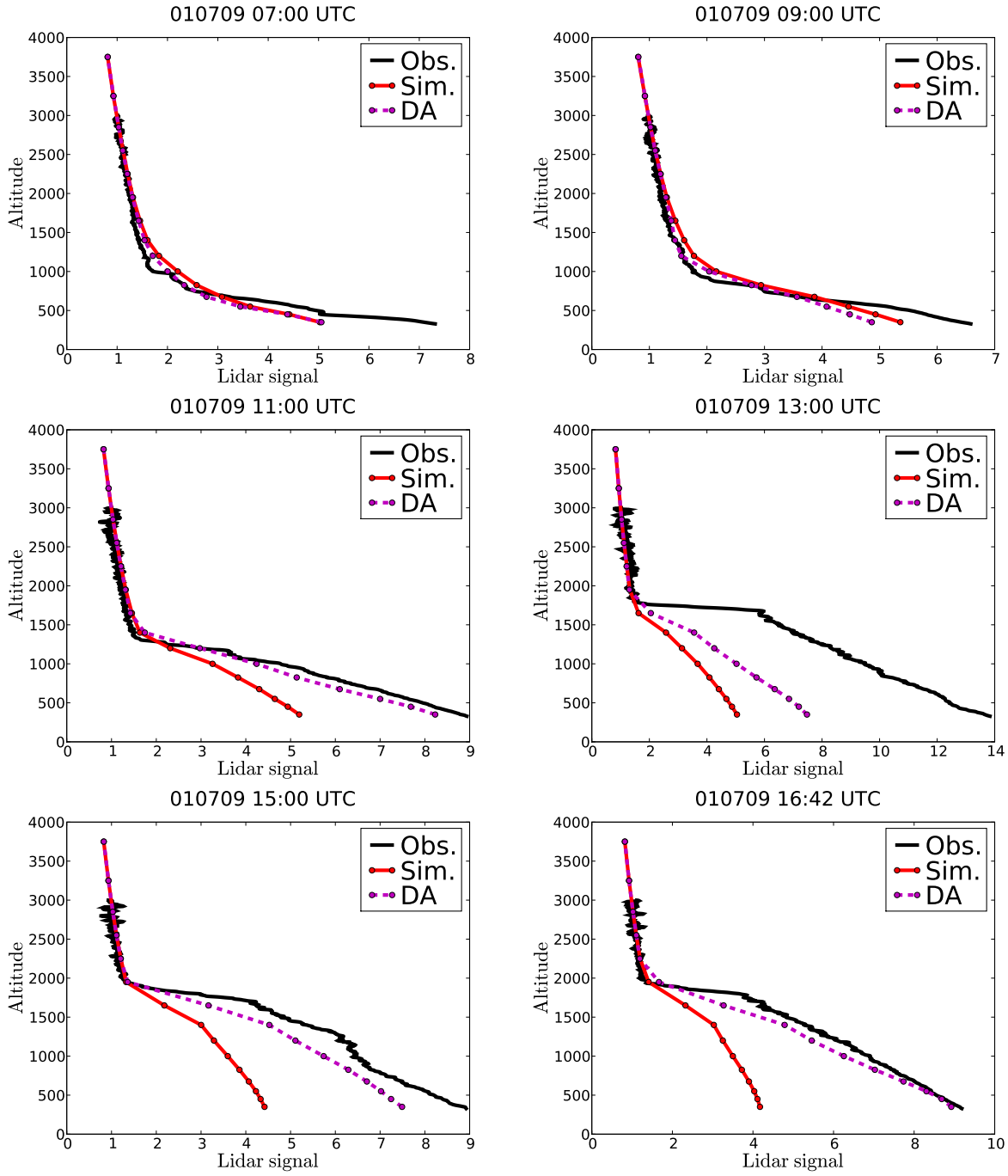

Figure 3.13: Lidar vertical profiles observed by the ground-based *in situ* lidar at Saclay (black lines), simulated without DA (red lines) and simulated with DA (magenta lines) on 01 July 2009.

against 6.67 $\mu g\,m^{-3}$ without DA. Because two circular GBML travelling patterns were performed around Paris (see Fig. 3.3), most of Airparif stations are leeward (the South wind) or they are close to the patterns of GBML. They could validate improvements of PM concentrations. At station *Paris 1er Les Halles* (48.86° N, 2.35° E, 35 m a.s.l.), the RMSE of PM_{10}

is 1.96 $\mu g\,m^{-3}$ in the simulation with DA ($PM_{2.5}$ and $PM_{2.5-10}$), against 4.71 $\mu g\,m^{-3}$ in the simulation without DA. Moreover, DA runs lead to better scores than the simulation without DA for $PM_{2.5}$. At leeward station *Creil Faiencerie* (49.26° N, 2.47° E, 28 m a.s.l.), the RMSE of $PM_{2.5}$ is 4.1 $\mu g\,m^{-3}$ in the simulation with DA ($PM_{2.5}$ and $PM_{2.5-10}$), against 4.9 $\mu g\,m^{-3}$ in the simulation without DA.

3.7 Conclusions

In order to investigate the ability of the CTM POLAIR3D of the air quality modelling platform POLYPHEMUS to simulate lidar vertical profiles, we performed a simulation over the Greater Paris area for the summer month of July 2009. The results (PM_{10} and $PM_{2.5}$ concentrations) are evaluated using Airparif data. We simulated aerosol optical properties and lidar signals from the model aerosol concentration outputs using the aerosol complex refractive index (ACRI) and the wet particle diameter. The AOD was evaluated using AERONET data: the RMSE ranges from 0.07 to 0.20, the MFB ranges from -58% to -21% and the MFE ranges from 29% to 58%. According to the criterion of Boylan and Russell [2006], the model performance criterion is met for AOD. Hourly comparisons between simulated lidar signals and lidar observations were described for six measurement days during the MEGAPOLI summer campaign. These comparisons showed a good agreement between GBML measurements and the simulation except for 04 July 2009, where an aerosol layer was not modelled at high altitudes but observed in lidar measurements, and for 21 July 2009, where an aerosol layer was modelled at high altitudes but not observed in lidar measurements. The statistics obtained for the lidar comparison are extremely good compared to the criterion of Boylan and Russell [2006] with low errors and bias: the MFB ranges from -38% to 8% and the MFE ranges from 3% to 38%. Because the criterion of Boylan and Russell [2006] was designed for PM concentration and light extinction, they may not be restrictive enough for lidar signals. A specific criterion would therefore need to be designed. Overall, the results show that the optical property module of POLYPHEMUS models well lidar signals.

Two new algorithms for the assimilation of lidar observations based on the optimal interpolation method were presented. One algorithm analyses PM_{10} concentrations. Another analyses $PM_{2.5}$ and $PM_{2.5-10}$ concentrations separately. DA tests were performed for only 01 and 26 July 2009, because the other measurement days were cloudy and our algorithms do not allow us to assimilate lidar data when there are clouds. Both of these algorithms lead to better scores (lower RMSE, MFB and MFE, and higher correlation) for PM_{10} and $PM_{2.5}$ on 26 July 2009. However, they did not improve $PM_{2.5}$ on 01 July 2009, because of the large horizontal correlation length. The simulation with DA ($PM_{2.5}$ and $PM_{2.5-10}$) leads to better scores than the simulation with DA (PM_{10}) because the error variances for backgrounds are set separately for fine ($PM_{2.5}$) and coarse ($PM_{2.5-10}$) particles. The results shown in this paper suggest that the assimilation of lidar observations that analyses $PM_{2.5}$ and $PM_{2.5-10}$ would perform better than the assimilation of lidar observations that analyses PM_{10}, but it is computationally more costly.

Comparing the simulation without DA and the simulation with DA ($PM_{2.5}$ and $PM_{2.5-10}$), the averaged RMSE of PM_{10} is 11.63 $\mu g\,m^{-3}$ with DA ($PM_{2.5}$ and $PM_{2.5-10}$), against 17.74 $\mu g\,m^{-3}$ without DA on 01 July 2009. The averaged RMSE of PM_{10} is 4.73 $\mu g\,m^{-3}$ with DA ($PM_{2.5}$ and $PM_{2.5-10}$), against 6.67 $\mu g\,m^{-3}$ without DA on 26 July 2009.

A forthcoming paper will present results about the assimilation of continuous measurements

from the ACTRIS/EARLINET network during a 72-hour period of intensive observations.

Chapter 4

Assimilation of lidar signals: Application to the Mediterranean basin

Preamble

The validation of the lidar observation operator in data assimilation (DA) was performed in Chapter 3 by a new model for simulating the lidar signal (PR^2). Simulated lidar signals were compared to hourly ground-based mobile and *in situ* lidar observations performed during the MEGAPOLI summer experiment in July 2009. We found that the model correctly reproduces the vertical distribution of aerosol optical properties and their temporal variability. In addition, two algorithms for assimilating lidar signals were presented and compared. DA tests were performed for both 01 and 26 July 2009. Although the evaluation using the Airparif demonstrated the feasibility and the usefulness of assimilating lidar profiles for aerosol forecasts, the improvements of DA were limited by the number of lidar stations (maximum 2 sites) and the short measurement period, 13 hours for 01 July and 5 hours for 26 July.

In this chapter, POLYPHEMUS with the model for assimilating lidar signals is applied to the Mediterranean basin, where 9 ground-based lidar stations from the ACTRIS/EARLINET network in the Mediterranean basin and one station in Corsica in the framework of the ChArMEx (Chemistry-Aerosol Mediterranean Experiment)/TRAQA(TRAnsport à longue distance et Qualité de l'Air) campaign (see Fig. 4.1) performed a 72-hour period (from 06:00 UTC 09 to 06:00 UTC 12 July) of intensive and continuous measurements in July 2012. Figure 4.2 shows the daytime mean AODs at 550 nm retrieved from MSG(Meteosat Second Generation)/SEVIRI satellites for 09, 10, 11 and 12 July 2012, which corresponds to the lidar measurement period. The high AODs observed over Spain and Italy are mostly made of Sahara dust. In addition, the Mediterranean basin is the receptacle of pollution from different origins, e.g. natural pollution from the Sahara, anthropogenic emissions from cities reacting with biogenic emissions [Sartelet et al., 2012], and forest fires or ecosystems plants. Aerosol concentrations are often high over the Mediterranean basin in summer. Therefore, we believe that the Mediterranean basin is a good place to test the usefulness of lidar data assimilation to improve the forecast of CTMs.

As shown in Chapter 3, analysing $PM_{2.5}$ and $PM_{2.5-10}$ respectively leads to better forecasts than analysing PM_{10} in lidar DA. Thus, we analyse the $PM_{2.5}$ and $PM_{2.5-10}$ respectively at each DA step in this chapter. First, we study the spatial and temporal influence of the assimilation of lidar signals on aerosol forecasting and conduct sensitivity studies on algorithm parameters,

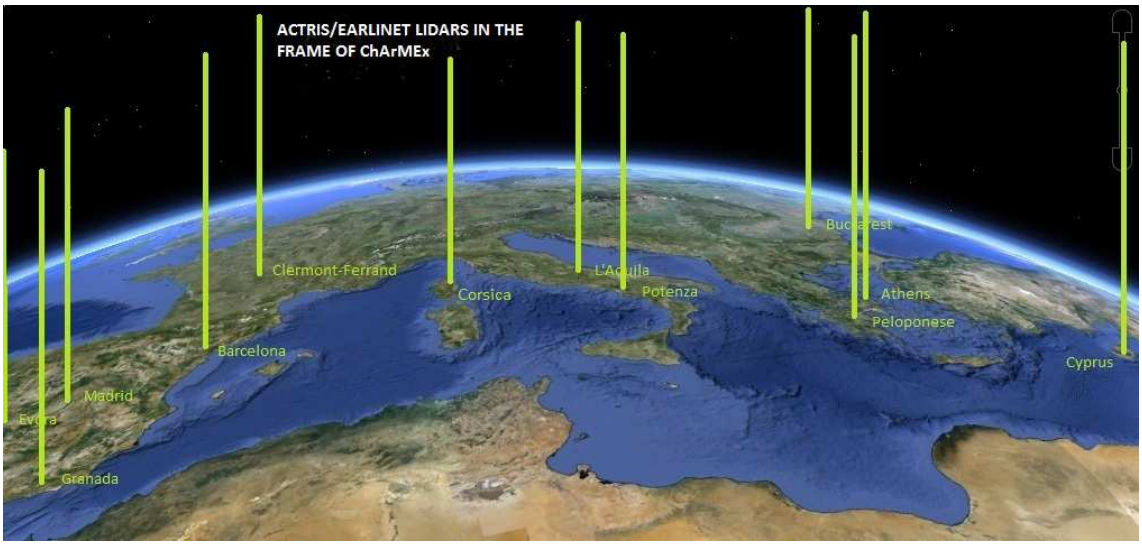

Figure 4.1: Distribution of the ACTRIS/EARLINET sites and the Corsica lidar site. The measurements of Peloponese and Cyprus stations are not used in this thesis.

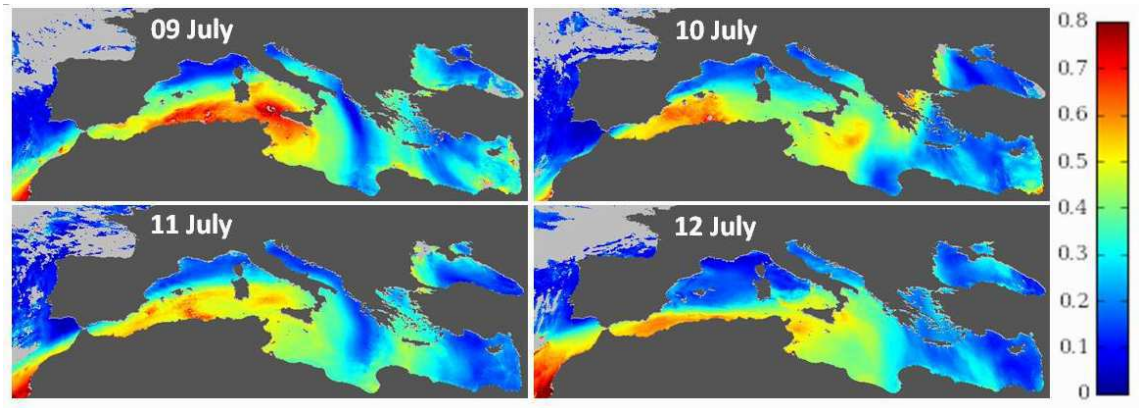

Figure 4.2: Daytime (from 04:00 to 18:00 UTC) mean AOD at 550 nm derived from MSG/SEVIRI.

e.g. the correlation length in the background error covariance matrix, altitudes at which DA is performed and the assimilation period length (12 hours or 24 hours). Secondly, DA experiments are carried out for 72-hour experiments. The aerosol simulation results without and with lidar DA are evaluated using the Aerosol Optical Depth (AOD) measurements from AERONET, and mass concentration measurements (PM_{10} or $PM_{2.5}$) from the EMEP-Europe network over Europe, the BDQA network in France and the EMEP-Spain/Portugal network. The results show that the simulation with lidar DA leads to better scores than the one without DA for aerosol forecasts ($PM_{2.5}$, PM_{10} and AOD). Additionally, the temporal impact of assimilating lidar signals is longer than 36 hours. However, the temporal impact of assimilating surface mass concentrations was estimated to be between 6 and 12 hours by Tombette et al. [2009] and Jiang et al. [2013].

This chapter consists of
Y. Wang, K. N. Sartelet, M. Bocquet, P. Chazette, M. Sicard, G. DAmico, J. F. Léon, L. Alados-Arboledas, A. Amodeo, P. Augustin, J. Bach, L. Belegante, I. Binietoglou, X. Bush, A. Comerón, H. Delbarre, D. García-Vízcaino, J. L. Guerrero-Rascado, M. Hervo, M. Iarlori, P. Kokkalis, D. Lange, F. Molero, N. Montoux, A. Muñoz, C. Muñoz, D. Nicola, A. Papayannis, G. Pappalardo, J. Preissler, V. Rizi, F. Rocadenbosch, K. Sellegri, F. Wagner, and F. Dulac: **Assimilation of lidar signals: Application to aerosol forecasting in the Mediterranean basin**, Atmos. Chem. Phys. Discuss., submitted.

Sommaire

4.1 Introduction

Aerosols consist of tiny pieces of solid or liquid matter suspended in the atmosphere. They have an impact on vegetation and human health by penetrating the respiratory system and can lead to respiratory and cardiovascular diseases [Dockery and Pope, 1996; Lauwerys et al., 2007]. They also influence visibility [Wang et al., 2009] and affect the Earth's environment and climate by changing the amount of incoming solar radiation and outgoing terrestrial long-wave radiation retained in the Earth's system [Intergovernment Panel on Climate Control (IPCC), 2013]. Furthermore, they have an indirect effect, by changing the microphysical properties of clouds [Intergovernment Panel on Climate Control (IPCC), 2013].

In order to understand the physical, chemical, and dynamical processes associated with aerosols, a variety of chemistry transport models (CTM) have been developed [Simpson et al., 2003; Schaap et al., 2004; Hodzic et al., 2006; Sartelet et al., 2007]. In air quality modelling, CTMs are often employed to forecast aerosol concentrations. For instance, the monitoring atmospheric composition & climate (MACC, `http://www.gmes-atmosphere.eu/`) model and the air quality modelling system POLYPHEMUS (`http://cerea.enpc.fr/en/prevision.html`) perform real-time forecast of aerosols over Europe. However, a CTM is always a simplification of the real atmosphere and there are large uncertainties in aerosol modelling [Roustan et al., 2010]. A CTM is limited in terms of spatial and temporal resolutions. It is also limited to a restricted selection of physical and chemical processes, which are often simplified or parameterised. In addition, input data are often highly uncertain. Initial and boundary conditions of pollutants are two crucial factors for forecasting. Since initial and boundary conditions are often outputs from a previous or larger-scale simulation, or from a fixed set of climatological average values based on long term observations, they are usually lacking accuracy. Furthermore, aerosol measurements provide a detailed insight into the atmosphere's current state, using satellite observations on a global scale or *in situ* measurements from ground based or airborne instruments. Unfortunately, although measurements can help improving the knowledge of the atmosphere, they do not directly provide the necessary initial or boundary conditions for aerosol modelling.

A technique referred to as *data assimilation* (DA hereafter) has been introduced to couple model and observations, and improve the accuracy of input data of model forecast, such as initial conditions or boundary conditions [Talagrand, 1997; Roustan and Bocquet, 2006]. In meteorology, DA has been employed to improve forecasts for more than three decades [Lorenc, 1986; Kalnay, 2003; Lahoz et al., 2010]. Common DA methods are the optimal interpolation (OI)/3-dimensional variational (3D-Var) method [Daley, 1991], the ensemble Kalman filter (EnKF) [Evensen, 2009] and 4-dimensional variational (4D-Var) method [Le Dimet and Talagrand, 1986]. Following efforts in DA for trace gase modelling [Austin, 1992; Fisher and Lary, 1995; Elbern and Schmidt, 1999], in recent years, DA has been increasingly applied to aerosol forecasts [Collins et al., 2001; Benedetti et al., 2009; Tombette et al., 2009; Pagowski et al., 2010; Li et al., 2013; Wang et al., 2013a].

The OI method was used in several studies for improving initial conditions of CTMs. For example, it was first developed to assimilate AOD (Aerosol Optical Depth) retrieved by satellite during the Indian Ocean Experiment (INDOEX) [Collins et al., 2001]. The OI method was also used in a simplified radiative transfer model by Huneeus and Boucher [2007] to assimilate synthetic observations of MODIS (Moderate Resolution Imaging Spectroradiometer) and CALIPSO (Cloud-Aerosol Lidar with Orthogonal Polarization). Adhikary et al. [2008]

assimilated monthly-mean AOD data from MODIS and AERONET using the OI method to produce three-dimensional distributions of AOD over Asia. Niu et al. [2008] improved dust storm forecast (dust concentrations) over China by assimilating satellite retrieval data and surface meteorological station data. Tombette et al. [2009] used the OI method over western Europe for assimilating PM_{10} (particulate matter with an aerodynamic diameter less than 10 μm) mass concentration observations from the BDQA (Base de Données de la Qualité de l'Air) network. The OI method was also employed in a study of inverse modelling of optical observations (lidar backscatter coefficients and AOD) by chemical DA [Kahnert, 2009]. Pagowski et al. [2010] used the OI over the United States of America for DA of $PM_{2.5}$ (particulate matter of an aerodynamic diameter lower than 2.5 μm) observations. Liu et al. [2011] developed a DA system using the OI method within the National Centers for Environmental Prediction (NCEP) for assimilating MODIS AOD retrieval products (at 550 nm wavelength) from both Terra and Aqua satellites and analysing aerosol mass concentrations. Huneeus et al. [2012] used the OI method to estimate the emission fluxes of a range of aerosol species at global scale by assimilating daily total and fine mode AOD at 550 nm from MODIS into a global aerosol model of intermediate complexity. The OI method was used by Schwartz et al. [2012] to individually or simultaneously assimilate AOD at 550 nm retrieved from MODIS sensors and surface $PM_{2.5}$ observations for the analysis of aerosol mass mixing ratios at each grid point. Recently, Wang et al. [2013a] used the OI within an Observing System Simulation Experiment (OSSE) to investigate the potential impact of future ground-based lidar networks on analysis and short-term forecasts of PM_{10} over Europe. They showed a potentially powerful impact of the future lidar networks for PM_{10} forecasts. Li et al. [2013] used the OI for multiple aerosol species and for prediction of $PM_{2.5}$ in the Los Angeles basin. The OI method was also employed into a mesoscale numerical weather prediction system GRAPES/CUACE_Dust to study dust aerosol assimilation in eastern Asian [Wang and Niu, 2013]. Jiang et al. [2013] developed a DA system in WRF-Chem model using the OI method to explore the impact of assimilating surface observations of PM_{10} over China.

The EnKF method was employed to simulate severe dust storm episodes occurring in March 2002 over China by assimilating surface dust concentration observations [Lin et al., 2008]. The EnKF method was used to assimilate lidar attenuated backscatter coefficients and depolarization ratios contained in the CALIPSO Level 1B dataset [Sekiyama et al., 2010]. Also, a global aerosol assimilation system was developed using the EnKF method for assimilating AOD and AAE (aerosol Ångström exponent) from the AERONET network and MODIS satellite [Schutgens et al., 2010a, b].

4D-Var was used to assimilate the lidar network Asian dust data [Sugimoto and Uno, 2009]. They showed that DA is effective for both improving the model results and estimating the emission in the dust source region. Benedetti et al. [2009] also used the 4D-Var method in the European Centre for Medium-Range Weather Forecasts (ECMWF), for the Global and regional Earth-system Monitoring using Satellite and *in situ* data (GEMS) project, in order to issue aerosol forecasts and reanalyses of aerosol fields using AOD data from satellite sensors.

In meteorology, OI has been surpassed by 4D-Var or the EnKF [Kalnay, 2003], but it is still a commonly used DA method in CTMs, as OI is simple to implement and is computationally cheaper than other DA methods [Wu et al., 2008]. By contrast, 4D-Var assimilates observations over a time window, which could yield better results [Benedetti and Fisher, 2007], when the model is reliable. However, it is more complex to implement because the adjoint of the model is required in the 4D-Var method [Benedetti et al., 2009; Sugimoto and Uno, 2009]. Denby

et al. [2008], Pagowski and Grell [2012] and Candiani et al. [2013] compared two different DA methods, the OI and the EnKF for aerosol forecasts. They reported that the EnKF delivers slightly better results than the OI, but the cost of implementation of the EnKF is higher than that of the OI, due to the high number of required model simulations. The OI is then employed in this paper to sequentially assimilate observations.

Several aerosol properties have been assimilated for aerosol forecasts, e.g. surface mass concentrations [Niu et al., 2008; Tombette et al., 2009; Pagowski et al., 2010; Li et al., 2013; Wang and Niu, 2013; Jiang et al., 2013], aerosol particle number size distributions [Viskari et al., 2012], AOD data from satellites or the AERONET network [Huneeus and Boucher, 2007; Adhikary et al., 2008; Benedetti et al., 2009; Schutgens et al., 2010a, b; Liu et al., 2011; Huneeus et al., 2012; Schwartz et al., 2012] and lidar backscatter coefficients [Huneeus and Boucher, 2007; Kahnert, 2009; Sekiyama et al., 2010]. Most studies showed the fast-fading DA impact on aerosol forecasting, especially in the early forecast hours [Tombette et al., 2009; Jiang et al., 2013]. Wang et al. [2013a] found that information on the vertical profile can extend the temporal influence of DA. However, *in situ* surface measurements and AOD data do not provide resolved information in the atmospheric column. Lidar backscatter coefficient profiles provide information on the aerosol vertical structure, but estimating the aerosol backscatter coefficient from only single wavelength lidar elastic signals through the Klett-Fernald method [Klett, 1985] using an apriori value of lidar ratio (extinction-to-backscatter ratio), brings in errors up to 30%. No assumptions are needed to calculate aerosol backscatter coefficient using the multi-wavelength aerosol lidar (e.g. Raman lidars), typically in nighttime conditions [Ansmann et al., 1992], but most operational lidar stations are equipped with a single wavelength lidar. Furthermore, a multi-wavelength aerosol lidar is more costly and mainly dedicated to scientific purpose than a single wavelength aerosol lidar and often performs at one visible light wavelength (e.g. 532 nm) which is not eye-safe (e.g. aviation near the city). Therefore, it is more realistic to put single wavelength aerosol lidar system for operational service. It is why Wang et al. [2013b] developed for the first time DA algorithms to directly assimilate normalised range corrected lidar signals (PR^2) at one wavelength (i.e. 355 nm).

This paper aims at investigating the usefulness of ground-based lidar network on analysis and short-term forecasts of aerosols based on a case study. The DA algorithm developed by Wang et al. [2013b] based on OI for assimilating PR^2 is employed. Important DA algorithm parameters are also studied, e.g. the correlation length in the background error covariance matrix, the altitudes at which DA is performed and the assimilation period length.

This paper is organised as follows. Section 4.2 describes the modelling system i.e. the CTM POLAIR3D, the OI method and the experiment design. Section 4.3 provides a description of the observations used. DA parameter tests are conducted in section 4.4. Results are shown and discussed in section 4.5. Our findings are summarised in section 4.6.

4.2 Modelling system

POLAIR3D [Sartelet et al., 2007] is the Eulerian chemistry transport model (CTM) of the air-quality platform POLYPHEMUS [Mallet et al., 2007] used to forecast atmospheric compositions such as ozone and PM concentrations (`http://cerea.enpc.fr/en/prevision.html`), available at `http://cerea.enpc.fr/polyphemus/`. The aerosol dynamic is modelled using the SIze-REsolved Aerosol Model (SIREAM-SuperSorgam), which is described in Debry

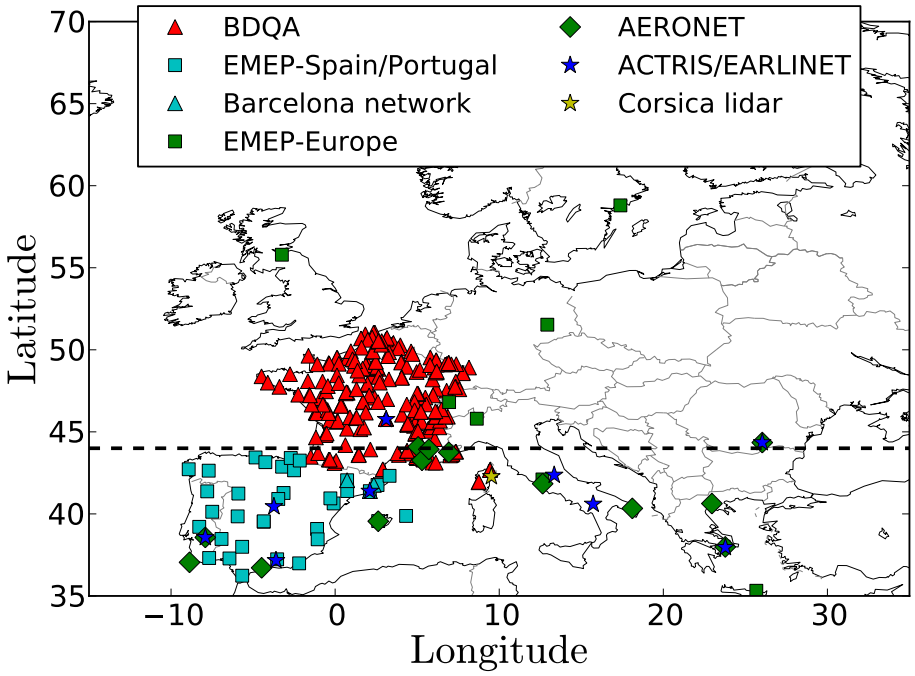

Figure 4.3: Map of the different measurement sites for the area of interest. The red triangles show the locations of French air quality network (BDQA). The cyan squares show the station locations of the EMEP-Spain/Portugal network. The cyan triangles show the locations of stations around Barcelona. The green squares show the locations of EMEP-Europe stations. The green diamonds show the locations of AERONET stations. The dark blue star markers show the locations of ACTRIS/EARLINET stations. The yellow star marker shows the location of the Corsica lidar station. The dashed line shows the latitude of 44° N which is used to split the French stations in section 4.5.1.

et al. [2007] and Kim et al. [2011a]. SIREAM-SuperSorgam includes 20 aerosol species: mineral dust, black carbon, ammonium, sulphate, nitrate, chloride, sodium, primary organics and 12 secondary organic species. It models coagulation and condensation/evaporation. Five bins logarithmically distributed over the size range 0.01 - 10 μm are used. The gas chemistry is solved with the chemical mechanism CB05 (Carbon Bond version 5) [Yarwood et al., 2005]. POLAIR3D/SIREAM has previously been used for DA [Tombette et al., 2009; Wang et al., 2013a, b].

The modelling domain covers western and part of eastern Europe ([15° W, 35° E] × [35° N, 70° N], see Fig. 4.3) with a horizontal resolution of $0.5° \times 0.5°$. In the simulation, 14 vertical levels are considered from the ground to an altitude of 12000 m above ground level (AGL). The heights of cell interfaces are 0, 30, 60, 100, 150, 200, 300, 500, 750, 1000, 1500, 2400, 3500, 6000 and 12000 m AGL. The time step of the simulation is 600 s. Meteorological inputs are interpolated from reanalysis provided every 3 hours by the European Centre for Medium-Range Weather Forecasts (ECMWF). Boundary conditions are climatological conditions obtained from averaging boundary conditions from MOZART4 (Model for OZone And

Related chemical Tracers version 4) [Emmons et al., 2010] over the years 2004-2008. Sea-salt emissions are assumed to be made of 39.33% of sodium, 55.025% of chloride and 7.68% of sulfate and modelled following Monahan et al. [1986]. Anthropogenic emissions of gases and aerosols are generated with the EMEP inventory for 2009. For example, the EMEP provides yearly emissions of $PM_{2.5}$ and coarse PM (PM with an aerodynamic diameter higher than 2.5 μm but lower than 10 μm). The $PM_{2.5}$ fraction is speciated into mineral dust, black carbon and primary organic aerosol. The coarse PM fraction is attributed to mineral dust. In the simulation, Saharan dust is only from boundary conditions.

The Optimal Interpolation (OI) approach for assimilating lidar signals was introduced by Wang et al. [2013b]. The analysed mass concentrations $\mathbf{x}_a$ is obtained from the equation

$$\mathbf{x}_a = \mathbf{x}_b + \mathbf{B}\mathbf{H}^{\mathrm{T}} \left(\mathbf{H}\mathbf{B}\mathbf{H}^{\mathrm{T}} + \mathbf{R}\right)^{-1} \left(\mathbf{y} - H[\mathbf{x}_b]\right), \tag{4.1}$$

where $\mathbf{x}_b$ is the model mass concentrations, $\mathbf{y}$ is the observation vector, H is the observation operator that simulates normalised PR^2 from the mass concentrations $\mathbf{x}_b$ through the module of PR^2 simulation developed in POLAIR3D [Wang et al., 2013b], $\mathbf{H}$ is the tangent linear operator of H, $\mathbf{B}$ and $\mathbf{R}$ are respectively the background and observation error covariance matrices. Wang et al. [2013b] provided two algorithms based on the OI method to compute the analysed state $\mathbf{x}_a$. One algorithm analyses PM_{10} concentrations. The other analyses $PM_{2.5}$ and $PM_{2.5-10}$ concentrations separately but simultaneously. Wang et al. [2013b] reported that the latter algorithm leads to better forecasts than the former, because the model often simulates $PM_{2.5}$ better than $PM_{2.5-10}$ and the background error variance of $PM_{2.5}$ and $PM_{2.5-10}$ are set separately in the latter algorithm. Therefore, we employ the latter algorithm in this paper. For the specification of the background and observation error covariance matrices, we refer to Wang et al. [2013b]. We set the background error of $PM_{2.5}$ and $PM_{2.5-10}$ to be 5 μg m^{-3} and 30 μg m^{-3} respectively in $\mathbf{B}$, since the model more accurately simulates $PM_{2.5}$ than $PM_{2.5-10}$ (see section 4.5). We take $\mathbf{R} = \sigma^2\mathbf{I}$ [Wang et al., 2013b], where σ is an observation standard deviation (depending on instrumental and representativeness error variances) and $\mathbf{I}$ is the identity matrix in the observation space. The value of σ is different in each DA test. It is determined by a χ^2 diagnosis, in which the scalar χ^2 at each DA step is defined by

$$\chi^2 = \left(\mathbf{y} - H[\mathbf{x}^b]\right)^{\mathrm{T}} \left(\mathbf{H}\mathbf{B}\mathbf{H}^{\mathrm{T}} + \mathbf{R}\right)^{-1} \left(\mathbf{y} - H[\mathbf{x}^b]\right). \tag{4.2}$$

On average, χ^2 should be equal to the number of observations [Ménard et al., 1999]. This χ^2 diagnosis could balance observation and background errors. After DA, the analysed concentrations are redistributed over the model variables following the initial (background) chemical and size distributions [Tombette et al., 2009; Wang et al., 2013a, b].

The simulation with DA, referred to as the DA experiment, consists of two periods: an assimilation period and a forecast period. During the assimilation period, at each time step, all available lidar data retrieved in the framework of the preChArMEx (Chemistry-Aerosol Mediterranean Experiment) / TRAQA (TRAnsport à longue distance et Qualité de l'Air) and ACTRIS/EARLINET campaign are assimilated. During the forecast period, DA is not performed. Hence, the model mass concentrations evolve depending on initial and boundary conditions, emissions and meteorology.

Table 4.1: The description of lidar systems used in this study. Reso. stands for resolution. ASL stands for above sea level. The letters "p" and "c" in the wavelengths stand for parallel and cross linear polarisation component respectively.

Lidar site	Site coordinates			Measurement information			
	Latitude	Longitude	Altitude ASL	Wavelengths	Raw range reso.	Raw time reso.	Zenith angle
	degree	degree	meter	nanometer	meter	second	degree
Athens	37.96	23.78	212	355, 532, 1064, 387, 607	7.5	100	0
Barcelona	41.389	2.112	115	355, 532, 1064, 387, 607	3.75	60	52
Bucharest	44.348	26.029	93	355, 532c, 532p, 1064, 387, 607	3.75	60	0
Clermont-Ferrand	45.761	3.111	420	355c, 355p, 387	7.5	60	0
Evora	38.568	-7.912	290	355, 532c, 532p, 1064, 387, 607	30	30	5
Granada	37.164	-3.605	680	355, 532c, 532p, 1064, 387, 607	7.5	60	0
L'Aquila	42.368	13.351	656	351, 382	30	300	0
Madrid	40.456	3.726	669	355, 532, 1064, 387, 607	7.5	60	0
Potenza	40.601	15.723	760	355, 532c, 532p, 1064, 387, 607	3.75	60	0
Corsica	42.280	9.520	50	355	15	50	15

4.3 Observations

In the following, we describe observations used in this study: lidar signals used for assimilation, and surface mass concentrations and AOD used for DA validation.

4.3.1 Lidar observations

An intensive measurement effort was performed by 9 ground-based lidar stations from the ACTRIS/EARLINET network [Bösenberg et al., 2003] in the Mediterranean basin and one station in Corsica in the framework of the preChArMEx/TRAQA and ACTRIS/EARLINET campaign in July 2012 during 72 hours. All stations were located on the northern side of the

Mediterranean. The goal of this campaign was to locate and track aerosols in the lower and mid troposphere in the Mediterranean region and help improving our forecast ability of CTMs using DA. It started on 09 July at 06:00 UTC following a dust alert for Saharan transport (see section 4.3.3). The ground-based lidar stations (blue and yellow star markers in Fig. 4.3) performed continuous measurements until 12 July at 06:00 UTC. The participant EARLINET stations include Athens, Barcelona, Bucharest, Evora, Granada, L'Aquila, Madrid, Potenza and Clermont-Ferrand. The ChArMEx station was situated at INRA (Institut National de la Recherche Agronomique), San Giuliano at about 3 km from the eastern coastline of Corsica (see Fig. 4.3).

Table 4.1 shows the site coordinates and raw data description of lidar systems used in this campaign. The vertical resolution of measurements ranges from 3.75 m to 30 m (depending on the lidar system). The temporal resolution of measurements ranges from 30 s to 300 s (depending on the lidar system). The raw data (except that of the Corsica station) were automatically treated by the Single Calculus Chain (SCC) developed by the lidar network EARLINET (`http://www.earlinetasos.org`) [D'Amico et al., 2012] to generate integrated profiles of range corrected lidar signals (PR^2) in near real time in cloud-free conditions. The SCC is an automatic tool to get different types of aerosol property products (e.g. PR^2, aerosol extinction and backscatter coefficients) from raw lidar data. In this work, only one type (PR^2) of the available products is used. All observations are integrated with a time resolution of one hour, the DA time step in this study, and normalised at an altitude in the range of the molecular zone. The altitude of normalisation was diagnosed as explained in Wang et al. [2013b]. In this paper, it is taken at 4750 m AGL, which corresponds to the model level of 3500 - 6000 km AGL (see section 4.2). Figure 4.4 shows normalised PR^2 at Athens, Clermont-Ferrand, Evora, Granada, L'Aquila and Potenza lidar stations. Those of the other stations are shown later in Fig. 4.5.

4.3.2 Observations for validation

We employ two independent data types for DA validation: surface mass concentration measurements (in terms of $PM_{2.5}$ and PM_{10}) and AOD data.

The surface mass concentration measurements are from the BDQA (Base de Données sur la Qualité de l'Air, the French national database for air quality which covers France) network, the Barcelona network (3 stations), the EMEP-Spain/Portugal network, and the EMEP-Europe database (see Fig. 4.3). The French and Barcelona networks (triangles in Fig. 4.3) provide hourly averaged mass concentration measurements of $PM_{2.5}$ and PM_{10}. The EMEP-Spain/Portugal and EMEP-Europe networks (squares in Fig. 4.3) provide daily averaged mass concentration measurements of PM_{10}. Table 4.2 shows the number of stations in the BDQA, Barcelona, EMEP-Europe and EMEP-Spain/Portugal networks, which provide PM_{10} or $PM_{2.5}$ measurements in July 2012. The BDQA network provides most measurements with 240 stations for PM_{10} and 70 stations for $PM_{2.5}$.

The hourly AOD data at 355 nm are derived by Level 2.0 (cloud-screened and quality-assured) AOD data at 340 and 380 nm retrieved from AERONET (AErosol RObotic NETwork, `http://aeronet.gsfc.nasa.gov/`) following the Ångström law. The procedure was described by Wang et al. [2013b]. The locations of AERONET stations considered (e.g. stations are close to the lidar network) are shown as green diamonds in Fig. 4.3.

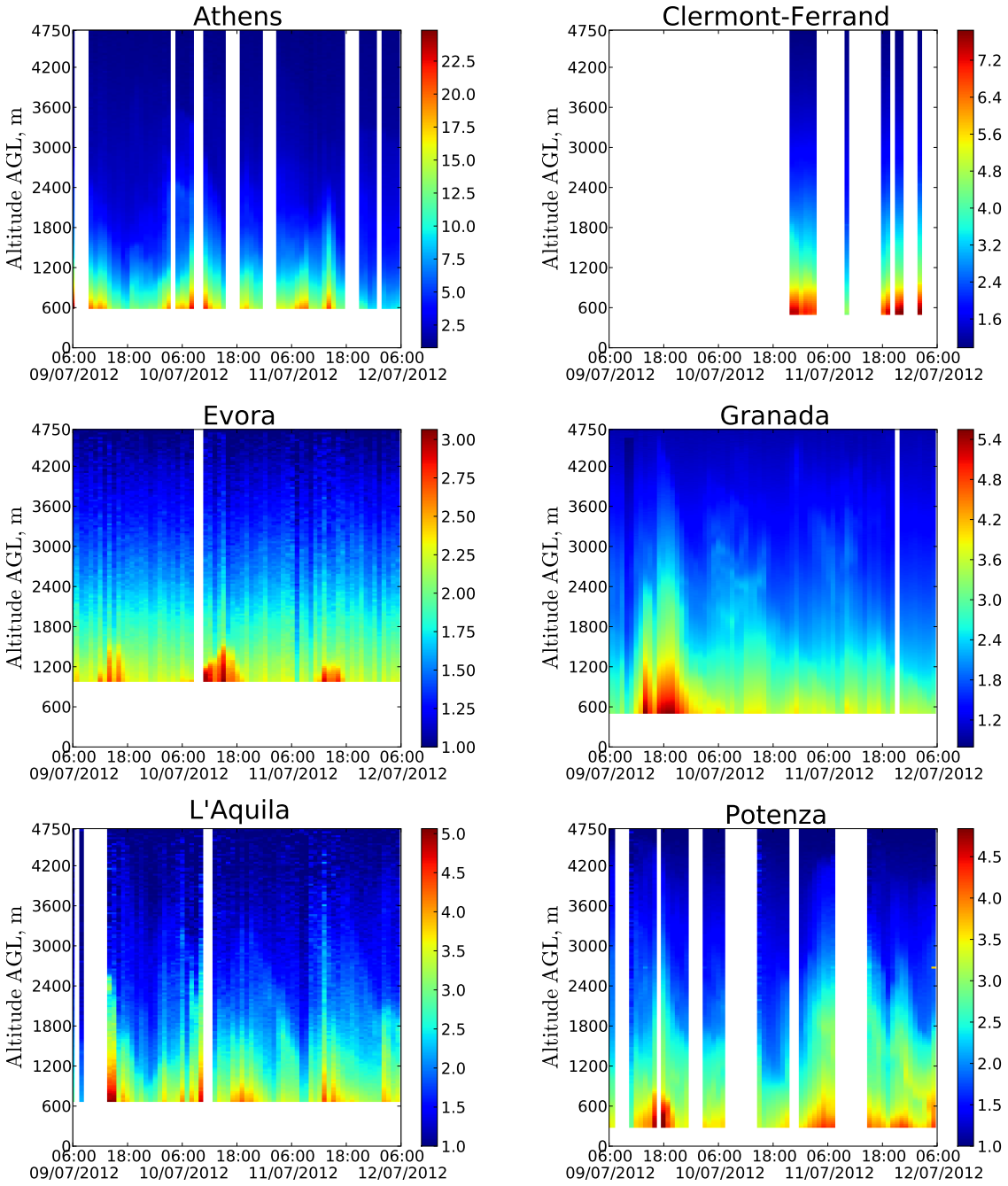

Figure 4.4: Normalised range corrected lidar signals (PR^2) from 06:00 UTC 09 July to 06:00 UTC 12 July at Athens, Clermont-Ferrand, Evora, Granada, L'Aquila and Potenza lidar stations. White columns mean that there is no available lidar data, mainly due to cloud presence.

4.3.3 Case study

The Mediterranean basin is the receptacle of aerosols from different origins, e.g. natural dust emissions from the Sahara [Moulin et al., 1998; Hamonou et al., 1999], anthropogenic emissions from the highly populated coastal areas, marine aerosols and wild fires. Additionally,

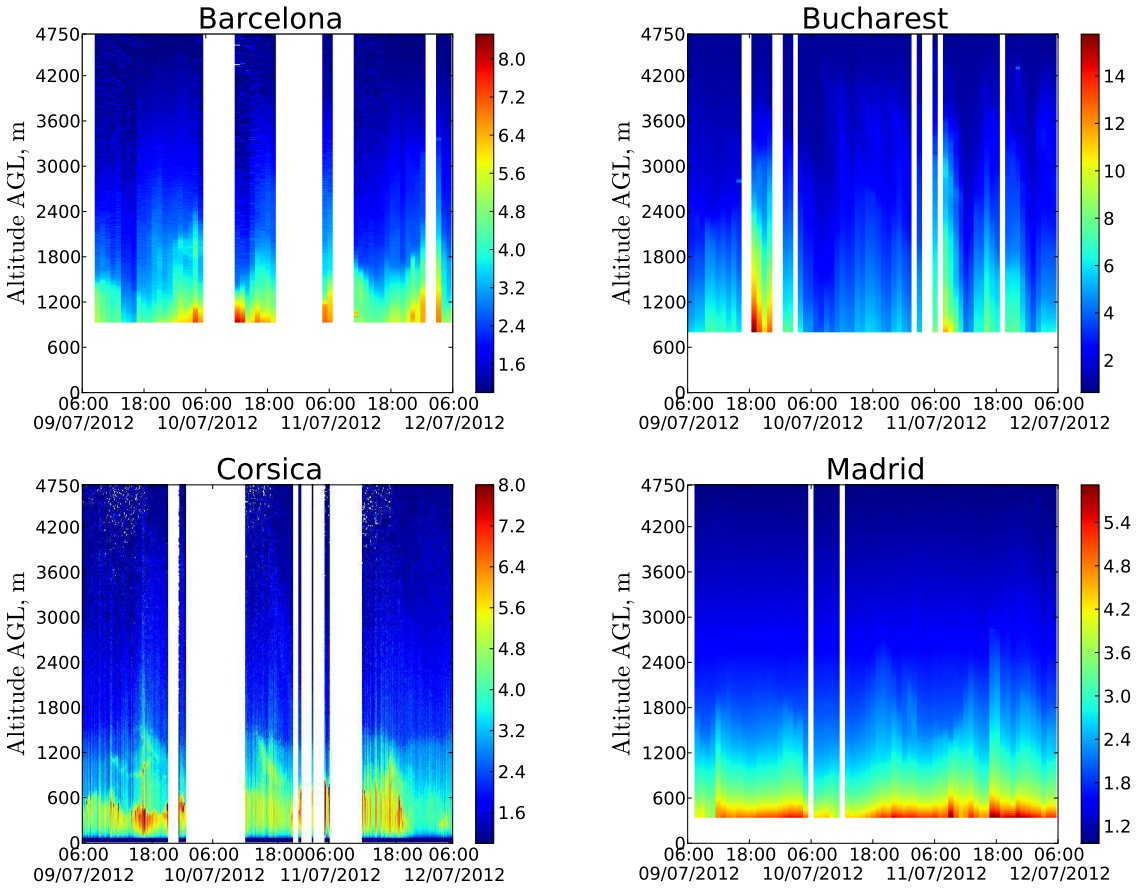

Figure 4.5: Normalised range corrected lidar signals (PR^2) from 06:00 UTC 09 July to 06:00 UTC 12 July at Barcelona, Bucharest, Corsica and Madrid lidar stations. White columns mean that there is no available lidar data, mainly due to cloud presence.

Table 4.2: The number of stations reporting $PM_{2.5}$ or PM_{10} in different networks.

Network name	Number of stations	
	PM_{10}	$PM_{2.5}$
BDQA	240	70
Barcelona	3	3
EMEP-Europe	7	0
EMEP-Spain/Portugal	22	0

these sources can potentially react with biogenic emissions of a very specific vegetation type [Sartelet et al., 2012]. Aerosol load is often high over the Mediterranean region [Putaud et al., 2010; Nabat et al., 2013]. Therefore, it is a good place to test the usefulness of lidar DA to improve the forecast of CTMs.

Figure 4.6 shows wind fields at about 2 km AGL interpolated from ECMWF data for 09 July

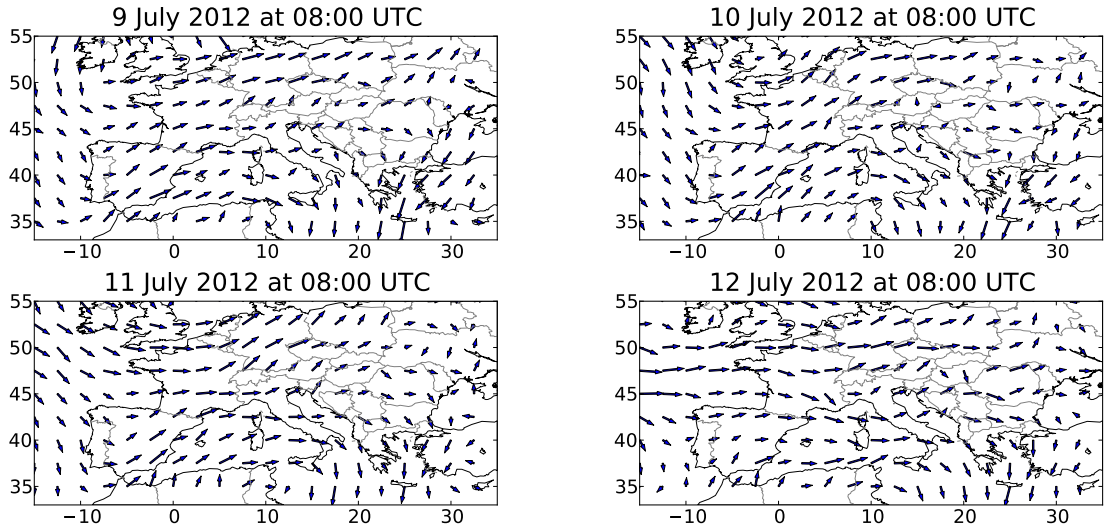

Figure 4.6: Wind fields (arrows) at about 2 km AGL at 08:00 UTC on 09, 10, 11 and 12 July 2012. These data are interpolated from ECMWF fields.

2012 at 08:00 UTC, 10 July 2012 at 08:00 UTC, 11 July 2012 at 08:00 UTC, and 12 July 2012 at 08:00 UTC. The west or north wind transported the pollution over the Mediterranean during the lidar campaign. Figure 4.2 shows the AODs at 550 nm retrieved from MSG (Meteosat Second Generation)/SEVIRI satellites 15-min image averaged from all available images between 04:00 and 18:00 UTC on 09, 10, 11 and 12 July 2012, that correspond to the lidar measurement period. The high AODs observed mainly in the southern part of the Mediterranean were mostly due to Saharan dust. But penetration of the Saharan dust plume over the continent of Europe was limited, except in the south of Italy and the south and east of Spain. For example, the PM_{10} records at the ChArMEx station of Ersa at 533 m in altitude (in the north of Cape Corsica) and at the regional background air quality station of Venaco at 655 m in altitude (in the center of Corsica) report only a small increase (about 5 $\mu g\ m^{-3}$) on 08 and 09 July 2012, that indicates small influence of the Saharan dust in surface stations in Corsica. Additionally, the chemical analysis of filters taken from the surface at Ersa during 12 hours until 12:00 UTC on 11 July 2012 did not detect Saharan dust [Nicolas, 2013] and the ChArMEx aerosol lidar in Corsica does not show evidence of a dust layer (see Fig. 4.5).

Figure 4.7 shows 48-hour backward trajectories (dashed lines) of air masses arriving at 2 km AGL and 72-hour forward trajectories (solid lines) of air masses departing at 2 km AGL at 10 lidar stations. These data are outputs of the Hybrid Single Particle Lagrangian Integrated Trajectory (HYSPLIT) Model (`http://ready.arl.noaa.gov/HYSPLIT.php`) [Draxler and Rolph, 2014; Rolph, 2014] using the Global Data Assimilation System (GDAS) meteorological data with a resolution of $1° \times 1°$. These backward (resp. forward) trajectories end (resp. start) respectively at 06:00 UTC on 09 July 2012, 10 July 2012, 11 July 2012 and 12 July 2012. They indicate that the aerosol represented by the assimilation of lidar signals measured in Spain, Portugal and France was transported to the North-East or East. The aerosol measured by lidars at other stations (i.e. Athens, L'Aquila, Potenza, Bucharest) was transported to the South or East. That matches with wind fields shown in Fig. 4.6. In addition, there is almost no rainfall along trajectories (not shown in this paper).

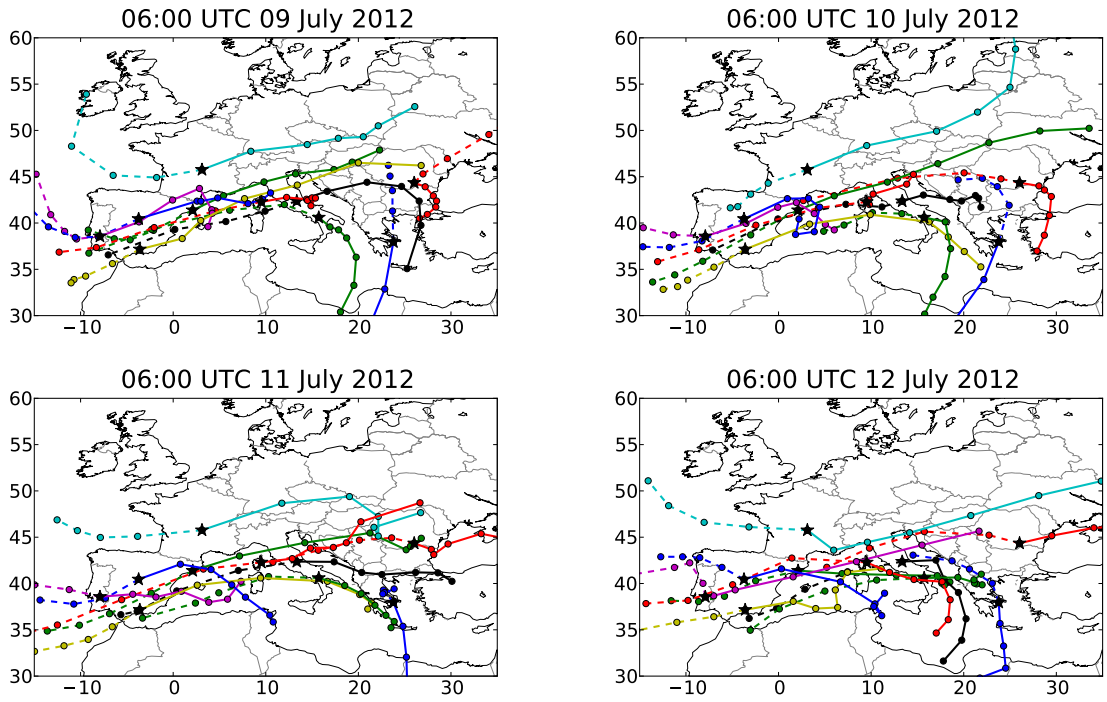

Figure 4.7: Backward (resp. forward) trajectories of 48 hours (resp. 72 hours) at lidar site locations (black stars) at 2 km AGL ending (resp. starting) at 06:00 UTC 09 July 2012, 06:00 UTC 10 July 2012, 06:00 UTC 11 July 2012 and 06:00 UTC 12 July 2012. Data are from the HYSPLIT Model. Dashed (resp. solid) lines show backward (resp. forward) trajectories, where the 12-hour spacing is given by the discs. The backward trajectories pertain to the source attribution problem of the lidar measurements whereas the forward trajectories show the prepagation of the DA updates around lidar locations.

4.4 Assimilation parameter tests

In this section, we perform sensitivity tests, first on the DA period length, and then on the horizontal correlation length used in the background error covariance matrix and on the assimilation altitude range.

4.4.1 Assimilation period length

Wang et al. [2013a] compared the aerosol forecasts performed after different assimilation periods varying from 6 hours to 3 days, during which surface mass concentration observations were assimilated. They suggested that an assimilation period of 12 hours is necessary to improve the aerosol forecast. In this work, two DA period lengths, 12 hours and 24 hours, are employed to study the impact of the assimilation period length on aerosol forecasting. The results are detailed in this section.

The 72-hour period of continuous lidar measurements from 06:00 UTC 09 July to 06:00 UTC 12 July 2012 is split into three experiments of 24 hours each. For the assimilation period of 12 (resp. 24) hours, for each of the three experiments, the lidar data are assimilated during

12 (resp. 24) hours, and 60-hour forecasts are issued at 06:00 UTC on 10, 11 and 12 July, respectively. All DA experiments use the same parameters (e.g. the horizontal correlation length is 100 km and the assimilation altitude range is from 1.0 to 3.5 km AGL) except the assimilation period length.

Figure 4.8 shows the scores, the RMSE (root mean square error) and the (Pearson) correlation calculated against the ground observations over France (the BDQA network) for PM_{10} and $PM_{2.5}$, since the BDQA network provides most measurements of PM_{10} and $PM_{2.5}$. We refer to appendix A for the definition of statistical indicators. Overall, the simulation with lidar DA leads to better scores than the simulation without DA during the forecast period for a period of less than 36 hours. The improvements of DA are significant for PM_{10}. The RMSE (resp. correlation) of PM_{10} averaged over the early 36 hours of forecast is 9.4 $\mu g\ m^{-3}$ (resp. 39%) without DA, 8.4 $\mu g\ m^{-3}$ (resp. 49%) with 12-hour DA and 8.4 $\mu g\ m^{-3}$ (resp. 50%) with 24-hour DA. For $PM_{2.5}$, the improvements of DA are not significant except for the correlation. The RMSE (resp. correlation) of $PM_{2.5}$ averaged over the early 36 hours of forecast is 4.5 $\mu g\ m^{-3}$ (resp. 37%) without DA and 4.4 $\mu g\ m^{-3}$ (resp. 43%) with either 12-hour DA or with 24-hour DA. Comparing DA with 24 hours of analysis (DA test "24h DA") to 12 hours of analysis (DA test "12h DA"), the simulation with 24 hours of analysis delivers slightly better scores during the forecast period (to the right of the black lines). However, the difference between DA test "24h DA" and "12h DA" after 6 hours forecasts is barely significant.

Since the measurement performance of the lidar campaign in July 2012 lasted only 72 hours and the simulation with 24 hours of analysis do not lead to much better scores than the one with 12 hours of analysis during the forecast period, we chose to perform DA experiments with an assimilation period of 12 hours in the following to obtain more number of DA experiments and statistically evaluate the results of DA. In this case, the 72-hour period of continuous lidar measurements is split into six 12-hour assimilation periods (24-hour DA be chosen, the 72-hour period of continuous lidar measurements would be split into only three disjoint 24-hour assimilation periods). Figure 4.9 shows the schematic representation of these six DA experiments. Each DA experiment includes a 12-hour assimilation period (gray bars) and a 60-hour forecast period (white bars). All DA experiments begin either at 06:00 UTC or at 18:00 UTC on 09, 10 or 11 July 2012. Figure 4.10 shows the schematic representation of the lidar measurement segments assimilated in six DA experiments. At each DA step, all available lidar data retrieved from 10 lidar stations are assimilated.

4.4.2 Assimilation correlation length

In Tab. 4.3, the different configurations of DA are summarised, where the horizontal correlation length L_h (e.g. 50, 100 and 200 km) and the assimilation altitude range are listed. The scores (i.e. RMSE and correlation) of the different configurations of DA for PM_{10} and $PM_{2.5}$ are shown in Fig. 4.11. These scores are calculated against the observations over the French air quality network (BDQA). In this section, the impact of the horizontal correlation length L_h of the error covariance matrix $\mathbf{B}$ is studied, since L_h is an important parameter that determines to what horizontal extent the fields are corrected by DA.

At the beginning of the assimilation period, all simulations have the same scores, since the simulations without DA and with DA use the same initial conditions. The improvement at stations over France appears 6 hours after the start of the DA experiment. This delay is due to the fact that the only lidar stations in France used for this study are in Clermont-Ferrand and

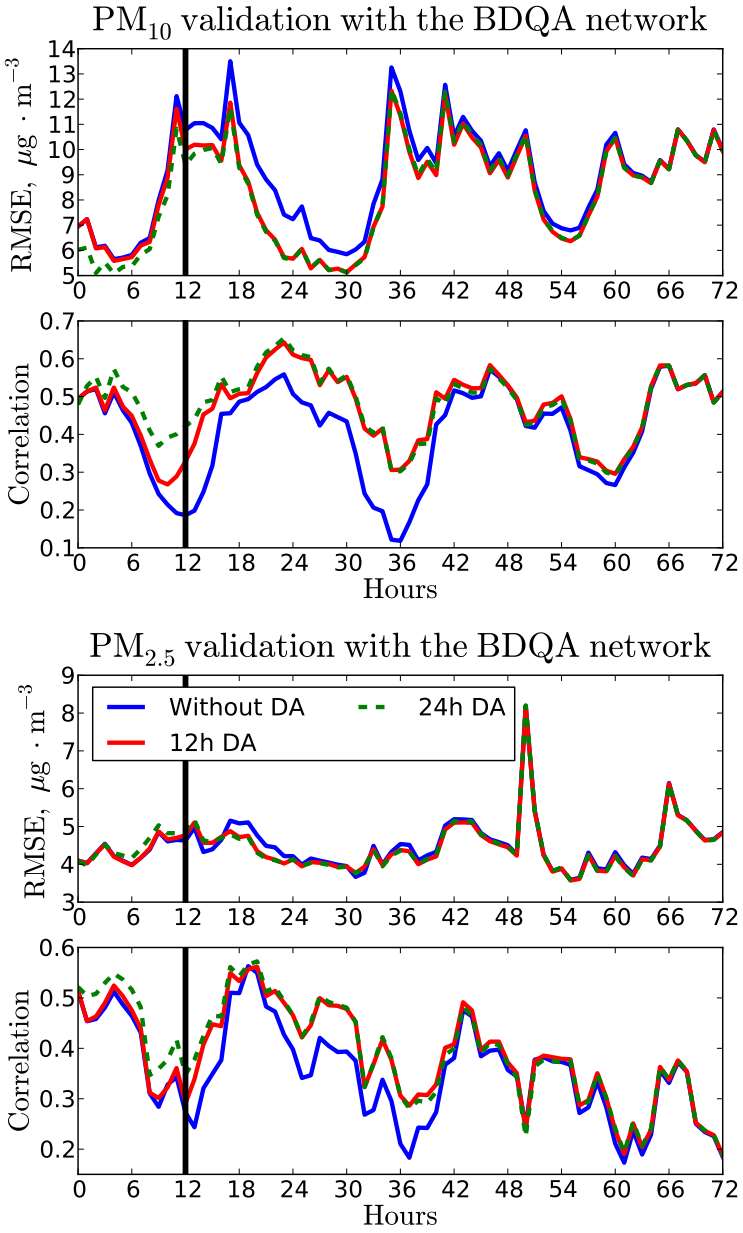

Figure 4.8: The top (resp. bottom) panel shows the time evolution of the RMSE (μg m^{-3}) and the correlation of PM_{10} (resp. $PM_{2.5}$) averaged over the different DA experiments for three experiment types: one without DA, one with 12 hours of DA and one with 24 hours of DA. The scores are computed for the BDQA network (hourly data). The vertical black lines denote the separation between the assimilation period (to the left of the black lines) and the forecast (to the right of the black lines). "12 DA" (resp. "24 DA") stands for DA with 12 (resp. 24) hours of analysis. The forecasts of "12 DA" and "24 DA" start at the same moment. The scores in the early 12 analysis hours of "24 DA" are not shown.

in Corsica. The station in Clermont-Ferrand provided too few observations due to bad weather during the campaign (see Fig. 4.10), and the improvement in aerosol mass concentrations due

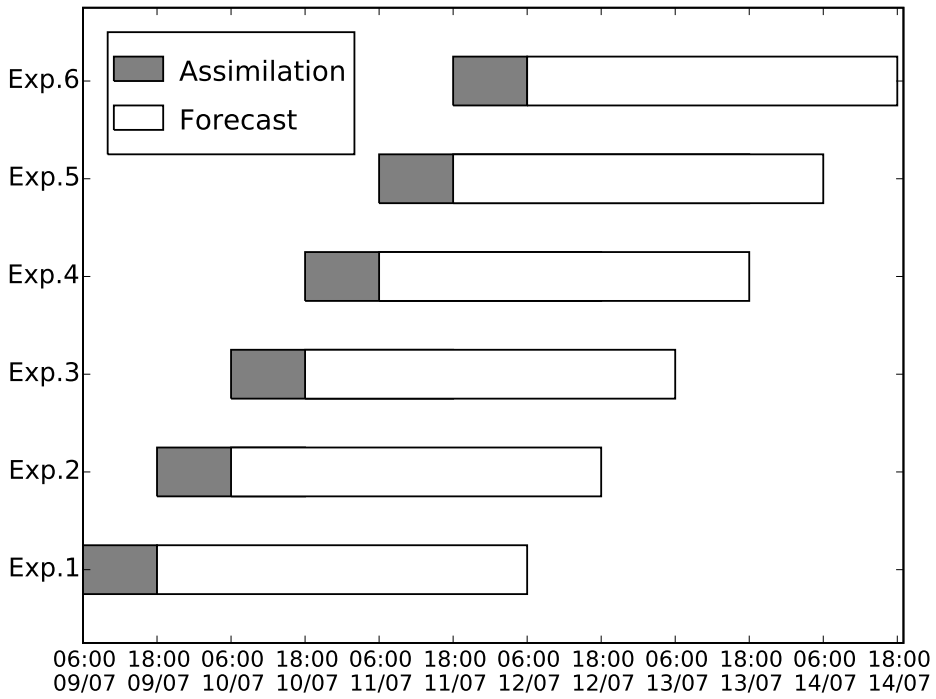

Figure 4.9: Schematic representation of six DA experiments with a 12-hour assimilation period (gray colour) and a 60-hour forecast period (white colour). Exp. stands for DA experiment.

Table 4.3: DA tests with different configurations for the evaluation of the impact of the assimilation parameters on the forecasts. L_h is the horizontal correlation length used in the Balgovind approach [Balgovind et al., 1983] to define the error covariance matrix $\mathbf{B}$.

Simulation name	L_h in $\mathbf{B}$	Assimilation altitude range
DA L_h = 50 km	50 km	1.0 - 3.5 km AGL
DA L_h = 100 km	100 km	1.0 - 3.5 km AGL
DA L_h = 200 km	200 km	1.0 - 3.5 km AGL
DA 0.75-3.5 km	100 km	0.75 - 3.5 km AGL
DA 1.5-3.5 km	100 km	1.5 - 3.5 km AGL

to DA originates from the zone out of continental France (see Figures 4.6 and 4.7). It is also because the assimilation altitude range is taken higher than 1.0 km AGL. The analysed mass concentrations spend time to arrive at the ground level. We find that the correlation length $L_h = 200$ km (yellow lines in Fig. 4.11) is too long, decreasing slightly the correlation coefficient for both PM_{10} and $PM_{2.5}$ at French stations during the assimilation period (to the left of the black lines in Fig. 4.11).

During the forecast period (to the right of the black lines in Fig. 4.11), the possible impact

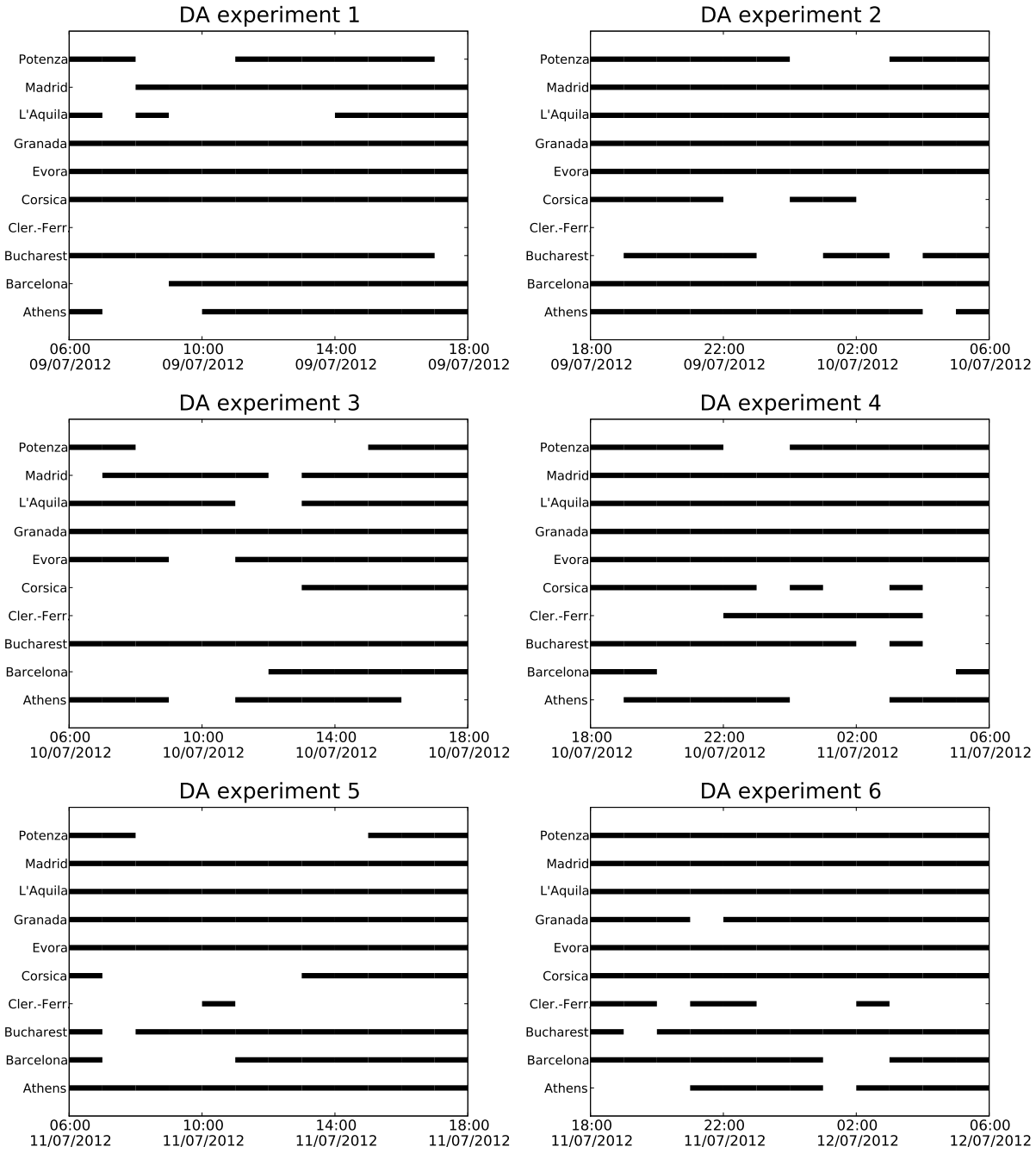

Figure 4.10: Schematic representation of the lidar measurement segments assimilated (black segments) during the assimilation period for six DA experiment. Cler.-Ferr. stands for Clermont-Ferrand.

of the assimilation of lidar signals is longer than 36 hours for all DA tests. Notice that the temporal impact of assimilating surface mass concentrations was estimated to be between 6 and 12 hours [Tombette et al., 2009; Jiang et al., 2013]. Comparing the DA tests with $L_h = 50$ km (green lines in Fig. 4.11), $L_h = 100$ km (red lines in Fig. 4.11) and $L_h = 200$ km (yellow

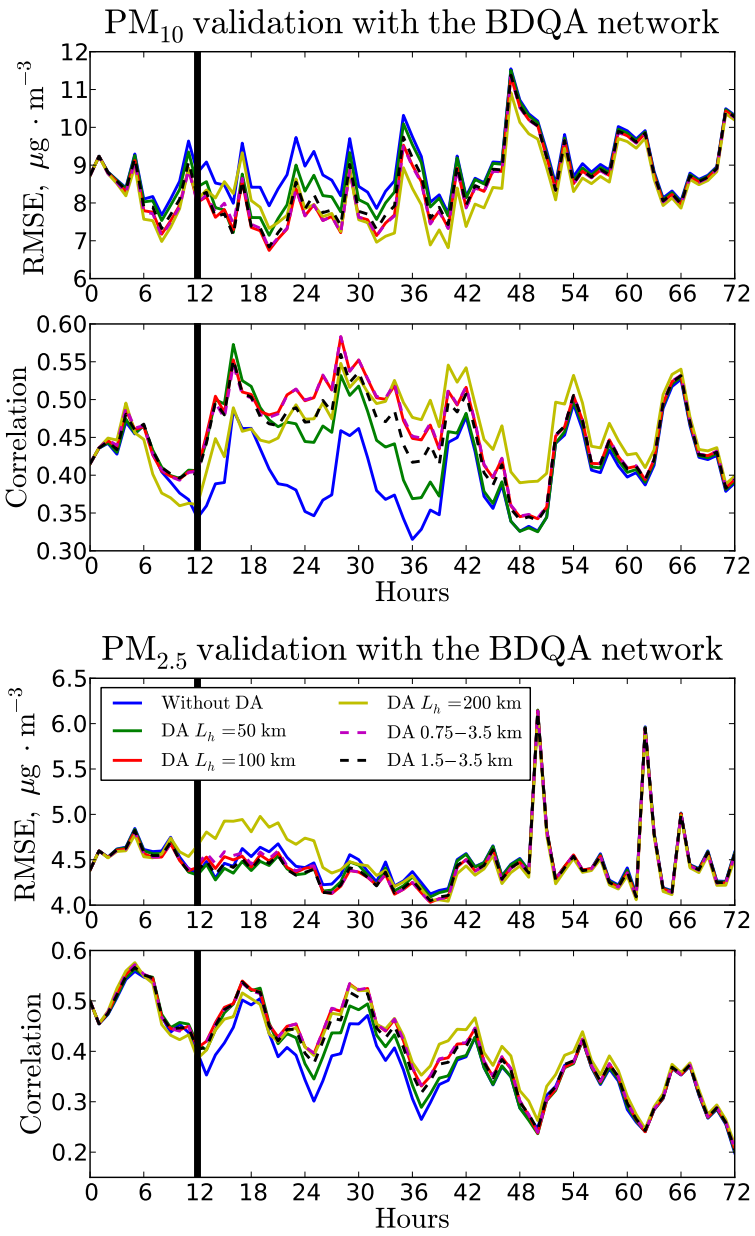

Figure 4.11: The top (resp. bottom) panel shows the time evolution of the RMSE (μg m^{-3}) and the correlation of PM_{10} (resp. $PM_{2.5}$) averaged for each of the six different experiments. The scores are computed for the BDQA network (hourly data). The vertical black lines denote the separation between the 12-hour assimilation period (to the left of the black lines) and the 60-hour forecast period (to the right of the black lines). The simulations "DA L_h = 50 km", "DA L_h = 100 km" and "DA L_h = 200 km" correspond to an assimilation altitude range from 1.0 to 3.5 km. The simulations "DA 0.75-3.5 km" and "DA 1.5-3.5 km" correspond to $L_h = 100$ km.

lines in Fig. 4.11) shows that using $L_h = 100$ km leads to better forecasts than using $L_h = 50$ km or $L_h = 200$ km in the first forecast day. In addition, using $L_h = 200$ km (yellow lines in Fig. 4.11) results in higher RMSE than the simulation without DA for $PM_{2.5}$ in the first forecast

day. This is because the analysed zone in the model is set to be isotropic (a horizontal disc, the centre of the disc being the measurement station, i.e. the lidar site) whereas the analysed zone should be horizontally anisotropic, which depends on the wind direction and the aerosol spatial distribution (e.g. aerosol origins). Using $L_h = 200$ km defines the isotropic analysed zone to be too large, which decreases the correlation coefficient. However, in the second forecast day, using $L_h = 200$ km leads to much better scores than using $L_h = 50$ km or $L_h = 100$ km for both PM_{10} and $PM_{2.5}$. Moreover, the beneficial impact of the assimilation with $L_h = 200$ km lasts longer than 48 hours. It is because using $L_h = 200$ km leads to higher corrections around the lidar site due to the use of the Balgovind approach [Balgovind et al., 1983] (the closer to lidar site the grid point is, the higher the correlation is). The corrections due to the higher correlation around lidar sites (far away from France) are more accurate and impact France later.

4.4.3 Assimilation altitude range

As the normalisation of lidar range corrected signals is done at high altitude, the lower the altitude is, the higher the error in the simulated lidar signal is. It is mostly because the integration of simulated extinction coefficients from the considered altitude to the normalisation altitude leads to accumulation of the error of simulated lidar signals at high altitude, especially in the case where high-altitude aerosol layers are not well modelled [Wang et al., 2013b]. That influences the improvement of lidar DA at lower altitudes. Furthermore, the numerical computations of the lidar operator H and its tangent lidar operator $\mathbf{H}$ (see Eq. (4.1)) are very costly. The larger the assimilation altitude range is, the more costly the numerical computation is. Hence, we investigate the impact of assimilation altitude ranges on aerosol forecasting in this section.

We employ three DA tests (0.75-3.5 km AGL, 1.5-3.5 km AGL and a reference case 1.0-3.5 km AGL in Fig. 4.11). As shown in Fig. 4.11, assimilating lidar signals from 0.75 to 3.5 km AGL (magenta lines) delivers similar scores (with respect to hourly data of BDQA) as assimilating from 1.0 to 3.5 km AGL (a reference case, red lines). A possible explanation is that we set high observation variances (sum of instrumental and representativeness variances, from the χ^2 diagnosis) due to considering the model level of 0.75-1.0 km AGL in DA. Consequently, its assimilation leads to limited improvements. Another explanation is that the scores in Fig. 4.11 are computed using the observations from the BDQA network where most improvements are from assimilation of lidar signals in Spain or Portugal (see Figures 4.6 and 4.7). However, of the lidar stations in Spain only Madrid and Granada provided data for DA of the model level of 0.75-1.0 km AGL (see Figures 4.4 and 4.5). In addition, assimilating lidar signals from 1.0 to 3.5 km AGL (magenta lines) leads to slightly better scores than from 1.5 to 3.5 km AGL (black lines).

4.5 Results and discussions

The US Environmental Protection Agency (EPA) has issued minimal guidance on PM model performance evaluation measures, goals, and criteria. Boylan and Russell [2006] suggested using the mean fractional bias (MFB, %) and the mean fractional error (MFE, %), because they bound the maximum bias and error (see appendix A). We evaluate the simulation without DA using the hourly observations from the French BDQA network with these criteria. For PM_{10}

(resp. $PM_{2.5}$), the MFB and MFE averaged over all six experiments are respectively -29% and 46% (resp. 6% and 43%). Thus, we find that the model simulates $PM_{2.5}$ better than PM_{10}. It is because road resuspension of PM is not considered neither in the model nor in input data (e.g. boundary conditions). As a consequence, we have set lower standard deviation for $PM_{2.5}$ (i.e. 5 $\mu g\ m^{-3}$) than for $PM_{2.5-10}$ (i.e. 30 $\mu g\ m^{-3}$) in the background error covariance matrix $\mathbf{B}$ (see Eq. (4.1)).

As discussed in section 4.4, the DA test "DA L_h = 100 km", which assimilates lidar signals retrieved from the lidar campaign from 1.0 to 3.5 km AGL during 12 hours with $L_h = 100$ km and performs 60-hour forecasts, delivers the best scores during the forecast period. Therefore, in the following, we consider the DA test "DA L_h = 100 km" ("Lidar DA" hereafter). Since most improvements are in the early 36 hours of forecast, we compute the scores for this period hereafter, instead of for the whole forecast period (i.e. 60 hours).

4.5.1 Validation with the BDQA network

For PM_{10}, the averaged RMSE (resp. correlation) over the early 36 hours of forecast is 8.8 $\mu g\ m^{-3}$ (resp. 40%) without DA and 8.0 $\mu g\ m^{-3}$ (resp. 49%) with DA. For $PM_{2.5}$, the averaged RMSE (resp. correlation) over the early 36 hours of forecast is 4.4 $\mu g\ m^{-3}$ (resp. 39%) without DA and 4.3 $\mu g\ m^{-3}$ (resp. 44%) with DA. Notice that DA improves PM_{10} more efficiently than $PM_{2.5}$. Therefore, DA would be very useful to reduce the uncertainties in the simulation due to road resuspension of coarse PM. However, these improvements are not very significant for $PM_{2.5}$. As should be expected, it is mostly because the improvements are limited at the stations far away from the lidar network, e.g. the stations in the north of France. When all the BDQA stations are used to calculate the scores, the improvements of DA are faded out.

Against the observations at French stations on the southern side of 44° N (dashed line in Fig. 4.3), the averaged RMSE (resp. MFB and MFE) of PM_{10} over the early 36 hours of forecast is 16.4 $\mu g\ m^{-3}$ (resp. -53% and 30%) without DA and 13.7 $\mu g\ m^{-3}$ (resp. -26% and 46%) with DA. The improvements are significant. For $PM_{2.5}$, the averaged RMSE (resp. MFB and MFE) over the early 36 hours of forecast is 7.1 $\mu g\ m^{-3}$ (resp. -20% and 47%) without DA and 6.5 $\mu g\ m^{-3}$ (resp. -6% and 44%) with DA.

Moreover, we compare simulations with DA in the daytime (DA is performed from 06:00 to 18:00 UTC) to simulations with DA in the nighttime (DA is performed from 18:00 to 06:00 UTC). We find that they lead to similar scores (results not shown in this paper).

4.5.2 Validation with the Barcelona network

Figure 4.12 shows the time evolution of the RMSE averaged over all six experiments without and with lidar DA for PM_{10} and $PM_{2.5}$. The RMSEs are computed at 3 surface stations around the Barcelona lidar station (cyan triangles in Fig. 4.3). We find that the impact of the assimilation of lidar signals is longer than 48 hours in the forecast period for both PM_{10} and $PM_{2.5}$. The averaged RMSE of PM_{10} over the early 36 hours of forecast is 8.9 $\mu g\ m^{-3}$ without DA and 7.0 $\mu g\ m^{-3}$ with DA. The averaged RMSE of $PM_{2.5}$ over the early 36 hours of forecast is 6.0 $\mu g\ m^{-3}$ without DA and 4.7 $\mu g\ m^{-3}$ with DA. We find that the aerosol error reduction around Barcelona is higher than the one over France (estimated using the BDQA network). That is because these surface stations are close to the Barcelona ground-based lidar station. They are sensitive to valid the improvements from assimilating lidar signals retrieved from the Barcelona

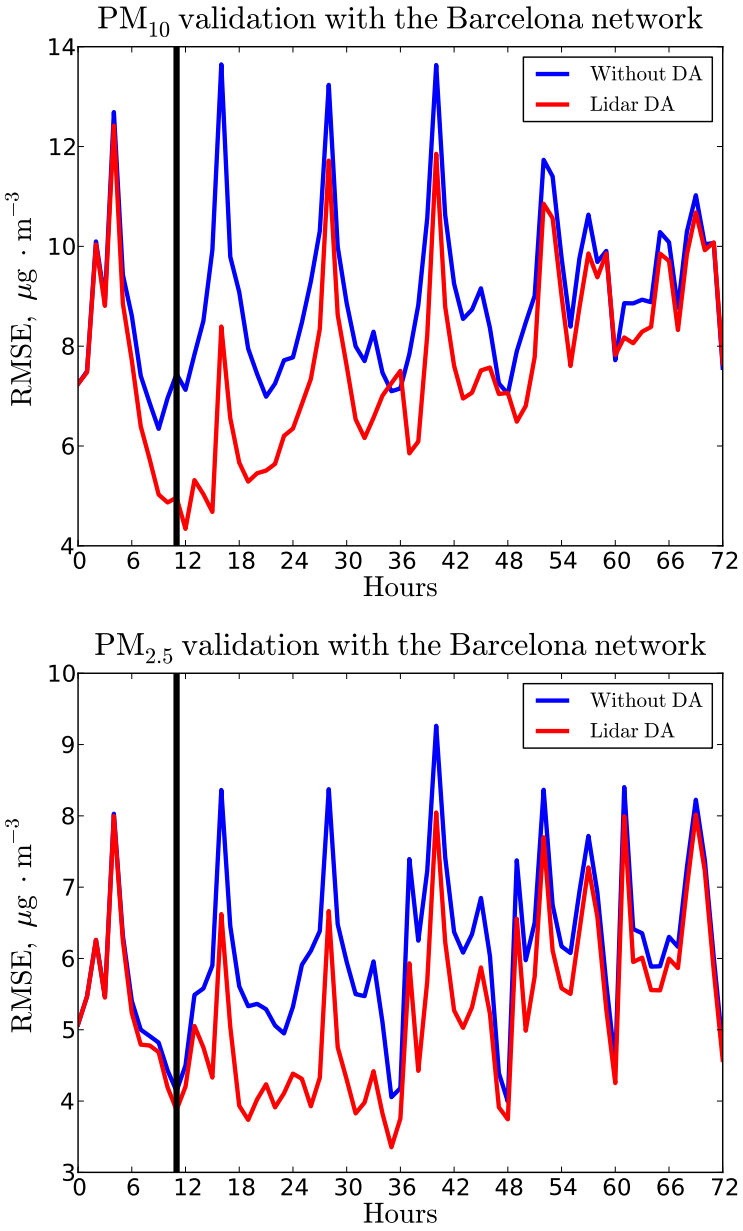

Figure 4.12: The top (resp. bottom) panel shows the time evolution of the RMSE (μg m^{-3}) of PM_{10} (resp. $PM_{2.5}$) averaged over the different experiments without and with DA (L_h = 100 km and altitude range 1.0-3.5 km). For the six successive experiments, the time origin corresponds respectively to 06 UTC on 9 July, 18 UTC on 9 July, 06 UTC on 10 July, 18 UTC on 10 July, 06 UTC on 11 July and 18 UTC on 11 July. The scores are computed for three stations around Barcelona (hourly data, see Fig. 4.3). The vertical black lines denote the separation between the 12-hour assimilation period (to the left of the black lines) and the 60-hour forecast period (to the right of the black lines).

lidar station. Additionally, they are also sensitive to the pollution contributions originating from the Evora and Madrid lidar sites due to wind fields, because Barcelona is on the leeward side

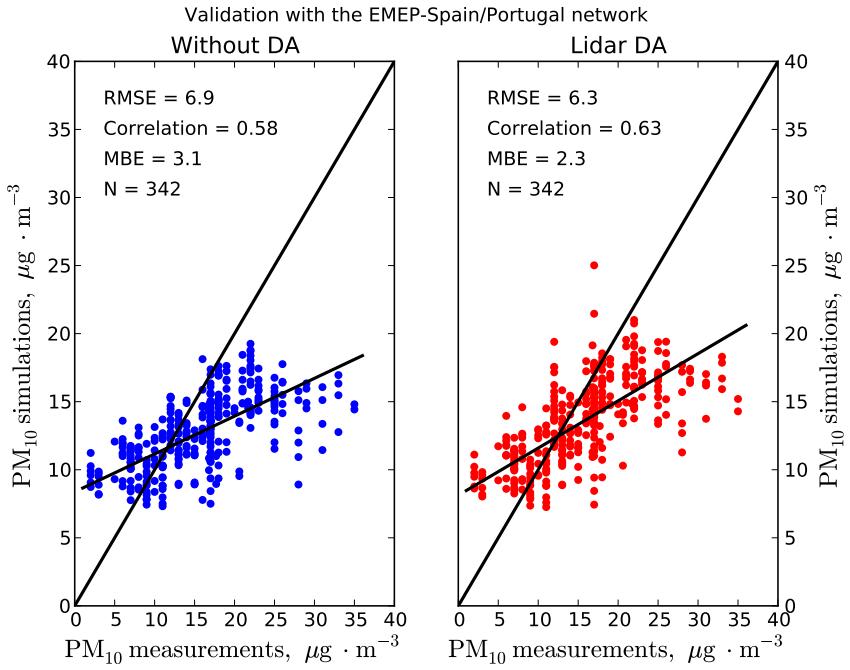

Figure 4.13: Scatter plots of simulated PM_{10} mass concentrations without DA (left panel) and with DA (right panel) against daily PM_{10} daily measurements at different EMEP-Spain/Portugal stations.

of these lidar sites during the lidar campaign in July 2012 (see Fig. 4.7). Therefore, the improvements due to lidar DA associated with a long-ranged transport pollution from Evora and Madrid are also validated.

4.5.3 Validation with the EMEP-Spain/Portugal network

Figure 4.13 shows the scatter plots of simulated PM_{10} concentrations without and with DA against PM_{10} daily measurements at EMEP-Spain/Portugal stations (cyan squares in Fig. 4.3). The PM_{10} correlation and RMSE are slightly improved. During the assimilation and forecast periods (72 hours), the RMSE averaged over all six experiments is 6.9 $\mu g\ m^{-3}$ without DA and 6.3 $\mu g\ m^{-3}$ with DA. Compared to the simulations without DA, DA ("Lidar DA") increases the correlation from 58% to 63%. Meanwhile, the Mean Bias Error (MBE) decreases from 3.1 to 2.3 $\mu g\ m^{-3}$. Also, we compute the statistics of the simulation results without and with DA using daily concentrations at EMEP-Europe stations (7 stations, green squares in Fig. 4.3). However, since EMEP-Europe stations are far away from the lidar network, the PM_{10} RMSE, correlation and bias are slightly but barely improved (not shown).

4.5.4 Validation with the AERONET network

Figure 4.14 shows the scatter plots of simulated AODs without and with DA against AOD from hourly measurements of the AERONET network over the early 36 hours of forecast, where only 13 AERONET stations being leeward and close to the lidar network are considered (see

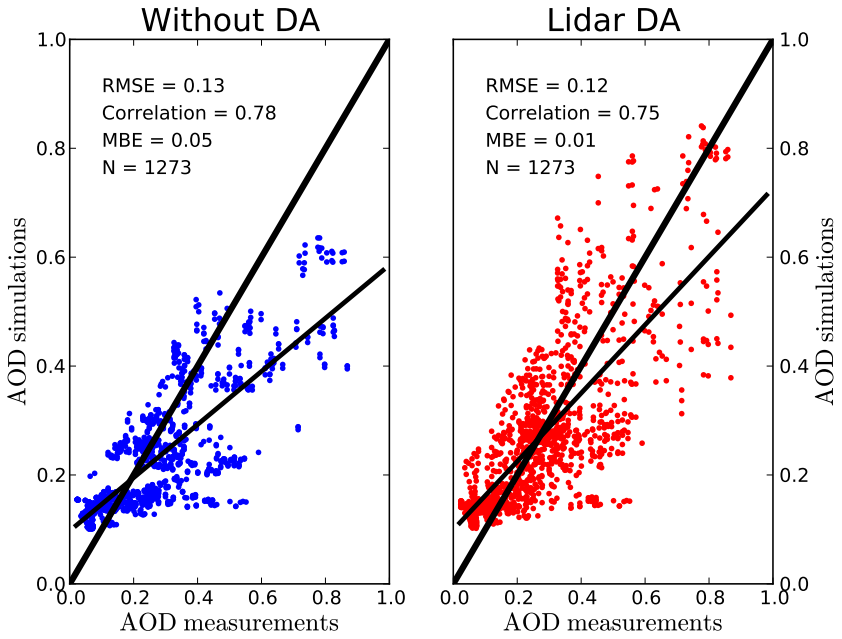

Figure 4.14: Scatter plots of simulated AODs without DA (left panel) and with DA (right panel) against AOD hourly measurements at different AERONET stations over the early 36 hours of forecast.

Fig. 4.3). As shown by comparing the left panels of Fig. 4.13 and 4.14, the model simulates AOD better than PM_{10}. This is mostly because the model simulates better fine particles ($PM_{2.5}$) over the modelling domain (horizontal and vertical) which tend to have larger contributions to optical properties than coarse particles when no Saharan dust event occurs [Chazette et al., 2005; Randriamiarisoa et al., 2006]. This is also probably because the model may simulate better the integrated mass concentration than vertically resolved mass concentrations.

As shown in Fig. 4.14, the AOD is significantly improved in the simulation with DA for high AOD observations (few cases). For the observed AODs larger than 0.4 ($N = 262$), the RMSE (resp. MBE) is 0.23 (resp. 0.2) without DA against 0.20 (resp. 0.13) with lidar DA. It is because most large AODs are associated with the transport of particle above the boundary layer, which is not well simulated by the model (probably due to large-scale model uncertainties) but followed by the lidars [Wang et al., 2013b]. It is also probably because the assimilation of lidar signals improves the estimation of aerosol mass concentrations more efficiently when aerosol concentrations are high, e.g. during air pollution events. In addition, since fine particles are well simulated, most lower AODs are well simulated, where there are very few coarse particles and DA slightly improves aerosol mass concentrations. Hence, the scores of AOD shown in Fig. 4.14 are slightly improved.

4.6 Conclusions

In this paper, a data assimilation (DA) algorithm based on the optimal interpolation (OI) method is used to assimilate lidar signals (normalised PR^2) for aerosol forecasts over Europe. The lidar data were retrieved from a 72-hour period of intensive and continuous measurements which was performed by 9 ground-based lidar stations of ACTRIS/EARLINET in the Mediterranean basin and one station in Corsica in the framework of the preChArMEx/TRAQA campaign in July 2012. That is a new application of the assimilation of lidar signals to aerosol forecasting.

First, we studied the impact of the length of the lidar DA period on aerosol forecasts. We found that 24-hour DA leads to slightly better forecasts than 12-hour DA. However, the difference between 24-hour DA and 12-hour DA is small after 6 hours of forecast. Considering that the impact of lidar DA is longer than 36 hours in the forecast period, we have used 12-hour as the assimilation period length in this paper. Also, we conducted sensitivity studies on algorithmic parameters, e.g. the horizontal error correlation length and altitudes at which DA is performed. DA with the error correlation length $L_h = 100$ km assimilating from 1.0 to 3.5 km AGL leads to the best scores for PM_{10} and $PM_{2.5}$ during the forecast period (the evaluation was done using measurements from the BDQA network).

The simulation results without and with lidar DA were evaluated using hourly concentration measurements from the BDQA network over France, daily concentration measurements from the EMEP-Spain/Portugal network and AOD measurements from the AERONET network over Europe. The results showed that the simulation with DA leads to better scores than the one without DA for aerosol forecasts ($PM_{2.5}$, PM_{10} and AOD). Moreover, the temporal impact of assimilating lidar signals is longer than 36 hours, whereas this temporal impact was estimated to be shorter, i.e. between 6 and 12 hours, by Tombette et al. [2009] and Jiang et al. [2013] when assimilating of surface mass concentrations. When the temporal impact was estimated using only the 3 stations around the Barcelona lidar site, the impact lasted for longer than 48 hours. Additionally, since the model simulates better fine particles than coarse particles, we set higher error in the background error covariance matrix [Wang et al., 2013b] for coarse particles than for fine particles, leading to larger corrections by DA of coarse particle concentrations than of fine particle concentrations.

However, since there are non-negligible errors in the estimation of optical properties and in the calculation of the tangent linear operator in the model, assimilation of normalised lidar signals can only roughly adjust/correct aerosol mass concentrations in the model, unlike the assimilation of mass concentrations. Moreover, using the measurements from only 10 lidar stations around the Mediterranean basin and validating the DA results mostly over France do not allow us conclude whether the assimilation of lidar signals lead to greatly better forecasts than the one of surface mass concentrations. One needs a denser lidar network and more surface mass concentration measurements around the lidar network for the DA validation. In addition, Schwartz et al. [2012] have shown that simultaneous DA of different aerosol observations ($PM_{2.5}$ and AOD) produced the best overall forecasts. Accordingly for future works, we suggest to perform DA with a combination of lidar signals and mass concentration measurements in the real-time forecast of aerosols. We also suggest to assimilate more complete lidar data in DA, e.g. PR^2 at all the channels, extinction/backscatter coefficients [Chaikovski et al., 2012; Lopatin et al., 2013] and directly mass concentration profiles derived from the lidar signal [Raut et al., 2009a; Ansmann et al., 2011; Royer et al., 2011]. Lidar signals would be assimilated to simultaneously improve the PBL height in the model. More accurate PBL heights

would improve the forecast ability of air quality models [Pielke and Uliasz, 1998], because the PBL height determines the volume in which pollutants are mixed. Finally, the maximum likelihood ensemble filter (MLEF) [Zupanski, 2005] or the iterative ensemble Kalman filter (IEnKF) [Bocquet and Sakov, 2013a, b] could be used in the real-time forecast of aerosols in place of the OI method in order to avoid the tangent linear approximation of the lidar observation operator, and would handle the nonlinearity of the lidar observation operator. They would also update and propagate the background error covariance matrix during the assimilation period.

Chapter 5

Summary

5.1 Conclusions

The objective of this thesis, assimilating the ground-based lidar network measurements so as to reduce the uncertainties in aerosol modelling and improve the forecast ability of air quality models, has been achieved. This thesis has demonstrated the usefulness and the feasibility of assimilating ground-based lidar observations for aerosol forecasts. The main work is split into four parts: the assimilation of synthetic surface concentrations and lidar observations, the validation of the lidar observation operator in a data assimilation (DA) framework, the development of algorithms for assimilating lidar signals (PR_2), and the application of the assimilation of lidar signals at different scales.

Firstly, a tool for assimilating PM_{10} concentration measurements on vertical profiles is developed. It is applied to an Observing System Simulation Experiment (OSSE) over Europe for one month in 2001, to investigate the potential impact of future ground-based lidar networks on analysis and short-term forecasts of PM_{10}. The efficiency of assimilating the lidar network (12 lidars) measurements is compared to the efficiency of assimilating concentration measurements from the AirBase ground network, which includes about 500 stations over western Europe in 2001. After 12 hours of assimilation and during the first forecast day, assimilating the lidar observations significantly decreases the root mean square error (RMSE) of PM_{10} concentrations and the assimilation of AirBase measurements leads to slightly better scores than assimilating the lidar observations. However, the assimilation of lidar observations leads to similar scores as AirBase's during the second forecast day. The results show a potentially powerful impact of the future lidar networks. In addition, a sensitivity study on the number and location of required lidars is performed to help define an optimal lidar network for PM_{10} forecasts. Comparing two lidar networks of 12 lidar stations, whose locations are very different, we find that spreading out the lidars regularly over Europe can improve the PM_{10} forecast. Note that increasing the number of lidar from 12 to 26 or 76 improves the forecast scores. For example, the improvement of the RMSE becomes as high as $65\,\%$ (compared to the RMSE for one-day forecasts without DA) if 76 lidars are used. However, a lidar network with many stations may be too expensive.

Secondly, a model for simulating the lidar signal (PR_2) is developed in POLYPHEMUS to validate the lidar observation operator (i.e. the operator H in section 1.4). Simulated lidar signals are compared to hourly ground-based mobile and *in-situ* lidar observations performed during the MEGAPOLI summer experiment in July 2009. It is found that the model correctly

reproduces the vertical distribution of aerosol optical properties and their temporal variability. This evaluation is also regarded as a preprocessing stage of DA. Additionally, we present two new algorithms for assimilating lidar signals which depends on whether PM_{10} is analysed or $PM_{2.5}$ and $PM_{2.5-10}$ are both analysed. The aerosol simulations without and with lidar DA are evaluated using the AIRPARIF database. The results demonstrate the feasibility and the usefulness of assimilating lidar signals for aerosol forecasting. Comparing those two algorithms, the simulation with DA of $PM_{2.5}$ and $PM_{2.5-10}$ leads to better scores than the simulation with DA of PM_{10} alone, because the background error variances are set separately for fine sections and coarse sections when $PM_{2.5}$ and $PM_{2.5-10}$ are analysed. Comparing the simulation without DA and the simulation with DA ($PM_{2.5}$ and $PM_{2.5-10}$), the averaged RMSE of PM_{10} is 11.63 $\mu g\,m^{-3}$ with DA ($PM_{2.5}$ and $PM_{2.5-10}$), against 17.74 $\mu g\,m^{-3}$ without DA on 01 July 2009. The averaged RMSE of PM_{10} is 4.73 $\mu g\,m^{-3}$ with DA ($PM_{2.5}$ and $PM_{2.5-10}$), against 6.67 $\mu g\,m^{-3}$ without DA on 26 July 2009. Hence, the gain of using a system coupling air quality models and lidar measurements via an assimilation tool for aerosol forecasting is significant.

Finally, POLYPHEMUS with the model for assimilating lidar signals is applied to the Mediterranean basin, where 9 ground-based lidar stations from the ACTRIS/EARLINET network in the Mediterranean basin and 1 station in Corsica in the framework of the ChArMEx campaign performed intensive and continuous measurements from 06:00 UTC on 09 July 2012 to 05:00 UTC on 12 July 2012. Because analysing respectively $PM_{2.5}$ and $PM_{2.5-10}$ leads to better forecasts than analysing PM_{10} (see Chapter 3), the algorithm for assimilating both $PM_{2.5}$ and $PM_{2.5-10}$ is employed. In order to study the impact of the lidar DA period length on the aerosol forecasts, simulations where DA is performed during 12 hours and 24 hours are compared. 24 hours DA leads to slightly better forecasts than 12 hours DA. However, the difference between 24 hours DA and 12 hours DA is very small after 6 hours forecasts. Also, sensitivity studies on critical algorithm parameters, e.g. horizontal correlation lengths and altitudes at which DA is performed, are conducted. The DA with the correlation length $L_h = 100$ km assimilating from 1 to 3.5 km leads to better scores during the forecast period (the evaluation is done using concentration measurements from the BDQA network). In addition, the simulation results without and with lidar DA are compared using hourly concentration measurements from the BDQA network over France, daily concentration measurements from the EMEP-Spain/Portugal network and AOT measurements from the AERONET network over Europe. The results show that the simulation with DA leads to better scores than the one without DA for aerosol forecasting ($PM_{2.5}$, PM_{10} and AOT). Moreover, the temporal impact of the assimilation of lidar signals is longer than 36 hours, whereas it was between 6 and 12 hours for the assimilation of surface mass concentrations in Tombette et al. [2009]; Jiang et al. [2013]. In particular, for the DA validation with three surface stations around the Barcelona lidar station, the impact of the assimilation of lidar signals is longer than 48 hours in the forecast period for both PM_{10} and $PM_{2.5}$. The averaged RMSE over 36-hour forecasts is 8.9 $\mu g\,m^{-3}$ without DA and 7.0 $\mu g\,m^{-3}$ with DA for PM_{10}. The averaged RMSE over 36-hour forecasts is 6.0 $\mu g\,m^{-3}$ without DA and 4.7 $\mu g\,m^{-3}$ with DA for $PM_{2.5}$. This shows that lidar DA leads to significant improvements in aerosol forecasting.

5.2 Outlook

This study is a first step towards the assimilation of lidar observations. The results show that lidar observations would be very useful for aerosol forecasting. The method developed in this thesis can be applied to other air quality models. However, it also needs several other test cases to evaluate the impact of assimilating lidar observations. The outlook of this thesis can be divided in three aspect: aerosol modelling, data assimilation and lidar observations.

5.2.1 Aerosol modelling

In Chapter 3, we found that the assimilation of lidar observations for analysing $PM_{2.5}$ and $PM_{2.5-10}$ leads to better forecasts than that for analysing PM_{10}. That is because the air quality modelling platform POLYPHEMUS simulates well $PM_{2.5}$, but underestimates $PM_{2.5-10}$ probably due to the underestimation of emissions and uncertainties in boundary conditions of coarse particles. For instance, road resuspension of PM is not considered in the model and boundary conditions are obtained from nested simulations over Europe and France where coarse particles are also underestimated. In addition, the improvements of DA in the assimilation period wane during the forecast time due to uncertainties in the model, such as uncertainties in emissions and boundary conditions. Thus, we need more accurate emissions and boundary conditions aerosols, especially for $PM_{2.5-10}$.

We used the optical property module of POLYPHEMUS to simulate lidar signals in Chapter 3 and 4. We found that the uncertainties of simulated lidar signals at a given altitude accumulate from higher altitudes due to the integration of extinction coefficients on the vertical profile. Thus, a more accurate assessment of the extinction and backscattering coefficients is needed. Additionally, simulated optical properties depended significantly on the wet diameter of aerosols. Thus, it is necessary to improve the estimation of the wet diameter in the model, by improving the modelling of the liquid water content of particles. For example, all organic compounds are considered hydrophobic in this work, whereas some may be hydrophilic.

5.2.2 Data assimilation

The optimal interpolation (OI) is used in our work, as it is computationally cheap. OI has been surpassed by the 4D-Var (4-dimensional variational) or EnKF (ensemble Kalman filter) method in meteorology [Kalnay, 2003]. Thus, we need to perform the assimilation of lidar observations using other advanced DA methods, e.g. 4D-Var and EnKF methods. Moreover, comparing different DA methods can help to demonstrate the feasibility of assimilating lidar signals for aerosol forecasting. Also, that can help to find a more suited DA method for assimilating lidar observations (the lidar observation operator is non-linear). We think that 4D-Var and EnKF would lead to better aerosol forecasts than OI in lidar DA. Additionally, the EnKF method do not need the linear tangent of lidar operator, unlike OI or 4D-Var. Let $\{\mathbf{x}_b^i,\, i = 1, \ldots, N_e\}$ be ensemble of the background state, where N_e is the size of ensemble. In EnKF, the analysis state $\mathbf{x}_a^i$ is given as follows,

$$\mathbf{x}_a^i = \mathbf{x}_b^i + \mathbf{K}\left(\mathbf{y} + H(\mathbf{x}_b^i)\right), \tag{5.1}$$

where the gain matrix $\mathbf{K}$ is defined as

$$\mathbf{K} = \mathbf{B}\mathbf{H}^{\mathrm{T}}\left(\mathbf{H}\mathbf{B}\mathbf{H}^{\mathrm{T}} + \mathbf{R}\right)^{-1}. \tag{5.2}$$

In order to avoid compute the linear tangent of the lidar operator H, we can define $\mathbf{BH}^{\mathrm{T}}$ and $\mathbf{HBH}^{\mathrm{T}}$ as

$$\mathbf{BH}^{\mathrm{T}} \simeq \frac{1}{N_e - 1} \sum_{i=1}^{N_e} \left(\mathbf{x}_b^i - \overline{\mathbf{x}_b}\right) \left(H(\mathbf{x}_b^i) - \overline{H(\mathbf{x}_b)}\right)^{\mathrm{T}}, \tag{5.3}$$

$$\mathbf{HBH}^{\mathrm{T}} \simeq \frac{1}{N_e - 1} \sum_{i=1}^{N_e} \left(H(\mathbf{x}_b^i) - \overline{H(\mathbf{x}_b)}\right) \left(H(\mathbf{x}_b^i) - \overline{H(\mathbf{x}_b)}\right)^{\mathrm{T}}. \tag{5.4}$$

One of the additional challenges could be to estimate the background error covariance matrix $\mathbf{B}$ and the observation error covariance matrix $\mathbf{R}$. Although we analyse separately but simultaneously $PM_{2.5}$ and $PM_{2.5-10}$ in Chapter 3 and 4, the same error correlation length is used for $PM_{2.5}$ and $PM_{2.5-10}$ in the matrix $\mathbf{B}$. Setting separately the error correlation length for $PM_{2.5}$ and $PM_{2.5-10}$ in the matrix $\mathbf{B}$ would lead to better forecasts. Additionally, we supposed that the matrix $\mathbf{R}$ is diagonal. As shown in our work, it works for the DA test, since we well set the most important factors of $\mathbf{R}$ (the diagonal elements), i.e. the observation error variances. To better predict the aerosol pollution level, a more accurate definition of the observation error covariance matrix is needed, e.g. the observation error variances and the covariances between two observing points [Huneeus and Boucher, 2007].

5.2.3 Lidar observations

In this thesis, we performed the simulation with DA using mostly lidar observations retrieved from the ACTRIS/EARLINET network over Europe and lidar observations retrieved from the MEGAPOLI summer campaign over Greater Paris. The results encourage to define a lidar network in megacities, like Paris and Beijing, and to operationally perform continuous measurements. Assimilating the lidar observations retrieved from the future lidar network will improve the aerosol forecasts. In addition, the model for assimilating lidar signals in POLYPHEMUS can also be applied to other domains and with other lidar networks. For instance, the eastern Asia is an interesting domain for air pollution studies, where PM concentrations are much higher than the PM regulation by the World Health Organization (WHO). Moreover, the Asian Dust Network, referred as AD-Net, provides continuous observation with automatic lidars. Since December 2012, the measured data are updated at 00:00 local time on the site of AD-Net. These data can be assimilated in the real-time forecast of aerosols.

Instead of the one-wavelength lidar, we need to employ more advanced lidar instruments with multi-wavelengths, e.g. the atmospheric Raman-N_2 lidar. They provide accurate retrieval of extinction and backscatter coefficient profiles without making assumptions on the aerosols. In this case, the assimilation of lidar observations would lead to better forecasts, because it does not need to estimate the normalisation altitude, and observations would be more accurate and independent.

The objective of this thesis was to study the impact of the assimilation of lidar observations. Simultaneous DA of different aerosol observations (mass concentrations and optical properties) [Schwartz et al., 2012] was not performed. However, the assimilation of lidar observations can only correct the aerosol concentrations at high altitudes, since the lidar measurements are available from hundreds meters to thousands meters above the ground [Raut and Chazette, 2009; Royer et al., 2011]. The assimilation of surface mass concentration measurements can

accurately correct aerosol concentrations at ground level. Furthermore, aerosol surface measurements may provide information on the aerosol composition and size distribution. Thus, in the real-time forecast of aerosols, we suggest assimilating both lidar observations and surface mass concentration measurements.

Appendix A

Statistical indicators

Let $\{o_i\}_{i=1,n}$ and $\{s_i\}_{i=1,n}$ be the observed and the modelled concentrations, respectively. Let n be the number of available observations. The statistical indicators used to evaluate the results with respect to the truth are: the Root Mean Square Error (RMSE), the (Pearson) correlation, the Mean Fractional Error (MFE), the Mean Fractional Bias (MFB) and the Mean Bias Error (MBE). MFE and MFB bound the maximum error and bias and do not allow a few data points to dominate the statistics. They are often used to evaluate model performances against observations for aerosols [Boylan and Russell, 2006]. The RMSE is a measure of the extent that the model deviates from the observations. Correlation is a measure of statistical relationships involving dependence between the observed and the modelled concentrations. The statistical indicators are defined as follow:

$$\text{RMSE} = \sqrt{\frac{1}{n}\sum_{i=1}^{n}(o_i - s_i)^2}, \tag{A.1}$$

$$\text{correlation} = \frac{\sum_{i=1}^{n}(o_i - \bar{o})(s_i - \bar{s})}{\sqrt{\sum_{i=1}^{n}(o_i - \bar{o})^2 \sum_{i=1}^{n}(s_i - \bar{s})^2}}, \tag{A.2}$$

$$\text{MFE} = \frac{1}{n}\sum_{i=1}^{n}\frac{|s_i - o_i|}{(s_i + o_i)/2}, \tag{A.3}$$

$$\text{MFB} = \frac{1}{n}\sum_{i=1}^{n}\frac{s_i - o_i}{(s_i + o_i)/2}, \tag{A.4}$$

$$\text{MBE} = \frac{1}{n}\sum_{i=1}^{n} s_i - o_i, \tag{A.5}$$

where $\bar{o} = \frac{1}{n}\sum_{i=1}^{n} o_i$ and $\bar{s} = \frac{1}{n}\sum_{i=1}^{n} s_i$.

Appendix B

Update formula for DA ($PM_{2.5}$ and $PM_{2.5-10}$)

In order to separately analyse $PM_{2.5}$ and $PM_{2.5-10}$ in the assimilation of lidar observations, the matrix $\mathbf{B}$ is modelled as follows

$$\mathbf{B} = \mathbf{PDP}^{\mathrm{T}}, \tag{B.1}$$

where $\mathbf{D}$ is the error covariance matrix for $PM_{2.5}$ and $PM_{2.5-10}$. The matrix $\mathbf{D}$ is defined by

$$\mathbf{D} = \begin{bmatrix} \mathbf{D_{2.5}} & \mathbf{0} \\ \mathbf{0} & \mathbf{D_{2.5-10}} \end{bmatrix},$$

and the matrix $\mathbf{P}$ is defined by

$$\mathbf{P} = \begin{bmatrix} \mathbf{P_{2.5}} \\ \mathbf{P_{2.5-10}} \end{bmatrix},$$

where each column k of $\mathbf{P_{2.5}}$ (resp.$\mathbf{P_{2.5-10}}$) corresponds to the proportion of the mass of particles for a given species in a given size section in $PM_{2.5}$ (resp. $PM_{2.5-10}$) mass concentrations at grid point k as section 3.6.2 shown.

The matrix $\mathbf{Z}$ is defined by

$$\mathbf{Z} = \begin{bmatrix} \mathbf{Z_{2.5}} \\ \mathbf{Z_{2.5-10}} \end{bmatrix},$$

where the matrix $\mathbf{Z_{2.5}}$ (resp. $\mathbf{Z_{2.5-10}}$) is a $M \times (M \cdot N_b \cdot N_s)$ matrix, which converts the state vector $\mathbf{x}$ into the $PM_{2.5}$ (resp. $PM_{2.5-10}$) state $\mathbf{c_{2.5}}$ (resp. $\mathbf{c_{2.5-10}}$).

Let $\mathbf{S}' = \mathbf{SP}$. After multiplying each side of equation (3.20) by the matrix $\mathbf{Z}$, we obtain

$$\begin{pmatrix} \mathbf{c^a_{2.5}} - \mathbf{c^b_{2.5}} \\ \mathbf{c^a_{2.5-10}} - \mathbf{c^b_{2.5-10}} \end{pmatrix} = \mathbf{D}(\mathbf{LS}')^{\mathrm{T}} \left((\mathbf{LS}')\mathbf{D}(\mathbf{LS}')^t + \mathbf{R} \right)^{-1} \left(\mathbf{y} - H(\mathbf{x}^b) \right).$$

Bibliography

Ackerman, A. S., Toon, O. B., Stevens, D. E., Heymsfield, A. J., Ramanathan, V., and Welton, E. J.: Reduction of tropical cloudiness by soot, Science, 288, 1042—-1047, 2000. 26

Adhikary, B., Kulkarni, S., Dallura, A., Tang, Y., Chai, T., Leung, L. R., Qian, Y., Chung, C. E., Ramanathan, V., and Carmichael, G. R.: A regional scale chemical transport modeling of Asian aerosols with data assimilation of AOD observations using optimal interpolation technique, Atmospheric Environment, 42, 8600–8615, 2008. 112, 114

Amann, M., Bertok, I., Cabala, R., Cofala, J., Heyes, C., Gyarfas, F., Klimont, Z., Schöpp, W., and Wagner, F.: A final set of scenarios for the Clean Air For Europe (CAFE) programme, Tech. rep., International Institute for Applied Systems Analysis (IIASA), 2005. 9, 24, 25

Ansmann, A., Wandinger, U., Riebesell, M., Weitkamp, C., and Michaelis, W.: Independent measurement of extinction and backscatter profiles in cirrus clouds by using a combined Raman elastic-backscatter lidar, Appl. Opt., 31, 7113–7131, doi:10.1364/AO.31.007113, URL http://ao.osa.org/abstract.cfm?URI=ao-31-33-7113, 1992. 114

Ansmann, A., Tesche, M., Seifert, P., Gro β, S., Freudenthaler, V., Apituley, A., Wilson, K. M., Serikov, I., Linné, H., Heinold, B., Hiebsch, A., Schnell, F., Schmidt, J., Mattis, I., Wandinger, U., and Wiegner, M.: Ash and fine-mode particle mass profiles from EARLINET-AERONET observations over central Europe after the eruptions of the Eyjafjallajökull volcano in 2010, Journal of Geophysical Research: Atmospheres, 116, doi: 10.1029/2010JD015567, URL http://dx.doi.org/10.1029/2010JD015567, 2011. 133

Anthony, H. K. and Mary-Scott, K.: The Long-Range Atmospheric Transport of Natural and Contaminant Substances, Springer, St. Georges, Bermuda, 1990. 22, 36

Austin, J.: Toward the four dimensional assimilation of stratospheric chemical constituents, J. Geophys. Res., 97, 2569–2588, doi:10.1029/91JD02603, 1992. 112

Baker, D. F.and BÖsch, H., Doney, S. C., O'Brien, D., and Schimel, D. S.: Carbon source/sink information provided by column CO_2 measurements from the Orbiting Carbon Observatory, Atmos. Chem. Phys., 10, 4145–4165, doi:10.5194/acp-10-4145-2010, 2010. 58

Balgovind, R., Dalcher, A., Ghil, M., and Kalnay, E.: A Stochastic-Dynamic Model for the Spatial Structure of Forecast Error Statistics, Mon.Weather Rev., 111, 701—-722, 1983. 15, 43, 63, 66, 102, 125, 128

Barker, J. and Tingey, D. T.: Air Pollution Effects on Biodiversity, Springer, New York, USA, 1992. 57

Benedetti, A. and Fisher, M.: Background error statistics for aerosols, Q. J. Roy. Meteor. Soc., 133, 391–405, 2007. 51, 59, 69, 113

Benedetti, A., Morcrette, J., Boucher, O., Dethof, A., Engelen, R. J., Fisher, M., Flentje, H., Huneeus, N., Jones, L., Kaiser, J. W., Kinne, S., Mangold, A., Razinger, M., Simmons, A. J., and Suttie, M.: Aerosol analysis and forecast in the European Centre for Medium-Range Weather Forecasts Integrated Forecast System: 2. Data assimilation, J. Geophys. Res., 114, 1–18, 2009. 112, 113, 114

Berthier, S., Chazette, P., Couvert, P., Pelon, J., Dulac, F., Thieuleux, F., Moulin, C., and T, P.: Desert dust aerosol columnar properties over ocean and continental Africa from Lidar in-Space Technology Experiment (LITE) and Meteosat synergy, J. Geophys. Res., 111, doi: 10.1029/2005JD006999, 2006. 29, 57

Bocquet, M. and Sakov, P.: Joint state and parameter estimation with an iterative ensemble Kalman smoother, Nonlinear Processes in Geophysics, 20, 803–818, doi:10.5194/npg-20-803-2013, URL http://www.nonlin-processes-geophys.net/20/803/2013/, 2013a. 134

Bocquet, M. and Sakov, P.: An iterative ensemble Kalman smoother, Q. J. R. Meteorol. Soc., doi:10.1002/qj.2236, 2013b. 134

Bosenberg, J. and Hoff, R.: Plan for theimplementation of the GAW Aerosol Lidar Observation Network, GALION, WMO GAW Report No 178, Hamburg, 2007. 31

Bösenberg, J., Matthias, V., Amodeo, A., Amoiridis, V., Ansmann, A., Baldasano, J. M., Balin, I., Balis, D., Böckmann, C., Boselli, A., Carlsson, G., Chaikovsky, A., Chourdakis, G., Comeron, A., De Tomasi, F., Eixmann, R., Freudenthaler, V., Giehl, H., Grigorov, I., Hagard, A., Iarlori, M., Kirsche, A., Kolarov, G., Kolarev, L., Komguem, G., Kreipl, S., Kumpf, W., Larchevêque, G., Linné, H., Matthey, R., Mattis, I., Mekler, A., Mironova, I., Mitev, V., Mona, L., Müller, D., Music, S., Nickovic, S., Pandolfi, M., Papayannis, A., Pappalardo, G., Pelon, J., Pérez, C., Perrone, R. M., Persson, R., Resendes, D. P., Rizi, V., Rocadenbosch, F., Rodrigues, J. A., Sauvage, L., Schneidenbach, L., Schumacher, R., Shcherbakov, V., Simeonov, V., Sobolewski, P., Spinelli, N., Stachlewska, I., Stoyanov, D., Trickl, T., Tsaknakis, G., Vaμghan, G., Wandinger, U., Wang, X., Wiegner, M., Zavrtanik, M., and Zerefos, C.: EARLINET: A European Aerosol Research Lidar Network to Establish an Aerosol Climatology, Tech. Rep. 348, Max-Planck-Institut für Meteorologie, Hamburg, Germany, 2003. 117

Bouttier, F. and Courtier, P.: Data assimilation concepts and methods, Meteorological Training Course Lecture Series, March 1999, ECMWF, Reading, United Kingdom, 2002. 41, 43, 57, 84

Boylan, J. W. and Russell, A. G.: PM and light extinction model performance metrics, goals, and criteria for three-dimensional air quality models, Atmos. Environ., 40, 4946—-4959, 2006. 40, 61, 92, 93, 100, 106, 128, 141

Brandt, J., Christensen, J. H., Frohn, L. M., Geels, C., Hansen, K. M., Hedegaard, G. B., Hvidberg, M., and Skjøth, C. A.: THOR – an operational and integrated model system for air pollution forecasting and management from regional to local scale, in: Proceedings of the 2nd ACCENT Symposium, Urbino (Italy), 2007. 57

Brandt, J., Silver, J. D., Frohn, L. M., Geels, C., Gross, A., Hansen, A. B., Hansen, K. M., Hedegaard, G. B., Skjøth, C. A., Villadsen, H., Zare, A., and Christensen, J. H.: An integrated model study for Europe and North America using the Danish Eulerian Hemispheric Model with focus on intercontinental transport of air pollution, Atmospheric Environment, 53, 156–176, doi:http://dx.doi.org/10.1016/j.atmosenv.2012.01.011, URL http://www.sciencedirect.com/science/article/pii/S1352231012000143, 2012. 83

Candiani, G., Carnevale, C., Finzi, G., Pisoni, E., and Volta, M.: A comparison of reanalysis techniques: Applying optimal interpolation and Ensemble Kalman Filtering to improve air quality monitoring at mesoscale, Science of the Total Environment, 458-460, 7–14, URL http://dx.doi.org/10.1016/j.scitotenv.2013.03.089, 2013. 114

Chaikovski, A., Dubovik, O., Pappalardo, G., Wandinger, U., Apituley, A., Arbroledas, L. A., Pappayannis, A., and Pietruczuk, A.: Algorithm and Software for the Retrieval of Vertical Aerosol Properties using combined Lidar/Radiometer Data: Dissemination in EARLINET, in: 26th International Laser Radar Conference, edited by Papayannis, A., Balis, D., and Amiridis, V., pp. 339–402, Porto Heli, Greece, 2012. 133

Chang, J. C. and Hanna, S. R.: Air quality model performance evaluation, Meteorol. Atmos. Phys., 87, 167–196, 2004. 39

Chazette, P.: The monsoon aerosol extinction properties at Goa during INDOEX as measured with lidar, J. Geophys. Res., 108(D6), doi:10.1029/2002JD002074, 2003. 30, 79

Chazette, P., Randriamiarisoa, H., Sanak, J., Couvert, P., and Flamant, C.: Optical properties of urban aerosol from airborne and ground-based in situ measurements performed during the Etude et Simulation de la Qualité de l'air en Ile de France (ESQUIF) program, J. Geophys. Res., 110, 1–20, doi:10.1029/2004JD004810, 2005. 30, 57, 58, 132

Chazette, P., Sanak, J., and Dulac, F.: New Approach for Aerosol Profiling with a Lidar Onboard an Ultralight Aircraft: Application to the African Monsoon Multidisciplinary Analysis, Environ. Sci. Technol., 41, 8335–8341, 2007. 57, 85

Chazette, P., Raut, J.-C., Dulac, F., Berthier, S., Kim, S. W., Royer, P., Sanak, J., Loaëc, S., and Grigaut-Desbrosses, H.: Simultaneous observations of lower tropospheric continental aerosols with a ground-based, an airborne, and the space-borne CALIOP lidar systems, J. Geophys. Res., 115, doi:/10.1029/2009JD012341, 2010. 29, 57

Chazette, P., Bocquet, M., Royer, P., Winiarek, V., Raut, J.-C., Labazuy, P., Gouhier, M., Lardier, M., and Cariou, J.-P.: Eyjafjallajökull ash concentrations derived from both lidar and modeling, J. Geophys. Res., 117, 1–17, doi:10.1029/2011JD015755, 2012. 10, 30, 53, 55, 58, 76, 83

Chen, S.-H., Chen, J.-Y., Chang, W.-Y., Lin, P.-L., Lin, P.-H., and Sun, W.-Y.: Observing System Simulation Experiment: Development of the system and preliminary results, J. Geophys. Res., 116, doi:10.1029/2010JD015103, 2011. 58, 66

Chevallier, F., Bréon, F.-M., and Rayner, P. J.: Contribution of the Orbiting Carbon Observatory to the estimation of CO_2 sources and sinks: Theoretical study in a variational data assimilation framework, J. Geophys. Res., 112, doi:10.1029/2006JD007375, 2007. 58

Chin, M., Rood, R. B., Lin, S.-J., Müller, J.-F., and Thompson, A. M.: Atmospheric sulfur cycle simulated in the global model GOCART: Model description and global properties, J. Geophys. Res., 105, 24 671–24 687, 2000. 60

Claeyman, M., Attié, J.-L., Peuch, V.-H., El Amraoui, L., Lahoz, W. A., Josse, B., Joly, M., Barré, J., Ricaud, P., Massart, S., Piacentini, A., von Clarmann, T., HÖpfner, M., Orphal, J., Flaud, J.-M., and Edwards, D. P.: A thermal infrared instrument onboard a geostationary platform for CO and O_3 measurements in the lowermost troposphere: Observing System Simulation Experiments (OSSE), Atmos. Meas. Tech., 4, 1637–1661, doi:10.5194/amt-4-1637-2011, 2011. 58

Collins, W. D., Rasch, P. J., Eaton, B. E., Khattatov, B. V., Lamarque, J.-F., and Zender, C. S.: Simulating aerosols using a chemical transport model with assimilation of satellite aerosol retrievals: Methodology for INDOEX, J. Geophys. Res., 106, 7313–7336, doi:10.1029/2000JD900507, 2001. 112

Collis, R. T. H. and Russell, P. B.: Lidar measurement of particles and gases by elastic backscattering and differential absorption, in: Laser Monitoring of the Atmosphere, edited by Hinkley, E., vol. 14 of *Topics in Applied Physics*, pp. 71–151, Springer Berlin Heidelberg, doi:10.1007/3-540-07743-X_18, URL http://dx.doi.org/10.1007/3-540-07743-X_18, 1976. 88

Couvidat, F., Debry, E., Sartelet, K., and Seigneur, C.: A hydrophilic/hydrophobic organic (H^2O) aerosol model: Development, evaluation and sensitivity analysis, J. Geophys. Res., 117, 1–19, doi:10.1029/2011JD017214, 2012. 40, 85

Couvidat, F., Kim, Y., Sartelet, K., Seigneur, C., Marchand, N., and Sciare, J.: Modeling secondary organic aerosol in an urban area: application to Paris, France, Atmos. Chem. Phys., 13, 983–996, doi:10.5194/acp-13-983-2013, 2013. 85

Daley, R.: Atmospheric data analysis, Cambridge University Press, Cambridge, 1991. 42, 69, 112

D'Amico, G., Binietoglou, I., Amodeo, A., Pappalardo, G., Baars, H., Engelmann, R., Freudenthaler, V., Nicolae, D., Chaikovsky, A., Apituley, A., and Adam, M.: EARLINET Single Calculus Chain for Automatic Lidar Data Processing: First Tests on Optical Products, in: 26th International Laser Radar Conference, edited by Papayannis, A., Balis, D., and Amiridis, V., pp. 331–334, Porto Heli, Greece, 2012. 118

DasGupta, M. and Mishra, S. K.: Least Absolute Deviation Estimation of Linear Econometric Models : A Literature Review, North-Eastern Hill University, Shillong, India, 2007. 90

de Rooij, W. A. and van der Stap, C. C. A. H.: Expansion of Mie scattering matrices in generalized spherical functions, Astron. Astrophys., 131, 237—248, 1984. 88

Debry, E., Fahey, K., Sartelet, K., Sportisse, B., and Tombette, M.: Technical Note: A new SIze REsolved Aerosol Model (SIREAM), Atmos. Chem. Phys., 7, 1537–1547, doi:10.5194/acp-7-1537-2007, 2007. 38, 59, 84, 114

Denby, B., Schaap, M., Segers, A., Builtjes, P., and Hora, J.: Comparison of two data assimilation methods for assessing PM_{10} exceedances on the European scale, Atmospheric Environment, 42, 7122–7134, doi:10.1016/j.atmosenv.2008.05.058, 2008. 51, 57, 58, 59, 62, 84, 100, 113

Dickerson, R. R., Kondragunta, S., Stenchikov, G., Civerolo, K. L., Doddrige, B. G., and Holben, B. N.: The impact of aerosols on solar ultraviolet radiation and photochemical smog, Science, 278, 827–830, 1997. 57

Dockery, D. and Pope, A.: Epidemiology of acute health effects: summary of time-series, in: Particles in Our Air: Concentration and Health Effects, Harvard University Press, pp. 123–147, 1996. 57, 83, 112

Draxler, R. R. and Rolph, G. D.: HYSPLIT (HYbrid Single-Particle Lagrangian Integrated Trajectory) Model access via NOAA ARL READY Website (http://ready.arl.noaa.gov/HYSPLIT.php), NOAA Air Resources Laboratory, Silver Spring, MD, 2014. 121

Edwards, D. P., Arellano Jr., A. F., and Deeter, M. N.: A satellite observation system simulation experiment for carbon monoxide in the lowermost troposphere, J. Geophys. Res., 114, doi:10.1029/2008JD011375, 2009. 58, 66

Elbern, H. and Schmidt, H.: A four-dimensional variational chemistry data assimilation scheme for Eulerian chemistry transport modeling, J. Geophys. Res., 104, 18 583–18 598, 1999. 112

Emmons, L. K., Walters, S., Hess, P. G., Lamarque, J.-F., Pfister, G. G., Fillmore, D., Granier, C., Guenther, A., Kinnison, D., Laepple, T., Orlando, J., Tie, X., Tyndall, G., Wiedinmyer, C., Baughcum, S. L., and Kloster, S.: Description and evaluation of the Model for Ozone and Related chemical Tracers, version 4 (MOZART-4), Geosci. Model Dev., 3, 43–67, doi:10.5194/gmd-3-43-2010, 2010. 116

EPA: Guideline for regulatory application of the urban airshed model, Tech. rep., EPA, 1991. 39

European Environment Agency (EEA): Spatial assessment of PM_{10} and ozone concentrations in Europe, EEA, 2009. 24

Evensen, G.: Sequential data assimilation with a nonlinear quasi-geostrophic model using Monte Carlo methods to forecast error statistcs, J. Geophys. Res., 99(C5), 10 143—-10 162, 1994. 42

Evensen, G.: Data Assimilation: the Ensemble Kalman Filter, Springer, Berlin, Germany, 2009. 42, 49, 112

Ferrare, R. A., Ismail, S., Browell, E., Brackett, V., Clayton, M., Kooi, S., Melfi, S. H., Whiteman, D., Schwemmer, G., Evans, K., Russell, P., Livingston, J., Schmid, B., Holben, B., Remer, L., Smirnov, A., and Hobbs, P. V.: Comparison of aerosol optical properties and water vapor among ground and airborne lidars and sunphotometers during TARFOX, J. Geophys. Res., 105(D8), 2000. 30

Fisher, M. and Lary, D. J.: Lagrangian four-dimensional variational data assimilation of chemical species, J. Geophys. Res., 121, 1681–1704, doi:10.1002/qj.49712152709, 1995. 112

Goliff, W. S. and Stockwell, W. R.: The Regional Atmospheric Chemistry Mechanism, version 2, an update, in: International conference on Atmospheric Chemical Mechanisms, University of California at Davis, 2008. 39

Guenther, A., Karl, T., Harley, P., Wiedinmyer, C., Palmer, P. I., and Geron, C.: Estimates of global terrestrial isoprene emissions using MEGAN (Model of Emissions of Gases and Aerosols from Nature), Atmos. Chem. Phys., 6, 3181–3210, 2006. 34

Hamonou, E., Chazette, P., Balis, D., Dulac, F., Schneider, X., Galani, E., Ancellet, G., and Papayannis, A.: Characterization of the vertical structure of Saharan dust export to the Mediterranean basin, Journal of Geophysical Research: Atmospheres, 104, 22 257–22 270, doi:10.1029/1999JD900257, URL http://dx.doi.org/10.1029/1999JD900257, 1999. 119

Hansen, J. E., Sato, M., and Ruedy, R.: Radiative forcing and climate response, J. Geophys. Res., 102, 6831–6864, 1997. 26

Hess, M., Koepke, P., and Schult, I.: Optical Properties of Aerosols and Clouds: The Software Package OPAC, Bull. Amer. Meteor. Soc., 79, 831–844, 1998. 88

Hobbs, P. V.: An overview of the University of Washington airborne measurements and results from the Tropospheric Aerosol Radiative Forcing Observational Experiment (TARFOX), J. Geophys. Res., 104(D2), 1999. 30

Hodzic, A., Chepfer, H., Vautard, R., Chazette, P., Beekmann, M., Bessagnet, B., Chatenet, B., Cuesta, J., Drobinski, P., Goloub, P., Haeffelin, M., and Morille, Y.: Comparison of aerosol chemistry transport model simulations with lidar and Sun photometer observations at a site near Paris, J. Geophys. Res., 109, 1–19, doi:10.1029/2004JD004735, 2004. 83

Hodzic, A., Vautard, R., Chazette, P., Menut, L., and Bessagnet, B.: Aerosol chemical and optical properties over the Paris area within ESQUIF project, Atmos. Chem. Phys., 6, 3257–3280, doi:10.5194/acp-6-3257-2006, 2006. 57, 83, 112

Holben, B. N., Eck, T. F., Slutsker, I., Tanré, D., Buis, J. P., Setzer, A., Vermote, E., Reagan, J. A., Kaufman, Y. J., Nakajima, T., Lavenu, F., Jankowiak, I., and Smirnov, A.: AERONET - A federated instrument network and data archive for aerosol characterization, Remote. Sens. Environ., 66, 1–16, 1998. 85

Holben, B. N., Tanré, D., Smirnov, A., Eck, T. F., Slutsker, I., Abuhassan, N., Newcomb, W. W., Schafer, J. S., Chatenet, B., Lavenu, F., Kaufman, Y. J., Castle, J. V., Setzer, A., Markham, B., Clark, D., Frouin, R., Halthore, R., Karneli, A., Neill, N. T. O., Pietras, C., Pinker, R. T.,

Voss, K., and Zibordi, G.: An emerging ground-based aerosol climatology: Aerosol optical depth from AERONET, J. Geophys. Res., 106, 12 067–12 097, 2001. 85

Hong, S. Y., Noh, Y., and Dudhia, J.: A New Vertical Diffusion Package with an Explicit Treatment of Entrainment Processes, Mon.Weather Rev., 134, 2318–2341, 2006. 85

Horowitz, L., Walters, S., Mauzerall, D., Emmons, L., Rasch, P., Granier, C., Tie, X., Lamarque, J.-F., Schultz, M., Tyndall, G., Orlando, J., and Brasseur, G.: A global simulation of tropospheric ozone and related tracers: Description and evaluation of MOZART, version 2, J. Geophys. Res., 108, doi:10.1029/2002JD002853, 2003. 60

Hudson, J. G. and Yum, S. S.: Cloud condensation nuclei spectra and polluted and clean clouds over the Indian Ocean, J. Geophys. Res., 107, INX2 21–1–INX2 21–12, 2002. 30

Huneeus, N. and Boucher, O.: One-dimensional variational retrieval of aerosol extinction coefficient from synthetic LIDAR and radiometric measurements, J. Geophys. Res., 112, 1–14, doi:10.1029/2006JD007625, 2007. 79, 112, 114, 138

Huneeus, N., Chevallier, F., and Boucher, O.: Estimating aerosol emissions by assimilating observed aerosol optical depth in a global aerosol model, Atmos. Chem. Phys., 12, 4585–4606, doi:10.5194/acp-12-4585-2012, 2012. 113, 114

Intergovernment Panel on Climate Control (IPCC): Climate Change 2007, the fourth Assessment Report of the IPCC, Cambridge Univ. Press, New York, USA, 2007. 9, 25, 26, 27, 57, 83

Intergovernment Panel on Climate Control (IPCC): The Physical Science Basis. Contribution of Working Group I to the Fifth Assessment Report of the Intergovernmental Panel on Climate Change, Tech. rep., Cambridge Univ. Press, Cambridge, United Kingdom and New York, NY, USA, 2013. 112

Jacobson, M. Z.: A physically-based treatment of elemental carbon optics: Implications for global direct forcing of aerosols, Geophys. Res. Lett., 27, 217—-220, 2000. 89

Jiang, Z., Liu, Z., Wang, T., Schwartz, C. S., Lin, H.-c., and Jiang, F.: Probing into the impact of 3DVAR assimilation of surface PM 10 observations over China using process analysis, J. Geophys. Res.: ATMOSPHERES, 118, 6738–6749, doi:10.1002/jgrd.50495, 2013. 110, 113, 114, 126, 133, 136

Kahnert, M.: On the observability of chemical and physical aerosol properties by optical observations: Inverse modelling with variational data assimilation, Tellus, 61B, 747–755, doi:10.1111/j.1600-0889.2009.00436.x, 2009. 113, 114

Kalman, R. E.: A new approach to linear filter and prediction problems, J. Basic. Eng., 82, 35–45, 1960. 42, 49

Kalnay, E.: Atmospheric modeling, data assimilation, and predictability, Cambridge University Press, Cambridge, 2003. 41, 57, 112, 113, 137

Katrinak, K. A., Rez, P., Perkes, P. R., and Buseck, P. R.: Fractal geometry of carbonaceous agregates from an urban aerosol, Environ. Sci. Technol., 27, 539—-547, 1993. 89

Kaufman, Y. J., Tanré, D., , and Boucher, O.: A satellite view of aerosols in the climate system, Nature, 419, 215–223, 2002. 29, 57

Kelly, J. T., Avise, J., Cai, C., and Kaduwela, A. P.: Simulating particle size distributions over California and impact on Lung deposition fraction, Aerosol Sci. Technol., 45, 148–162, doi: 10.1080/02786826.2010.528078, 2011. 83

Kim, Y., Sartelet, K., and Seigneur, C.: Comparison of two gas-phase chemical kinetic mechanisms of ozone formation over Europe, J. Atmos. Chem., 62, 89–119, doi:10.1007/s10874-009-9142-5, 2010. 59, 61

Kim, Y., Couvidat, F., Sartelet, K., and Seigneur, C.: Comparison of different gas-phase mechanisms and aerosol modules for simulating particulate matter formation, J. Air Waste Manage. Assoc., 61, 1218–1226, doi:10.1080/104732.89.2011.603939, URL http://dx.doi.org/10.1080/104732.89.2011.603939, 2011a. 32, 37, 59, 84, 115

Kim, Y., Sartelet, K., and Seigneur, C.: Formation of secondary aerosols over Europe: comparison of two gas-phase chemical mechanisms, Atmos. Chem. Phys., 11, 583–598, doi: 10.5194/acp-11-583-2011, 2011b. 61

Kim, Y., Sartelet, K., Raut, J.-C., and Chazette, P.: Evaluation of the Weather Research and Forecast/urban model over Greater Paris, Boundary Layer Meteor., 149, 105–132, doi:10.1007/s10546-013-9838-6, 2013. 85

Kinne, S., Schulz, M., Textor, C., Guibert, S., Balkanski, Y., Bauer, S. E., Berntsen, T., Berglen, T. F., Boucher, O., Chin, M., Collins, W., Dentener, F., Diehl, T., Easter, R., Feichter, J., Fillmore, D., Ghan, S., Ginoux, P., Gong, S., Grini, A., Hendricks, J., Herzog, M., Horowitz, L., Isaksen, I., Iversen, T., Kloster, S., Koch, D., Kristjansson, J. E., Krol, M., Lauer, A., Lamarque, J. F., Lesins, G., Liu, X., Lohmann, U., Montanaro, V., Myhre, G., Penner, J. E., Pitari, G., Reddy, S., Seland, O., Stier, P., Takemura, T., Tie, X., Centre, H., Office, M., Unit, C. C., Sciences, G. E., Northwest, P., Fluid, G., and Arbor, A.: An AeroCom initial assessment - optical properties in aerosol component modules of global models, Atmos. Chem. Phys., 6, 1815–1834, doi:10.5194/acp-6-1815-2006, 2006. 83

Klett, J. D.: Stable analytic inversion solution for processing lidar returns, Appl. Opt., 20, 211–220, 1981. 63

Klett, J. D.: Lidar inversion with variable backscatter/extinction ratios, Appl. Opt., 24, 1638–1643, 1985. 114

Kolb, C. E.: Iodine's air of importance, Nature, 417, 1–2, 2002. 9, 22

Konovalov, I. B., Beekmann, M., Meleux, F., Dutot, A., and Foret, G.: Combining deterministic and statistical approaches for PM_{10} forecasting in Europe, Atmospheric Environment, 43, 6425–6434, doi:10.1016/j.atmosenv.2009.06.039, URL http://dx.doi.org/10.1016/j.atmosenv.2009.06.039, 2009. 28, 83

Kuo, Y.-H. and Anthes, R. A.: Accuracy of diagnostic heat and moisture budgets using SESAME-79 field data as revealed by observing system simulation experiments, Mon. Weather Rev., 112, 1465–1481, 1984. 58

Lahoz, W., Khattatov, B., and Ménard, R. E.: Data Assimilation Making Sense of Observations, Springer, Berlin, Germany, 2010. 41, 57, 112

Lauwerys, R., Haufroid, V., Hoet, P., and Lison, D.: Toxicologie industrielle et intoxications professionnelles, Elsevier-Masson, Issy-les-Moulineaux, France, 2007. 57, 83, 112

Le Dimet, F.-X. and Talagrand, O.: Variational algorithms for analysis and assimilation of meteorological observations: theoretical aspects, Tellus, Ser. A, 38, 97–110, 1986. 112

Lee, K. H., Li, Z., Kim, Y. J., and Kokhanovsky, A.: Atmospheric Aerosol Monitoring from Satellite Observations: A History of Three Decades, in: Atmospheric and Biological Environmental Monitoring, edited by Kim, Y. J., Platt, U., Gu, M. B., and Iwahashi, H., pp. 13–38, Springer, Netherlands, doi:10.1007/978-1-4020-9674-7_2, 2009. 29

Léon, J. F., Chazette, P., Pelon, J., Dulac, F., and Ramdriamarisoa, H.: Aerosol direct radiative impact over the INDOEX area based on passive and active remote sensing, J. Geophys. Res., 107, doi:10.1029/2000JD000116, 2002. 57

Li, Z., Zang, Z., Li, Q. B., Chao, Y., Chen, D., Ye, Z., Liu, Y., and Liou, K. N.: A three-dimensional variational data assimilation system for multiple aerosol species with WRF/Chem and an application to $PM_{2.5}$ prediction, Atmos. Chem. Phys., 13, 4265–4278, doi:10.5194/acp-13-4265-2013, 2013. 51, 84, 100, 112, 113, 114

Lin, C., Wang, Z., and Zhu, J.: An Ensemble Kalman Filter for severe dust storm data assimilation over China, Atmos. Chem. Phys., 8, 2975–2983, 2008. 113

Liu, J. and Kalnay, E.: Simple Doppler wind lidar adaptive observation experiments with 3D-Var and an ensemble Kalman filter in a global primitive equations model, Geophys. Res. Lett., 34, doi:10.1029/2007GL030707, 2007. 65, 66

Liu, Z., Liu, Q., Lin, H.-c., Schwartz, C. S., Lee, Y.-h., and Wang, T.: Three-dimensional variational assimilation of MODIS aerosol optical depth: Implementation and application to a dust storm over East Asia, J. Geophys. Res., 116, 1–19, doi:10.1029/2011JD016159, 2011. 113, 114

Lopatin, A., Dubovik, O., Chaikovsky, A., Goloub, P., Lapyonok, T., Tanré, D., and Litvinov, P.: Enhancement of aerosol characterization using synergy of lidar and sun-photometer coincident observations: the GARRLiC algorithm, Atmospheric Measurement Techniques, 6, 2065–2088, doi:10.5194/amt-6-2065-2013, URL http://www.atmos-meas-tech.net/6/2065/2013/, 2013. 133

Lorenc, A.: Analysis methods for numerical weather prediction, Quart. J. Roy. Meteor. Soc., 112, 1177–1194, 1986. 112

Mallet, V. and Sportisse, B.: Uncertainty in a chemistry-transport model due to physical parameterizations and numerical approximations : An ensemble approach applied to ozone modeling, J. Geophys. Res., 111:D01302, 2006. 39, 41

Mallet, V., Quélo, D., Sportisse, B., Ahmed de Biasi, M., Debry, E., Korsakissok, I., Wu, L., Roustan, Y., Sportisse, B., Sartelet, K., Tombette, M., and Foudhil, H.: Technical Note: The air quality modeling system Polyphemus, Atmos. Chem. Phys., 7, 5479–5487, doi:10.5194/acp-7-5479-2007, 2007. 32, 33, 59, 84, 114

Masutani, M., Woolen, J. S., Lord, S. J., Emmitt, G. D., Kleespies, T. J., Wood, S. A., Greco, S., Sun, H., Terry, J., Kapoor, V., Treadon, R., and Campana, K. A.: Observing system simulation experiments at the National Centers for Environmental Prediction, J. Geophys. Res., 115, doi:10.1029/2009JD012528, 2010. 58, 65

Ménard, R., Cohn, S. E., Chang, L.-P., and Lyster, P. M.: Assimilation of stratospheric chemical tracer observations using a Kalman filter. Part I: Formulation, Mon. Weather Rev., 128, 2654—-2671, 1999. 101, 116

Mishchenko, M. I., Travis, L. D., and Lacis, A. A.: Scattering, Absorption, and Emission of Light by Small Particles, Cambridge University Press, Cambridge, UK, 2002. 80, 88

Mokdad, A. H., James, S. M., Donna, F. S., and Julie, L. G.: Actual Causes of Death in the United States, 2000, J. Amer. Med. Assoc., 291 (10), 1238–1245, doi:10.1001/jama.291.10.1238, 2004. 24

Monahan, E. C., Spiel, D. E., and Davidson, K. L.: A model of marine aerosol generation via whitecaps and wave disruption, in: Oceanic Whitecaps, edited by Monahan, E. C. and Niocaill, G. M., pp. 167–174, Springer Netherlands, Netherlands, 1986. 116

Moulin, C., Lambert, C. E., Dayan, U., Masson, V., Ramonet, M., Bousquet, P., Legrand, M., Balkanski, Y. J., Guelle, W., Marticorena, B., Bergametti, G., and Dulac, F.: Satellite climatology of African dust transport in the Mediterranean atmosphere, Journal of Geophysical Research: Atmospheres, 103, 13 137–13 144, doi:10.1029/98JD00171, URL http://dx.doi.org/10.1029/98JD00171, 1998. 119

Nabat, P., Somot, S., Mallet, M., Chiapello, I., Morcrette, J. J., Solmon, F., Szopa, S., Dulac, F., Collins, W., Ghan, S., Horowitz, L. W., Lamarque, J. F., Lee, Y. H., Naik, V., Nagashima, T., Shindell, D., and Skeie, R.: A 4-D climatology (1979 - 2009) of the monthly tropospheric aerosol optical depth distribution over the Mediterranean region from a comparative evaluation and blending of remote sensing and model products, Atmospheric Measurement Techniques, 6, 1287–1314, doi:10.5194/amt-6-1287-2013, URL http://www.atmos-meas-tech.net/6/1287/2013/, 2013. 120

Nenes, A., Pandis, S., and Pilinis, C.: ISORROPIA: A new thermodynamic equilibrium model for multiphase multi-component inorganic aerosols, Aquat. Geoch., 4, 123—-152, 1998a. 37, 89

Nenes, A., Pilinis, C., and Pandis, S. N.: Continued Development and Testing of a New Thermodynamic Aerosol Module for Urban and Regional Air Quality Models, Atmos. Env., 33, 1553–1560, 1998b. 89

Nicolas, J.: Caractérisation physico-chimique de l'aérosol troposphérique en Méditerranée : sources et devenir, Ph.D. thesis, Univ. Versailles Saint-Quentin, 2013. 121

Nicolet, M.: On the molecular scattering in the terrestrial atmosphere, Planet. Space Sci., 32, 1467–1468, doi:10.1016/0032-0633(84)90089-8, 1984. 80, 88

Niu, T., Gong, S. L., Zhu, G. F., Liu, H. L., Hu, X. Q., Zhou, C. H., Wang, Y. Q., Quality, A., Branch, T., and Satellite, N.: Data assimilation of dust aerosol observations for the CUACE/-dust forecasting system, Atmos. Chem. Phys., 8, 3473–3482, doi:10.5194/acp-8-3473-2008, 2008. 57, 113, 114

Nocedal, J. and Wright, S. J.: Numerical Optimization (2nd ed.), Springer, Berlin, New York, 2006. 45

Pagowski, M. and Grell, G. A.: Experiments with the assimilation of fine aerosols using an ensemble Kalman filter, J. Geophys. Res., 117, 1–15, doi:10.1029/2012JD018333, 2012. 84, 114

Pagowski, M., Grell, G. A., Mckeen, S. A., Peckham, S. E., and Devenyi, D.: Three-dimensional variational data assimilation of ozone and fine particulate matter observations: some results using the Weather Research and Forecasting – Chemistry model and Grid-point Statistical Interpolation, Q. J. R. Meteorol. Soc., 136, 2013–2024, doi:10.1002/qj.700, 2010. 51, 57, 59, 69, 84, 100, 112, 113, 114

Pappalardo, G., Amodeo, A., Ansmann, A., Apituley, A., Arboledas, L., Balis, D., Böckmann, C., Chaikovsky, A., Comeron, A., D'Amico, G., De Tomasi, F., Freudenthaler, V., Giannakaki, E., Giunta, A., Grigorov, I., Gustafsson, O., Gross, S., Haeffelin, M., Iarlori, M., Kinne, S., Linné, H., Madonna, F., Mamouri, R., Mattis, I., McAuliffe, M., Molero, F., Mona, L., Müller, D., Mitev, V., Nicolae, D., Papayannis, A., Perrone, M., Pietruczuk, A., Pujadas, M., Putaud, J. P., Ravetta, F., Rizi, V., Serikov, I., Sicard, M., Simeonov, V., Spinelli, N., Stebel, K., Trickl, T., Wandinger, U., Wang, X., Wagner, F., and Wiegner, M.: EARLINET observations of the Eyjafjallajökull ash plume over Europe, SPIE Proceedings, 7832, doi:10.1117/12.869016, 2010. 76

Park, S. K. and Xu, L.: Data Assimilation for Atmospheric, Oceanic and Hydrologic Applications, Springer, Berlin, Germany, 2009. 41

Parrish, D. F. and Derber, J. C.: The National Meteorological Center's spectral statistical interpolation analysis system, Mon. Weather Rev., 120, 1747–1763, 1992. 68

Péré, J. C., Mallet, M., Pont, V., and Bessagnet, B.: Evaluation of an aerosol optical scheme in the chemistry-transport model CHIMERE, Atmospheric Environment, 44, 3688–3699, doi:10.1016/j.atmosenv.2010.06.034, URL `http://dx.doi.org/10.1016/j.atmosenv.2010.06.034`, 2010. 83

Perez, C., Sicard, M., Jorba, O., Comeron, A., and Baldasano, J. M.: Summertime recirculations of air pollutants over the north-eastern Iberian coast observed from systematic EARLINET lidar measurements in Barcelona, Atmos. Environ., 38, 3983–4000, 2004. 62

Pielke, R. A. and Uliasz, M.: Use of meteorological models as input to regional and mesoscale air quality models - limitations and strengths, Atmospheric Environment, 32 (8), 1455–1466, 1998. 35, 134

Pilinis, C., Capaldo, K. P., Nenes, A., and Pandis, S. N.: MADM-A new Multicomponent Aerosol Dynamics Model, Aerosol Sci. Technol., 32(5), 482–502, 2000. 37

Pop, C. A., Ezzati, M., and Dockery, D. W.: Fine-Particulate Air Pollution and Life Expectancy in the United States, The New England Journal of Medicine, 2009. 24

Putaud, J.-P., Dingenen, R. V., Alastuey, A., Bauer, H., Birmili, W., Cyrys, J., Flentje, H., Fuzzi, S., Gehrig, R., Hansson, H., Harrison, R., Herrmann, H., Hitzenberger, R., Hüglin, C., Jones, A., Kasper-Giebl, A., Kiss, G., Kousa, A., Kuhlbusch, T., Löschau, G., Maenhaut, W., Molnar, A., Moreno, T., Pekkanen, J., Perrino, C., Pitz, M., Puxbaum, H., Querol, X., Rodriguez, S., Salma, I., Schwarz, J., Smolik, J., Schneider, J., Spindler, G., ten Brink, H., Tursic, J., Viana, M., Wiedensohler, A., and Raes, F.: A European aerosol phenomenology – 3: Physical and chemical characteristics of particulate matter from 60 rural, urban, and kerbside sites across Europe, Atmospheric Environment, 44, 1308 – 1320, doi: http://dx.doi.org/10.1016/j.atmosenv.2009.12.011, URL http://www.sciencedirect.com/science/article/pii/S1352231009010358, 2010. 120

Rabier, F., Järvinen, H., Klinker, E., Mahfouf, J. F., and Simmons, A.: The ECMWF operational implementation of four-dimensional variational assimilation. I: Experimental results with simplified physics, Q. J. R. Meteorol. Soc., 126, 1143–1170, 2000. 41

Raes, F., Bates, T., McGovern, F., and Liedekerke, M. V.: The 2nd Aerosol Characterization Experiment (ACE-2): general overview and main results, Tellus, 52, doi:10.1034/j.1600-0889.2000.00124.x, 2000. 30

Ramanathan, V., Crutzen, P. J., Lelieveld, J., Mitra, A. P., Althausen, D., Anderson, J., Andreae, M. O., Cantrell, W., Cass, G. R., Chung, C. E., Clarke, A. D., Coakley, J. A., Collins, W. D., Conant, W. C., Dulac, F., Heintzenberg, J., Heymsfield, A. J., Holben, B., Howell, S., Hudson, J., Jayaraman, A., Kiehl, J. T., Krishnamurti, T. N., Lubin, D., McFarquhar, G., Novakov, T., Ogren, J. A., Podgorny, I. A., Prather, K., Priestley, K., Prospero, J. M., Quinn, P. K., Rajeev, K., Rasch, P., Rupert, S., Sadourny, R., Satheesh, S. K., Shaw, G. E., Sheridan, P., and Valero, F. P. J.: Indian Ocean Experiment: An integrated analysis of the climate forcing and effects of the great Indo-Asian haze, J. Geophys. Res., 106, 28 371–28 398, 2001. 30, 57

Randriamiarisoa, H., Chazette, P., and Mégie, G.: The columnar retrieved single scattering albedo from NO_2 photolysis rate, Tellus, 56, 118–127, 2004. 57

Randriamiarisoa, H., Chazette, P., Couvert, P., and Sanak, J.: Relative humidity impact on aerosol parameters in a Paris suburban area, Atmos. Chem. Phys., 6, 1389–1407, doi:10.5194/acp-6-1389-2006, 2006. 58, 104, 132

Raut, J.-C. and Chazette, P.: Retrieval of aerosol complex refractive index from a synergy between lidar, sunphotometer and in situ measurements during LISAIR experiment, Atmos. Chem. Phys., 7, 2797–2815, doi:10.5194/acp-7-2797-2007, 2007. 57

Raut, J.-C. and Chazette, P.: Assessment of vertically-resolved PM_{10} from mobile lidar observations, Atmos. Chem. Phys., 9, 8617–8638, doi:10.5194/acp-9-8617-2009, 2009. 10, 53, 54, 58, 60, 62, 66, 79, 138

Raut, J.-C., Chazette, P., and Fortain, A.: New approach using lidar measurements to characterize spatiotemporal aerosol mass distribution in an underground railway station in Paris, Atmospheric Environment, 43, 575–583, doi:10.1016/j.atmosenv.2008.10.002, URL http://dx.doi.org/10.1016/j.atmosenv.2008.10.002, 2009a. 53, 83, 84, 133

Raut, J.-C., Chazette, P., and Fortain, A.: Link between aerosol optical, microphysical and chemical measurements in an underground railway station in Paris, Atmospheric Environment, 43, 860–868, doi:10.1016/j.atmosenv.2008.10.038, URL http://dx.doi.org/10.1016/j.atmosenv.2008.10.038, 2009b. 83

Robinson, R. A. and Stokes, R. H.: Electrolyte solutions, Dover Publications, United Kingdom, 2002. 89

Rolph, G. D.: Real-time Environmental Applications and Display sYstem (READY) Website (http://ready.arl.noaa.gov), NOAA Air Resources Laboratory, Silver Spring, MD, 2014. 121

Roustan, Y. and Bocquet, M.: Inverse modelling for mercury over Europe, Atmospheric Chemistry and Physics, 6, 3085–3098, doi:10.5194/acp-6-3085-2006, URL http://www.atmos-chem-phys.net/6/3085/2006/, 2006. 112

Roustan, Y., Sartelet, K., Tombette, M., Debry, E., and Sportisse, B.: Simulation of aerosols and gas-phase species over Europe with the Polyphemus system. Part II : Model sensitivity analysis for 2001, Atmos. Environ., 44(34), 4219–4229, 2010. 40, 57, 112

Royer, P.: Lidars à rétrodiffusion Rayleigh-Mie et Raman mobiles pour l'étude des cycles couplés des aérosols et de la vapeur d'eau, Ph.D. thesis, Université Pierre et Marie Curie, 2011. 30

Royer, P., Chazette, P., Sartelet, K., Zhang, Q. J., and Beekmann, M.: Comparison of lidar-derived PM_{10} with regional modeling and ground-based observations in the frame of MEGAPOLI experiment, Atmos. Chem. Phys., 11, 10 705–10 726, doi:10.5194/acp-11-10705-2011, 2011. 30, 53, 54, 58, 59, 66, 83, 85, 93, 133, 138

Russell, A. and Dennis, R.: NARSTO critical review of photochemical models and modeling, Atmospheric Environment, 34, 2283–2324, 2000. 34, 39

Sachdeva, K. and Attri, A. K.: Morphological characterization of carbonaceous aggregates in soot and free fall aerosol samples, Atmospheric Environment, 42, 1025–1034, 2007. 89

Sartelet, K. N., Hayami, H., Albriet, B., and Sportisse, B.: Development and preliminary validation of a Modal Aerosol Model for tropospheric chemistry: MAM, Aerosol Sci. and Technol., 40(2), 188–127, 2006. 38

Sartelet, K. N., Debry, E., Fahey, K. M., Roustan, Y., Tombette, M., and Sportisse, B.: Simulation of aerosols and gas-phase species over Europe with the Polyphemus system. Part I: model-to-data comparison for 2001, Atmos. Environ., 29, 6116—-6131, 2007. 28, 39, 40, 57, 59, 60, 61, 83, 84, 112, 114

Sartelet, K. N., Couvidat, F., Seigneur, C., and Roustan, Y.: Impact of biogenic emissions on air quality over Europe and North America, Atmospheric Environment, 53, 131–141, doi:10.1016/j.atmosenv.2011.10.046, URL http://dx.doi.org/10.1016/j.atmosenv.2011.10.046, 2012. 39, 40, 85, 109, 120

Satariano, A.: Pollution Particles Lead to Higher Heart Attack Risk, Bloomberg, 2008. 24

Schaap, M., Spindler, G., Schulz, M., Acker, K., Maenhaut, W., Berner, A., Wieprecht, W., Streit, N., Müller, K., Brüggemann, E., Chi, X., Putaud, J. P., Hitzenberger, R., Puxbaum, H., Baltensperger, U., and ten Brink, H.: Artefacts in the sampling of nitrate studied in the "INTERCOMP" campaigns of EUROTRAC-AEROSOL, Atmos. Environ., 48, 6487–6496, 2004. 57, 83, 112

Schell, B., Ackermann, I. J., Hass, H., Binkowski, F. S., and Ebel, A.: Modeling the formation of secondary organic aerosol within a comprehensive air quality model system, J. Geophys. Res., 106, 28 275–28 293, 2001. 32, 37

Schutgens, N. A. J., Miyoshi, T., Takemura, T., and Nakajima, T.: Applying an ensemble Kalman filter to the assimilation of AERONET observations in a global aerosol transport model, Atmos. Chem. Phys., 10, 2561–2576, 2010a. 113, 114

Schutgens, N. A. J., Miyoshi, T., Takemura, T., Nakajima, T., and Science, O.: Sensitivity tests for an ensemble Kalman filter for aerosol assimilation, Atmos. Chem. Phys., 10, 6583–6600, doi:10.5194/acp-10-6583-2010, 2010b. 113, 114

Schwartz, C. S., Liu, Z., Lin, H.-c., and Mckeen, S. A.: Simultaneous three-dimensional variational assimilation of surface fine particulate matter and MODIS aerosol optical depth, J. Geophys. Res., 117, 1–22, doi:10.1029/2011JD017383, 2012. 113, 114, 133, 138

Scott, B. C.: Theoretical estimates for scavenging soefficient for soluble aerosol as function of precipitation type, rate, and altitude, Atmos. Eviron., 16, 1735–1762, 1982. 36

Seigneur, C.: Air pollution: Current challenges and future opportunities, AIChE Journal, 51, 356–364, doi:10.1002/aic.10458, 2005. 33

Seigneur, C., Pun, B., Pai, P., Louis, J.-F., Solomon, P., Emery, C., Morris, R., Zahniser, M., Worsnop, D., Koutrakis, P., White, W., and Tombach, I.: Guidance for the performance evaluation of three-dimensional air quality modeling systems for particulate matter and visibility, J. Air Waste. Manage. Assoc., 50, 588–599, 2000. 39

Seinfeld, J. H.: Air pollution: A half century of progress, AIChE Journal, 50, 1096–1108, doi:10.1002/aic.10102, 2004. 33

Seinfeld, J. H. and Pandis, S. N.: Atmospheric chemistry and physics, Wiley-Interscience, New York, 1998. 33, 36, 37, 83

Sekiyama, T. T., Tanaka, T. Y., Shimizu, A., Miyoshi, T., and Science, O.: Data assimilation of CALIPSO aerosol observations, Atmos. Chem. Phys., 10, 39–49, 2010. 79, 113, 114

Sheridan, P. J., Jefferson, A., and Ogren, J. A.: Spatial variability of submicrometer aerosol radiative properties over the Indian Ocean during INDOEX, J. Geophys. Res., 107, doi: 10.1029/2000JD000166, 2002. 57

Simpson, D., Fagerli, H., Jonson, J. E., Tsyro, S., Wind, P., and Tuovinen, J. P.: Transboundary acidification, euthrophication and ground level ozone in Europe. Part I: unified EMEP model description, Technical Report, EMEP, 2003. 34, 57, 83, 112

Skamarock, W. C., Klemp, J. B., Dudhia, J., Gill, D. O., Barker, D. M., Duda, M., Huang, X. Y., Wang, W., and Powers, J. G.: A Description of the Advanced Research WRF Version 3, NCAR Technical Note, URL `http://www.mmm.ucar.edu/wrf/users/docs/arw_v3.pdf`, 2008. 35, 85

Sportisse, B.: A review of parameterizations for modelling dry deposition and scavenging of radionuclides, Atmospheric Environment, 41, 2683–2698, 2007a. 35

Sportisse, B.: A Review of current issues in air pollution modeling and simulation, Computational Geoscience, 11, 159–181, 2007b. 9, 37, 38, 41

Sportisse, B.: Pollution atmosphérique : des processus à la modélisation, Springer, Paris, 2008. 9, 33

Sportisse, B., Debry, E., Fahey, K., Roustan, Y., Sartelet, K., and Tombette, M.: PAM project (Multiphase Air Pollution): description of the aerosol models SIREAM and MAM, Tech. rep., CEREA, 2006a. 38

Sportisse, B., Debry, E., Fahey, K., Roustan, Y., Sartelet, K., and Tombette, M.: Rapport du projet Primequal-Predit PAM (Pollution Atmosphérique Multiphasique). Modélisation, Tech. rep., CEREA, 2006b. 38

Stockwell, W. R., Kirchner, F., Kuhn, M., and Seefeld, S.: A new mechanism for regional atmospheric chemistry modeling, Journal of Geophysical Research, 102(D22), 25 847–25 879, 1997. 39

Stromatas, S., Turquety, S., Menut, L., Chepfer, H., Pépé, J. C., Cesana, G., and Bessagnet, B.: Lidar signal simulation for the evaluation of aerosols in chemistry-transport models, Geosci. Model Dev., 5, 1543—-1564, doi:10.5194/gmd-5-1543-2012, 2012. 83

Sugimoto, N. and Uno, I.: Observation of Asian dust and air-pollution aerosols using a network of ground-based lidars (ADNet): Realtime data processing for validation/assimilation of chemical transport models, IOP Conf. Series: Earth and Environmental Science, 7, doi: 10.1088/1755-1307/7/1/012003, 2009. 113

Talagrand, O.: Assimilation of observations, an introduction, J. Meteor. Soc. Japan, 75, (1B), 191–209, 1997. 41, 112

Tan, D. G. H., Andersson, E., Fisher, M., and Isaksen, L.: Observing system impact assessment using a data assimilation ensemble technique: application to the ADM-Aeolus wind profiling mission, Q. J. Roy. Meteorol. Soc., 133, 381–390, 2007. 58

Timmermans, R. M. A., Segers, A. J., Builtjes, P. J. H., Vautard, R., Siddans, R.and Elbern, H., Tjemkes, S. A. T., and Schaap, M.: The added value of a proposed satellite imager for ground level particulate matter analyses and forecasts, IEEE J. Sel. Topics Appl. Earth Obs. Remote Sens., 2, 271–283, 2009. 58

Tombette, M., Chazette, P., Sportisse, B., and Roustan, Y.: Simulation of aerosol optical properties over Europe with a 3-D size-resolved aerosol model: comparisons with AERONET data, Atmos. Chem. Phys., 8, 7115–7132, doi:10.5194/acp-8-7115-2008, 2008. 39, 51, 79, 80, 83, 85, 89, 90, 100

Tombette, M., Mallet, V., and Sportisse, B.: PM_{10} data assimilation over Europe with the optimal interpolation method, Atmos. Chem. Phys., 9, 57–70, doi:10.5194/acp-9-57-2009, 2009. 40, 43, 51, 57, 59, 60, 62, 67, 72, 84, 100, 110, 112, 113, 114, 115, 116, 126, 133, 136

Trémolet, Y.: Accounting for an imperfect model in 4D-Var, Q. J. R. Meteorol. Soc., 132, 2483–2504, doi:10.1256/qj.05.224, 2006. 49

Twomey, S.: The influence of pollution on the shortwave albedo of clouds, Journal of the Atmospheric Sciences, 34(7), 1149—-1152, 1977. 23, 26

Vautard, R., Moran, M. D., Solazzo, E., Gilliam, R. C., Matthias, V., Bianconi, R., Chemel, C., Ferreira, J., Geyer, B., Hansen, A. B., Jericević, A., Prank, M., Segers, A., Silver, J. D., Werhahn, J., Wolke, R., Rao, S., and Galmarini, S.: Evaluation of the meteorological forcing used for the Air Quality Model Evaluation International Initiative (AQMEII) air quality simulations, Atmospheric Environment, 53 (0), 15 – 37, 2012. 33

Venkatram, A. and Pleim, J.: The electrical analogy does not apply to modelling dry deposition of particles, Atmospheric Environment, 33, 3075–3076, 1999. 35

Viskari, T., Asmi, E., Kolmonen, P., Vuollekoski, H., Petäjä, T., and Järvinen, H.: Estimation of aerosol particle number distributions with Kalman Filtering – Part 1: Theory, general aspects and statistical validity, Atmos. Chem. Phys., 12, 11 767–11 779, doi:10.5194/acp-12-11767-2012, 2012. 114

Wang, H. and Niu, T.: Sensitivity studies of aerosol data assimilation and direct radiative feedbacks in modeling dust aerosols, Atmospheric Environment, 64, 208–218, doi:10.1016/j.atmosenv.2012.09.066, URL http://dx.doi.org/10.1016/j.atmosenv.2012.09.066, 2013. 113, 114

Wang, K. C., Dickinson, R. E., and Liang, S. L.: Clear sky visibility has decreased over land globally from 1973 to 2007, Science, 323, 1468–1470, 2009. 83, 112

Wang, Y., Sartelet, K. N., Bocquet, M., and Chazette, P.: Assimilation of ground versus lidar observations for PM_{10} forecasting, Atmos. Chem. Phys., 13, 269–283, doi:10.5194/acp-13-269-2013, 2013a. 83, 84, 100, 102, 112, 113, 114, 115, 116, 122

Wang, Y., Sartelet, K. N., Bocquet, M., and Chazette, P.: Modelling and assimilation of lidar signals over Greater Paris during the MEGAPOLI summer campaign, Atmos. Chem. Phys. Discuss., 13, 27 115–27 161, doi:10.5194/acpd-13-27115-2013, 2013b. 114, 115, 116, 118, 128, 132, 133

Wesely, M. L.: Parameterization of surface resistance to gaseous-dry deposition in regional scale numerical models, Atmospheric Environment, 23, 1293—-1304, 1989. 35

Williams, K., Fairchild, C., and Jaklevic, J.: Dynamic mass measurement techniques, in: Aerosol Measurement: Principles, techniques and applications, edited by Willeke, K. and Baron, P. A., Van Norstrand Reinhold, New York, 1993. 28

Winker, D. M., Couch, R. H., and McCormick, M. P.: An overview of LITE: NASA's Lidar In-space Technology Experiment, Proc. IEEE., 84, 164–180, 1996. 69

Winker, D. M., Pelon, J., and McCormick, M. P.: The CALIPSO mission: Spaceborne lidar for observation of aerosols and clouds, Proc. SPIE, 4893, doi:10.1117/12.466539, 2003. 29, 57

Winker, D. M., Hunt, W. H., and McGill, M. J.: Initial performance assessment of CALIOP, Geophysical Research Letters, 34, doi:10.1029/2007GL030135, URL http://dx.doi.org/10.1029/2007GL030135, 2007. 83

Wiscombe, W. J.: Improved Mie scattering algorithms, Applied Optics, 19(9), 1505–1509, 1980. 80

Wu, L., Mallet, V., Bocquet, M., and Sportisse, B.: A comparison study of data assimilation algorithms for ozone forecasts, J. Geo. Res., 113, 1–17, doi:10.1029/2008JD009991, 2008. 43, 51, 58, 59, 67, 100, 113

Yarwood, G., Rao, S., Yocke, M., and Whitten, G.: Updates to the Carbon Bond Chemical Mechanism: CB05 Final Report to the US EPA, RT-0400675, URL http://www.camx.com/publ/pdfs/CB05_Final_Report_120805.pdf, 2005. 32, 39, 59, 84, 115

Zhang, Y., Liu, P., Liu, X. H., Jacobson, M. Z., McMurry, P. H., Yu, F., Yu, S., and Schere, K. L.: A comparative study of nucleation parameterizations : 2. three-dimensional model application and evaluation, J. Geophys. Res., 115:D20213, 2010a. 36

Zhang, Y., McMurry, P. H., Yu, F., and Jacobson, M. Z.: A comparative study of nucleation parameterizations : 1. examination and evaluation of the formulations, J. Geophys. Res., 115:D20212, 2010b. 36

Zhang, Y., Bocquet, M., Mallet, V., Seigneur, C., and Baklanov, A.: Real-time air quality forecasting, part II: State of the science, current research needs, and future prospects, Atmos. Environ., 60, 656–676, 2012. 51, 57

Zhang, Y., Sartelet, K., Zhu, S., Wang, W., Wu, S.-Y., Zhang, X., Wang, K., Tran, P., Seigneur, C., and Wang, Z.-F.: Application of WRF/Chem-MADRID and WRF/Polyphemus in Europe – Part 2: Evaluation of chemical concentrations, sensitivity simulations, and aerosol-meteorology interactions, Atmos. Chem. Phys., 13, 6845–6875, doi:10.5194/acp-13-6845-2013, 2013. 85

Zupanski, M.: Maximum Likelihood Ensemble Filter: Theoretical Aspects, Monthly Weather Review, 133, 1710–1726, doi:http://dx.doi.org/10.1175/MWR2946.1, 2005. 134